UNIVERSITY OF SOUTHAMPTON

FACULTY OF ENGINEERING, SCIENCE AND MATHEMATICS

School of Chemistry

Synthesis and Characterisation of New Framework Materials

By

Kate Victoria Redrup

Thesis for the Degree of Doctor of Philosophy

June 2009

UNIVERSITY OF SOUTHAMPTON

ABSTRACT

FACULTY OF ENGINEERING, SCIENCE & MATHEMATICS
SCHOOL OF CHEMISTRY
Doctor of Philosophy

SYNTHESIS AND CHARACTERISATION OF NEW FRAMEWORK MATERIALS

by Kate Victoria Redrup

Inorganic framework materials, with structures based on arsenate and phosphate, AsO_4 and PO_4, tetrahedra and a variety of octahedral metal units, such as hafnium, niobium and iron, have been synthesised and fully characterised. These materials have been synthesised by solvothermal techniques and the principal analytical technique to characterise the resulting single crystals has been Single Crystal X-ray Diffraction. Supporting analysis was carried out, using techniques such as Powder and Neutron Diffraction, Thermogravimetric Analysis, Electron Dispersive Spectroscopy and Infrared Spectroscopy.

Of the hafnium arsenates and phosphates that have been synthesised, several are fluorinated and one is templated, such as $Hf_2F_2(H(PO_4)_2)(NH_4)_2$ and $[Hf_2F_8(AsO_4)][DABCO\text{-}H_2](NH_4)$ respectively. Similar layered frameworks have also been characterised and reported for titanium, zirconium and niobium. These structures all offer ion exchange potential, due to their ammonium cations and/or water molecules.

The hydrogen iron phosphates that are discussed include two novel frameworks and one material which offers an improved model for the mineral lipscombite, $Fe_{1.34}(PO_4)OH_{0.96}$. One of the new frameworks presented, $(NH_4)_3Fe3(HPO_4)_6$, offers particularly interesting potential applications as a high capacity battery material *via* lithium exchange reactions.

The hydrothermal synthesis of two novel hydrated sodium tungstate structures is also discussed. One of these materials was found to contain a very high H : Na ratio, resulting in strong hydrogen bonding and a densely packed framework, which may be of interest in the field of high density liquids.

ACKNOWLEDGEMENTS

I am indebted to a great number of people who have helped me during the course of this research and it is probably impossible for me to thank every one of them individually. If I forget to mention anyone here, please accept my apologies and many thanks to anyone I have inadvertently omitted from this list.

Firstly, many thanks are due to my supervisor, Prof. Mark Weller, who oversaw my work and who provided me with support, advice and ideas along the way

Huge thanks are also due to the University of Southampton Crystallography Department, especially Dr. Mark Light, for trusting me with their machines and putting up with me asking for technical help whenever there was a problem with the equipment. I am also very grateful for the expert advice on solving one or two particularly awkward crystal structures.

Thanks are due, of course, to members of the Weller group, both past and present, for all of their help and also the regular tea breaks when some time off was needed. Thanks in particular must go to Bob and Rina for their advice in the early days, to Jenny and Valeska for the proof-reading and to Jess, Rosa and Eleni for being there over the last three years, whether for scientific advice or just a chat.

Thank you to Dr. Robert Raja and Dr. Paul Wright for not making my viva too much of a nightmare and also for the helpful comments.

Massive thanks are due to my parents and brother who helped to make my PhD possible with all their support and encouragement over the years. I wouldn’t have got this far without you.

Finally, extra-special thanks to David, who was always there for support and also to provide tea and cake, which definitely helped the writing of this thesis along. You’re a star.

Contents

Contents for Figures and Tables

Page

Chapter 1 **Introduction**

Page

Chapter 2 **Experimental Techniques**

Page

Chapter 3 Group IV and V Arsenate Frameworks

Page

Chapter 4 Group IV and V Phosphate Frameworks

Page

Chapter 5 Group IV and V Templated Frameworks

Page

Chapter 6 Iron Phosphate Materials

Page

Chapter 7 Sodium Tungstate Materials

Chapter 1

Introduction

1.1-General Introduction

Inorganic materials chemistry is made up of a wide variety of different categories of compounds. These can range from open frameworks, such as zeolites, to the more densely packed structures of complex metal oxides for use in batteries or as superconductors. Most of these materials are crystalline, which is a major factor in defining both the chemical and physical properties that are exhibited. Inorganic materials have potential for many different applications. In order to exploit their properties in applications, research needs to be carried out into the synthesis of novel materials with either new, or to improve existing, properties. As well as producing new structures in order to introduce new, and also improve, existing properties, such work can also lead to an insight into a better understanding of the formation of this type of framework.

Many inorganic materials can be described as comprised of linked polyhedra, commonly tetrahedra and/or octahedra. For example, naturally occurring zeolites are made up of frameworks of aluminate and silicate TO_4 tetrahedra, (where T is a tetrahedral cation). Synthetic analogues are commonly used as molecular sieves due to their porosity. Layered oxide materials, such as Ruddlesden-Popper phases are also known. These are layered perovskite structures containing corner-sharing octahedra and can display unusual electronic properties.

1.2-Framework Materials

Over the last thirty years, the field of open-framework inorganic materials chemistry has vastly expanded. As well as aluminosilicate zeolites, aluminium phosphates and systems related to these, there are now documented frameworks based on over 25 different elements, including both main block and transition metal elements. These systems may be anything from simple, "zero-dimensional" structures with discrete units to complex, three-dimensional frameworks. In recent years, open-framework structures have been developed that are not limited to oxygen-containing phases such as phosphates. For example, structures which are linked through nitride and sulphide frameworks have been synthesised. The increase in the number of known systems has led to an inevitable increase in the type of structural units that have been found. As well as the traditional linked tetrahedral units, there are now known octahedral and pentahedral units.

The first microporous framework materials to be formally identified were the zeolites. There are known to be over forty common structure topologies of these naturally-occurring aluminosilicate structures. As well as naturally-occurring zeolites, there are also over 130 synthetic framework structures that have been described. These are documented by the International Zeolite Association[1]. In 2006, eight companies in the United States reported mining a total of 63,200 tonnes of natural zeolites. A further three companies were reported to be working from stockpiled materials[2]. Approximately 55,800 tonnes of this total was sold in the United States. Animal feed, pet litter and water purification accounted for almost 70 % of the tonnage sold within the United States.

All zeolites, whether natural or synthetic, share the same basic general formula. This can be described as $\{[M^{n+}]_{x/n}\cdot[m\mathrm{H_2O}]\}\{[\mathrm{AlO_2}]_x[\mathrm{SiO_2}]_{1-x}\}$, (where M = metal cation, m, n and x = integers), which shows the three components that make up a zeolite structure. These are respectively the charge-balancing cations, usually from Group 1 or 2, the absorbed water and the framework itself.

Under mild hydrothermal conditions Al–O–Al linkages are forbidden, which makes the maximum allowed Al : Si ratio 1. This is known as Löweinstein's Rule of

Aluminium Avoidance, which is well-known in mineralogy. The ratio of silicon to aluminium can result in a wide range of properties. For example, the more aluminium that is present within the framework, the greater the hydrophilicity of the material. This is caused by the larger negative charge on the framework and the extra framework cations which coordinate strongly to water. This hydrophilicity results in an ability to take up water, leading to uses as molecular sieves[3]. Sodium zeolite A has a small pore size (≈ 4 Å) and is able to reversibly absorb water molecules. The absorbed water can be readily removed by heating, thus making Zeolite A a drying agent that is easy to regenerate. However, structures with a high level of aluminium tetrahedra will not be stable in acidic conditions because the H^+ cations will attack the oxygen atoms which lie adjacent to the aluminium centres, thus dissolving the structure and causing the framework to break down. Hydrophobic zeolites can also be found, in the form of silicon-rich frameworks.

The majority of the current research into zeolites focuses on producing similar frameworks but with substituted elements, in order to obtain a wider range of properties. At the same time, it is desirable to maintain the thermal and chemical stability of the natural zeolites that makes them so useful in industrial applications[4]. There have now been over 25 different elements incorporated into synthetic zeolites[5]. These are main block or transition metal elements and these new structures are mainly based on oxygen-containing materials, such as phosphates. Recently, other units to link the metal centres have been considered, such as oxyfluorides, nitrides and sulfides. After full characterisation, synthetic analogues of natural zeolites have also been produced in recent years, allowing possible exploitation of useful properties[6]. As previously mentioned, zeolites have many industrial uses. These materials are easy to produce using mild hydrothermal conditions and are, thermally, very stable. Aluminosilicates are also more environmentally friendly, by breaking down into soil-like minerals, than materials with similar properties, such as polyphosphates that are used for ion exchange.

Framework materials can have large, complicated unit cells but all zeolites are made up of a combination of simple building blocks. These are known as secondary building units (SBUs) and are, in turn, made up of the TO_4 tetrahedra, which are the primary building units[7, 8]. Only the tetrahedral aluminium and silicon atoms are considered in SBUs. Figure 1.1 shows the finite units that have been found to make up these tetrahedral frameworks, where the tetrahedral oxygen atoms are omitted for simplicity. These SBUs contain up to 16 T-atoms and make the assumption that the entire structure is made up of only one type of SBU. For example, zeolite A is commonly described as being made up of β-cages; these are larger units which are made up of a combination of the 4- and 6-ring SBUs, as shown in Figure 1.1. Figure 1.2 shows a representation of the β-cages as part of the overall structure of Zeolite A and also depicts the SBUs that make up these cages. It may be seen that an arrangement of eight β-cages forms one large unit that subsequently surrounds an α-cage, in which a cation such as Na^+ or K^+ may be present, which may easily by exchanged for other cations, leading to uses such as water purification or as molecular sieves.

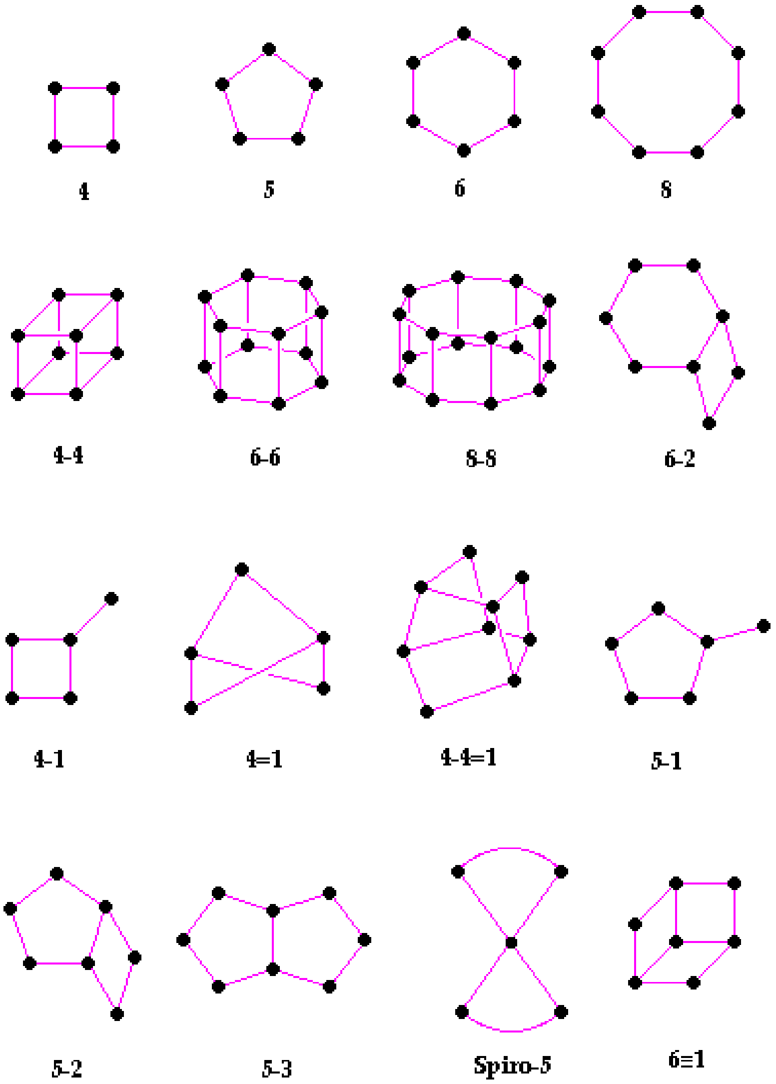

Figure 1.1: Secondary Building Units in zeolites, where the corners of the polyhedra represent tetrahedral atoms.

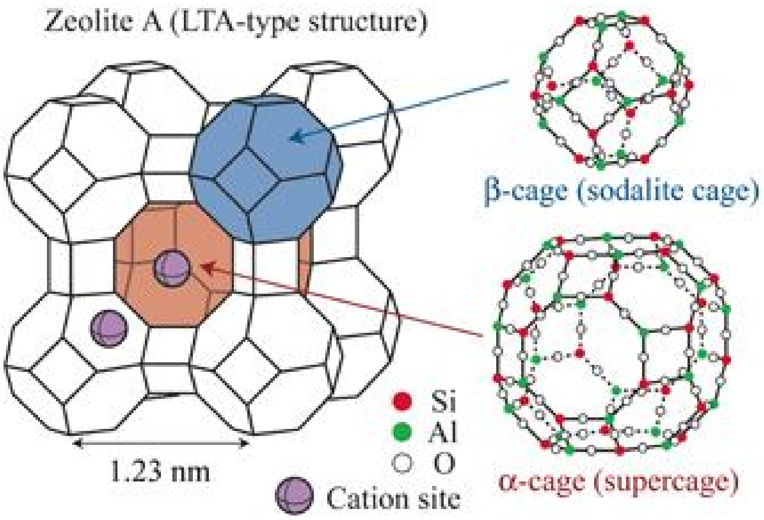

Figure 1.2-Representation of Zeolite A, showing both the α- and β-cages[9].

In zeolites with different sized cavities and channels, it is possible to manipulate their selective molecular adsorption properties, for molecules or ions other than water. Zeolites can have pore sizes of up to ≈ 7 Å[10], thus allowing a wide range of ions or molecules, such as Group 1 and 2 cations, CO_2, methanol and small hydrocarbons, to be present. The charge-balancing cations found within the zeolite structure only have a weak interaction with the framework so may undergo exchange reactions, thus further altering the properties of the material. This principle is used in detergents and water softeners and purification, which often contain zeolite A, for replacing the Ca^{2+} and Mg^{2+} ions that are present in hard water. Ion exchange removes the cations and prevents them from forming an insoluble "scum" with the surfactant. Zeolites are able to participate in ion exchange at low temperatures, making them ideal for these industrial uses. Annually, the world-wide production of zeolite A for detergent applications alone exceeds 250, 000 tonnes[11].

Another common use of zeolite frameworks is in catalysis. For example, ZSM-5, $Na_n[Al_nSi_{96-n}O_{192}]\cdot{\approx}16H_2O$ ($n < 27$), is a synthetic zeolite which is used, amongst other things, to catalyse the conversion of methanol to hydrocarbons for motor fuels[3]. It is the acidic form of zeolites that are often used as catalysts. If the zeolite itself has acidic properties, it may be used as a heterogeneous catalyst, or it can be used as part of a multiphase catalyst. Here, the large surface area of the zeolite can be exploited by acting as a support for another catalytic material[12]. Acidic zeolites can be used to catalyse reactions that are commonly associated with very strong acids, such as dehydration and isomerisation. However, ion exchange between zeolites and strong acids is not possible. As previously mentioned, the exchange of H^+ with the cations in a zeolite can cause the framework to be destroyed.

The crystalline zeolite lattice has a fixed geometry, which results in selectivity over which reagents are able to enter the pores. This will, in turn, affect the products that can easily leave the pores once they have formed. In some reactions, it is even possible to be specific enough so that a zeolite can strongly favour a particular isomer. ZSM-5 is a common zeolite that is widely used in the petroleum industry. The channels in ZSM-5 have a diameter of ≈ 5.4 Å, which favour the 1,4-dimethylbenzene isomer over the 1,2 and 1,3 forms by $\approx 10^4:1$. The 1,4-isomer is narrower than the others, causing it to be less hindered as it passes through the zeolite channels[13]. The production of a specific isomer can affect the overall outcome of a reaction. If certain intermediates do not fit into the zeolite pores, the reaction mechanism will be forced to change, possibly leading to a different final product.

Clinoptilolite, $(Na,K,Ca)_{2-3}Al_3(Al,Si)_2Si_{13}O_{36}\cdot 12(H_2O)$, and mordenite, $(Ca,Na_2,K_2)Al_2Si_{10}O_{24}\cdot 7H_2O$, are two examples of naturally-occurring aluminosilicates that have interesting synthetic equivalents. These synthetic zeolites have been shown to have useful industrial properties, due to their stability, lack of toxicity and evenly-spread and sized pores.

Reaction under hydrothermal conditions has recently become a popular route for the synthesis of metal frameworks. These are formed from a variety of species such as TiO_n, VO_n and ZnO_n, often in combination with oxotetrahedral species such as PO_4^{3-} and SiO_4^{4-}. For example, numerous zinc phosphates have been synthesised in this manner producing a vast range of structures and compositions formed from the linked polyhedra[14] including 0-D monomers, 1-D chains, 2-D layers or 3-D structures[15]. Variation of the hydrothermal conditions, *e.g.* temperature, solvent and pH, can allow the nature of the product to be determined by influencing reaction outcomes such as the particle size and water content[16]; the degree of condensation and, thus, the dimensionality of any framework can also be controlled. This effect of pH on dimensionality can be seen for many open framework metal phosphates, such as zinc and cobalt phosphates[17], where amines, which can also act as templates, can be used to alter and control the pH of the reaction mixture. This control of dimensionality and pore size has permitted the synthesis of structures that may be exploited in applications such as shape- or size-selective catalysis and in molecular recognition uses[18].

When researching new inorganic frameworks, one of the main objectives is to be able to find new advantageous properties, whilst not losing any of the primary benefits of basic zeolite chemistry. These investigations can take many paths, such as incorporating a different metal or altering the pore size and this is often achieved by varying the reaction conditions used in the synthetic process.

1.3-Transition Metal Arsenate and Phosphate Framework Materials

The first non-zeolite framework materials to be synthesised and studied were the aluminium phosphates, AlPOs. In recent years, extensive research has been carried out into the aluminophosphate ($AlPO_4$) family[19] and there are now over 200 open-framework aluminophosphates that have been characterised[20]. In these materials, both the aluminium and phosphorus are present with tetrahedral coordination, forming AlO_4 and PO_4 units, which result in a neutrally-charged framework, as shown in Figure 1.3. $AlPO_4$ is isoelectronic with SiO_2, thus meaning that aluminophosphate analogues of zeolite frameworks may be synthesised. Naturally-occurring zeolites generally have a low ratio of Si : Al and can usually be reproduced synthetically under hydrothermal conditions. By altering the reaction conditions, such as temperature, pH or time of reaction, a variety of low-silica aluminosilcate zeolites can be produced. This principle was then applied to many reactions over the next couple of decades, which is where much of the research into synthesising and characterising this huge family of open-framework structures began.

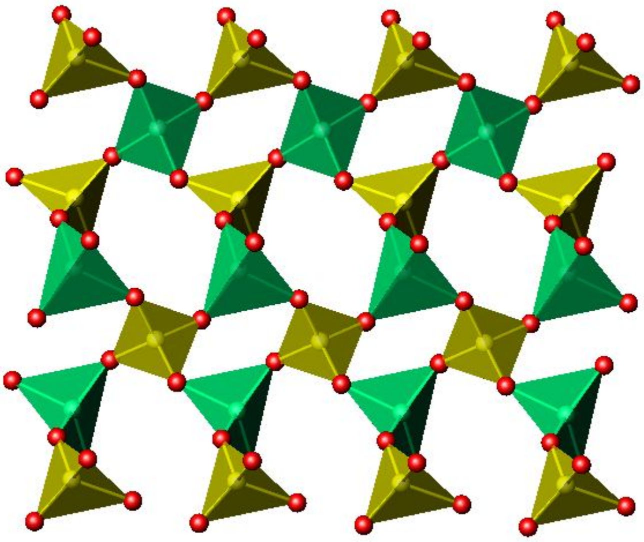

Figure 1.3: Structure of $AlPO_4$ viewed down the *a*-axis, where the aluminium tetrahedra are shown in pale green, the phosphate tetrahedra in yellow and the oxygen atoms in red.

However, this family of AlPOs must also meet the requirements of Löwenstein's Rule[21], so that Al–O–Al bonds are avoided and the framework is made up of Al–O–P linkages. The similarities between these frameworks and the isoelectronic silicas led to the development of a new group of microporous materials[22], $AlPO_4$-*n*, where *n* refers to a structural type, which may be either two- or three-dimensional. A number of the frameworks that were synthesised were found to be structurally related to the zeolite family, such as the sodalite type ($AlPO_4$-20) and the analcime type ($AlPO_4$-24) structures[23], thus resulting in interest for potential industrial uses similar to those known for zeolites. Therefore, the aluminophosphate family of materials has potential applications such as molecular sieves, adsorbants in molecular separations or catalysts and catalyst supports, resulting from their surface selectivity characteristics.

In the mid-1980s, research into this type of framework was extended to microporous phosphates that contained other elements besides simply aluminium and phosphorus. The first metal to be incorporated into the family of $AlPO_4$-*n* structures was gallium[24], with the series $GaPO_4$-*n*. The families of metal phosphates were divided into three groups, depending on the type of metal-centred polyhedra in the framework. The groups were classified by frameworks made up of a) alternating corner-sharing tetrahedra, b) densely-packed structures which contained only octahedra and tetrahedra and also c) frameworks that consisted of a combination of 4-, 5- and 6-coordinated metal polyhedra and PO_4 tetrahedra. Within this study, it was found that the frameworks were the same for both $AlPO_4$-12 and $GaPO_4$-12, which was also predicted to be the case for the other materials in the analogous aluminium and gallium series.

By the end of the 1980s, work had progressed to arsenate analogues of these materials and both alumino-[25,26] and galloarsenates[27], $AlAsO_4$-1, $AlAsO_4$-2 and $GaAsO_4$-2, had been reported. Both of the aluminoarsenates cited here were synthesised hydrothermally using organic templates to produce single crystals. It was found that they were both made up of three-dimensional open frameworks with channels present, in a very similar way to the original $AlPO_4$ structures. The same outcome was also seen in the production of $GaAsO_4$-2, as would have been expected due to the similarity in chemistry of aluminium and gallium and also phosphorus and arsenic. The primary difference between using aluminium and gallium is the coordination number of the metal. Aluminium phosphates are found with a tetrahedral metal, whereas gallium may be four-, five- or six-coordinate.

After the investigation of aluminum and gallium frameworks, both phosphates and then arsenates, the general opinion was that the discovery of these materials was only the start of a very large and potentially lucrative family of nanoporous crystalline materials. The next logical step was to look at the way in which indium, again in Group 13, reacted in similar processes. Due to its larger size, it was predicted that indium phosphates would contain only octahedral metal environments. The first work to confirm this was the synthesis of $H_3NCH_2CH_2NH_3[In_2(HPO_4)_4]$[28]. The crystalline product was once again produced hydrothermally, using ethylenediamine (en) as a template, with the en being incorporated into the channels of the final open-framework.

The synthetic route to make these phosphate materials[29] is similar to the one commonly used to produce zeolites. The aluminophosphates are synthesised hydrothermally under autogeneous pressure, in the temperature range 100-250 °C. The temperature, pH, reaction duration and reactant composition can all affect the outcome of the reaction.

However, the first synthetic variable to be altered was the solvent, with studies being conducted which investigated the effect of changing the solvent[30]. All of the early phosphate compounds were synthesised by using water as the main solvent in the reactions. It was found that some control may be had over the structure and size of the crystals by changing the solvent. The early solvents tested were mainly alcohols and were generally found to improve the crystallisation process. When choosing a solvent to use, it is first necessary to find a solvent which is suitable for all of the starting materials, organic as well as inorganic if they are present. Many hybrid reactions are carried out in non-aqueous or mixed solvents, such as has been the case with purely inorganic frameworks for many years. More recently, ionic liquids have also been shown to be effective as solvents in both inorganic[31], and hybrid[32] reactions. For example, 1-methyl, 3-ethyl imidazolium bromide was used as both a solvent and templating agent in the formation of the zeolite SIZ-1, as demonstrated by Cooper *et al.* Two new iron oxalatophosphates were synthesised by Sheu *et al* using a mixture of choline chloride and malonic acid as the solvent, showing that ionic solvents can also be used in the formation of this type of hybrid framework.

There are many other possible alterations that may be made to the reaction conditions of this type of solvothermal synthesis[33], such as pH, solvent, concentration, temperature and length of the reaction. One particular study comprehensively researched several of these factors, by looking at the effect of pH, temperature, concentration and time on the synthesis of cobalt succinates[34]. During the work detailed in this piece of literature, it was found that the reagent ratios and the temperature of the reaction played the greatest role in altering the outcome of the reaction, which supports the idea that thermodynamic factors are important in hybrid synthesis. This is the opposite to inorganic frameworks, where hydrothermal crystallisation often proceeds kinetically. As for the length of the reaction, it was concluded that the reactions were all more or less complete after twenty-five hours. It was found that a high pH favoured the formation of the desired extended inorganic hybrid frameworks, where the M–O–M linkages are formed by the elimination of water or hydroxide groups due to condensation. The role played by the duration of the reactions was found to be minor, again supporting the thermodynamic theory. Finally, this study also concluded that the concentration of the reagents made little difference to the phases that were formed. It was found that once sufficient succinic acid had been added to neutralise the hydroxide ions of the cobalt (II) hydroxide, there was little change in the resulting phases if additional acid was added.

The influence of pH on hydrothermal reaction chemistry has also been studied[35]. It was concluded that the acidity has a pronounced effect on the outcome of the reaction where, for example, particle size and the morphology of the product can be influenced. The pH of the reaction mixture has also been found to be a factor in the dimensionality of framework structures. For example, pH-regulated reactions of metal phosphates that include an amine in the reaction mixture can form 0-D, 1-D or 2-D structures[36]. The effect of pH on the formation of dawsonite, $MAl(OH)_2CO_3$, (M = Na, K, NH_4), has also been investigated[37]. In this study, it was found that the greater the alkalinity of the reaction, the greater the yield of the desired product, with the optimum pH found to be 10.8. However, the highest level of crystallinity was found to occur at pH 10.3. Reactions that contain phosphates as one of the starting materials are particularly susceptible to the influence of pH. In strongly basic solutions the PO_4^{3-} anion predominates while in strongly acidic conditions, aqueous H_3PO_4 predominates. In a weakly basic or weakly acidic case, HPO_4^{2-} and $H_2PO_4^-$ will be the main components respectively[38,39]. Thus, by controlling the pH of a metal phosphate solution it is possible to control the nature of (hydrogen-)phosphate species incorporated into any framework structure crystallised from it under hydrothermal conditions.

Fluoride sources have been used in phosphate reactions for their mineralising properties since the end of the 1980s[40,41]. As well as having a mineralising or structure-directing[42] effect, the fluoride anion was also thought to have a catalytic role. This was seen in the synthesis of $AlPO_4$-14A, where the fluoride is necessary for the formation of the product but is not present in the final framework[43]. The synthesis of new alumino- and gallophosphates which incorporate fluoride into their open frameworks was achieved by the fluoride's ability to stabilise the cages of polyhedra that form the channels within the structure.

The fluoride may either form an M–F–M linkage or be present as an anion within the channel, where it may or may not be weakly bonded to the metal. In the case of the former, the presence of a fluoride greatly alters the environment in which the metal is found, resulting in an increase in its coordination, such as from five- to six-coordination in the case of CJ2[44,45], where the fluoride anions may either fully occupy their sites or partially share them with hydroxyl groups. In the latter case, the structure-directing role of the anion causes much larger cavities to be present, with a far more extended cage and a three-dimensional channel system, as in cloverite[46], which may be of industrial use due to the ability to accommodate larger intermediates in zeolite catalytic processes.

Another useful feature of fluorinated materials is that the fluoride anion is able to form strong hydrogen bonds with the rest of the framework. This means that there are readily available anchoring points at which amines or ammonium cations, (which may exist within cavities or channels), may be stabilised within the structure, through hydrogen bonding *via* the N–H groups to the highly electronegative fluorine atoms.

During the early 1990s, the research into phosphates broadened to include metals other than those in Group 13. Within the mineral world, iron phosphates are very widespread and are one of the most important families of materials after silicates and aluminates. They are discussed in greater detail in Section 1.8. There are many natural and synthetic iron phosphates, which have octahedral metal groups and tetrahedral phosphates. The frameworks may be either open or densely-packed. An example of an open-framework is cacoxenite[47], $[AlFe_{24}(OH)_{12}(PO_4)_{17}(H_2O)_{24}]\cdot 51H_2O$, which is a common mineral, most commonly found in gossans, heavily decomposed rocks in the exposed part of an ore deposit. After single crystal analysis, this framework was found to contain huge cylindrical channels, with a diameter of over 14 Å, which contain the water molecules. When the first synthetic iron phosphates were produced, it became clear that these open-framework structures would have applications in the catalysis sector, such as in the oxidative dehydrogenation of isobutyric acid into methacrylic acid[3], where dense iron phosphates are used as selective catalysts.

Once research progressed to investigating the Group 4 metals, it was found that materials which were made up of tetravalent metal cations and phosphate groups possessed two-dimensional features, such as layered structures. This was shown during work that studied the ion exchange properties of these materials[48]. The Group 4 metals are discussed in more detail in Sections 1.4, 1.5 and 1.6. Once the crystal structures of these layered titanium and zirconium phosphates had been understood, it was possible to appreciate the ion exchange reactions, which had previously been only poorly understood. It was found that proton-containing layered materials possessed good ion exchange properties, as did those frameworks which were made up of organic and inorganic layers. These structures were found to once again have potential uses in the ion exchange, catalysis and sensor fields.

One further, and very current, application for metal arsenates is their possible role as decontaminants of aqueous ecosystems and human body fluids[49]. The solubility of arsenic compounds may be used to control both their form and mobility. During this study, solid metal arsenates were dissolved into solutions with differing concentrations of arsenic acid. The saturated solutions were then analysed to calculate to solubility products and, therefore, the effectiveness of each material at removing arsenic waste from an aqueous environment. This study showed that stable metal arsenates, such as $Fe(AsO_4H)^+$ and $Zn(AsO_4H)$, could be used to remove arsenic from an aqueous environment.

As has been displayed above, the use of phosphate reagents in the synthesis of framework materials is significantly more common than the use of analogous arsenate species. On the other hand, investigations into arsenate systems have shown that they may often offer advantages over their phosphate counterparts. They have regularly been found to be successfully synthesised under milder conditions than the phosphate versions of these species. This phenomenon is displayed by the 3-D framework $Li_3Fe_2(XO_4)_3$, (X = P or As), which has been synthesised by solid-state methods[50]. The arsenate analogue was successfully produced with a reaction temperature of 1133 K, whereas the phosphate material required a temperature of 1203 K. Work which investigated the mild hydrothermal synthesis of $Mn_7(HOAsO_3)_4(AsO_4)_2$ has also shown a similar outcome[51]. The results of this study showed that single crystals of the arsenate were produced with a reaction temperature of 443 K at autogeneous pressure. However, the phosphate analogue could not be made under these relatively mild conditions. In order for this species to be synthesised, it was necessary to heat the reaction mixture in a gold capsule to temperatures of between 473 and 873 K, with reaction pressures of 300-600 atm. Single crystals were not present, so analysis of the phosphate was carried out via powder X-ray diffraction.

Both of the examples described above are characteristic of the general trend that arsenate materials require less severe reaction conditions than those needed by their phosphate equivalents. Therefore, it may be expected that a wide range of arsenate materials are likely to be discovered when using conventional solvothermal techniques, such as those used in the synthesis of $Mn_7(HOAsO_3)_4(AsO_4)_2$, where these structures are likely to differ from the wide variety of phosphates that have been reported. The procedures employed to produce these new frameworks may then be modified in order to produce a route to synthesise isostructural compounds. Therefore, arsenate hydrothermal chemistry presents a good starting point for the synthesis of novel and potentially useful framework structures.

In spite of the greater success when working with arsenates than phosphates, it is not necessarily the case that the existence of a phosphate framework guarantees the feasibility of the arsenate analogue. Nor is it the case that the phosphate and arsenate reagents may simply be interchanged to produce analogous results. There are several others factors that also need to be taken into account. For example, an As–O bond is longer and also has a weaker bond affinity in comparison with a P–O bond. This may result in different structures being produced. For example, the mixed arsenate-phosphate species $[Fe_2(AsO_4)_{1.54}(PO_4)_{0.46}F_2(H_2O)](C_2H_{10}N_2)$ is synthesised using an As : P ratio of 2 : 1 but the final product sees a ratio of 3.3 : 1. This is an indication that, under the conditions used, there is a bonding preference for arsenate over phosphate[52]. Another difference between arsenic and phosphorus is their standard potentials. Phosphorus may adopt an oxidation state of +1, +2, +3, +4 or +5, whereas arsenic may only exist as +1, +3 or +5, (in their positive forms). This wider range of possible oxidation states may alter the reaction pathway that is taken under hydrothermal conditions in the formation of a phosphate when compared with the analogous arsenate reaction. The common starting materials arsenic acid (H_3AsO_4) and phosphoric acid (H_3PO_4) possess different pK_a values, 2.248 and 2.148 respectively, meaning that phosphoric acid will dissociate to a greater extent within a reaction mixture. This subtle difference would result in a more acidic solution for a phosphate-based reaction, which could in turn result in the formation of different materials for the analogous arsenic acid- and phosphoric acid-based reactions.

1.4-Titanium Phosphate Frameworks

Titanium has long been of interest as a framework component, particularly due to its potential as a substitute for silicon, owing to the availability of a +4 oxidation state and its similarity in size. The substitution of titanium into zeolites and microporous titanosilicates has been particularly documented, such as in the case of ETS-4 and ETS-10, both of which have shown catalytic properties[53,54]. Titanium phosphates have also been shown to have ion exchange and adsorptive properties, such as in α-$Ti(HPO_4)_2$[55] and γ-$Ti(H_2PO_4)(PO_4)\cdot H_2O$[56].

Until recently, there were only a few synthetic examples of open-structured titanophosphates; the first being two rubidium titanium phosphate phases, $Rb_2Ti_3O_2(PO_4)_2(HPO_4)_2$ and $Rb_3Ti_3O(P_2O_7)(PO_4)_3$[57]. After these first discoveries, various layered and porous structures were developed. The first microporous titanophosphate was reported just ten years ago and was synthesised hydrothermally using 1, 3-diaminopropane as an organic template[58]. The final structure, TPO-1, contains mixed valent titanium cations, with both +3 and +4 being present, resulting in a final formula of $Ti(III)Ti(IV)(PO_4)(HPO_4)_2(H_2O)_2\cdot(NH_2CH_2CH_2CH_2NH_2)_{0.5}$. The TPO-1 framework is made up of titanium octahedra and tetrahedrally coordinated phosphorus centres which form channels within the structure that contain diaminopropane units. This material was also found to possess both catalytic and magnetic properties.

Another synthetic titanophosphate that had been reported and was found to contain filled channels is TJPU-2, $[NH_4][Ti(III)Ti(IV)(H_2O)_2(PO_4)(HPO_4)]$, which again contains mixed valence titanium cations[59]. This hydrothermal synthesis used Zn(II) as a mineraliser, in the form of $ZnCl_2$, and resulted in the formation of blue rectangular single crystals. The framework was found to have chains of alternating titanium and phosphorus polyhedra running along the *b*-axis, causing 12-ring channels to form in the framework. The channels were calculated to have a maximum diameter of 8.5 Å, which are partially filled by ammonium cations, each of which was found to have 0.125 occupation.

There have been other titanophosphate materials reported that contain these large rings, which subsequently result in channels within the framework. These rings may be even larger than the 12-membered one reported above. $[Ti_3(PO_4)_4(H_2O)_2]{\cdot}NH_3$ and $(NH_4)_2[(Ti_3O_2)(HPO_4)_2(PO_4)_2]$ were both synthesised hydrothermally and are made up of 16- and 24-membered pores respectively[60]. The channels in the first of these two structures are filled by ammonia molecules, whereas the channels in the second contain ammonium cations to charge-balance the framework.

Potassium titanyl phosphate, $KTiOPO_4$, (KTP), is a non-linear optical material which has received much attention over the last twenty years[61] and its structure is shown in Figure 1.4. KTP belongs to a family of materials which has the general formula $M\mathrm{TiO}X\mathrm{O}_4$, (where M may be K, Rb, Tl, NH_4 or partial Cs and X may be P or As[62]. These non-linear properties exist due to the presence of two formula units in the asymmetric unit, resulting in a correct solid-state formula of $K_2(TiOPO_4)_2$. KTP is synthesised either by flux methods or hydrothermally and its structure is made up of TiO_6 octahedra which are linked to one another by alternating long and short Ti–O bonds, giving rise to the material's non-linear optical properties. The octahedra are linked by phosphate bridges, leading to an open framework. It is within the resulting cavities that there are cations, which charge-balance the structure. The open nature of the basic $TiOPO_4$ framework has led to many studies into the feasibility of the modifying the internal structural characteristics. By altering the cation species that is present in the channels, it may be possible to achieve gas-phase adsorption and desorption. This was seen in a study aimed at substituting ammonium cations into the channels, where large single crystals of $(NH_4)(TiOPO_4)_2$ were synthesised, demonstrating that chemical modification of the KTP structure is possible to alter the non-linear properties[61]. Due to these properties, KTP-type materials have been widely applied in commercial and military laser systems which require high power, high efficiency and durability[63].

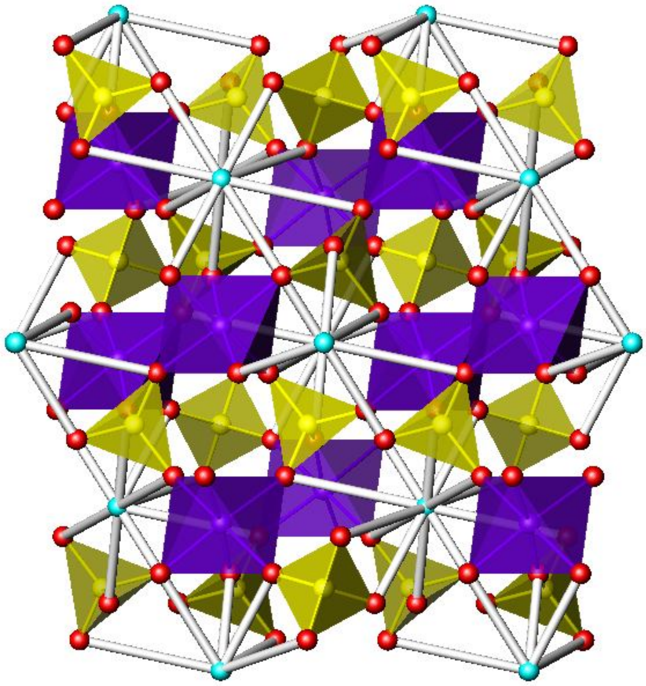

Figure 1.4: Structure of KTP[64] viewed down the *a*-axis, where the titanium octahedra are shown in purple, the phosphate tetrahedra in yellow, the oxygen atoms in red and the potassium cations in pale blue.

1.5-Zirconium Phosphate Frameworks

One of the recently well-studied zirconium phosphate structures is in fact the pyrophosphate ZrP_2O_7[65]. The pyrophosphate family of frameworks has attracted much attention in the last few years due to the presence of phases which display negative thermal expansion. However, the phosphates that will be discussed within this work are the layered type, of which there are only relatively few simple examples, such as $SrZr(PO_4)_2$[66]. This strontium zirconium diorthophosphate framework was synthesised via solid-state methods and analysed by powder X-ray diffraction. Many of the studied structures contain multiple charge-balancing species. The framework consists of linked ZrO_7 and PO_4 polyhedra which form the layered structure, with strontium cations present between the layers to charge-balance the overall material.

There are in fact two different types of crystalline layered phosphates, and more specifically, this has commonly been found to be the case for zirconium layered phosphates. These are the α-type compounds, which have the general formula α-$M(IV)(HPO_4)_2 \cdot H_2O$, (with M = Ti, Zr, Sn, Pb, *etc.*), and the γ-type compounds, which have the general formula γ-$M(IV)(PO_4)(H_2PO_4)_2 \cdot 2H_2O$, (with M = Ti, Zr)[67], where the protons of the dihydrogen phosphate groups are exchangeable. When these layered M(IV) phosphates are converted to their respective insoluble acid salts, in particular the α-type, they have been found to possess interesting properties[68]. These salts display characteristics typical of an intercalating agent and may be considered as hosts for the design and preparation of supramolecular solids with various functions[69]. There are also several potential applications for the α-type M(IV) phosphates when they are not present as salts but in their acid forms. There has been interest in using these materials as highly selective ion exchangers and protonic conductors[70].

Although it is well-known that hydrogen phosphates generally form layered structures when present alongside tetravalent metal cations, there are also some examples of three-dimensional frameworks, such as τ-$Zr(HPO_4)_2$[67]. This structure was found to be made up of ZrO_6 octahedra and PO_4 tetrahedra, forming a four-membered ring channel along the *c*-axis. The hydroxyl groups on the hydrogen phosphate tetrahedra were determined to point into the channels and form hydrogen bonds across them.

Although there were a few positive early results, little work has been carried out that looks into templated zirconium phosphates. One of the first to be synthesised was a one-dimensional double-stranded polymer, with the formula $[ZrF_2(PO_4)(HPO_4)][enH_2]_{1.5}$[71], which was produced under solvothermal conditions. Four years on, a series of organically templated zirconium fluoride phosphates was reported[72], which used a fluoride source as a mineraliser. All of the structures in this series contained the basic $[Zr_2(PO_4)(HPO_4)_2F_x]\cdot nH_2O$ framework, with various amine groups acting as templates and present in the structural cavities. Of particular interest is $[(CH_3)_2NH(CH_2)_2NH(CH_3)_2]_{0.5}[Zr_2F_2(PO_4)(HPO_4)_2]\cdot 0.5H_2O$, which forms a layered structure. The layers are formed by alternating ZrO_5F octahedra and PO_4 and HPO_4 tetrahedra, which are connected to one another via bridging oxygen atoms. These layers then form weak hydrogen bonds to the protonated template units which are present between the layers.

Nonaqueous, solvothermal syntheses have also been successfully employed in the production of templated zirconium phosphates[73], such as the two dimensional $[NH_4]_2[H_3N(CH_2)_2NH_3]_2[Zr_3(OH)_6(PO_4)_4]$, which again used a fluoride mineralising agent. This layered structure is made up of alternating $ZrO_4(OH)_2$ octahedra and PO_4 tetrahedra which build up to an infinite, two-dimensional layer, formed from eight- and four-membered rings. The template cations are present between these sheets, with an equal number of NH_4^+ and $[H_3N(CH_2)_2NH_3]^{2+}$ cations found to hydrogen-bond to the polyhedral oxygen atoms, which act to both charge-balance and strengthen the framework as a whole. These two different types of cation, with different charges, lead to potential ion exchange properties.

Although only layered zirconium phosphates have been discussed above, they may actually exist as one-, two- or three-dimensional frameworks[74]. However, it has been found that the octahedral coordination of zirconium generally lends itself to chain or layered formations, rather than three-dimensional, open-frameworks. However, it has been known for an open-framework to develop if one of more of the octahedral oxygen or fluorine atoms is terminal rather than bridging, such as in the templated $[C_5H_{16}N_2]_{0.5}[Zr_3(PO_4)_3(HPO_4)F_2])\cdot 1.5H_2O$[75].

As previously discussed, it is sometimes relatively easy to synthesise a metal arsenate but it is far harder to produce the analogous phosphate material. Although there has been little work on the corresponding arsenate structures, there are still one or two examples. This ease of synthesis is displayed by the hydrothermal synthesis of $[Zr_3(AsO_4)_4(H_2O)_2]\cdot 2H_2O$[76]. During this study, it was not possible to produce and characterize the zirconium phosphate with the same Zr : P ratio, 3 : 4, as seen for the arsenate.

1.6-Hafnium Arsenate and Phosphate Frameworks

Very little work has been reported on the synthesis or characterisation of hafnium arsenates and phosphates. Although there is not a great deal of specific information available for these materials, much of what is known about inorganic frameworks in general and, more specifically, arsenate and phosphate frameworks may be carried over into this area of work. These principles are discussed above in Sections 1.1-1.3. However, more is known about hafnium phosphates than arsenates so these shall be discussed here first.

As with zirconium, hafnium may form layered phosphate materials, such as α-$Hf_2O(PO_4)_2$. This material has been characterised *via* Rietveld analysis of powder X-ray and neutron diffraction patterns, having been synthesised by using solid-state methods[77]. The structure of α-$Hf_2O(PO_4)_2$, shown in Figure 1.5, was almost identical to that of the isotypic α-$Zr_2O(PO_4)_2$. However, on further heating of the sample, above 1773 K, an irreversible transition to the β-phase occurred, resulting in the transformation of the very distorted HfO_6 octahedra to HfO_7 polyhedra, whereas this change occurs at a considerably lower temperature, 1373 K, in the zirconium phosphate.

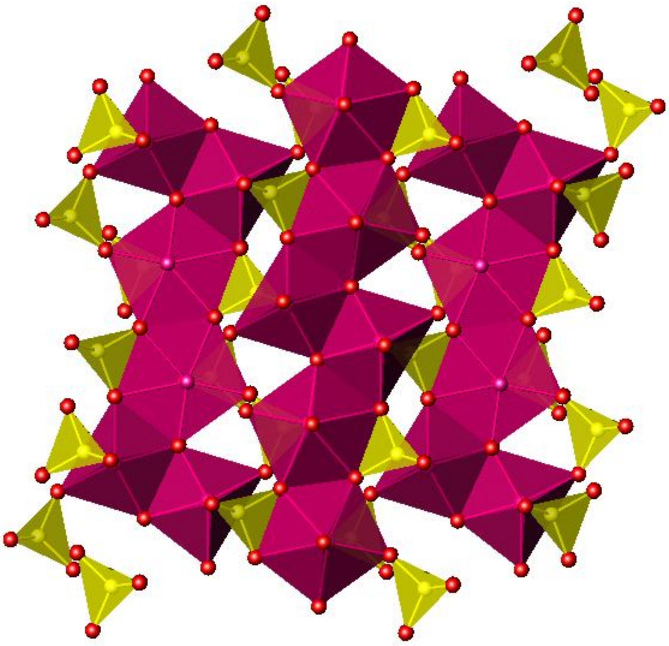

Figure 1.5: Structure of α-$Hf_2O(PO_4)_2$ viewed down the *b*-axis, where the hafnium polyhedra are shown in magenta, the phosphate tetrahedra in yellow and the oxygen atoms in red.

The structure of α-$Hf(HPO_4)_2{\cdot}H_2O$ has been suggested as having a zeolitic-type structure[78]. This is due to the presence of the cavities within the framework, where the active centres, (the hydrogen atoms), of the material are located. It is inside these cavities that the water molecules are positioned, thus hydrogen-bonding to the hydrogen atoms of the HPO_4 groups. This was confirmed by the neutron data collected as the hydrogen atom positions were able to be fully refined.

A further, well-discussed example of a hafnium phosphate is $Hf(PO_4)(H_2PO_4){\cdot}2H_2O$[79], which was prepared via a partially substituted γ-hafnium phosphate sodium phase, which was first synthesised following a reflux method which had previously been used in the production of a γ-zirconium phosphate[80]. This was the first report of a γ-type hafnium phosphate and, as well as discussing the crystal structure, this study also looked at the intercalation properties of this material. The structure of this framework was determined via powder X-ray diffraction and the structural parameters of the zeotypic zirconium phosphate[81] were used in the Rietveld refinement. $Hf(PO_4)(H_2PO_4){\cdot}2H_2O$ is isostructural with the zirconium analogue, so it was concluded that this framework has a layered structure, built from HfO_6 octahedra and phosphate and dihydrogen phosphate tetrahedra. The water molecules which exist between the layers are hydrogen-bonded to the oxygen atoms of the polyhedra. After the full characterisation of $Hf(PO_4)(H_2PO_4){\cdot}2H_2O$, its intercalation properties were investigated and this was achieved by studying the reaction products when various alkylamines and cyclic amines was incorporated into the reaction. The subsequent X-ray analysis showed that new phases were present which had greater interlayer distances than the starting phosphate. The conclusion of this piece of work was that $Hf(PO_4)(H_2PO_4){\cdot}2H_2O$ displayed behaviour as an intercalation host that makes it a potential precursor for the insertion of large species into the interlayer space.

The crystal structure of $LiHf_2(PO_4)_3$ has been investigated for its electrical properties[82] and was found to undergo a high-temperature phase change, where the framework adopts a rhombohedral structure similar to the NASICON, sodium superionic conductor, materials[83]. The principle difference between the structure of $LiHf_2(PO_4)_3$ and that of a NASICON material is the location of the cation[84]. Here, the lithium cations are displaced from their expected, central position with respect to one of the metal sites and are randomly disordered. The result of this disorder is that the structure of the overall framework changes, which has important implications for the ionic conductivity properties of the material. The low-temperature phase of $LiHf_2(PO_4)_3$ is triclinic. The framework is built up of HfO_6 octahedra and PO_4 tetrahedra and contains ordered lithium cations, which are five-fold coordinated to the polyhedral oxygen atoms. Although the lithium cations are ordered within the channels, this low-temperature phase is a very poor ionic conductor due to narrow channels so that the Li^+ motion may not occur properly. In comparison, the disordered lithium cations in the high-temperature phase cause the framework to be more suitable for Li^+ movement, thus increasing the conductivity properties.

In one of the very few literature examples of the occurrence of a hafnium arsenate, the thermodynamic properties of one particular structure, $Hf(AsO_4H)_2$, have been studied[85]. The α-type layered material $Hf(AsO_4H)_2$ was synthesised according to an earlier technique for zirconium hydrogen phosphate[86]. A solution of $Hf(AsO_4H)_2$ was measured calorimetrically to derive the standard enthalpy of formation, which was then used to calculate the dehydration enthalpy of the monohydrate, $Hf(AsO_4H)_2 \cdot H_2O$. These calculations were also carried out for the phosphate analogue.

1.7-Niobium Arsenate and Phosphate Frameworks

There are examples of both niobium arsenates and phosphates but, as is often the case with transition metals, there are far more phosphate structures known. Crystalline niobium phosphates, both the α- and γ-types, have been of recent interest because of their potential applications is areas such as luminescence[87,88], non-linear optical materials[89], ion-exchange and heterogenous catalysis[90].

Probably the most simple of these is $NbOPO_4$, of which there are two known phases[91]. This structure undergoes a readily reversible phase transition at 565 K and its symmetry changes from monoclinic to orthorhombic. Both phases of this material are based on corner-sharing NbO_6 octahedra and PO_4 tetrahedra, which form a three-dimensional framework. It has been shown that this structure possesses negative thermal expansion properties, thought to result from either a decrease in the Nb–O–Nb bond angles or shorter Nb–O bonds as the temperature is increased. It was observed that this behaviour was strongest in the higher temperature, orthorhombic phase, as would be expected, and this was seen at 673-973 K. Within this temperature range, there was no evidence of a decrease in either the Nb–O–Nb or Nb–O–P bond angles and there was also no shortening of the Nb–O bond lengths. However, a significant reduction in the P–O bond lengths was observed, from 1.535 to 1.495 Å over this 300 K temperature range. Although these values were not accurate enough to be used quantitatively, the data could still be used to support a model for the negative thermal expansion of the unit cell above 673 K. This effect was concluded to be due to the thermal motion of the oxygen atoms in the Nb–O–P linkages, where the P–O lengths decrease but the Nb–O bond lengths do not alter at all. A similar effect had previously been observed for $Y_2W_3O_{12}$, where the W–O bond lengths decreased as the temperature is increased but the Y–O lengths did not[92].

Niobium phosphates are most commonly synthesised via either solid-state or flux reactions. However, there are a few examples of structures which have been synthesised hydrothermally[93] and then analysed *via* single crystal diffraction. It has generally been found that relatively low temperature hydrothermal syntheses, (< 533 K), of niobium phosphates require a mineraliser such as HF_2^- in order to be successful; this has recently been shown for two organically-templated niobium phosphates[94,95]. The first of these, $[(NbOPO_4)_4{\cdot}(H_3NCH_2CO_2H)_2][PO_4H_2][OH, F]$, contains fluoride ions only in the interlayer regions. However, the second of these structures, $[H_3N(CH_2)_2NH_3]NbCoOF(PO_4)_2(H_2O)_2$, is more interesting as the fluoride anions actually form part of the niobium polyhedra. By using low temperature hydrothermal syntheses, it is possible to use organic templates, which increases the possibility of synthesising novel open-framework niobium phosphates which would be both more chemically and thermally stable.

Even more recently, the synthesis of two novel fluorinated niobium phosphates has been reported[96]: $Ba_2[NbOF(PO_4)_2]$ and $Ba_3[Nb_3O_3F(PO_4)_4(HPO_4)]{\cdot}7H_2O$. These frameworks were both synthesised under relatively low temperature hydrothermal conditions, resulting in layered structures. In the first of these materials, the main structure was built up from NbO_5F octahedra and phosphate tetrahedra, with interlayer barium cations. The layers were found to be held together by Ba–O and Ba–F bonds. In the second material discussed in this paper, there were found to be both NbO_5F and NbO_6 octahedra and also both PO_4 and HPO_4 tetrahedra. Once again, there were found to be barium cations between the layers of the framework but there were also disordered water molecules present. In both of these materials, the interlayer cations are exchangeable with other ions, providing possible ion exchange applications.

At least three novel niobium arsenate frameworks have previously been reported when investigating the $Na_2O–Nb_2O_5–As_2O_5$ system: $Na_3NbO(AsO_4)_2$[97], $Na_2NbO_2AsO_4$[98] and $NaNb_4O_9AsO_4$[99], all of which were synthesised *via* solid-state methods. The first of these exists as a three-dimensional framework built up from corner-sharing NbO_6 octahedra and AsO_4 tetrahedra, which results in three different channels running along [100], [010] and [001]. At the point at which these three tunnels intersect, six-coordinate sodium cations are located in two different environments. The second structure, $Na_2NbO_2AsO_4$, consists of a very similar structure, again being made up of chains of NbO_6 octahedra and PO_4 tetrahedra, as shown in Figure 1.6. However, there are now three different Na^+ environments occupying the interlayer space rather than the two seen in $Na_3NbO(AsO_4)_2$. The third of these frameworks, $NaNb_4O_9AsO_4$, is again made up of similar NbO_6 and AsO_4 building blocks, resulting in a corner-sharing chain. The three-dimensional network also has large cavities, of maximum diameter 2.87 Å, in which lie both five- and seven-coordinate sodium cations. All three of these structures may be considered for their ion exchange properties, in which the Na^+ may be replaced by a different cation of the same charge.

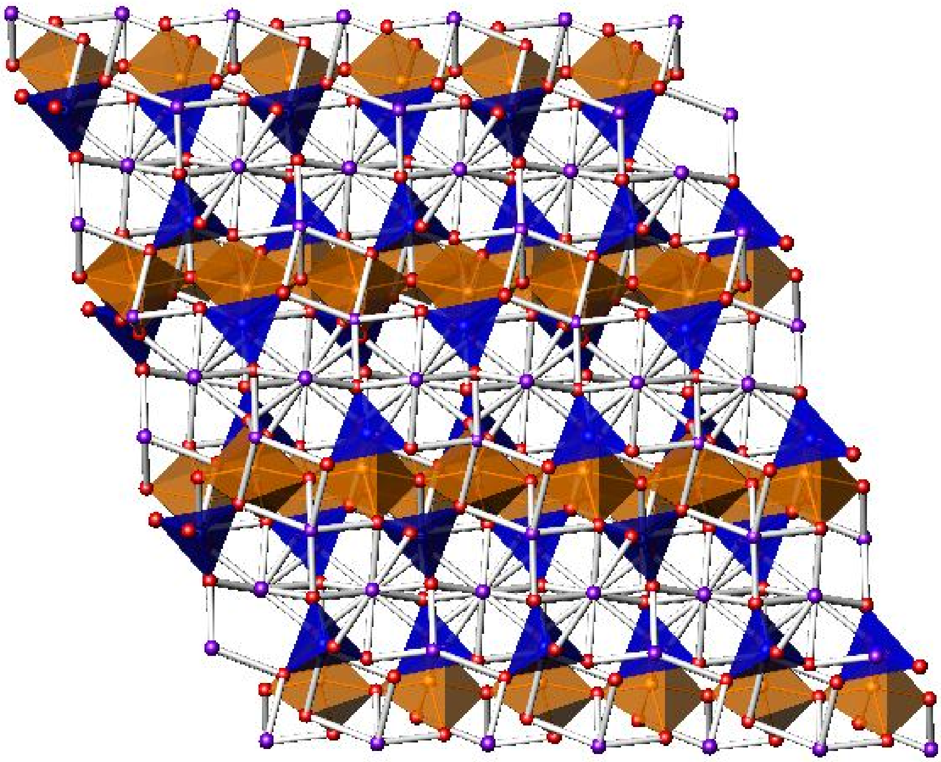

Figure 1.6: Structure of $Na_2NbO_2AsO_4$ viewed down the *b*-axis, where the niobium octahedra are shown in orange, the arsenate tetrahedra in blue, the sodium cations in purple and the oxygen atoms in red.

1.8-Natural and Synthetic Iron Phosphate Frameworks

As mentioned in Section 1.3, phosphate research was broadened to include iron as the metal. There are many natural species which contain iron phosphates, over one hundred of which have been structurally analysed. There are now also many synthetic iron phosphates, both novel and analogous to natural frameworks.

Oxoframework materials with small channels, such as NASICON, $Na_3Zr_2Si_2PO_{12}$[100], and ETS-1[101] have been of interest over the last few years. This is primarily due to their useful properties: high ionic mobility in the case of NASICON and ionic exchange ability in ETS-1. One family of oxoframework materials which is currently of considerable interest is the iron phosphates, which are formed from linked PO_4 tetrahedra and, primarily, FeO_6 octahedra. This family has been well-known in preventing and slowing corrosion of metal surfaces which are in regular contact with water[102]. Iron phosphates have also been of recent interest in terms of their magnetic properties[103]. The complex iron phosphate hydrogen-phosphate $NaFe_2(PO_4)(HPO_4)$[37], prepared under hydrothermal conditions, shows antiferromagnetic interactions with a μ_{eff} of 6.21 μ_B at 27 °C. This structure consists of a double-layered framework, with FeO_4 and PO_4 tetrahedra bonded together via the Fe–O–P and Fe–O–Fe bonds.

More recently, iron phosphates have been investigated in terms of their use in rechargeable lithium batteries[104, 105, 106] and their potential use as either the anode[107] or the cathode[108]. $LiFePO_4$ provides an attractive material for rechargeable batteries as all of the elements are naturally abundant, inexpensive and of low toxicity. When the material is fully charged, it is also able to provide a cell voltage, versus Li, of 3.5V[109]. $LiFePO_4$ is found as a naturally occurring mineral, as a member of the olivine-type family; synthetic versions may easily be obtained by reaction of $Li(OH)\cdot H_2O$ and H_3PO_4 at high temperature[110], followed by the addition of an alcoholic solution of iron (III) acetylacetonate. Various synthetic routes have been investigated with the aim of optimising the properties of $LiFePO_4$, particularly its conductivity. Direct solid-state reactions[111], hydrothermal syntheses[112] and sol-gel methods[111] have all been studied and intercalation of lithium into iron phosphates, such as $FePO_4$, also provide a possible route to cathode materials of this type. The lithium insertion chemistry of an iron phosphate with the composition $Fe_{1.19}PO_4F_{0.11}(OH)_{0.46}(H_2O)_{0.43}$, which adopts a structure related to that of the natural mineral lipscombite, has also recently been investigated[113] and was found to develop a similar cell-voltage to that of $LiFePO_4$.

There are a number of well-documented iron phosphate minerals[114]. These vary from the compositionally simple barbosalite $Fe_3(PO_4)_2(OH)_2$[115,116], to the more complex, lipscombite solid solution, which includes $Fe_{1.176}(PO_4)(OH)_{0.57}(H_2O)_{0.43}$[113], shown in Figure 1.7. The structure of $Fe_3(PO_4)_2(OH)_2$ has been determined from single crystal X-ray diffraction and shown to contain both Fe^{2+} and Fe^{3+}. The structure of lipscombite has been analysed by powder X-ray diffraction and this phase can also contain mixed valence iron centres. The solid solution general formula of lipscombite can be represented by $Fe_{2-y}(PO_4)[OH,F,H_2O]$ and formally the structure consists of chains of face-sharing FeO_6 octahedra, though adjacent iron sites are only partially occupied. However, synthetic analogues of lipscombite have only previously been analysed by powder X-ray diffraction.

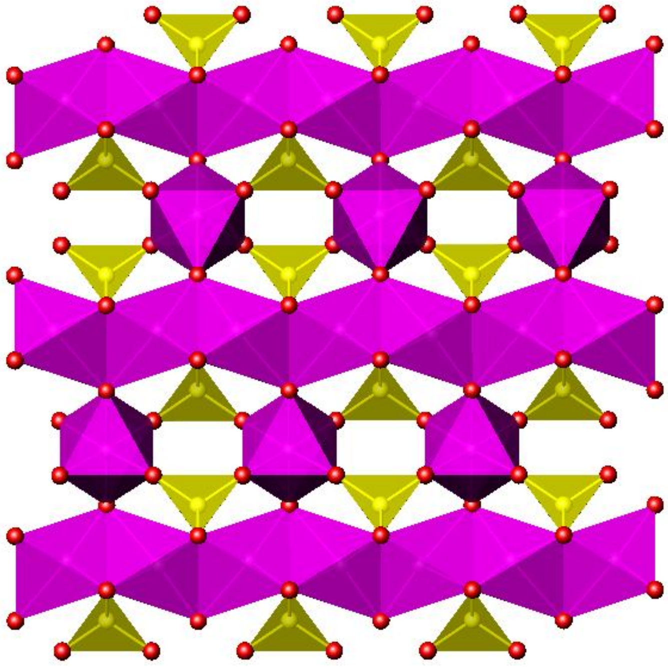

Figure 1.7: Structure of lipscombite, with the formula $Fe_{1.176}(PO_4)(OH)_{0.57}(H_2O)_{0.43}$ viewed down the *a*-axis[113], where the iron octahedra are shown in pink, the phosphate tetrahedra are shown in yellow and the oxygen atoms are shown in red.

Much of the early work on synthetic iron phosphates concentrated on mineral-like compounds that were templated by alkali metals, such as the caesium-templated framework $CsFe_3(PO_4)_3(H_2O)_2$[117] and the sodium-templated $Na_7Fe_4(PO_4)_6$[118]. More recent work has been primarily aimed at hybrid organic-inorganic frameworks. There are literature examples of iron phosphate structures which incorporate organic sub-units such as oxalate[119] and bipyridyl[120] ions.

1.9-Sodium Tungstate Materials

The sodium tungstate materials presented in this work are more generically known as polyoxometallate (POM) structures. These POM clusters are a large family of compounds based on transition metal oxo-anions connected through oxygen and have been extensively studied since their discovery in 1826[121]. Families of compounds within the POM grouping include the Keggin anions, the Dawson clusters and the parent isopolyacids. Contemporary interest has focused on attempting to functionalise these materials in terms of their electronic and magnetic properties. For example, the synthesis of a new polyoxovandate, $K_{10}[H_2V_{16}O_{38}]\cdot 13H_2O$, has recently been reported and studied, with respect to potentially useful magnetic properties[122], where strong intramolecular antiferromagnetic exchange interactions between the vanadium atoms were expected.

The ability of Group V and VI metals, particularly vanadium, molybdenum and tungsten, to form isopoly acids and their salts in aqueous solutions at intermediate and low pHs, is well-known. On dissolving either molybdenum or tungsten oxides in strongly alkaline solutions, tetrahedral MO_4^{2-} ions are formed, from which the simple sodium tungstates, such as Na_2WO_4[123], can be crystallised. At lower, intermediate pHs, polymerisation takes place and crystallisation of POM salts is possible[124], while at very low pHs the metal oxide is precipitated from solution. The behaviour of these systems at intermediate pHs can be illustrated by considering a solution of the sodium tungstate salt $Na_{10}[W_{12}O_{36}(OH)_{10}]\cdot 23H_2O$[125]. As the pH of such a solution is decreased, the ψ-*meta*-tungstate ion, $[H_3W_6O_{21}]^{3-}$, forms, which then transforms to the *meta*-tungstate ion, $[W_{12}O_{38}(OH)_2]^{6-}$. As pH 1 is reached, tungsten (VI) oxide is precipitated. In the tungsten system, the basic octahedral unit contained within the POM normally has only one short terminal oxygen, (W=O), compared with two *cis*-terminal oxygen atoms in the molybdate, "MoO_2," POMs. Other oxygen atoms can be doubly or triply bridging between tungsten atoms or terminal as O^- or OH.

The structures of several compositionally different sodium polytungstates have been reported. All of the known forms of sodium polytungstate hydrates have complex structures based on polyoxometallate clusters that are generally highly hydrated.

Examples include $Na_5(H_3W_6O_{22})\cdot 18H_2O$[126], $Na_{10}(H_2W_{12}O_{42})\cdot 27H_2O$[127], $Na_{10}(H_2W_{12}O_{42})\cdot 20H_2O$[128] and $Na_6W_7O_{24}\cdot 14H_2O$[129]. The general method for the syntheses of these species is relatively simple: when the primary starting material, $NaWO_4\cdot 2H_2O$, is dissolved in water at pH 7 hydrolysis occurs, resulting in the formation of the POM precipitate. $WO_3\cdot H_2O$ can be added to the reaction mixture to control the hydrolysis reaction, producing slightly different sodium tungstate hydrate stoichiometries. To produce $Na_5(H_3W_6O_{22})\cdot 18H_2O$, $NaWO_4\cdot 2H_2O$ is dissolved alongside $HClO_4$ and for $Na_{10}(H_2W_{12}O_{42})\cdot 20H_2O$, $Al(NO_3)\cdot 9H_2O$ is used to decrease the solution pH and its structure is shown in Figure 1.8. In all of these polytungstate syntheses, the product is obtained by crystallisation from solutions near room temperature.

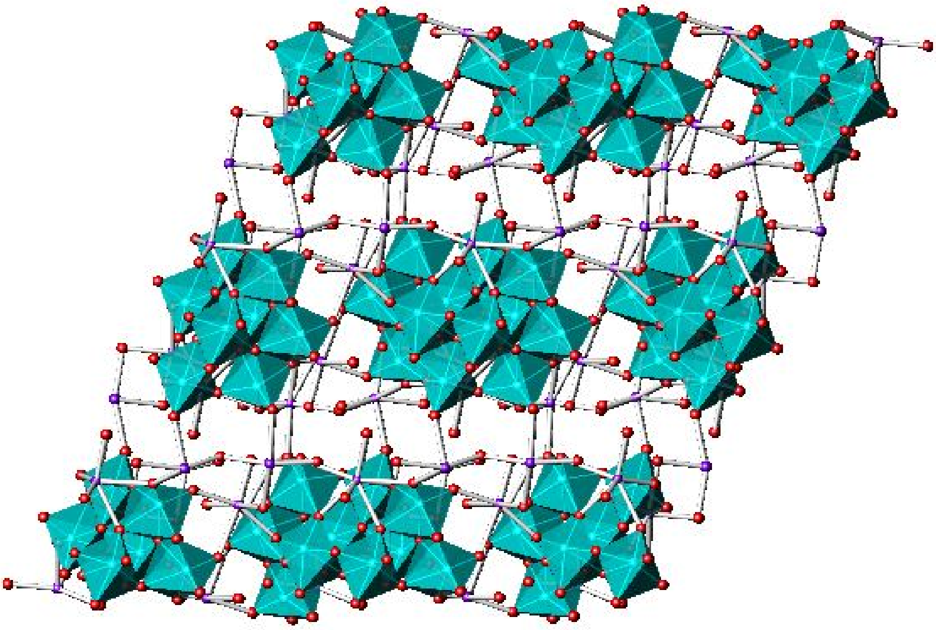

Figure 1.8: Structure of $Na_{10}[H_2W_{12}O_{42}]\cdot 12H_2O$ viewed down the *b*-axis, where the tungsten octahedra are shown in turquoise, the sodium cations as purple spheres and the oxygen atoms in red.

The polytungstate unit in $Na_5(H_3W_6O_{22})\cdot 18H_2O$ contains two types of WO_6 octahedra, each with three terminal oxygen atoms in a *fac* configuration; the remaining three oxygen atoms bridge to other WO_6 octahedra. Originally it was thought that polymetallates containing MO_6 octahedra with more than two neighbouring terminal oxygen atoms were unstable[130,131]. However, the terminal oxygen atoms in

$Na_5(H_3W_6O_{22})\cdot18H_2O$ are partially protonated as OH groups and thus stabilised. These polytungstate anions have further ionic-type interactions involving the sodium ions to generate a three dimensional array. The majority of the water molecules coordinate to sodium ions, though in this POM four of the water molecules only interact, (through strong hydrogen-bonding), with oxygen atoms of the polytungstate or with other water molecules.

$Na_{10}(H_2W_{12}O_{42})\cdot27H_2O$ and $Na_{10}(H_2W_{12}O_{42})\cdot20H_2O$ do not have the same arrangement of terminal oxygen atoms within the WO_6 octahedra as in $Na_5(H_3W_6O_{22})\cdot18H_2O$, with only two protonated terminal oxygen atoms in each polytungstate unit. In $Na_{10}(H_2W_{12}O_{42})\cdot20H_2O$, the sodium ions form ionic interactions with a mixture of polytungstate ion oxygen atoms and water molecules but again there are free water molecules present in the structure. Further stabilisation of these POM arrays involves hydrogen bonding to adjacent water molecules.

One of the main uses of sodium polytungstates is to produce high-density liquids. For example, $Na_2WO_4\cdot H_2O$ is commonly used as a non-toxic, high density separating compound in the separation of minerals. These solutions contain a variety of polytungstate species, are of low viscosity and have a pH of ≈ 6, resulting in ideal properties in the separation of minerals[132, 133, 134].

1.10-Templated Frameworks

During the 1960s, a synthetic route to create framework materials was developed which used organic amines instead of alkali metals to create basic conditions within the reaction vessel. These nitrogen-containing compounds act as templates and are present within the final framework structure, where they replace the charge-balancing cations that are usually present. These templating cations perform two important roles. Firstly, their size and shape can result in novel pore structures. These cations also have far larger ionic radii than the metal cations that are normally present, meaning that they count for only a relatively small proportion of the framework charge, which in turn leads to the formation of high-silica materials for aluminosilicate materials.

There are in fact two types of template; direct and indirect[135]. In order for a template to be classed as “direct,” the templated material must be a 1 : 1 copy of the template structure. There must not be any changes in order of length scale of the template during synthesis. Indirect templating results from a metamorphic reconstruction during synthesis, such as phase separation.

By using solvothermal synthesis techniques in the synthesis of hybrid open-frameworks, a larger range of structural types can be produced for each metal-organic system[136]. In a hydrothermal reaction vessel, the water dielectric constant is lower than in ambient conditions, resulting in different interactions between the organic and inorganic reagents[137]. When positively-charged organic starting materials are used, such as protonated amines, the inorganic network condenses *via* weak electrostatic interactions between the inorganic framework and the organic groups. This is known as the “templating effect,” which may give rise to a larger variety of structures[138, 139]. When the organic species is negatively-charged, such as phosphonate ions, coordination bonds form as a result of an electron pair donor being present and acting as a Lewis base. When an anionic organic source is used, the final product is commonly either a neutral open-network[140] or an extended solid with an open-framework[141].

Entirely novel frameworks were produced during a comprehensive aluminophosphate study by Union Carbide Corporation[19], such as $AlPO_4$-5, which was analysed *via* single crystal X-ray diffraction techniques. Some of these novel structures were synthesised using templating agents. A direct correlation was observed between the templating, or structure-directing, agents that were used in some of these reactions and the resulting aluminium phosphates with zeolite topolgies, such as $AlPO_4$-20. In this case, tetramethylammonium hydroxide (TMAOH) was used as a template, which resulted in a sodalite framework topology with a template stoichiometry of around one unit per sodalite cage. A TMAOH molecule has a diameter of 0.62 nm so fits neatly into the sodalite-type cage and its use is the only known way to successfully crystallise $AlPO_4$-20. Due to the neutrality of the $AlPO_4$ structure, it is not necessary for the templating agent in this case to charge-balance the material but is incorporated into the structure on the basis of size and shape relative to the channel that needs to be filled, thus stabilising the void. If the template is non-bonding, it will be held in place within a cavity or channel by van der Waals interactions and often hydrogen bonding[19].

When a templating agent, usually an organic molecule, is present within the reaction mixture, it becomes trapped in the pores and plays a vital role in producing the microporous framework of the resulting aluminophosphate. However, both experimental[142] and theoretical[143] research has shown that open structures are less stable than their condensed analogues. Silica-based nanoporous materials are generally very thermally stable, which is due to their very strong T–O bonds, making them stable with respect to framework rearrangement. As the framework bonds become weaker, the kinetic stability of these materials decreases. As a result, open-framework aluminophosphate structures that contain organic cations within the channels may be stable but it is often very difficult to remove these cations without the structure collapsing. Even so, there are now over 100 organic species that have been used as successful templates in the formation of open-frameworks[19], most commonly quaternary ammonium cations and various organic amines.

1.11-Scope of Work

The general aim of this project is to synthesise and characterise new framework materials. The intention is to extend the range of known structures by using a variety of polyhedral, primarily octahedral and tetrahedral, building units. The octahedral units to be investigated will be produced using mainly transition metals, such as hafnium and iron. The tetrahedra to be studied will primarily be phosphate and arsenate units. By using such a range of building units, the aim is to produce new framework species which either have new or improved properties for a range of applications, such as ion exchange and energy storage.

Chapters 3-5 discuss a wide range of both Group Four and Group Five arsenate and phosphate frameworks. These structures have been synthesised and fully characterised using techniques such as single crystal analysis, thermogravimetric analysis and energy dispersive spectroscopy. All of these techniques are described in Chapter 2.

Chapter 6 details several iron phosphate structures including two entirely novel frameworks which have been synthesised and characterised. A third framework is a synthetic lipscombite structure, a well-known and widely-reported mineral.

Chapter 7 examines two new sodium tungstate materials. Although there are many existing structures of this type, both of these frameworks possess potentially interesting properties.

1.12-References

---

[1] H. Gies, R. Kirchner, H. van Koningsveld, M. Treacy, *Proc. 12th. International Zeolite Conference*, 1999, 2999.

[2] R. L. Verta, *USGS Minerals Yearbook-Zeolites*, 2006, 83.1.

[3] C. E. Housecroft, A. G. Sharpe, *Inorg. Chem.*, Prentice Hall, 2001.

[4] W. T. Lim, S. Y. Choi, J. H. Choi, Y.H. K., N. H. Heo, K. Seff, *Micro. and Meso. Mater.*, 2006, **92**, 234–242.

[5] A. K. Cheetham, G. Férey, T. Loiseau, *Angew. Chem. Int. Ed.*, 1999, **38**, 3268-3292.

[6] J. A. Armstrong, M. T. Weller, *Dalton Trans.*, 2006, **2006**, 2998–3005.

[7] S. B. Wiggin, *Synthesis and Characterisation of Inorganic Framework Materials*, PhD Thesis, University of Southampton, 2006.

[8] S. Bhatia, *Zeolite Catalysis: Principles and Applications*, CRC Press, 1990, 9.

[9] T. C. Duan, T. Nakamo, Y. Nozue, Conference Paper at Handai Nano Conference, 2007.

[10] H. J. Emeleus, A. G. Sharpe, *Modern Aspects of Inorganic Chemistry*, Routledge & Kegan Paul, 1978.

[11] A. Cheetham, P. Day, *Solid State Chemistry Compounds*, Oxford Science Publications, Oxford, 1993.

[12] D. Shriver, P. Atkins, C. Langford, *Inorganic Chemistry 2nd. Ed.*, Oxford University Press, 1999.

[13] P. Atkins, T. Overton, J. Rourke, M. Weller, F. Armstrong, *Inorganic Chemistry*, Oxford University Press, 2006.

[14] A. K. Cheetham, G. Ferey, T. Loiseau, *Angew. Chem., Int. Ed.*, 1999, **38**, 3268-3292.

[15] Y. Xing, G. Li, H. Meng, Z. Shi, Y. Liu, X. Wei, Y. Yang, W. Pang, *Inorg. Chem. Comm.*, 2004, **7**, 475-477.

[16] Z. Matamoros-Veloza, K. Yanagisawa, J. C. Rendón-Angeles, S. Oishi, *J. Phys.: Condens. Matter.*, 2004, **16**, S1361–S1372.

[17] C. N. R. Rao *Proc. Indian Acad. Sci.* (*Chem. Sci.*), 2001, **113**, 363–374.

[18] H. Li, A. Laine, M. O'Keefe, O. M. Yaghi, *Science*, 1999, **283**, 1145-1147.

[19] A. K. Cheetham, G. Férey, T. Loiseau, *Angew. Chem. Int. Ed.*, 1999, **38**, 3269-3292.

---

[20] J. Yu, R. Xu, *Chem. Soc. Rev.*, 2006, **35**, 593-604.

[21] W. Löwenstein, *Am. Miner.*, 1954, **39**, 92-96.

[22] S. T. Wilson, B. M. Lok, C. A. Messina, T. R. Cannan, E. M. Flanigen, *J. Am. Chem. Soc.*, 1982, **104**, 1146-1147.

[23] D W Breck, *Zeolite Molecular Sieves*, Wiley:New York, 1974.

[24] J. B. Parise, *J. Chem. Soc. Chem. Comm.*, 1985, **22**, 606-607.

[25] G. Yang, L. Li, J. Chen, R. Xu, *J. Chem. Soc. Chem. Comm.*, 1989, 810-811.

[26] L. Li, L. Wu, J. Chen, R. Xu, *Acta. Cryst. C*, 1991, **47**, 246-249.

[27] J. Chen, L. Li, G. Yang, R. Xu, *J. Chem. Soc. Chem. Comm.*, 1989, 1217-1218.

[28] S. S. Dhingra, R. C. Haushalter, *J. Chem. Soc. Chem. Comm.* 1993, 1665-1667.

[29] S. T. Wilson, *Stud. Surf. Sci. Catal.*, 1991, **58**, 137.

[30] R. E. Morris, S. J Weigel, *Chem. Soc. Chem. Rev.*, 1997, **26**, 309-317.

[31] E. R. Cooper, C. D. Andrews, P. S. Wheatley, P. B. Webb, P. Wormald, R. E. Morris, *Nature*, 2004, **430**, 1012-1016.

[32] C.-Y. Sheu, S.-F. Lee, K.-H. Lii, *Inorg. Chem.*, 2006, **45**, 1891-1893.

[33] A. K. Cheetham, C. N. R. Rao, R. K. Feller, *Chem. Comm.*, 2006, 4780-4795.

[34] P. M. Forster, N. Stock. A. K. Cheetham, *Angew. Chem. Int. Ed.*, 2005, **44**, 7608-7611.

[35] X. Zhang, Z. Wen, Z. Gu, X. Xu, Z. Lin, *J. Solid State Chem.*, 2004, **177**, 849–855.

[36] C. N. R. Rao, *Proc. Indian Acad. Sci.* (*Chem. Sci.*), 2001, **113**, 363–374.

[37] Z.-F. Zhao, B.-B. Zhou, Z.-H. Su, X. Zhang, G.-H. Li, *Crystal Growth and Design*, 2006, **6**, 632-635.

[38] K. L. Elmore, J. D. Hatfield, R. L. Dunn, A. D. Jones, *J. Phys. Chem.*, 1965, **69**, 3520-3525.

[39] J. Chengfa, *Chemical Engineering Science*, 1996, **51**, 689-693.

[40] H. Kessler, *Stud. Surf. Sci. Catal.*, 1989, **52**, 17.

[41] H. Kessler, *Mater. Res. Soc. Symp. Ser.*, 1991, **233**, 47.

[42] S. L. Suib, *Annu. Rev. Mater. Sci.*, 1996, **26**, 135-151.

[43] M. Goepper, J. L. Guth, *Zeolites*, 1989, **11**, 477-482.

[44] L. Yu, W. Pang, L. Li, *J. Solid State Chem.*, 1990, **87**, 241-244.

---

[45] G. Férey, T. Loiseau, P. Lacorre, F. Taulelle, *J. Solid State Chem.*, 1993, **105**, 179-190.

[46] M. Estermann, L. B. McCusker, C. Baerlocher, A. Merrouche, H. Kessler, *Nature*, 1991, **352**, 320-323.

[47] P. B. Moore, J. Shen, *Nature*, 1983, **306**, 356-358.

[48] A. Clearfield, *Comments Inorg. Chem.*, 1990, **10**, 89-128.

[49] J. S. Lee, J. O. Nriagu, *Environ. Chem.*, 2007, **4**, 123-133.

[50] C. Masquelier, A. K. Padhi, K. S. Nanjundaswamy, J. B. Goodenough, *J. Solid State Chem.*, 1998, **135**, 228-234.

[51] J. Rojo, A. Laarañaga, J. Mesa, M. Urtiaga, J. Pizarro, M. Arriortua, T. Rojo, *J. Solid State Chem.*, 2002, **165**, 171-177.

[52] B. Bazán, J. Mesa, J. Pizarro, M. Arriortua, J. Rojo, *Mater. Res. Bull.*, 2003, **38**, 1193-1202.

[53] J. Rocha, M. W. Anderson, *Eur. J. Inorg. Chem.*, 2000, **2000**, 801-818.

[54] L. Balducci, D. Bianchi, R. Bortolo, R. D’Aloisio, M. Ricci, R. Tassinari, R. Ungarelli, *Angew. Chem. Int. Ed.*, 2003, **42**, 4937-4940.

[55] G. Alberti, P. Cardini-Galli, U. Costantino, E. Torracca, *J. Inorg. Nucl. Chem.*, 1967, **29**, 571-578.

[56] A. N. Christensen, E. K. Anderson, I. G. Anderson, G. Alberti, M. Nielson, E. k. Lehmann, *Acta. Chem. Scand.*, 1990, **44**, 865-872.

[57] W. T. A. Harrison, T. E. Gier, J. C. Calabrese, G. D. Stucky, *J. Solid State Chem.*, 1994, **111**, 257-266.

[58] S. Ekambaram, S. C. Sevov, *Angew. Chem. Int. Ed.*, 1999, **38**, 372-375.

[59] Y. Zhao, Y. Yang, X. Yang, W. Guo, *Chem. Lett.* 2007, **36**, 456-457.

[60] D. M. Poojary, A. I. Bortun, L. N. Bortun, A. Clearfield, *J. Solid State Chem.*, 1997, **132**, 213-223.

[61] R. Cini, L. G. Marzilli, *Inorg. Chem.*, 1988, **27**, 1856-1858.

[62] J. D. Bierlien, H. Vanherzeele, *J. Opt. Soc. Am. B*, 1989, **6**, 622-633.

[63] Nothrop Grumman Corporation, 2003.

[64] E. S. Lunezheva, B. A. Maksimov, O. K. Mel'nikov, *Soviet Physics, Cryst.*, 1989, **34**, 674-676.

---

[65] H. Birkedal, A. M. K. Andersen, A. Arakcheeva, G. Chapuis, P. Norby, P. Pattison, *Inorg. Chem.*, 2006, **45**, 4346-4351.

[66] K. Fukuda, A. Moriyama, S. Hashimoto, *J. Solid State Chem.* 2004, **177**, 3514–3521.

[67] A. M. K. Andersen, P. Norby, J. Hanson, *Inorg. Chem.*, 1998, **37**, 876-881.

[68] J. Rodríguez, M. Suárez, M. L. Rodríguez, R. Llavona, M. J. Arce, M. A. Salvadó, P. Pertierra, S. García-Granda, *Eur. J. Inorg. Chem.*, 1999, 61-65.

[69] A. Clearfield, *Progress in Inorg. Chem.*, 1998, **47**, 373-509.

[70] A. I. Bortun, A. Clearfield, M. Suárez, R. Llavona, J. Rodríguez, *Mater. Chem. And Phys.*, 1998, **55**, 152-154.

[71] M. B. Hursthouse, K. M. A. Malik, J. M. Thomas, J. Chen, J. Xu, T. Song, R. Xu, *Russ. Chem. Bull.*, 1994, **43**, 1787.

[72] M. Wloka, S. I. Troyanov, E. Kemnitz1, *J. Solid State Chem.*, 1998, **135**, 293-301.

[73] D. Wang, R. Yu, N. Kumada, N. Kinomura, *Chem. Mater.*, 2000, **12**, 956-960.

[74] J. Dong, L. Liu, J. Li, Y. Li, C. Baerlocher, L. B. McCusker, *Micro. And Meso. Mater.*, 2007, **104**, 185-191.

[75] M. Wloka, S. I. Troyanov, E. Kremnitz, *J. Solid State Chem.*, 2000, **149**, 21-27.

[76] D. M. Poojary, A. I. Bortun, L. N. Bortun, C. Trobajo, J. R. García, A. Clearfield, *Micropor. And Mesopor. Mater.*, 1998, **20**, 77-85.

[77] G. Wallez, J.-P. Souron, M. Quarton, *Solid State Sci.*, 2006, **8**, 1061-1066.

[78] M. A. Salvado, P. Pertierra, S. García-Granda, J. R. García, J. Rodríguez, M. T. Fernández-Díaz, *Acta. Cryst. B*, 1996, **B52**, 896-898.

[79] M. Suárez, L. M. Barcina, R. Llavona, J. Rodríguez, M. A. Salvadó, P. Pertierra, S. García-Granda, *J. Chem. Soc., Dalton Trans.*, 1998, 99-102.

[80] A. Clearfield, J. M. Kalnins, *J. Inorg. Nucl. Chem.* 1978, **40**, 1933-1936.

[81] D. M. Poojary, B. Shpeizov, A. Clearfield, *J. Chem. Soc., Dalton Trans.*, 1995, 111-113.

[82] H. Aono, E. Sugimoto,Y. Sadaoka, N. Imanaka, G. Adachi, *Solid State Ionics*, 1993, **62**, 309-316.

[83] H. Y.-P.Hong, *Mater. Res. Bull.*, 1976, **11**, 173-182.

[84] E. R. Losilla, M. A. G. Aranda, M. Martínez-Lara, S. Bruque, *Chem. Mater.*, 1997, **9**, 1678-1685.

---

[85] N. Karyakin, N. Chernorukov, A. Koryttseva, G. Chernorukov, *High Temperatures – High Pressures*, 1998, **30**, 471-478.

[86] G. Alberti, S. Allulli, U. Constantino, M. Massucci, *J. Inorg. Nucl. Chem.* 1975, **37**, 1779-1786.

[87] G. Blasse, G. J. Dirksen, M. F. Hazenkamp, A. Verbaere, S. Oyetola, *Eur. J. Solid State Chem.*, 1989, **26**, 175.

[88] M. F. Hazenkamp, G. Blasse, J. J. Zah-Ketho, A. Verbaere, *Eur. J. Solid State Chem.*, 1992, **29**, 1263.

[89] C. S. Liang, W. T. A. Harrison, M. M. Eddy, T. E. Gier, G. Stucky, *Chem. Mater.*, 1993, **5**, 917-924.

[90] I. Nowak, M. Ziolek, *Chem. Rev.*, 1999, **99**, 3603-3624.

[91] T. G. Amos, A. W. Sleight, *J. Solid State Chem.*, 2001, **160**, 230-238.

[92] P. M. Forster, A. W. Sleight, *Int. J. Inorg. Mater.*, 1999, **1**, 123-127.

[93] X. Wang, L. Liu, A. J. Jacobson, *J. Mater. Chem.*, 2000, **10**, 2774-2778.

[94] X. Wang, L. Liu, H. Cheng, A. J. Jacobson, *Chem. Comm.*, 1999, 2531-2532.

[95] X. Wang, L. Liu, H. Cheng, K. Ross, A. J. Jacobson, *J. Mater. Chem.*, 2000, **10**, 1203-1208.

[96] X. Wang, L. Liu, A. J. Jacobson, *J. Mater. Chem.*, 2002, **12**, 1824-1827.

[97] K. Hizaoui, N. Jouini, T. Jouini, *J. Solid State Chem.*, 1999, **144**, 53-61.

[98] K. Hizaoui, N. Jouini, A. Driss, T. Jouini, *Acta Cryst. C*, 1999, **55**, 1972-1974.

[99] N. Bestaoui, A. Verbaere, Y. Piffard, *Eur. J. Solid State Inorg. Chem.*, 1998, **35**, 473-482.

[100] Y Shimizu, T Ushijima, *Solid State Ionics*, 2000, **132**, 143–148.

[101] H Liu, T Grundström, *Mol. Biol. Cell*, 2002, **13**, 4497-4507.

[102] W. Meisel, H. J. Guttmann, P. Gutlich, *Corros. Sci.*, 1983, **23**, 1373.

[103] C. C. Torardi, W. M. Reiff, L. Takacs, *J. Solid State Chem.*, 1989, **82**, 203-215.

[104] Y. Song, P. Y Zavalij, M. Suzuki, M. S. Whittingham, *Inorg. Chem.*, 2002, **41**, 5778-5786.

[105] P. P. Prosini, M. Lisi, S. Scaccia, M Carewska, F Cardelline, M. Pasquali, *J. Electrochem. Soc.*, 2002, **149**, A297-A301.

---

[106] Y. Song, S. Sang, P. Y. Zavalij, M. S. Whittingham, *Mater. Res. Bull.*, 2002, **37**, 1249-1257.

[107] J.-M. Chen, Y. j Li, W.-M. Hurng, M. S. Whittingham, U.S. Patent 5,514,490, 1996.

[108] A. K. Padhi, K. S. Nanjundaswamy, J. B. Goodenough, *J. Electrochem. Soc.*, 1997, **144**, 1188-1194.

[109] S Shi, C Ouyang, Z Xiong, L Liu, Z Wang, H Li, D-S Wang, L C, L X Huang, *Phys. Rev.* B, 2005, 71, 144404.1-144404.6.

[110] M A E Sanchez, G E S Brito, M C A Fantini, G F Goya, J R Matos, *Solid State Ionics*, 2006, **177**, 497–500.

[111] A S Andersson, B Kalska, L Häggström, J O Thomas, *Solid State Ionics*, 2000, **130**, 41-52.

[112] S Yang, P Y Zavalij, M S Whittingham, *Electrochem. Comm.*, 2001, **3**, 505-508.

[113] M. Dollé, S. Patoux, T. Richardson, *J. Power Sources*, 2005, **144**, 208-213.

[114] Y. Song, P. Y. Zavalij, N. A. Chernova, M. S. Whittingham, *Chem. Mater.*, 2005, **17**, 1139-1147.

[115] M. L. Lindberg, C. L. Christ, *American Crystallographic Association: Program and Abstracts*, 1959, 20-21.

[116] G. J. Redhammer, G. Tippelt, G. Roth, W. Lottermoser, G. Amthauer, *Phys. Chem. Miner.*, 2000, **27**, 419-429.

[117] K.-H. Lii, C.-H. Huang, *J. Chem. Soc., Dalton Trans*, 1995, **1995**, 571-574.

[118] K.-H. Lii, *J. Chem. Soc., Dalton Trans*, 1996, **1996**, 819-822.

[119] Y.-C. Jiang, S.-L. Wang, K.-H. Lii, N. Nguyen, A. Ducouret, *Chem. Mater.*, 2003, **15**, 1633-1638.

[120] W.-J. Chang, P.-C. Chang, K.-H. Lii, *J. Solid State Chem.*, 2003, **172**, 6-11.

[121] J. Berzelius, *Poggendorff's Ann. Phys.*, 1826, **6**, 369-.380.

[122] L. De-Liang, D. Orr, G Seeber, P. Kögerler, L. J. Farrugia, L. Cronin, *J. Cluster Science*, 2003, **14**, 313-324.

[123] N. N. Greenwood, A. Earnshaw, *Chemistry of the Elements: Second Edition*, Elsevier Butterworth Heinemann 2003, 1009-1016.

[124] A. P. Guisberg, *Inorganic Syntheses*, Wiley, Chichester, 1990, **27**, 71-135.

---

[125] H. J. Emeleus, A. G. Sharpe, *Modern Aspects of Inorganic Chemistry*, Routledge & Kegan Paul, London, 1978, 281-283.

[126] H. Hartl, R. Palm, J. Fuchs, *Angew. Chem.*, 1993, **105**, 1545-1547.

[127] A. Chrissafidou, J. Fuchs, H. Hartl, R. Palm, *Zeits. Natur.*, *Teil B. Anorg. Chem., Org. Chem.*, 1995, **50**, 217-222.

[128] H. T. Evans, O. W. Rollins, *Acta. Cryst. B*, 1976, **B32**, 1565-1567.

[129] K. G. Burtseva, T. S. Cehrnaya, M. I. Sirota, *Dokl. Akad. Nauk SSSR*, 1978, **243**, 104-107.

[130] W. N. Lipscomb, *Inorg. Chem.*, 1965, **4**, 132-134.

[131] M. T. Pope, *Heteropoly And Isopoly Oxometalates*, Springer, Berlin, 1983, 19.

[132] S. T. Krukowski, *J. Paleontology*, 1988. **62**, 314-316.

[133] J. A. Commeau, L. J. Poppe, R. F. Commeau, *U. S. Geological Suvery Circular*, 1992, **1071**, 13.

[134] M. R. Gregory, K. A. Johnston, *New Zealand J. Geology and Geophys.* 1987, 30, 317-320.

[135] H.-P. Hentze, M. Antonietti, *Curr. Opin. Solid State And Mater. Sci.*, 2001, **5**, 343-353.

[136] M. J. Rosseinsky, *Micro. And Meso. Mater.*, 2004, **73**, 15-30.

[137] C. Livage, C. Egger, G. Férey, *Chem. Mater.* 2001, **13**, 410-414.

[138] G. Férey, *C. R. Acad. Sci. Paris*, 1998, **1**, 1-13.

[139] P. J. Hagrman, D. Hagrman, J. Zubieta, *Angew. Chem. Int. Ed.*, 1999, **38**, 2638-2684.

[140] C. Livage, C. Egger, G. Férey, *Chem. Mater.*, 1999, 11, 1546–1550.

[141] C. Livage, C. Egger, M. Noguesb, G. Férey, *J. Mater. Chem.*, 1998, 8, 2743-2747.

[142] I. Petrovic, A. Navrotsky, M. E. Davies, S. I Jones, *Chem. Mater.*, 1993, **5**, 1805-1813.

[143] N. J. Henson, J. D. Gale, A. K. Cheetham, *Chem. Mater.*, 1994, **6**, 1647-1650.

Chapter 2

Experimental Techniques

The materials produced within this work were synthesised using solvothermal methods. These methods involve subjecting solutions to heat and autogenous pressure in Teflon-lined steel autoclaves, as described in Section 2.2.1. A range of analytical techniques was used in the characterisation and structure solution of the various synthesised materials.

The primary analytical technique used in characterising the novel materials produced was single crystal X-ray diffraction, as detailed in Section 2.3.2. Although this was the dominant method used to identify the inorganic materials produced, other analyses were carried out in order to support the findings of the single crystal refinements.

Powder X-ray diffraction was used in order to verify the purity of novel materials in the bulk powder sample and also to determine the nature of the materials post-thermogravimetric analysis. Neutron diffraction data were combined with single crystal analysis in order to assign the hydrogen atom positions more accurately within one of the crystal structures within this work.

Several other analytical techniques were also employed to support the crystallographic refinements. Energy Dispersive X-ray Spectroscopy (EDS) data were collected. This was then used to show, qualitatively and semi-quantitatively, that the stated elements were present in each of the structures produced and solved. Thermogravimetric analysis (TGA) was carried out on many of the novel materials. For example, TGA was able to support the theory that water molecules and ammonium cations were present within the frameworks of several of the arsenate and phosphate materials. Infrared (IR) spectra were obtained for several structures. These spectra were used as evidence for the presence of water molecules and ammonium cations within some of these materials. IR was of use in strengthening the theory that hydrogen-containing ammonium and water groups were present where X-ray diffraction was not of use in locating the hydrogen atoms, due to their low electron density. Bond valence calculations[1] were regularly carried out on new materials and indicated that all of the atoms present were fully occupied, for the given structural formulae. These calculations were also used to predict the positions of hydrogen atoms in many of the structures.

When this range of analytical techniques is combined to solve a new crystal structure, a definitive solution can be reached. The next stage of research into any of these compounds would involve further investigation of properties that could be of use industrially.

2.1-Synthetic Methods

When researching inorganic framework materials, most of the starting materials available are relatively inert, meaning that a large amount of energy is required in order for a reaction to take place. This can often be achieved via a solid-state reaction, which relies on long reaction times under high temperatures and thorough mixing of the reagents to compensate for the lack of ion mobility. This mixing is commonly brought about by grinding the starting materials together with a pestle and mortar. However, the product formed in these types of reaction will commonly be the low energy, thermodynamic product. Many materials that are used in applications such as ion exchange and catalysis often require the *meta*-stable form. Properties of use within industry, such as large pore size or large surface area, usually need a higher energy product; the kinetic form of the material. In order to produce different forms of a material, different synthetic methods need to be used, so that, for example, the kinetic product is favoured rather than the thermodynamic one.

2.1.1-Solvothermal Synthesis

In all cases, the solvothermal syntheses presented here were carried out in Teflon-lined steel autoclaves with an internal volume of 23 mL, produced by the Parr Instrument Company[2]. The autoclaves used within this work had a maximum operating temperature of 523 K (250 ºC) and a maximum advised operating pressure of 8000 kPa (1200 psig). If more severe reaction conditions are required, this can be achieved by using an external pressure source. This can then lead to reactions being carried out under supercritical conditions, for solvents other than water.

Solvothermal synthesis, or hydrothermal synthesis if the solvent being used is water, offers several advantages over the use of solid-state techniques. Within a solvothermal reaction mixture, the reagents are suspended within a solution, allowing far greater ion mobility than when in the solid phase. This leads to the possibility of shortened reaction times and also lower temperatures. Another advantage of this greater mobility is that the formation of single crystals is more likely, which are easier to analyse than the powders that are normally produced in a solid-state reaction. Solvents, other than water, that can be used within this type of environment include ethanol and acetonitrile, amongst many others, including those that are primarily made up of water such as hydrochloric acid and sodium hydroxide solutions. Most solvents can be used, as long as the vapour pressure at the synthesis temperature has been calculated and deemed safe, with respect to the maximum pressure that can be withstood by the autoclaves. It is also necessary to ensure that there are no gases produced that will increase the pressure above the safe limit within the reaction environment.

Hydrothermal methods are not just confined to water-soluble reagents. This is due to the change in the properties of water as it reaches its supercritical boundary, when put under higher temperatures and pressures. A supercritical fluid possesses the properties of both a liquid and a gas and its density is greatly affected by just a small change in either temperature or pressure. Water in its supercritical state exists as discrete hydrogen-bonded clusters and acts more like a gas than a liquid. It becomes an almost non-polar fluid and its density drops to 0.348 g/cm^3 when in this state[3]. This drop in density increases the ability of the reagents to diffuse through the system. A reaction which contains supercritical water has also been shown to be more acidic than expected, based purely on the temperature of the environment. However, these conditions were not used within this work but rather the solvent was altered in order to improve the solubility of the starting materials in many of these reactions. The solvent was also commonly used as to alter the pH of the reaction mixture.

Many reagents that are not normally soluble in a particular solvent will become so at an elevated temperature. This allows better movement of ions within the solution. The product, which will not be soluble in the solvent, will precipitate out of solution and can be filtered off for analysis.

Unfortunately, solvothermal techniques present several problems. The greatest of these is the difficulty in determining the likely reaction mechanisms which may take place in a reaction vessel. Solvothermal reaction vessels are closed systems and the reactions may be influenced by many different factors, which cannot readily be recorded and regulated. The time, temperature and pressure, (which is a function of the fill level), and also the pH and concentration of the reagents, may all be significant factors in the outcome of a reaction. The way in which the reagents are added can also play a part in the reaction due to their effect on the level of homogeneity. It is impossible to carry out theoretical calculations as to how each of these myriad factors will influence the outcome of an individual reaction. Therefore, little is known about the reaction mechanisms that take place under these conditions. The result of this is that a trial-and-error route must be taken, which is both time-consuming and labour-intensive. Solvothermal reactions are known as a good way to produce single crystals but these are often poor quality. Single crystals synthesised in this way are often small, may possess high levels of defects or be twinned, making analysis complicated. This is due to the speed at which the crystals are produced, especially when compared with natural crystal growth which generally takes place at similar temperatures and pressures but over years rather than days.

Solvothermal techniques are widely used in the synthesis of inorganic framework materials because of the accessibility of synthetic conditions which are unavailable with other techniques. For example, some templated frameworks could not be produced using solid state methods, due to the breakdown of the organic unit at high temperatures.

2.2-X-ray Diffraction

The primary method for sample identification within this work was X-ray diffraction. X-rays range in wavelength from 10 to 0.1 nm and a typical wavelength used for crystallography is in the region of 0.1 nm, i.e. 1 Å. This is on the same length scale as bonds within a structure and also the radius of an atom, thus resulting in a useful structural analysis. Diffraction occurs when the scattering of X-rays causes their interaction with the electron density present in atoms and bonds.

2.2.1-Diffraction Theory

This phenomenon was first noted by Laue in 1912[4], after the discovery that X-rays have a similar wavelength to interatomic distances. The work of W. H. Bragg and W. L. Bragg greatly advanced the field of X-ray diffraction and they were the first to explain why crystals were able to “reflect” X-rays only at certain angles of incidence. Diffraction is often explained using Bragg’s Law[5], which is explained in terms of reflection rather than diffraction for convenience. Figure 2.1 shows a schematic representation of Bragg’s Law.

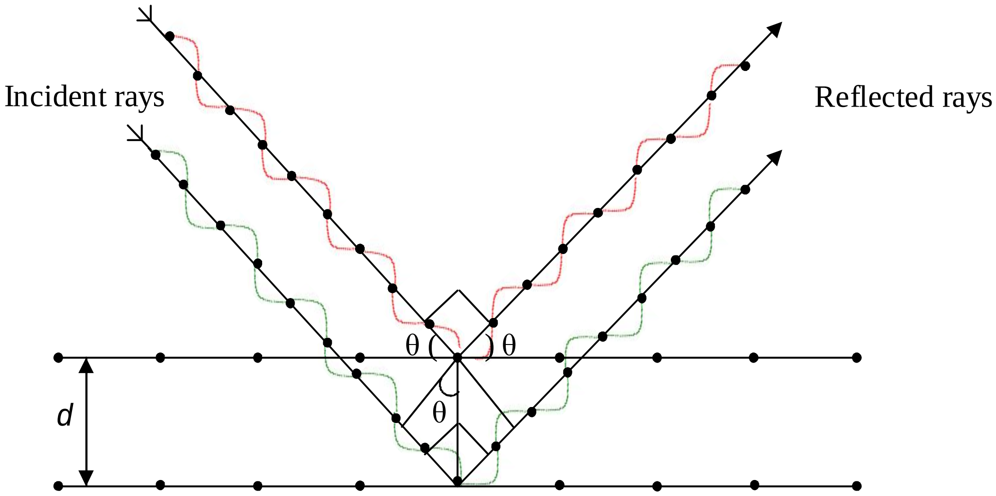

Figure 2.1: Schematic representation of Bragg's Law[6]; in this case the path difference is 2λ and where *d* represents the spacing between planes.

Crystals are commonly thought of as regularly spaced planes of atoms, where the distance between each plane is referred to as the d-spacing. When an X-ray hits an atom, it is scattered, primarily by the electrons, which are known as scatterers. When an incoming X-ray beam strikes an atomic plane at an angle of θ to the plane, it needs to maintain this coherence after reflection at angle θ, (which needs to be known in advance of the measurement). Simple trigonometry can be used to establish the requirements for this. The difference in path length for X-rays scattered by reflecting off different planes needs to be a whole number of wavelengths for constructive interference to be observed. (See Figure 2.1 once again.) This principle is known as Bragg's Law and is written in Equation 2.1.

$$n\lambda = 2d\sin\theta \qquad (2.1)$$

λ = wavelength, d = spacing between planes, θ = angle of incidence.

This approach to X-rays applies to repeating structures, such as crystals, as well as single atoms. In crystalline materials, the planes of the atoms are defined by Miller indices, which are given the notation *hkl*. This refers to the point of interception along the *a*, *b* and *c*-axes of the unit cell. The Miller indices are in fact the reciprocal of the intercept upon the cell axis, from a defined origin. The Miller indices are related to a defined unit cell and are not uniquely defined for a given crystal face. This means that whatever the unit cell that is chosen, any face can be defined by this method.

Each atom in a structure acts as a point scatterer, where the incoming X-ray interacts with and is scattered by the electrons in the atom, causing the X-ray to be emitted in all directions. When a second atom is added into the scenario, there will be interference between the two sets of scatterers, resulting in diffraction maxima and minima being observed in certain directions. As more and more scatterers are placed evenly within the structure, the peaks within the pattern will constructively interfere, resulting in distinct peaks. When a 3D crystalline system is examined, the situation becomes far more complex, due to the different types of scatterer, which have different X-ray scattering powers that are dependent on their electron count.

The concept of crystals being made up of small repeating units was conceived long before conclusive evidence was provided by X-ray diffraction. As long ago as 1784, Haüy proposed that the mineral calcite consisted of a rhombohedral unit cell[7]. He deduced this fact after noting that the mineral's structure was retained when a sample was broken into increasingly small pieces.

There are seven crystal systems into which all crystal structures can be classified. Each of these has distinctive symmetry requirements, allowing further division into fourteen Bravais lattices, including the lattice types primitive, P, body-centred, I, or face-centred, F, (or A, B or C when only one face is centred). Each of these systems has different possible symmetry arrangements, comprising of mirror planes, screw axes, glide planes, *etc*.. In addition, there are 32 crystal classes, shown in Table 2.1. The simplest example is a triclinic cell, which can only possess a primitive lattice. It is defined as having no special relationships in terms of cell lengths or angles. There may or may not be a centre of symmetry present, giving two triclinic crystal classes, *P*1 and *P*-1. All of the different combinations of crystal system, Bravais lattice and crystal class lead to a total of 230 possible space groups.

Table 2.1: Crystal systems and their corresponding classes.

Crystal System	Minimum Criteria	Crystal Classes
Triclinic	None	1, -1
Monoclinic	$\alpha = \beta = 90°$	2, m, 2/m
Orthorhombic	$\alpha = \beta = \gamma = 90°$	mmm, mm2, 222
Tetragonal	$a = b \neq c, \alpha = \beta = \gamma = 90°$	4, -4, 4/m, 422, 4mm, -42m, 4/mmm
Trigonal	$a = b = c, \alpha = \beta = \gamma \neq 90°$	3, -3, 3m, -3m, 32
Hexagonal	$a = b \neq c, \alpha = \beta = 90°, \gamma = 120°$	6, -6, 6/m, 622, 6mm, -62m, 6/mmm
Cubic	$a = b = c, \alpha = \beta = \gamma = 90°$	23, m-3, 432, -43m, m-3m

By measuring a set of reflections in the form of a diffraction pattern, a lot of information about the unit cell of a crystal can be obtained. By using computer software to combine all of the data collected, it is possible to determine the unit cell of a material. From just a short powder diffraction collection, it is possible to calculate the d-spacing of a crystalline sample by applying Bragg's Law to a selection of peaks given in 2θ. From these values, the Miller planes that are responsible for the reflections can be determined, and thus the unit cell dimensions.

Systematic absences can be used to determine the Bravais lattice of a particular crystal. For a primitive lattice, all of the possible reflections are generally observed but this is not the case for either body-centred or face-centred lattices. Absences exist because the lattice type can impose restrictions upon which reflections are observed and which are not. In these lattices, there will be restrictions on the values which h, k and l may take if there is to be any intensity present. As a result, there will be peaks that are not seen in a diffraction pattern and these are known as systematic absences[8]. For example, a cubic, body-centred lattice with an atom at the position (x, y, z) will have another at (x+½, y+½, z+½). As a result of the systematic absences in this type of lattice, the {111} reflection will not be seen, along with any other plane where $h+k+l \neq 2n$. Constructive interference is present between sets of {111} planes but is cancelled out by destructive interference originating in the scattering from atoms in planes halfway between the {111} planes, resulting in there being no observed intensity. By noting the systematic absences which exist in a sample, the number of space groups consistent with the unit cell is greatly decreased. The possible space groups can then be reduced further by examination of the intensity of the diffraction from different planes. By combining these deductions, the unit cell and the space group can be determined.

However, to fully interpret a crystal structure, whether a powder or single crystal sample is being used, requires much more information. It is intensely difficult to solve a structure from powder diffraction data, for example due to peak overlap. For a single crystal sample, many more data are collected, making solving an unknown structure a simpler task. When solving a structure by single crystal diffraction methods, the level of symmetry characteristic of different space groups means that different amounts of data will need to be collected in order to carry out a refinement. In general, the fewer the number of symmetry elements in a unit cell, the greater the amount of data that will need to be collected in order to solve the structure. This can be represented graphically by Ewald's sphere, which uses the idea of a reciprocal lattice to allow meaningful information to be extracted from a diffraction pattern, as seen in Figure 2.2.

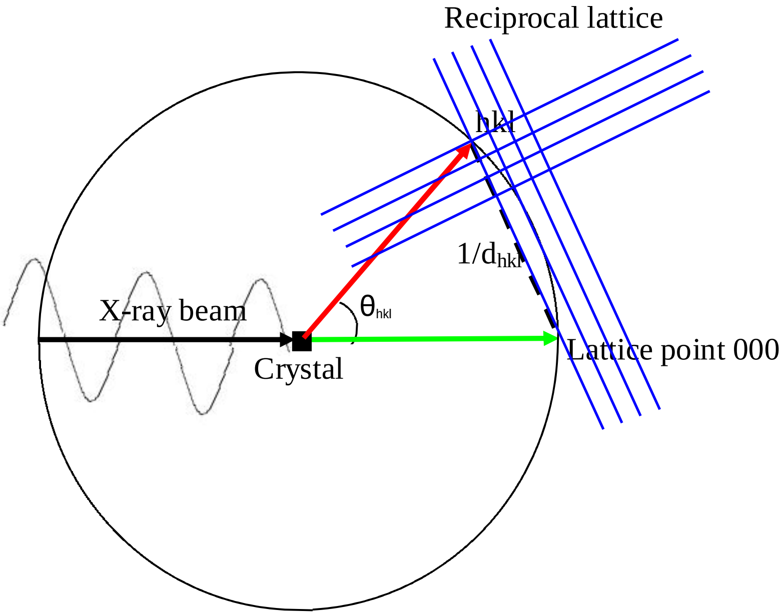

Figure 2.2: Ewald's sphere showing the angle and dimension for a lattice point *hkl*.

When an X-ray beam hits a crystal, the straight-through, unaffected beam has the lattice point 000. By convention, this appears on the surface of the Ewald sphere, (as indicated in the above diagram), and the crystal is centred upon the sphere, which has radius $1/\lambda$. Any other diffraction spots that are present are due to the reflection of atoms in the plane hkl. However, this appears as a reciprocal lattice after diffraction has occurred and the unit cell edges are a*, b* and c*, where a* = 1/a, *etc*.. The reciprocal lattice points are where the Bragg diffraction conditions are satisfied. For diffraction to occur, the reciprocal lattice vector must equal the scattering vector. The distance of the lattice point (000) from the diffraction point on the surface of the Ewald sphere, *hkl*, is equal to $1/d_{hkl}$ for that particular plane.

By rotating a single crystal during data collection, further reflections that intercept the surface of the sphere can be recorded. This allows full characterisation of the crystal structure. During a diffraction experiment, the detector will only cover a small proportion of the sphere, meaning that several scans may be required in order to cover enough of the surface of the sphere to solve the structure. For example, a cubic crystal will display the same diffraction pattern for all six of its faces, meaning that only 1/6th of the full sphere needs to be analysed. After a full data set has been collected, it will be presented as a list of angles at which reflections occur and their intensities. This list must be interpreted in terms of the crystal structure, in order to solve the structure.

The main control of intensity of a reflection is a scattering factor, which is related to the electron density of the atoms. The scattering factors of all the atoms within a unit cell can be combined to form the structure factor, shown Equation 2.2. This structure factor expression incorporates a phase factor, which is due to the varying lengths of time that it takes the X-ray beams to scatter from different planes. This phase factor is also represented within Bragg's Law as the $n\lambda$ value. If both the structure and phase factors are known, then the electron density, and therefore the contents of the unit cell, can be ascertained, by using Equation 2.3. A complication in calculating these values arises because the measured intensities are proportional to the square modulus of the structure factor. Therefore it is not known whether the structure factor ought to be positive or negative. There is even greater difficulty when considering noncentrosymmetric unit cells because the structure factor is expressed as a complex number, $|F_{hkl}|\ e^{i\alpha}$, where $|F_{hkl}|$ is its magnitude, which can be calculated, and $e^{i\alpha}$ is its phase. Nothing about this phase is known and it could be anything between 0 and 2π. Therefore, it is not possible to get back to the structure from this point. This is known as the phase problem.

$$F_{hkl} = \Sigma_n f_n \exp[2\pi i(_h x_n + k y_n + l z_n)] \tag{2.2}$$

F = scattering factor, *f* = atomic form factor.

$$\rho(xyz) = \Sigma_h \Sigma_k \Sigma_l\ |F_{hkl}| \cos[2\pi(hx + ky + lz) - \alpha_{hkl}] \tag{2.3}$$

ρ = electron density.

The most common way of solving the phase problem is by using Direct Methods. Here, statistical techniques are exploited in order to estimate the phases of the Fourier Transform of the scattering density from the corresponding magnitudes. The basic idea for solving this phase problem relies on an equation known as the Sayre equation[9]. The equation for the case of a centrosymmetric structure, where the phases can be + or -, is shown in Equation 2.4.

"Sign of F(h-h', k-k', l-l') is probably equal to F(hkl) * F(h'k'l')" (2.4)

The fact that electron density must be a positive real number and may not take a negative value must also be taken into account as this would limit the phase choice. However, it must be expected that a number of random selections calculated by statistical techniques will result in negative electron density. These will then be discounted. When an approximate model has been reached, it can be refined. This iterative process will gradually give the positions of the other atoms within the unit cell. The Direct Methods technique uses these constraints between the phases of different Fourier components in order to help refine the atomic positions of a structure. In many cases, the hydrogen atoms will not be observed and/or resolved due to their small and diffuse electron density. Once a model has been obtained, least squares refinement is used to optimise the model. Eventually, other parameters, such as anisotropic temperature factors, can be included to give a very accurate idea of the crystal structure.

An alternative to Direct Methods is the Patterson, ("Heavy Atom"), Method. This technique was developed before Direct Methods and is only effective if the structure to be solved contains atoms with a much larger atomic mass than the rest of the elements present. When using this method to solve a structure, the phase problem is not an issue. The Fourier transformation of the measured intensities is proportional to F^2, which removes the need for phase information. A three-dimensional map is then produced, which represents the vectors between the atoms and not the atoms themselves. Due to X-ray scattering being dependent on the amount of electron density within an atom, the greatest level of diffraction is generated by the heavier atoms within a structure. Therefore, the vector between two heavy atoms will be more intense when compared with those for the smaller elements. From this, it is possible to approximate the atom positions within the unit cell. The structure factor can be calculated from this information about just the large atoms and results in a good enough model to continue the refinement.

When refining a model, the accuracy is shown by the reliability, R, factor, shown in Equation 2.5. In crystallography, there is a standard crystallographic R-factor that is used as a measure of the level of disagreement between the properly scaled observed structure factors, F_{obs}, and the calculated structure factors, F_{calc}. This value is commonly displayed as a percentage by multiplying an R-value by one hundred, *e.g.*, an R-value of 0.05 would translate to an error of 5 %, where an error below 5 % is generally accepted as a refinement of publishable quality.

$$R = \frac{\sum_{hkl}(|F_{hkl}^{obs}|-|F_{hkl}^{calc}|}{\sum_{hkl}|F_{hkl}^{obs}|} \qquad (2.5)$$

R = reliability factor, F_{obs} = observed structure factor, F_{calc} = calculated structure factor.

When quoting the R-factor for a refinement, it is used as a way of reporting the extent to which a set of calculated diffraction intensities for a complex atomic model, where there are four or more parameters per atom, agrees with a large number of individual diffraction observations, using just one number. However, this simplified approach means that an R-factor is not very sensitive to errors, particularly in certain cases. For example, if there is a low observation to parameter ratio due to a low resolution data set structure or if a structure is basically correct with a few localised errors, the R-factor may not be an accurate measure of any errors that could be present. It is for this reason that the weighted R-factor, wR_2, shown in Equation 2.6, and/or the Goodness of Fit, GooF or S, shown in Equation 2.7, will be quoted in a publication. Both wR_2 and GooF are based on F^2, which means that the value of wR_2 is likely to be much larger than R_1, which is based on F. The GooF is a fit parameter which takes into account not only the F difference, but also how many reflections and parameters are being used. The GooF value should proceed towards 1 for the model to be considered a good fit.

$$wR_2 = \frac{[\sum w\,(|F_{obs}|^2 - |F_{calc}|^2)^2}{\sum \sqrt{[w\,(|F_{obs}|^2)]}} \qquad (2.6)$$

wR_2 = weighted reliability factor, F_{obs} = observed structure factor, F_{calc} = calculated structure factor, w = weight of reflection.

$$S = \frac{\sum w\,\sqrt{(|F_{obs}|^2 - |F_{calc}|^2)}}{\sqrt{(m-n)}} \qquad (2.7)$$

S = goodness of fit, *m* = number of observed structures, *n* = number of parameters.

When a least squares refinement is being carried out, a weight (w) is normally assigned to each of the reflections. This is done using the criterion $1/\sigma^2$ (F), where σ is the standard deviation. An estimated standard deviation comes from the counting statistics, meaning that a reflection will be given a higher weight if it has a low standard deviation. Therefore, it will be of greater significance when calculating the R-factor. In reality, the weighting system is more complex than a simple $1/\sigma^2$ (F) relationship. Otherwise, the result would be that the highest intensity reflections had the highest weight, which is also not welcome. The weighting factor that is actually used is shown in Equation 2.8.

$$w = 1/\,[\sigma 2|F_{obs}|^2 + (xp)^2] \qquad (2.8)$$

w = weighting factor, where x is a constant, $p = [|F_{obs}|^2 + 2|F_{calc}|^2]/3$.

2.2.2-Single Crystal X-ray Diffraction

At the University of Southampton, the EPSRC National Crystallography Service has two Bruker-Nonius Kappa CCD diffractometers. These both run from a single Bruker-Nonius FR591 rotating anode X-ray generator with a molybdenum target. The K_α radiation produced is of wavelength λ = 0.71703 Å. One diffractometer has confocal focusing mirrors. The other has a graphite monochromator and an automatic sample changing robot. This confocal system allows a much greater flux, approximately six times greater than the one with a graphite monochromator. This allows the data collection times to be shorter but large crystals cannot be run in the more focussed beam. Both instruments are capable of running at high or low temperatures, with a range of 80-500 K, via a pair of Oxford cryostreams. In-house software also allows automated variable temperature experiments to be run. The single crystal diffraction data presented in this work were collected at 120 K.

Diffraction data are collected via a 95 mm CCD camera, which can be seen in Figure 2.3. When a crystal is being run, it is mounted on a glass fibre, which in attached to a brass “pip.” The crystal is affixed to the glass fibre with amorphous silicon grease that hardens at low temperatures and does not diffract during the experiment. This brass pip is then placed in the goniometer.

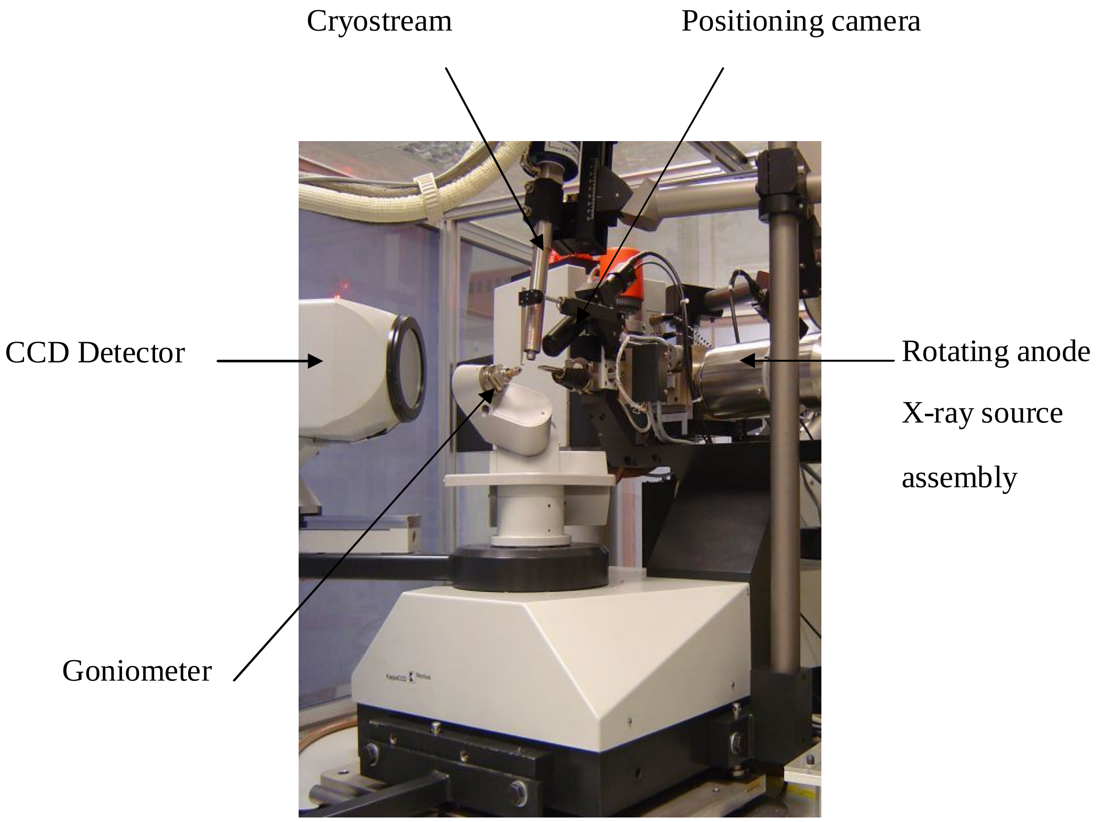

Figure 2.3: Photograph of a Bruker-Nonius Kappa CCD[10].

During a typical data collection, the quick scan, (usually of about 10-20 seconds), is normally run first of all, in order to check that the crystal gives a good quality diffraction pattern. For example, the crystal needs to be fully crystalline, with no powder attached to it and also a single crystal should be used rather than a twinned sample. If the sample is amorphous, there will not be any diffraction spots present after the quick scan. Rings of density will be present if the sample is a crystalline powder rather than a single crystal. A quick scan will also show whether or not a single crystal is good enough quality to collect a data set from. Doubled diffraction spots indicate that the single crystal in actually twinned and blurred spots commonly mean that there is disorder present within the crystal. When the quick scan has been run, the spots will give an indication of how long each frame of data will take to collect. Weaker spots mean that the diffractometer will take longer to collect the data.

If the quick scan suggests that a good quality crystal sample has been successfully mounted, a slightly longer run will be set up in order to try and identify the unit cell of the crystal. A series of eight phi/chi scans will be run and this usually last for two to four minutes. Before the scans take place, more information about the crystal needs to be entered into the computer data collection program, which will be of use when the complete data collection takes place. When these scans are being run, the quality of the crystal will once again be assessed, the program DirAx[11,12] will suggest a probable unit cell, and also give an indication of how well the model fits with the collected data. If a crystal is either poorly diffracting or twinned, the unit cell can often not be calculated. This is also the case if a sample has high mosaicity due to the imperfections within the crystal. Once a unit cell has been suggested by DirAx, it can be compared with a database of known unit cells[13], to see if either the same structure or an isostructural material has been previously characterised.

When a full data set is to be collected, the software package COLLECT[14] is used to calculate the number of frames required. It also suggests a data collection time, which is based on the unit cell data. When collecting the data, the program aims to obtain 100 % data completeness with further redundancies, resulting in an excess of data. However, this helps to lower the impact that any poor quality frames have on the final outcome and also gives a greater degree of statistical accuracy to the results.

Once a full run of data has been collected, it undergoes absorption correction and the SADABS[15] system is used for this purpose. This program estimates the amount of X-ray absorption encountered by the crystal. This is achieved by using the data that were supplied by the user about the crystal size and its composition. If the crystal is of an unknown composition, this correction is an approximation.

All analysis of single crystal X-ray data presented within this work was carried out using the WinGX set of packages[16], version 1.70.01, incorporating XPREP[17] and SHELX-97[18].

2.2.3-Powder X-ray Diffraction

Powder X-ray diffraction can be used to acquire information about the structure of a sample instead of single crystal X-ray diffraction if it is not possible to obtain single crystals or if the composition of a bulk, perhaps multiphase, sample is required. The principle of this technique is the same as in single crystal diffraction, in that an X-ray diffraction technique is used. However, a powder sample is made up of many microcrystallites, which are randomly orientated, thus resulting in less information being obtained due to peak overlap in the pattern. When a pattern has been recorded, it can be compared against the many structures stored in the JCPDS database[19]. This comprehensive database means that a powder X-ray pattern can be used as quick and convenient method to identify a sample, or the phases contained within it. During the course of this work, a Siemens D5000 diffractometer was used to record powder X-ray diffraction patterns, which is capable of identifying crystalline phases down to as low as 3 % of the bulk, (if the scattering powers and crystal complexity are optimum).

The D5000 diffractometer uses copper $K_{\alpha1}$ radiation with a wavelength of $\lambda = 1.54056$ Å. The X-rays are generated from a fixed anode and are focused by a Ge crystal primary monochromator. There is a range of aperture slit settings to collimate the radiation but the normal beam width before interaction with the sample is 2 mm, the post-sample slit is also generally 2 mm and the detector slit is usually 0.2 mm. The detector used to collect the diffracted beam is a standard scintillation counter. The sample is mounted on either an aluminium or a perspex sample holder. A schematic diagram of a D5000 diffractometer can be seen in Figure 2.4.

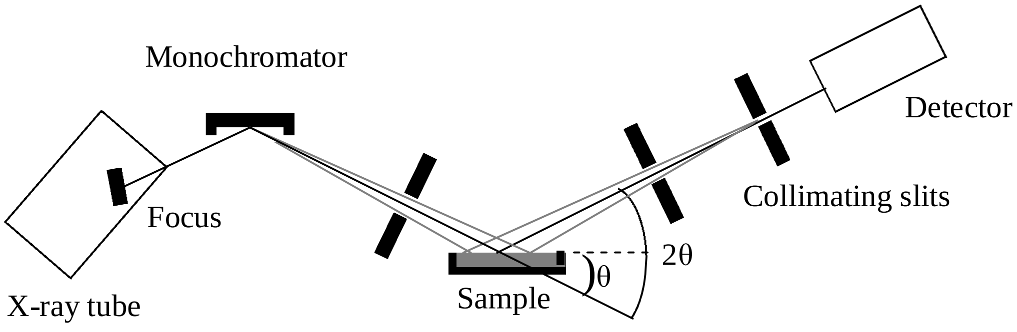

Figure 2.4: Schematic diagram of D5000 diffractometer.

The diffractometer is controlled by a PC and this also collects the data. The 2θ range to be studied can be set by the user and the machine will also count the time or degrees per minute scanned. The detector is always set at 2θ and the sample surface is always at θ to the fixed incident beam. This is known as the diffractometer being set up in Bragg-Brentano, or θ-2θ, geometry. After the pattern has been recorded, it can be viewed and compared with others with a program called DIFFRAC*plus* Evaluation Package[20].

2.2.4-Neutron Diffraction

X-rays are diffracted by electron density, which can cause problems when trying to characterise certain materials. This is predominantly due to the scattering power of an element being a linear function of its atomic number. Therefore, light elements, those with low atomic number, scatter weakly. This in turn results in only a weak contribution to the diffraction pattern, allowing little information on their positions to be extracted. For example, it is often almost impossible to locate hydrogen atoms in inorganic structures which contain heavily scattering elements with X-ray data alone. X-ray diffraction is also unable to distinguish between atoms that have very similar electron densities, such as fluorine and oxygen. Another disadvantage of X-rays is that they are absorbed by matter and this causes an angular dependence. This, in turn, leads to a loss of intensity at high 2θ values. X-ray diffraction equipment can also be limited by high temperature and pressure factors, which can restrict the experiments that may be run.

Neutrons are scattered by nuclei rather than electrons and their scattering power is dependent on resonant scattering as well as the size of the nucleus. The level of resonant scattering varies widely for different sized nuclei. This means that neighbouring elements and even different isotopes can be distinguished from one another. It is also possible to analyse light elements that are weak scatterers when carrying out analysis with X-ray diffraction. Light elements often have an increased relative scattering ability in neutron diffraction compared with X-ray diffraction[21]. This enables their atomic parameters to be determined, even in the presence of heavy elements. This phenomenon was utilised within this work, where hydrogen atoms were present alongside hafnium ions, allowing accurate position determination.

In this project, one sample was analysed using the D20 high-intensity two-axis diffractometer with variable resolution at the Institut Laue-Langevin neutron source in Grenoble. A schematic diagram of this instrument is shown in Figure 2.5.

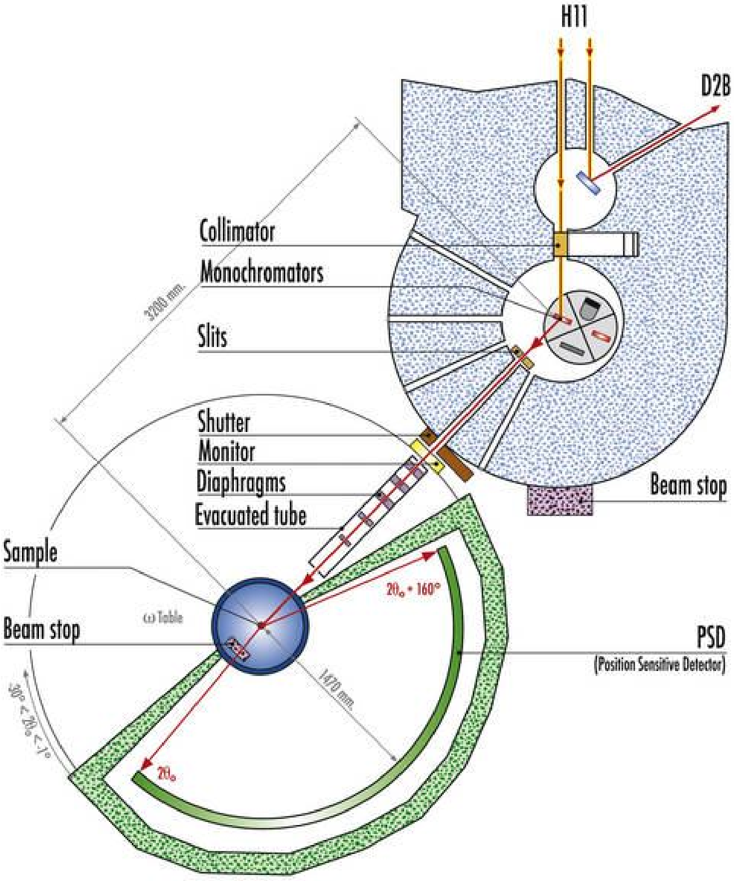

Figure 2.5: Schematic diagram of the D20 instrument[22].

There are two main types of neutron radiation suitable for diffraction techniques. These are constant wavelength and time-of-flight, with the former being used on the D20 instrument. The theory behind constant wavelength diffraction is fundamentally the same as for powder X-ray diffraction, as explained in Section 2.2.1 and, more specifically, in Section 2.2.3. The powder neutron data collected within this work were analysed *via* a joint refinement with single crystal data. The neutron data were collected by Dr. Valeska Ting and the framework structure was refined by Prof. Mark Weller.

2.3-Scanning Electron Microscopy and Energy Dispersive Spectroscopy

Scanning Electron Microscopy (SEM) and Energy Dispersive X-Ray Spectroscopy (EDS) were carried out on a JEOL JSM 5910 Scanning Electron Microscope. This was fitted with an Oxford Instruments Inca Energy 300 Energy-Dispersive X-ray Spectrometry analysis system.

In SEM, a high-energy electron beam is scanned across the surface of a sample. When these electrons strike the sample, they interact with the atoms within the sample, generating a range of signals. These signals are produced by the reflection of high energy electrons which occurs as a result of an energy exchange between the electron beam and the sample. It is the detection of specific signals which produces an image of the sample and also the sample’s elemental composition. The three signals that provide the most information in SEM are the secondary electrons, backscattered electrons and X-rays.

Secondary electrons are emitted from the atoms occupying the top surface of a sample and can be used to create an image of the surface. The contrast that is seen in the image is determined by the morphology of the sample. It is possible to obtain a high resolution image due to the small diameter of the primary electron beam.

The backscattered electrons are primary beam electrons which have been “reflected” by atoms in the solid. The contrast in this image results from the differences in atomic number of the elements that are in the sample. Therefore, the image will show the distribution of different chemical phases that may be present in the sample. However, the resolution of this image will not be as good as the one from the secondary electrons. This is due to the electrons being emitted from a depth within the sample.

X-rays are emitted due to shell transitions, which can occur when the primary beam interacts with atoms in the sample. These emitted X-rays will have an energy which is characteristic of the parent element. By detecting and measuring the energy of these X-rays, elemental analysis, or EDS, data can be collected. It is also possible to use the emitted X-rays to form maps or line profiles, which show the elemental distribution in the surface of a sample.

EDS can provide rapid qualitative analysis of the elements which are present within a sample. This is generally carried out with a sampling depth of 1-2 µm. In some cases, it is possible to quantitatively analyse the elemental composition of the sample. This is generally only possible if the sample does not contain only elements lighter than sodium or elements that have very similar X-ray energies. If either of these situations arise, it is almost impossible to accurately determine how much of an element is in the sample. If quantitative results are possible for a sample, the percentage weight of each element present is given in the EDS data, which may be used to support the solved structural formula of a material.

2.4-Thermogravimetric and Differential Thermal Analysis

Thermogravimetric analysis (TGA) is used to measure the mass of a sample as a function of temperature. This analytical method can be used, for example, to determine the water loss from a sample as it is heated. Any mass loss can then be calculated as a percentage of the sample's stoichiometry, thus showing how many water molecules were present within the crystal structure.

Differential thermal analysis (DTA) heats both the sample and a reference material in identical conditions. Any difference in temperature between the two materials will be recorded as either differential temperature or change in energy against time. Many changes within a structure do not involve a change in mass but a physical or chemical change, such as an endo- or exothermic phase change, which will result in a different temperature being recorded for the sample and reference materials. For example, this technique can be used to show a phase change within a sample as it is either heated or cooled, which would not necessarily be seen with TGA analysis alone.

Both the TGA and DTA analyses were carried out on the same machine. The equipment used was a Polymer Laboratories STA 1500 Simultaneous Thermogravimetric Analysis System. A schematic diagram can be seen in Figure 2.6. A typical TGA experiment uses approximately 20 mg of sample, which is weighed on the machine to an accuracy of 0.001 mg. Samples are generally heated at a rate of around 10 °C/min. Temperatures of up to approximately 650 °C can be reached in air but higher than this requires the atmosphere of inert gas, such as nitrogen or argon.

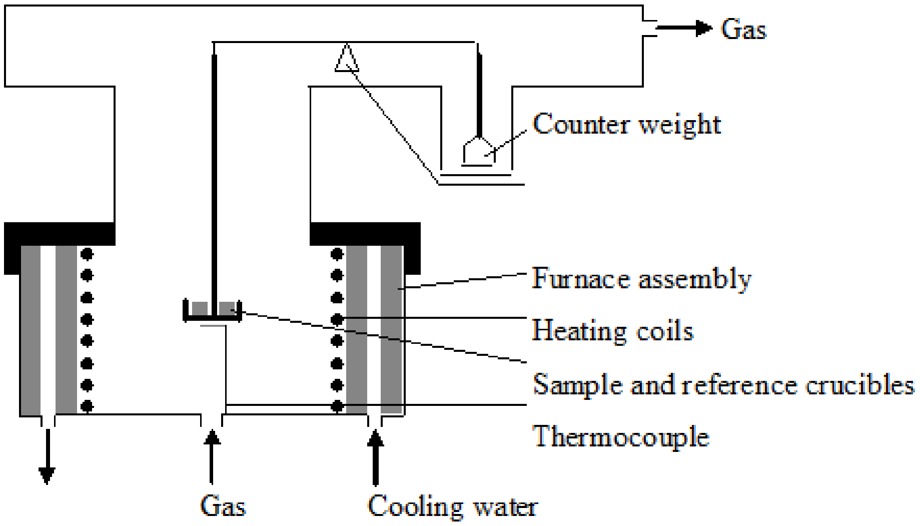

Figure 2.6: Schematic diagram of STA 1500 TGA/DTA equipment.

2.5-Infrared Spectroscopy

Fourier Transform Infrared Spectroscopy was carried out on some of the samples within this work. This technique was used primarily to confirm the presence of water molecules and ammonium cations. Spectra were collected on a Perkin-Elmer Instruments Spectrum-One FT-IR Spectrometer and in the range 4000-150 cm^{-1}. This range will include O–H and N–H stretches, as well as M–O and M–F stretches. The recorded spectrum for each sample was then examined with Spectrum software, in order to verify that the expected peaks were present.

2.6-Bond Valence Calculations

Bond valence calculations[1] were carried out on the new materials presented in this work. They were used to show that all of the atom positions present were fully occupied, for the given structural formulae. These calculations were also used to predict where hydrogen atoms were likely to be found in many of the structures. For example, in one of the sodium tungstate structures, it was shown that the terminal oxygen atoms within the $W_{12}O_{42}$ clusters were lacking bond valency. These calculations were then used, alongside considering the bond lengths, to show that the oxygen atoms were in fact hydroxyl groups, leading to the conclusion that the clusters actually had the formula $H_7W_{12}O_{42}$.

In a study by N. E. Brese and M. O'Keefe in 1991[1], it was shown that a strong linear correlation exists between the parameters for bonds from cations to pairs of anions. This knowledge has been used to estimate bond-valence parameters for almost 1000 pairs of atoms. By using the generally very accurate approximation that bond length is a unique function of bond valence for a pair of atoms, it is possible to calculate the bond valence of a known bond, thus indicating whether a stated structure is accurate and the atoms concerned are all fully coordinated. This may be achieved by using the equation shown in Equation 2.9. However, it is also possible to rearrange this expression in order to predict likely bond lengths within the structure.

$$\nu_{ij} = \exp[(R_{ij} - d_{ij})/b)] \qquad 2.9$$

ν = valence of two bonds between *i* and *j*, R = quoted bond valence parameter[1], d = bond length, b = "universal" constant (0.37Å)[23].

2.7-References

---

[1] N. E. Brese, M O’Keefe, *Acta. Cryst. B*, 1991, B**47**, 192-197.

[2] Parr Instrument Company, 211 Fifty Third Street, Moline. Illinois. 61265-9984. U.S.A..

[3] R. C. Reid, J. M. Prausnitz, B. E. Poling, *The Properties of Gases and Liquids*, McGraw Hill Book Co., 1987.

[4] J. Mehra, H. Rechenberg, *The Historical Development of Quantum Theory*, Springer, 2001, 142.

[5] W. L. Bragg, *Proc. Camb. Phil. Soc.*, 1913, **17**, 43-57.

[6] Based on original drawing from R. Chang, *Physical Chemistry for the Chemical and Biological Sciences*, University Science Books, 2000, 835.

[7] W. E. Wilson, *The Mineralogical Record, 1994.*

[8] M. T. Weller, *Inorganic Materials Chemistry*, Oxford Chemistry Primers, 2004, 20-23.

[9] D. Sayre. *Acta. Cryst.*, 1952, 5, 60-65.

[10] Photograph courtesy of EPSRC National Crystallography Service.

[11] A. Duisenberg, *J. Appli. Cryst.*, 1992, **25**, 92-96.

[12] A. Duisenberg, R Hooft, A Schreurs, J Kroon, *J. Appl. Cryst.*, 2000, **33**, 893-898.

[13] D. Fletcher, R McMeeking, D Parkin, *J. Chem. Inf. Comput. Sci.*, 1996, **36**, 746-749.

[14] R. Hooft, *COLLECT Data Collection Software*, Nonius B V, 1998.

[15] G. Sheldrick, *SADABS Version 2.10*, Bruker AXS Inc., Madison, Wisconsin, USA, 2003.

[16] L. J. Farrugia, *J. Appl. Cryst.*, 1999, **32**, 837-838.

[17] XPREP Bruker AXS, Inc., Madison, Wisconsin, USA.

[18] G. Sheldrick, *SHELX-97, (includes SHELXS-97 and SHELXL-97), Programs for Crystal Structure Analysis, Release 97-2*, University of Göttingen, Göttingen, Germany, 1997.

[19] International Centre for Diffraction Data, Campus Boulevard, Newton Square, Pennsylvania, 19073-3273, USA, 1995.

---

[20] DIFFRAC^{plus} Evaluation Package, Regents of the University of California, Sun Microsystems, Inc., 2004.

[21] C. S. Knee, *Synthesis, Structure and Magnetic Properties of Complex Metal Oxides*, PhD Thesis, University of Southampton, 1999.

[22] Diagram courtesy of Institut Laue-Langevin.

[23] I. D. Brown, D. Altermatt, *Acta. Cryst. B*, 1985, B**41**, 244-247.

Chapter 3

Group IV and V Arsenate Frameworks

Although arsenate frameworks have been shown to be synthesised under milder conditions than the phosphate analogues[1], there are still relatively few examples of arsenates of Group IV and V metals and some of these known structures are discussed in Chapter 1. The work presented here aims to synthesise novel materials within this poorly investigated structure group. By producing and characterising new frameworks that are built up of tetrahedral arsenate groups and octahedral metal units, this work hopes to give a better understanding of the structure of these arsenate materials and of their properties.

Solvothermal reaction conditions were used for all of the syntheses described within this arsenate study. Most of the arsenate work reported in the literature has used solvothermal conditions, suggesting that this will be a successful route to producing novel frameworks, such as in the case of $Mn_7(AsO_3OH)_4(AsO_4)_2$[2]. This material was successfully synthesised under mild hydrothermal conditions, with a reaction temperature of 170 °C and autogeneous pressure resulting in the formation of single crystals of the manganese arsenate $Mn_7(AsO_3OH)_4(AsO_4)_2$. Arsenate frameworks have been synthesised *via* hydrothermal methods since the very first examples were produced; with two frameworks known as $AlAsO_4$-1 and $AlAsO_4$-2 synthesised and characterised in the 1980s[3, 4]. Therefore, as an initial starting point, it was decided to synthesise these Group IV and V arsenates solvothermally. This work was then extended to further investigate the effects of varying the reaction conditions on the materials synthesised: namely concentration, pH, temperature and reaction time.

By using a fluoride source as a mineralising agent, it was hoped that these reactions would proceed more readily under solvothermal conditions. Fluorides have been used as mineralising agents in phosphate reactions since the end of the 1980s[5, 6], thus suggesting that they may have a similar role when used in arsenate reactions. In some of the cases detailed in the work presented here, the fluoride group did not just act as a mineraliser but was actually incorporated into the structure. In some cases, there were M–F bonds present in the metal arsenate framework, forming MF_xO_{6-x} octahedra, which was previously unknown for hafnium and niobium arsenates.

The novel arsenate frameworks characterised herein were produced after much altering and fine-tuning of the reaction conditions. The reactions produced single crystals within bulk powder and their structures were solved by X-ray single crystal diffraction, with other techniques to support the refinement, such as EDS, IR, TGA and in one case collecting neutron diffraction data. The bulk powders were analysed *via* powder X-ray diffraction and found to be a mixture of product and starting materials.

Electron Dispersive Spectroscopy (EDS) measurements were made to show semi-quantitatively whether or not oxygen and fluorine were present in the structures. In a single crystal refinement, oxygen and fluorine are very similar in size and there is only a small difference in their thermal parameters, so it is very difficult to distinguish between the two. Therefore, EDS was used in confirm the presence or absence of these two elements. For the structures discussed below which were found to contain nitrogen or carbon, these elements were not seen during EDS data collections, due to being too light to allow interaction between the sample and the electron beam. Infrared (IR) spectra were recorded to support the single crystal refinement by showing whether certain absorptions were present due to bond stretches and bends within the structure, such as in N–H and O–H. Thermogravimetric Analysis (TGA) was used in order to confirm the number of water molecules and ammonium cations within the structures. TGA was also implemented to investigate the thermal stability of many of these materials. By analysing the data collected with this technique, the temperature at which structural decomposition started was calculated and also the temperature at which water molecules and ammonium cations were removed from the frameworks. Neutron diffraction data was collected for one sample, as described in Section 3.1. Hydrogen atoms cannot generally be seen with X-rays but neutron diffraction is an ideal technique to locate protons due to the fact that scattering is by the nucleus and not the electrons. This neutron data was collected on a powder sample of ground up single crystals rather than a single crystal neutron diffraction experiment. This neutron diffraction data was collected at ILL, France on the D20 diffractometer and showed that there were two hydrogen atoms bonded to this terminal oxygen atom. Finally, bond valence calculations were used in order to verify that all of the atoms within each structure were fully bonded and that there were no atoms missing from the single crystal refinement.

These calculations also supported where hydroxyl groups or water molecules may exist. These methods are all described in more detail in Chapter 2.

Not all of the reactions carried out resulted in the synthesis of single crystals of new materials. Table 3.1 summarises the starting materials and reactions conditions of the successful reactions, the results of which are discussed in this chapter, and also those reactions which resulted in the formation of non-novel single crystals, such as starting materials or known structures. In a typical reaction, the starting materials were mixed and stirred briefly, then transferred to a 23 mL Parr hydrothermal bomb. The bomb was heated in an oven at the temperature and duration detailed in Table 3.1. The product in each case was retrieved by filtration under vacuum, washed with hot distilled water and dried in air. The following reactions in this chapter are a description and discussion of the new materials synthesised. A large number of other reactions were carried out, where the reaction conditions were altered; around 100 reactions for the different metals discussed here. Conditions such as different reaction durations, temperatures and solution pH were investigated and, other than the reactions detailed in Table 3.1, resulted in either just powders being produced or a minor phase of glasses or tiny single crystals, which were too small to be analysed *via* single crystal diffraction with the equipment available.

Table 3.1: Reaction conditions for successful Group IV and V arsenate syntheses.

Starting materials	Temp. / °C	Reaction period / h	Type of single crystals produced	Product	Section in thesis
Hafnium (IV) fluoride (0.393 mmol, 0.100 g) and arsenic (V) oxide (1.179 mmol, 0.271 g) were dissolved in concentrated hydrochloric acid (10 cm^3).	180	120	Colourless sheet	$HfF(H_2O)(AsO_4)$	3.1
Hafnium (IV) fluoride (0.393 mmol, 0.100 g) and ammonium dihydrogen arsenate (0.73 mmol, 0.188 g) were dissolved in ethanol (10 cm^3). Starting pH = 1.7; final pH = 3.3.	180	144	Colourless block	$Hf_2F_9(AsO_4H)\cdot(NH_4)_3(H_2O)$	3.2
Hafnium (IV) fluoride (0.393 mmol, 0.100 g) and arsenic (V) oxide (1.179 mmol, 0.271 g) were dissolved in concentrated ammonia solution (10 cm^3).	180	144	Colourless plate	$HfF(AsO_4)_2(NH_4)_3$	3.3
Niobium (IV) fluoride (0.532 mmol, 0.100 g), ammonium dihydrogen arsenate (1.597 mmol, 0.184 g) and 1,4-diazabicyclo[2.2.2]octane (DABCO) (0.598 mmol, 0.0671g) were dissolved in concentrated ammonia solution (10 cm^3).	175	144	Colourless needle	$NbF_2(AsO_4)(NH_4)_3$	3.4
Hafnium (IV) nitride (0.520 mmol, 0.100 g) and arsenic (V) oxide (0.730 mmol, 0.228 g) were dissolved in ethanol (10 cm^3).	180	144	Black octahedral-shaped blocks within major phase of black powder	Arsenic acid: H_3AsO_4	

Starting pH = 2.4.					
Zirconium (IV) bromide (0.243 mmol, 0.100 g) and arsenic (V) oxide (0.730 mmol, 0.168 g) were dissolved in ethanol (10 cm^3). Starting pH = 2.0.	180	144	Black octahedral-shaped blocks as minor phase within black powder	Arsenic acid: H_3AsO_4	
Zirconium (IV) bromide (0.243 mmol, 0.100 g) and arsenic (V) oxide (0.730 mmol, 0.168 g) were dissolved in ethanol (10 cm^3). Starting pH = 1.8.	180	144	Colourless blocks within majority phase of grey powder	ZrO_2	
Niobium (V) fluoride (0.532 mmol, 0.100 g) and ammonium dihydrogen arsenate (1.597 mmol, 0.254 g) were dissolved in ethanol (10 cm^3). Starting pH = 0.5.	175	144	Colourless blocks with major phase of grey powder	Single crystals were stacked in layers and thus twinned so could not be analysed *via* single crystal diffraction	
Zirconium (IV) fluoride (0.598 mmol, 0.100 g) and arsenic (V) oxide (1.794 mmol, 0.412 g) were dissolved in sodium hydroxide solution (10 cm^3). Starting pH = 9.4.	175	144	Colourless sheets present as a minor phase within white powder	$Na_3AsO_4\cdot H_2O$	
Zirconium (IV) fluoride (0.598 mmol, 0.100 g), arsenic (V) oxide (1.79 mmol, 0.412 g) and oxalic acid dihydrate (0.598 mmol, 0.754g) were dissolved in distilled water (10 cm^3). Starting pH = 2.6.	140	168	Colourless blocks within major phase of white powder	Single crystals were twinned and could not be sufficiently separated to be analysed *via* single crystal analysis.	

3.1-$HfF(H_2O)(AsO_4)$

A colourless sheet-like crystal was selected for single crystal X-ray diffraction and a summary of the crystallographic information that was collected is shown in Table 3.2. The monoclinic unit cell extends to give a framework that is made up of HfF_2O_5 decahedra and AsO_4 tetrahedra and their bond lengths are shown in Table 3.3. The decahedra are each linked to their two neighbouring HfF_2O_5 decahedra by bridging fluorine atoms, forming a backbone of Hf–F–Hf linkages. The result is that corner-sharing chains exist along the length of the *c*-axis, as shown in Figure 3.1.

Along both the *a*- and *b*-axes, the AsO_4 tetrahedra are bonded to the HfF_2O_5 decahedra. Of the five oxygen atoms in each decahedron, four bridge to the four closest arsenic atoms, making up part of the relevant arsenate tetrahedra and meaning that the AsO_4 tetrahedra are all fully coordinated and there is only one terminal oxygen atom in each of the HfF_2O_5 decahedra. Consequently, a rigid and tightly packed three-dimensional framework builds up to give $HfF(H_2O)(AsO_4)$.

Table 3.2: Crystal data for $HfF(H_2O)(AsO_4)$.

Chemical Formula	$HfF(H_2O)(AsO_4)$		
Crystal Appearance	Colourless sheet	T/ K	120
Crystal Size/ mm	0.04 x 0.02 x 0.01	λ/Å	0.71073
M	354.42288	Reflections collected	2524
Crystal System	Monoclinic	Unique reflections	577
Space Group	*C*2/*m*	R_{int}	0.0598
a, b, c/ Å	8.8626(5), 6.7314(4), 7.9015(5)	$R_1[I > 2\sigma(I)]^a$	0.0366
α, β, γ / °	90.000(0), 100.541(3), 90.000(0)	*R*1(all data)	0.0392
V/ $Å^3$	463.64(3)	wR_2(all data)	0.1069
Z	2		

Table 3.3: Bond lengths within in $HfF(H_2O)(AsO_4)$.

Bond	Bond length/ Å	Bond	Bond length/ Å
Hf1–O2	2.142(13)	As1–O2	1.690(12)
Hf1–O3	2.062(10)	As1–O3	1.669(10)
Hf1–O3	2.062(10)	As1–O3	1.669(10)
Hf1–O4	2.105(14)	As1–O4	1.668(13)
Hf1–O5	2.198(14)		
Hf1–F1	2.0922(6)		
Hf1–F2	2.0498(6)		

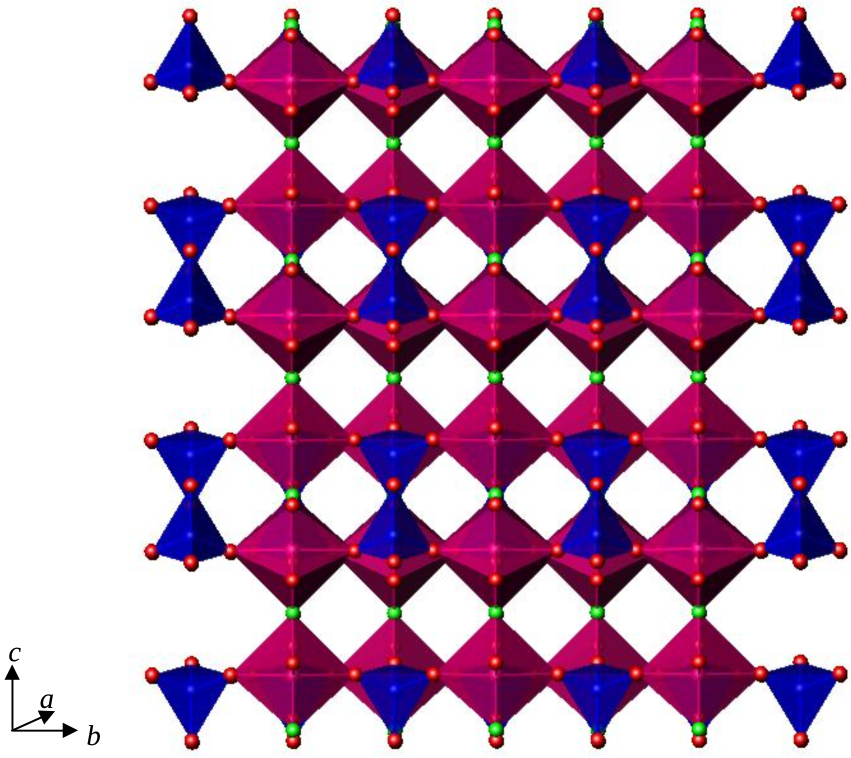

a)

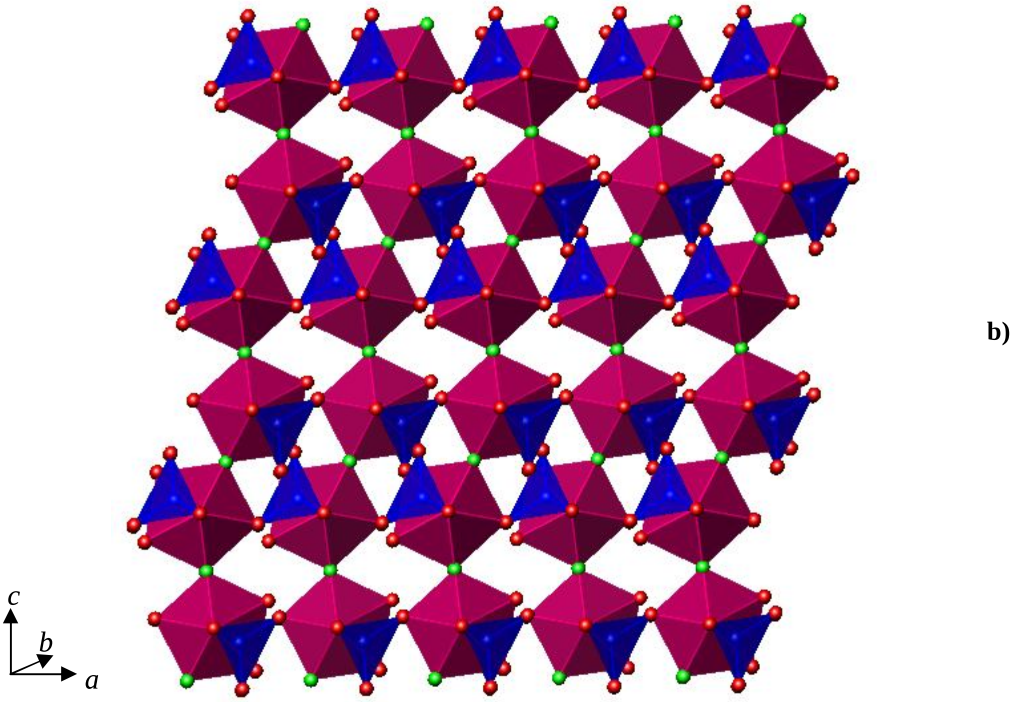

Figure 3.1: Structure of $HfF(H_2O)(AsO_4)$ viewed down the a) *a*- and b) *b*-axes, where the hafnium decahedra are shown in magenta, the arsenate tetrahedra in blue, the oxygen atoms in red and the fluorine atoms in green.

The terminal oxygen atom (O5) within each HfF_2O_5 decahedron was calculated *via* both refinement of the neutron diffraction data and bond valence calculations[7] to be a water molecule but is shown as just an oxygen atom in Figure 3.1 for clarity. The Hf–O bond for the terminal oxygen atom was found to be longer than the rest of the Hf–O bonds in each decahedron; 2.20 Å as opposed to 2.00-2.10 Å, due to only being weakly bonded to the hafnium centre. When refined as just an oxygen atom, this terminal oxygen atom was also found to be lacking bond valency, as shown by bond valency calculations[7], requiring the addition of two protons to be fully bonded. Table 3.4 gives a summary of these calculations, showing that O5 is underbonded in comparison with the other oxygen and fluorine atoms, (where the oxygen atoms should have a total valence of approximately 2 and fluorine of approximately 1).

Table 3.4: Bond lengths and bond valence calculations for HfF_2O_5 decahedra.

Atom	Hf–O/F bond length/ Å	As–O/F bond length/ Å	Bond valence
O2	2.142(13)	1.69	1.78
O3	2.062(10)	1.67	2.00
O3	2.062(10)	1.67	2.00
O4	2.105(14)	1.67	1.91
O5	2.198(14)	N/A	0.48
F1	2.0922(6)	N/A	1.26
F2	2.0498(6)	N/A	1.42

Neutron data were also collected of this material and were collected from a 30 mg sample cooled to 120 K on the D20 diffractometer operating in high-take off angle mode with a wavelength of 1.848 Å at ILL for a period of 90 minutes. The data were normalised and then analysed using the EXPGUI/GSAS Rietveld suite. In order to investigate the existence and nature of hydrogen atoms attached to the terminal O5 position located in the SXD analysis, a combined single crystal X-ray diffraction-powder neutron diffraction (SXD-PND) analysis was undertaken. This method allows the determination of hydrogen positions in materials containing heavy atoms even from relatively poor quality neutron diffraction data; where a structural model is refined tensioned against the SXD and PND data sets[8]. Initial stages of the refinement used solely the SXD model (no hydrogen atoms) refined against both the SXD and PND. Significant discrepancies in the profile fit were evident yielding RwP(-background) = 7.54% and chi sq of 3.39. Difference Fourier maps were calculated using the neutron diffraction data and revealed two sites of "negative" scattering intensity approximately 1Å from O5. Hydrogen atoms were assigned to these sites and, except for soft constraints applied to the O–H distances (of 0.97+/- 0.005Å), a fully unconstrained refinement was undertaken with RwP(-background) falling to 4.57% and chi sq to 2.65. The final refinement is shown in Figure 3.2 and Figure 3.3 shows the located hydrogen atoms, where it may be seen that the two O–H bond lengths are 0.97 Å, with an internal angle of 118.4 °, which are acceptable values for a water molecule.

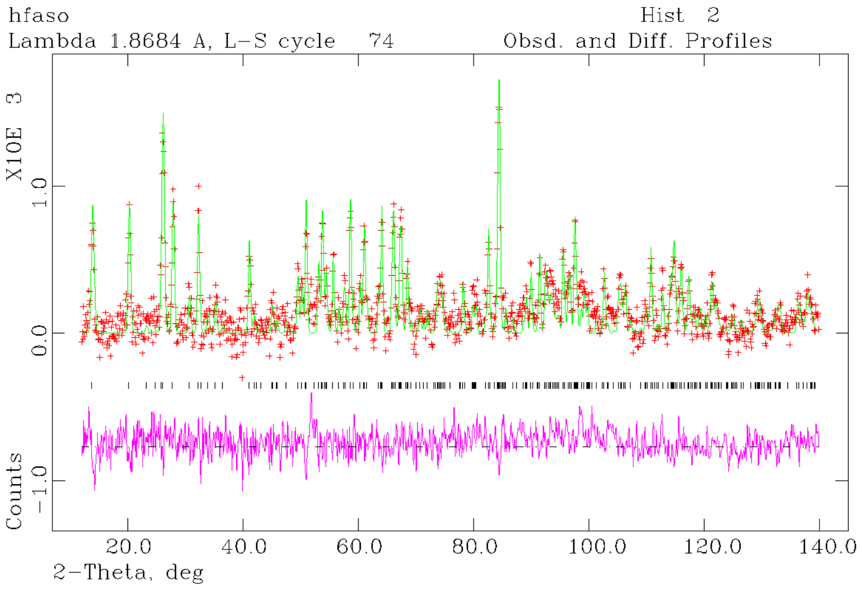

Figure 3.2: Final combined SXD-PND refinement for $HfF(H_2O)(AsO_4)$.

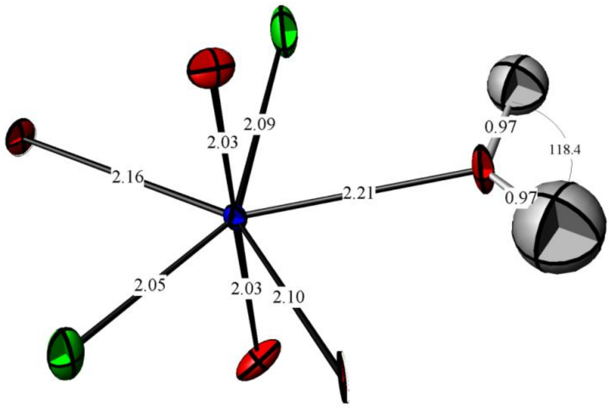

Figure 3.3: Located hydrogen atoms in $HfF(H_2O)(AsO_4)$, showing thermal parameters.

By combining the information from these sources, this oxygen atom was determined to be a weakly bonded water molecule. Hydrogen bonding is present between the water molecule and the surrounding oxygen atoms, which stabilises the framework, as well as supporting the neutron data to show where the hydrogen atoms lie. The expected direction of the hydrogen bonding interactions can be seen in

Figure 3.4. The black dotted lines in this figure show the directions along which the hydrogen atoms of the water molecule lie, as indicated by the neutron data and also the hydrogen bonding.

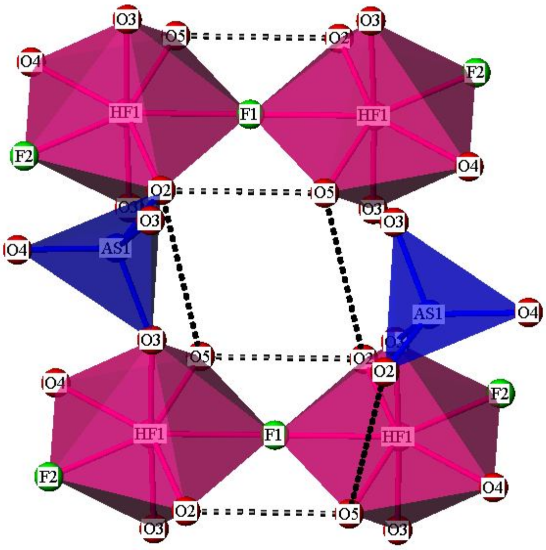

Figure 3.4: Hydrogen bonding between the terminal oxygen atom and neighbouring oxygen atoms in $HfF(H_2O)(AsO_4)$, with the hydrogen bonding shown as black dotted lines.

TGA data showed that there was a mass loss of 5.08 % at around 250 °C which was calculated to correspond to the loss of the polyhedral water molecule. If there had only been a hydroxyl group present, there would have been very little difference in the mass lost compared with a water molecule but the change would have been seen at around 400 °C. A broad absorption was observed at 3300-3150 cm $^{-1}$ in the IR spectrum of this material, which is due to the O–H stretch for the water molecule that is hydrogen bonded within the framework. An EDS collection confirmed the presence of both fluorine and oxygen in the structure and, when coupled with bond valence calculations, the final formula of $HfF(H_2O)(AsO_4)$ ensures that the framework is charge-balanced and also the fluorine atoms are all in the same environments, by being present as bridging Hf–F–Hf. During the EDS analysis, an SEM image was collected of the single crystals of $HfF(H_2O)(AsO_4)$ and is shown in Figure 3.5.

Figure 3.5: SEM image of a single crystal of $HfF(H_2O)(AsO_4)$.

3.2-$Hf_2F_9(AsO_4H)\cdot(NH_4)_3(H_2O)$

A colourless block-like crystal was selected for single crystal X-ray diffraction and a summary of the crystallographic information that was collected is shown in Table 3.5. The structure exhibits monoclinic symmetry and consists of alternating HfF_4O_2 octahedra and AsO_4 tetrahedra along the *b*-axis to form an elongated "zig-zag" chain where the octahedral fluorine atoms are always terminal, which point into the open regions of the framework. The octahedra are all corner-sharing with the tetrahedra and Hf–O–As linkages occur *via* the single axial oxygen atom in each octahedron, as shown in Figure 3.6 and the bond lengths within this structure are given in Table 3.6.

Each arsenate tetrahedron has a third hafnium-centred octahedron bonded to it, in addition to those in the chain along the *b*-axis. This third octahedron is in fact HfF_5O and is directed along the *c*-axis, as seen more clearly when the structure is viewed down the *a*-axis, as in Figure 3.6. Along the "zig-zag" chain the AsO_4 tetrahedra alternate between facing up and down, where the apical oxygen atom is always terminal. It was calculated *via* bond valence calculations[7] that this slightly underbonded oxygen atom (O10) in fact exists as a hydroxyl group. Table 3.7 shows a summary of these calculations, showing the slight underbonding of O10. Although the As–O bond length (1.67 Å) is comparable with those for the other arsenate oxygen atoms, the fact that O10 does not bridge to a hafnium cation means that a proton is required to overcome the underbonding that is otherwise seen. A hydroxyl group at this position also ensures that the overall formula is correctly charge-balanced. This hydroxyl group prevents a chain forming along this direction, causing a two-dimensional material to be produced, along with the fluorine atoms in the hafnium-centred octahedra having the same affect. The other three oxygen atoms within each hydrogen arsenate tetrahedron are always bonded to the three hafnium-centred octahedra, as discussed above, causing the third, non-chain octahedron to alternately face opposite directions.

Table 3.5: Crystal data for $Hf_2F_9(AsO_4H)\cdot(NH_4)_3(H_2O)$.

Chemical Formula	$Hf_2F_9(AsO_4H)\cdot(NH_4)_3(H_2O)$
Crystal Appearance	Colourless block
Crystal Size/ mm	0.05 x 0.05 x 0.03
M	740.02355
Crystal System	Monoclinic
Space Group	$P2_1$
a, b, c/ Å	6.1867(2), 11.6476(5), 10.6755(4)
α, β, γ / °	90.000(0), 105.894(3), 90.000(0)
V/ $Å^3$	739.87(7)
Z	6
T/ K	120
λ/Å	0.71073
Reflections collected	8423
Unique reflections	2955
R_{int}	0.0418
$R_1[I > 2\sigma(I)]^a$	0.0356
$R1$(all data)	0.0461
wR_2(all data)	0.0788

Table 3.6: Bond lengths in $Hf_2F_9(AsO_4H)\cdot(NH_4)_3(H_2O)$.

Bond	Bond length/ Å	Bond	Bond length/ Å	Bond	Bond length/ Å
Hf1–O9	2.031(9)	Hf2–O6	2.062(9)	As3–O6	1.665(10)
Hf1–F1	1.99(2)	Hf2–O13	2.073(11)	As3–O9	1.679(9)
Hf1–F2	1.998(18)	Hf2–F8	1.99(2)	As3–O10	1.668(7)
Hf1–F3	1.94(2)	Hf2–F11	1.98(2)	As3–O13	1.719(11)
Hf1–F4	1.976(18)	Hf2–F12	1.992(11)		
Hf1–F7	1.959(7)	Hf2–F16	2.006(12)		

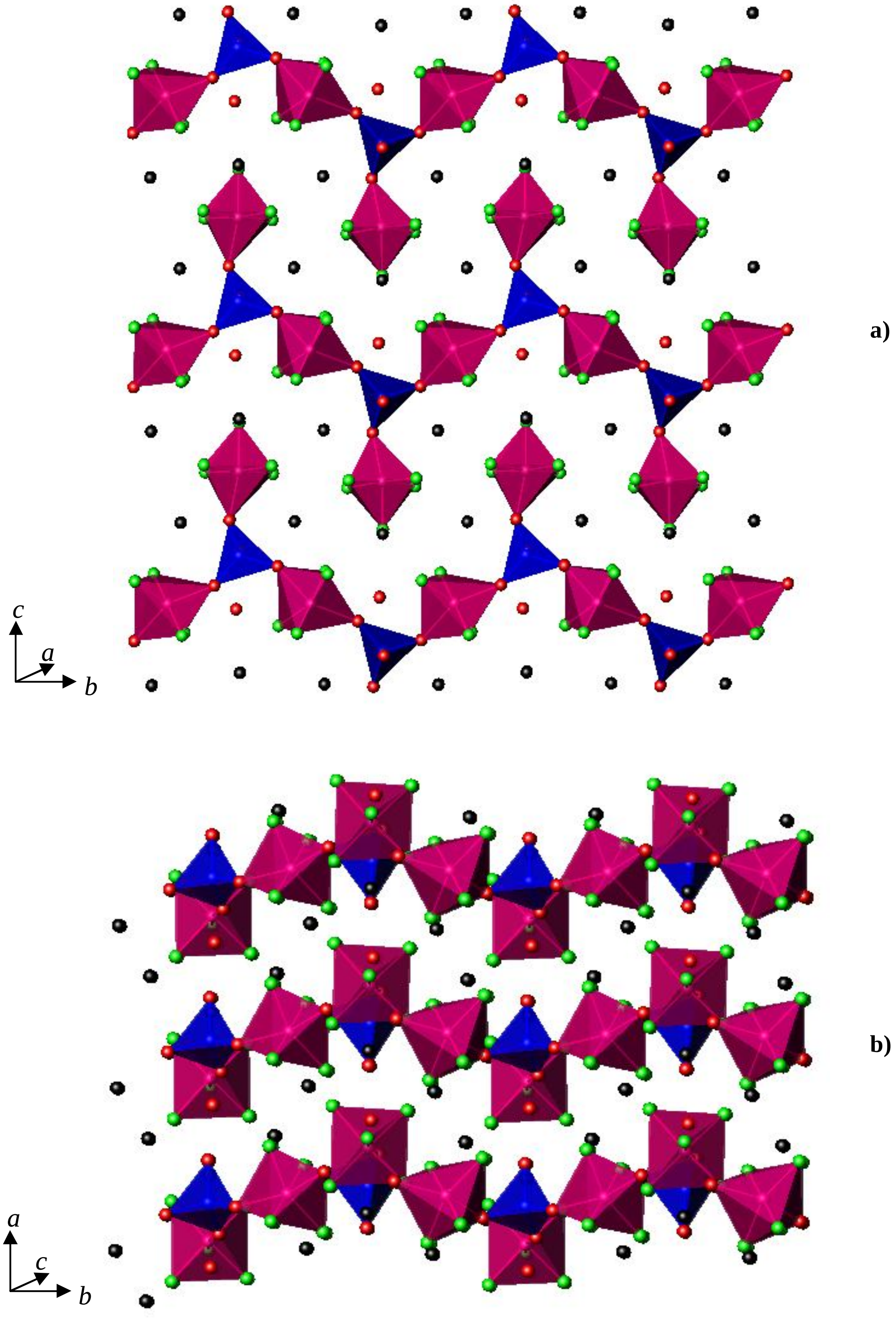

Figure 3.6: Structure of $Hf_2F_9(AsO_4H)\cdot(NH_4)_3(H_2O)$ viewed down the a) *a*- and b) *c*-axes, where the hafnium octahedra are shown in magenta, the arsenate tetrahedra in blue, the oxygen atoms in red, the fluorine atoms in green and the ammonium cations as black spheres to represent the nitrogen atoms.

Table 3.7: Bond lengths and bond valence calculations for hydrogen arsenate tetrahedra.

Atom	Hf–O bond length/ Å	As–O bond length/ Å	Bond valence
O6	2.062(9)	1.665(10)	2.02
O9	2.031(9)	1.679(9)	2.01
O10	N/A	1.668(7)	1.32
O13	2.073(11)	1.719(11)	1.76

As may be seen in the above figure, there are both ammonium cations and water molecules present between the polyhedral chains in this structure. Both these species exist in the spaces created by the chains along two different axes and are held in place by hydrogen bonding to the layered backbone of this framework. The hydrogen bonding in this material is shown in Figure 3.7, where a small section of the interlayer region is depicted. This diagram is highly simplified with only a very small region shown for clarity, thus meaning that not all of the possible hydrogen bonds are shown. However, it may clearly be seen that the hydrogen bonding occurs between the interlayer species and the fluorine and oxygen atoms of the polyhedra, due to the presence of appropriate distances over which hydrogen bonding commonly occurs. Although the actual hydrogen atom positions of the ammonium cations and water molecules could not be determined *via* single crystal analysis, their likely positions may be seen by the direction in which the hydrogen bonds lie. The black dotted lines indicate where O/N–H - - F/O hydrogen bonds are likely to lie. For example, N3 is shown in hydrogen-bond to F1, F2, F8 and O10, with distances of between 2.76 Å and 2.98 Å and bond angles such as 106.53 ° for F1–N3–O10. Table 3.8 gives a summary of the probable hydrogen bonding interactions within $Hf_2F_9(AsO_4H)\cdot(NH_4)_3(H_2O)$.

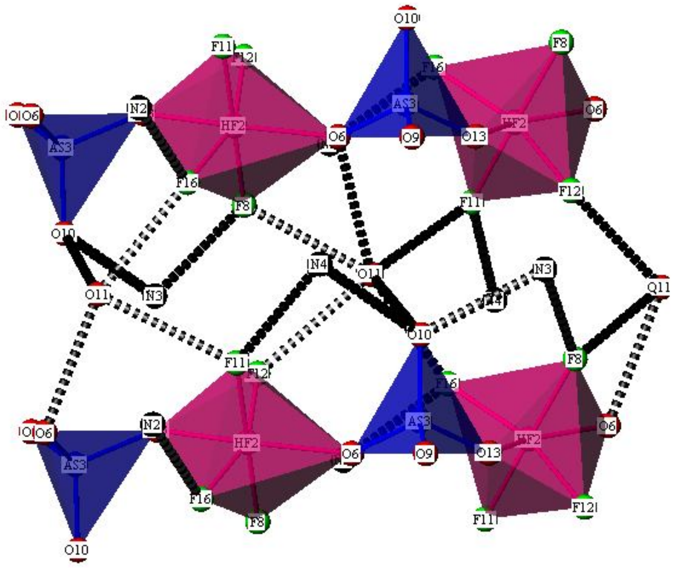

Figure 3.7: Hydrogen bonding between the terminal oxygen atom and neighbouring oxygen atoms in $Hf_2F_9(AsO_4H)\cdot(NH_4)_3(H_2O)$, with the hydrogen bonding shown as black dotted lines.

Table 3.8: Hydrogen bonding of $Hf_2F_9(AsO_4H)\cdot(NH_4)_3(H_2O)$, (where *d* = distance between stated atoms and *A* = acceptor).

N - - A	d(N - - A)/ Å	N - - A	d(N - - A)/ Å
N2 - - F1	2.80	N4 - - F1	3.00
N2 - - F2	2.91	N4 - - F2	2.89
N2 - - F8	3.09	N4 - - F11	2.90
N2 - - F16	2.78	N4 - - O10	2.97
N3 - - F1	2.81	O11 - - F8	2.85
N3 - - F2	2.98	O11 - - F11	3.04
N3 - - F8	2.84		
N3 - - O10	2.76		

EDS analysis showed semi-quantitatively that there was a large proportion of fluorine present in this structure. The HfF_5O octahedra in this structure were found to only bridge *via* one point per octahedron, the oxygen atom, so the other five octahedral atoms were found to all be fluorine atoms. These five terminal polyhedral atoms are all in a similar environment to one another, so it may be assumed they are the same element, in this case fluorine. By allocating these five atoms as fluorine atoms, the overall structure of $Hf_2F_9(AsO_4H)\cdot(NH_4)_3(H_2O)$ was also calculated to be correctly charge-balanced. An SEM image of a single crystal of $Hf_2F_9(AsO_4H)\cdot(NH_4)_3(H_2O)$ was also taken during the EDS data collection and is shown in Figure 3.8.

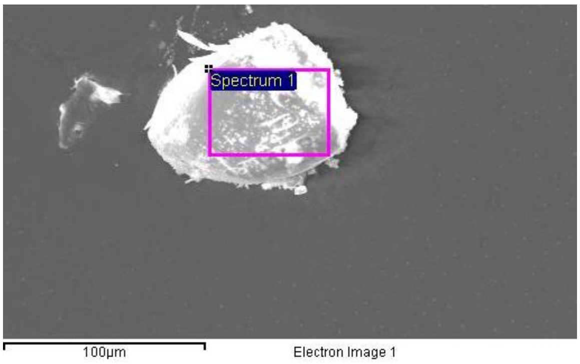

Figure 3.8: SEM image of a single crystal of $Hf_2F_9(AsO_4H)\cdot(NH_4)_3(H_2O)$.

The presence of water molecules and ammonium cations in this structure was confirmed by TGA. A weight loss of 2.43 % was observed at approximately 240 °C which corresponds to the loss of water. The TGA data also suggested that the three ammonium cations per formula unit were lost in two stages. Two ammonium cations were lost at approximately 300 °C, where a mass loss of 4.88 % was observed, and the third was removed from the structure at around 390 °C, when a mass loss 2.43 & was seen. This greater temperature suggests that the third ammonium cation is more strongly hydrogen-bonded within the structure, which results in its removal requiring a greater amount of thermal energy than the other two ammonium cations. A further mass loss was observed at 460 °C, which was calculated to be equivalent in mass to a hydroxyl group, and was concluded to be this portion of the hydrogen arsenate unit being lost from the structure, representing the start of the main framework decomposing.

The IR spectrum of this material revealed an absorption at 3320-3058 cm^{-1}. This position is lower than expected, which is due to the hydrogen bonding present in the structure. Peaks were also observed in the IR spectrum at 3482, 3436 and 1637 cm^{-1} and these absorptions correspond to the N–H stretching vibrations of the ammonium cations.

A further peak at 622 cm^{-1} was found to be due to the stretching of the Hf–F bonding with this structure, further supporting the presence of HfF_5O octahedra.

3.3-$HfF(AsO_4)_2(NH_4)_3$

A colourless hexagonal plate-like single crystal was selected for single crystal X-ray diffraction and a summary of the crystallographic information is shown in Table 3.9. The framework possesses monoclinic symmetry and is built up of alternating $HfFO_5$ octahedra and AsO_4 tetrahedra, which are connected *via* bridging oxygen atoms, as seen in Figure 3.9, with the bond lengths shown in Table 3.10. These octahedra and tetrahedra alternate as corner-sharing units and form four-membered rings which run along both the *b*- and *c*-axes, as demonstrated in Figure 3.9. The result of these rings running along two axes is a framework consisting of two-dimensional layers of polyhedra. Between these layers there are ammonium cations, with further ammonium cations present in the cavities created within the layers themselves.

For each of the $HfFO_5$ octahedra, all five oxygen atoms bridge to form part of the neighbouring arsenate groups. The sixth polyhedral atom was deduced to be fluorine rather than another oxygen atom/hydroxyl group. Within the single crystal refinement, the thermal parameters were a significantly better fit for fluorine than oxygen and also EDS confirmed semi-quantitatively that a small amount of fluorine is present within the material. Bond valence calculations[7] and charge-balancing of the overall structure also supported the presence of single fluorine atom per octahedron rather than a hydroxyl group or water molecule, for example. Bond valence calculations confirmed that if this site of electron density was to be refined as an oxygen atom, there would be a significant level of underbonding. This site was also determined to be too close to the ammonium cations, (2.76 Å from the closest nitrogen atom, N2), for a hydroxyl group to exist in place of the fluoride anion, again supporting the EDS data which confirms fluorine to be present. Table 3.11 gives a summary of these calculated values and also the corresponding bond lengths. It may be seen that the bond valence values and bond lengths are all satisfactory for Hf–O/F and As–O/F bonds. The fluorine atoms in this structure are directed into the large channels between the two-dimensional layers of polyhedra but are not close enough to any of the ammonium cations to become involved in hydrogen bonding with the N–H bonds. An SEM image of a single crystal of $HfF(AsO_4)_2(NH_4)_3$ was recorded during the EDS analysis and is shown in Figure 3.10.

Table 3.9: Crystal data for $HfF(AsO_4)_2(NH_4)_3$.

Chemical Formula|	$HfF(AsO_4)_2(NH_4)_3$
Crystal Appearance	Colourless sheet
Crystal Size/ mm	0.1 x 0.1 x 0.02
M	529.4423032
Crystal System	Monoclinic
Space Group	$P2_1/c$
a, b, c/ Å	10.3654(5), 6.6582(3), 32.2682(2)
α, β, γ / °	90.000(0), 91.606(2), 90.000(0)
V/ Å3	2226.1(2)
Z	15
T/ K	120
λ/Å	0.71073
Reflections collected	16228
Unique reflections	5038
R_{int}	0.0496
$R_1[I > 2\sigma(I)]a$	0.0596
R1(all data)	0.0845
wR2(all data)	0.1476

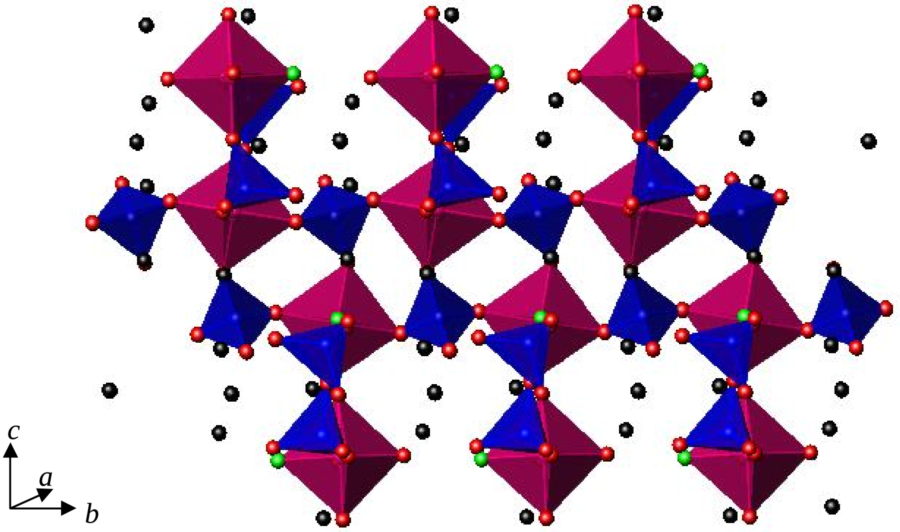

a)

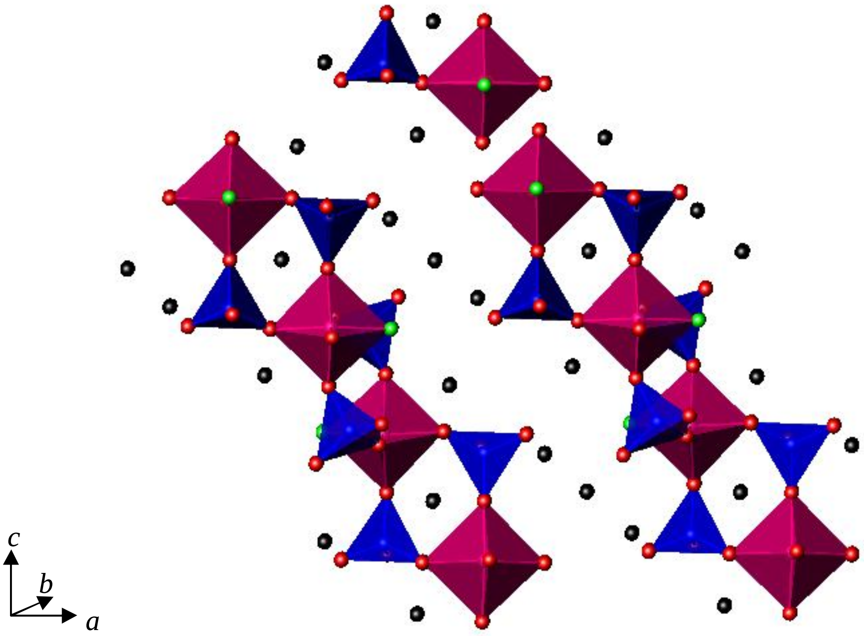

b)

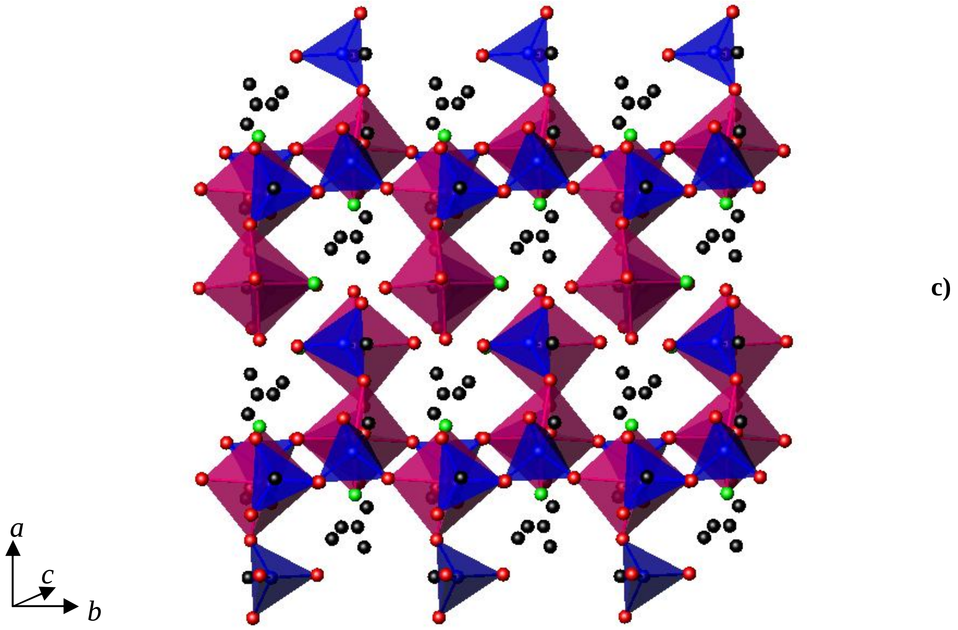

Figure 3.9: Structure of $HfF(AsO_4)_2(NH_4)_3$ viewed down the a) *a*-, b) *b*- and c) *c*-axes, where the hafnium polyhedra are shown in magenta, the arsenate polyhedra in blue, the oxygen atoms in red and the ammonium cations are shown as black spheres to represent the nitrogen atoms.

Table 3.10: Bond lengths in $HfF(AsO_4)_2(NH_4)_3$.

Bond	Bond length/ Å	Bond	Bond length/ Å	Bond	Bond length/ Å
Hf1–O4	2.019(11)	As3–O15	1.666(9)	As5–O6	1.666(9)
Hf1–O12	2.109(10)	As3–O14	1.646(10)	As5–O7	1.679(9)
Hf1–O13	2.035(12)	As3–O13	1.661(12)	As5–O8	1.684(10)
Hf1–O17	2.016(9)	As3–F2	1.662(11)	As5–O5	1.651(9)
Hf1–O15	2.069(9)	As3–O15	1.666(9)	As6–O9	1.699(10)
Hf1–F2	2.048(10)	As4–O1	1.670(10)	As6–O10	1.655(9)
Hf2–O3	2.100(10)	As4–O2	1.670(10)	As6–O11	1.691(10)
Hf2–O6	2.057(10)	As4–O3	1.688(10)	As6–O12	1.679(10)
Hf2–O7	2.101(9)	As4–O4	1.682(10)		
Hf2–O8	2.060(9)				
Hf2–O9	2.010(10)				
Hf2–F1	2.007(9)				

Table 3.11: Bond lengths and bond valence calculations for $HfFO_5$.

Atom	Hf–O/F bond length/ Å	As–O/F bond length/ Å	Bond valence
O3	2.100(10)	1.688(10)	1.83
O6	2.057(10)	1.666(9)	1.98
O7	2.101(9)	1.679(9)	1.89
O8	2.060(9)	1.684(10)	1.93
O9	2.010(10)	1.699(10)	1.98
F1	2.007(9)	N/A	1.78

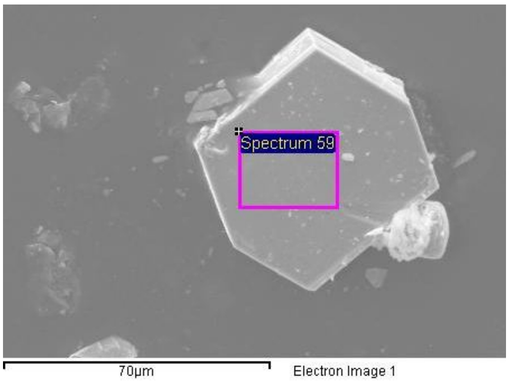

Figure 3.10: SEM image of a single crystal of $HfF(AsO_4)_2(NH_4)_3$.

When viewed down the *b*-axis, it can clearly be seen that there are multiple ammonium cation environments. There are five different ammonium cation environments present between the layers of chains of $HfFO_5$ octahedra and AsO_4. The cations are held in place between the layers by forming hydrogen bonding interactions with the polyhedral oxygen atoms, as seen in Figure 3.11. There is one further ammonium cation environment, where the cations are found in the centre of cavities created by the rings, which are also held in place by hydrogen bonding, as shown in Figure 3.12. Whether the ammonium cations are in the interlayer spaces or in the cavities, it is possible for hydrogen-bonding to occur with the electronegative atoms within the framework backbone. Although the hydrogen atoms were not located *via* single crystal analysis, their probable positions may be estimated by looking at the directions along which the hydrogen bonds lie. As can be seen in the following diagrams, the directions along which the hydrogen atoms are likely to lie are reasonable for tetrahedral ammonium cations. Table 3.12 details the likely distances over which the hydrogen bonds will form in this structure, which are all reasonable hydrogen bonding distances between the polyhedra and central nitrogen atoms.

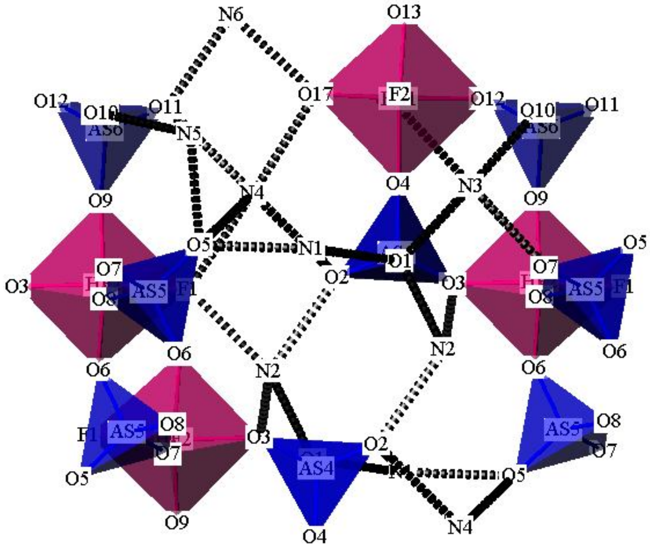

Figure 3.11: Hydrogen bonding in $HfF(AsO_4)_2(NH_4)_3$ for the interlayer ammonium cations.

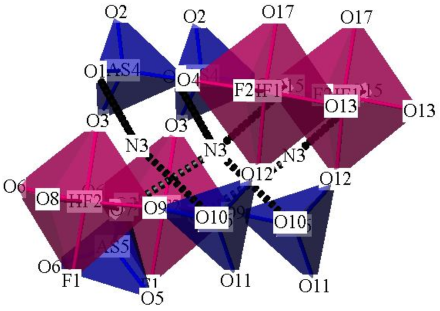

Figure 3.12: Hydrogen bonding in $HfF(AsO_4)_2(NH_4)_3$ for the cavity ammonium cations.

Table 3.12: Hydrogen bonding of $HfF(AsO_4)_2(NH_4)_3$, (where *d* = distance between stated atoms and *A* = acceptor).

N - - A	d(N - - A)/ Å
N1 - - O1	2.78
N1 - - O2	2.72
N1 - - O5	2.79
N2 - - F1	2.76
N2 - - O1	2.87
N2 - - O2	2.76
N2 - - O3	3.04
N3 - - O1	2.85
N3 - - O7	2.84
N3 - - O10	2.73
N3 - - F15	2.94

N - - A	d(N - - A)/ Å
N4 - - F1	2.86
N4 - - O2	3.02
N4 - - O5	3.04
N4 - - O11	3.05
N4 - - O17	2.90
N5 - - O5	2.79
N5 - - O10	2.79
N5 - - O11	2.75
N6 - - O11	2.75
N6 - - O12	3.07
N6 - - O15	3.13

TGA data of $HfF(AsO_4)_2(NH_4)_3$ is shown graphically in Figure 3.13 and it may be seen that there were mass losses corresponding to the ammonium cations. They were lost in stages, at two different temperatures, due to the difference in the strength of the hydrogen bonding. Firstly, the interlayer ammonium cations were lost at around 180 °C, when a mass loss of 6.81 % was seen. At a higher temperature of 270 °C, the cavity ammonium cation was removed from the structure, with a loss of 3.41 %. The interlayer cations were presumably more weakly hydrogen-bonded than those within the four-membered rings, as is suggested by the longer hydrogen bond distances in Table 3.12. These were more strongly bonded with, on average, shorter, (on average 0.04 Å shorter), and stronger hydrogen bonds and thus required more energy to be removed from the structure. Both of these losses are shown graphically in Figure 3.13.

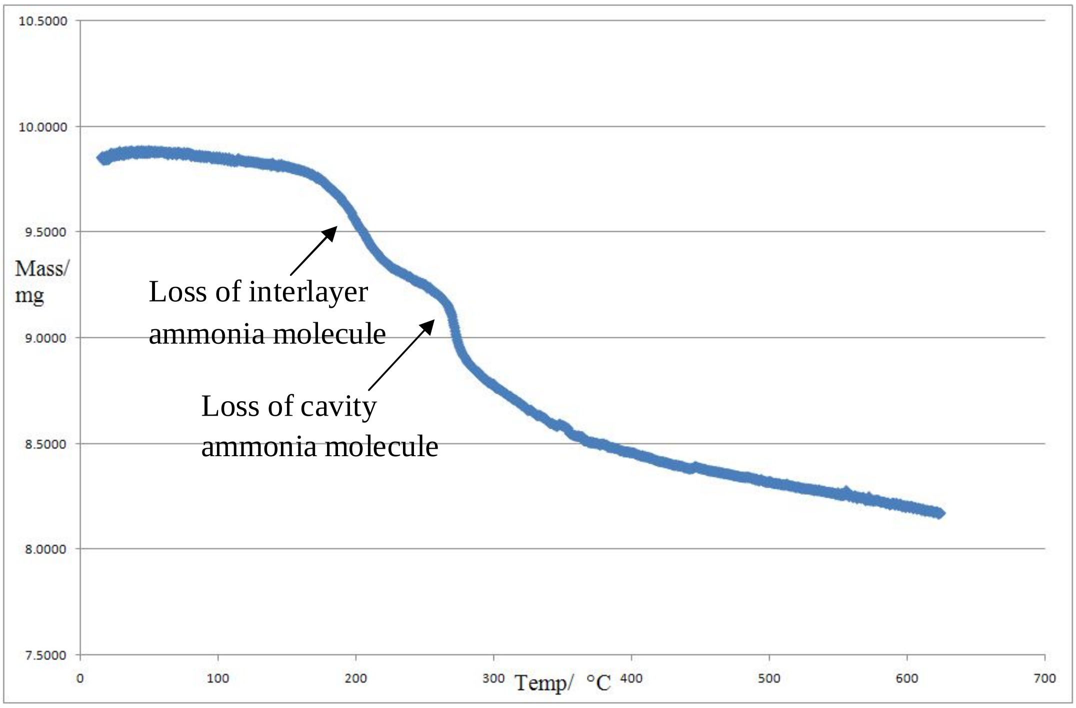

Figure 3.13: TGA for $HfF(AsO_4)_2(NH_4)_3$, with the mass losses for both all of the ammonium environments shown.

A broad absorption at 3392-2980 cm^{-1} may be observed in the IR spectrum of this material. This peak is due to the stretching of the N–H bonds in the ammonium cations and is quite low due to the hydrogen bonding that occurs in this structure. There is also an absorption due to the N–H bend within the ammonium cations, which is present at 1686 cm^{-1}.

3.4-$NbF_2(AsO_4)(NH_4)_3$

A colourless needle-like single crystal was selected for single crystal X-ray diffraction and the structural information of the material is summarised in Table 3.13. The orthorhombic unit cell extends to give a structure that consists of highly disordered NbF_2O_4 octahedra and AsO_4 tetrahedra, as seen in Figure 3.14, resulting in a complex single crystal refinement. The octahedra and tetrahedra are connected to each other *via* disordered bridging oxygen atoms, where the polyhedra are corner-sharing. The polyhedra link together to form a chain of four-membered rings along the *b*-axis. These rings each contain two NbF_2O_4 octahedra and two AsO_4 tetrahedra, with the bond lengths displayed in Table 3.14. Although there is a high level of disorder in this structure, all of the sites are shown in Figure 3.14 for clarity. This disorder means that almost all of the oxygen atoms being partially occupied over two sites and has resulted in the error values in the refinement being quite high, even though the structure is fully refined and accurate. The mirror plane that exists in the space group in which this structure was solved (*Pnma*) means that there is this high level of partial occupancy seen.

Table 3.13: Crystal data for $NbF_2(AsO_4)(NH_4)_3$.

Chemical Formula	$NbF_2(AsO_4)(NH_4)_3$
Crystal Appearance	Colourless needle
Crystal Size/ mm	0.1 x 0.02 x 0.01
M	323.9378864
Crystal System	Orthorhombic
Space Group	*Pnma*
a, b, c/ Å	12.2779(9), 5.2803(4), 16.5713(1)
α, β, γ / °	90.000(0), 90.000(0), 90.000(0)
V/ $Å^3$	1074.33(1)
Z	4
T/ K	120
λ/Å	0.71073
Reflections collected	7849
Unique reflections	1061
R_{int}	0.1100
$R_1[I > 2\sigma(I)]^a$	0.0999
$R1$(all data)	0.1261
wR_2(all data)	0.2603

Within each NbF_2O_4 octahedron, all four oxygen atoms are disordered over two sites, (≈ 0.85 Å away from one another and with an internal angle of ≈ 0.25 °), but bridge to neighbouring arsenate groups, thus building up the previously mentioned chain of four-member rings. The cavities produced by these rings were found to be empty. The two remaining sites within each octahedron, the two axial positions, were refined as fluorine atoms by comparing the thermal parameters and also *via* the use of bond valence calculations[7]. However, when calculating the bond valences, it was necessary to remember that the partial occupancy of the oxygen atoms would distort the values. EDS data was used semi-quantitatively to confirm the presence of approximately 20 % of fluorine in comparison with oxygen in this framework, as shown in the formula

$NbF_2(AsO_4)(NH_4)_3$, which is also charge-balanced. At 2.83 Å from the nearest nitrogen atom, N2, this site is too close for a hydroxyl atom to exist, which would also have resulted in a charge-balanced formula. Therefore, it is reasonable to assume that both of the terminal sites, where the atoms are in similar environments, are fluorine atoms. These fluorine atoms exist at the terminal positions of each octahedron and are therefore directed into the cavities between the layers of polyhedra, resulting in hydrogen bonding interactions with the interlayer ammonium cations, as discussed later. The positions of these fluorine atoms could be fully refined and there is no disorder present. During the EDS data collection, an SEM image of single crystals of $NbF_2(AsO_4)(NH_4)_3$ was recorded and is shown in Figure 3.15.

In the AsO_4 units, two of the oxygen atoms are disordered and bridge to the niobium polyhedra and the other two are terminal, one of which could be fully refined. There are two different arsenic environments seen within this structure, with one of each existing per four-membered, polyhedral ring. This results in the terminal oxygen atoms in the arsenate tetrahedra being angled to opposite sides of the chains, meaning that the two arsenate groups are able to form hydrogen bonds with ammonium cations on either side of the chain. This hydrogen bonding is discussed in more detail further on in this section.

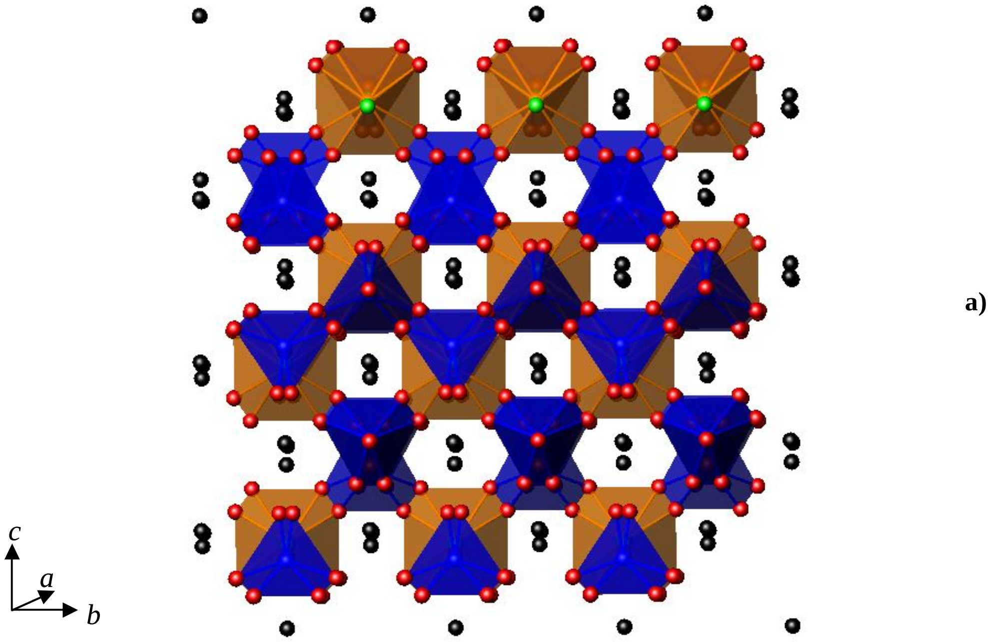

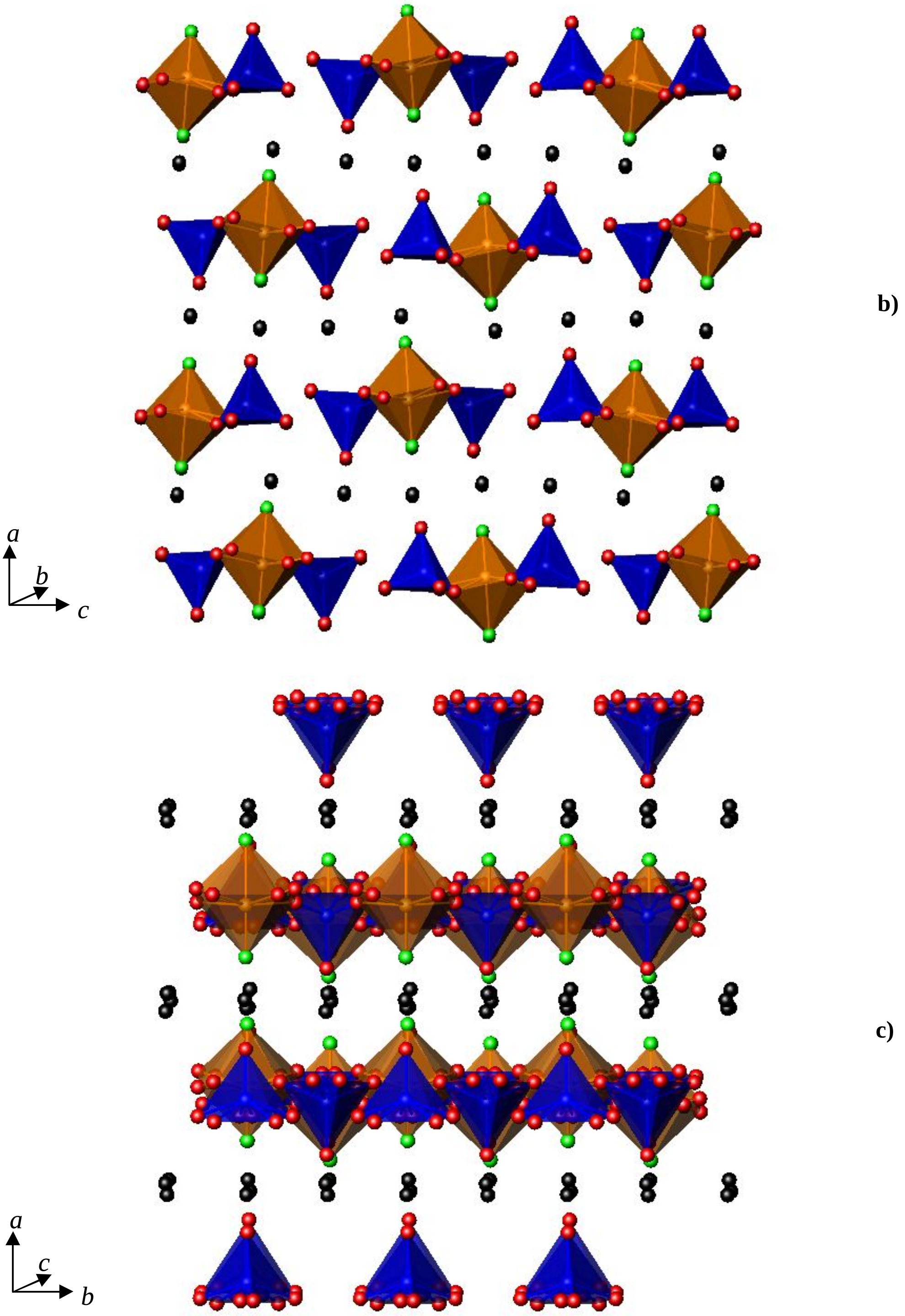

Figure 3.14: Structure of $NbF_2(AsO_4)(NH_4)_3$ viewed down the a) *a*-, b) *b*- and c) *c*-axes, where the niobium octahedra are shown in orange, the arsenate tetrahedra in blue, the oxygen atoms in red, the fluorine atoms in green and the ammonium cations as black spheres to represent the nitrogen atoms.

Table 3.14: Bond lengths in $NbF_2(AsO_4)(NH_4)_3$.

Bond	Bond length/ Å	Bond	Bond length/ Å
Nb1–O1	1.704(8)	As1–O3	1.638(10)
Nb1–O2	2.125(8)	As1–O4A	1.772(12)
Nb1–O4A	2.000(11)	As1–O4B	1.720(11)
Nb1–O4B	1.874(12)	As1–O5	1.728(8)
Nb1–O6A	2.069(12)	As2–O7	1.588(9)
Nb1–O6B	2.055(11)	As2–O6A	1.666(11)
		As2–O6B	1.743(12)
		As2–O8	1.659(8)

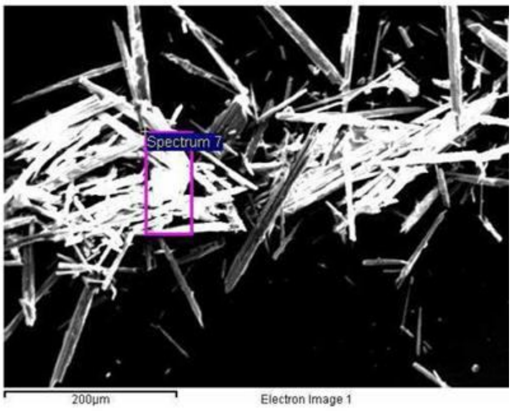

Figure 3.15: SEM image of a single crystal of $NbF_2(AsO_4)(NH_4)_3$.

There are ammonium cations present in the cavities between the layers of polyhedral chains. The nitrogen atoms were located *via* single crystal analysis but it was not possible to determine the hydrogen atoms positions during the refinement. These ammonium cations are held in place within the structure by hydrogen bonds that form between the oxygen and fluorine atoms in the polyhedra and the ammonium cations. Figure 3.16 shows the probable direction along which these bonds would lie, which also indicates the likely directions in which the N–H bonds may form, if it had been possible to locate the hydrogen atoms. These hydrogen bonds will be relatively strong due to the number of bonds which may form in the cavities of this structure. Table 3.15 gives a summary of the probable distances of the hydrogen bonding interactions between the nitrogen atoms of the ammonium cations and the polyhedral fluorine/oxygen atoms. Due to the disorder within this material, these interactions exist between both of the possible sites for each of the affected oxygen atoms but only one of each is given in the table below. As has been detailed above, the fluorine atoms in this structure were not disordered and in the case of N2, this ammonium cation was found to be able to form hydrogen bonds with two different fluorine atoms but with bonds of the same length and strength. By considering the TGA data, it may be seen that one ammonium cation was removed from the structure at a significantly higher temperature than the other two. Although it is not possible to calculate for certain which ammonium cation this relates to, it is possible to make a prediction based on the values given in Table 3.15. The probable interactions between the ammonium cation represented by N2 are on average 0.06 Å shorter than the mean value for all of the interactions. These shorter hydrogen bonding interactions will therefore be stronger than for the other two ammonium cations, resulting in more thermal energy being required for the removal of the ammonium cations in this environment from the structure. Figure 3.17 gives a graphical representation of the TGA data.

TGA showed that weight losses which represent two of three ammonium cation environments required a temperature of 230 °C to start being removed from the framework, when a 9.31 % weight loss was observed. However a considerably higher temperature of just over 400 °C was necessary to overcome the hydrogen bonding interactions involving the third ammonium cation, with a 5.46 % loss seen. As a result of the hydrogen bonding in this structure, a thermally stable material exists where two of the three ammonium cations may be removed from the structure without any further decomposition of the framework. The decomposition of the backbone of this material appears to commence at around 500 °C, as shown in Figure 3.17 below.

Table 3.15: Hydrogen bonding of $NbF_2(AsO_4)(NH_4)_3$, (where *d* = distance between stated atoms and *A* = acceptor).

N - - A	d(N - - A)/ Å
N1 - - F1	2.96
N1 - - O3	3.02
N1 - - O5	2.83
N1 - - O8	2.93
N2 - - F2	2.83
N2 - - F2	2.83
N2 - - O5	2.91
N2 - - O6B	2.89
N3 - - F1	3.04
N3 - - F2	2.93
N3 - - O4A	3.02
N3 - - O5	2.95

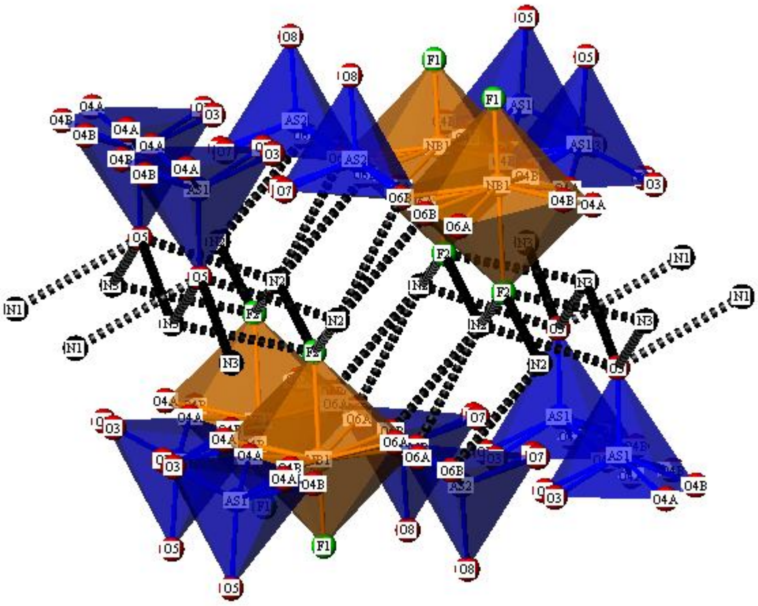

Figure 3.16: Hydrogen bonding between the oxygen and fluorine atoms and the ammonium cations in $NbF_2(AsO_4)(NH_4)_3$.

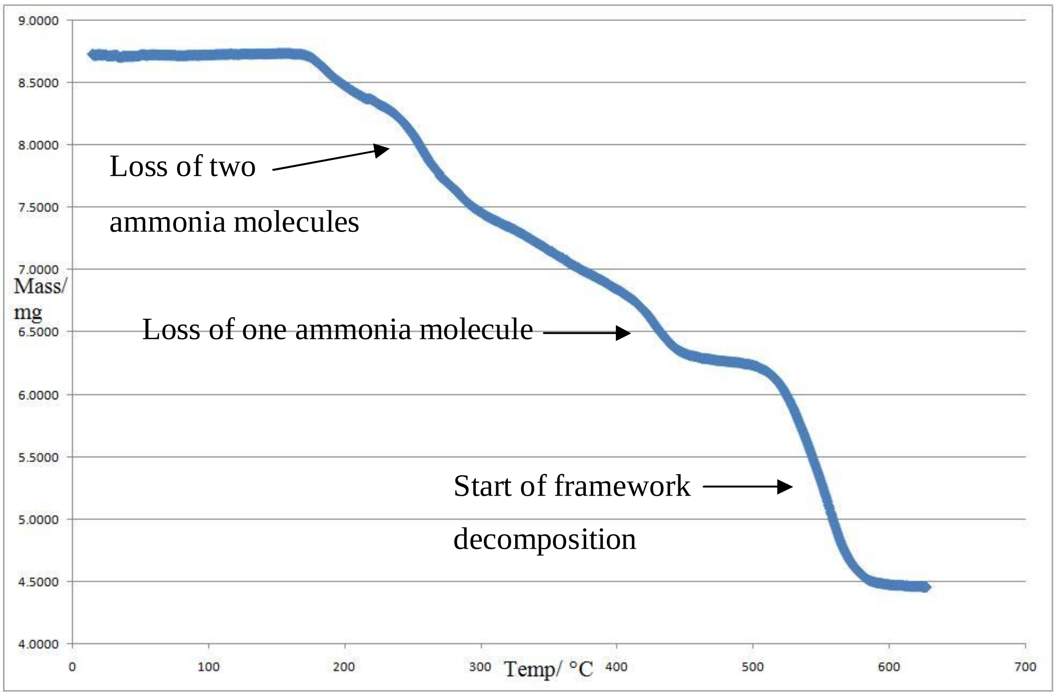

Figure 3.17: TGA for $NbF_2(AsO_4)(NH_4)_3$, showing the loss of all three ammonium cations and the start of the framework decomposition.

A broad absorption exists at 3583-3281 cm^{-1} in the IR spectrum of this material. This peak is present at a relatively low value due to the N–H stretches within the hydrogen bonded ammonium cations. There is also an N–H bend within these cations, resulting in an absorption at 1304 cm^{-1}. There is a peak seen at 1077-965 cm^{-1} which is due to the P–O stretches[9].

3.5-Conclusions for Group IV and V Arsenate Frameworks

Four new arsenate frameworks have been synthesised solvothermally and fully characterised, primarily by single crystal X-ray diffraction. There are very few previously reported hafnium or niobium arsenates, as discussed in detail in Chapter 1, so there is therefore little to directly compare the structures presented here with. The structurally simple α-$Hf_2O(PO_4)_2$ was synthesised and characterised *via* solid state methods[10], where the distorted HfO_6 octahedra undergo a phase change on heating to exist of HfO_7. However, there are no examples within the literature of fluorinated structures of this type; hafnium or niobium arsenates. There are also very few fluorinated phosphate species similar in structure to those presented in this work, for any of the Group IV and V Transition Metals, where a fluoride anion is present within the main framework rather than as an anion between in the cavities. However, $Ba_2[NbOF(PO_4)_2]$ is one such example, where this layered structure was synthesised under mild hydrothermal conditions[11]. Given the large number of phosphate, and to a lesser extent arsenate, frameworks for other groups, this lack of reported materials comes as a surprise and opens up a wide range of opportunities to further this work, especially when considering the mild conditions which may often be used in the synthesis of arsenates. Presumably this gap in framework knowledge is due to the toxicity of the starting materials, rather than due to a lack of successful results, having seen that transition metal arsenate frameworks may be synthesised under relatively mild conditions.

As may be concluded from the details given in Table 3.1, a reaction period of at least 120 h and a temperature of around 175 °C was generally required in order for single crystals to form. Those reactions which were carried out under milder conditions did not result in the formation of single crystals, with powders of unreacted starting materials commonly being present after filtration. Although the novel materials were produced at a range of pH values, from highly acidic to strongly alkaline, it may be seen that the ammonium cation of the ammonium dihydrogen arsenate appears to play a structure-directing role by acting as a *pseudo*-template in those reactions in which it was present as a starting material. The affect of pH and/or solvent may be seen in a reaction which resulted in colourless sheet-like crystals of $Na_3AsO_4{\cdot}H_2O$ being produced, which were synthesised at 175 °C for 144 h in sodium hydroxide solution. The starting pH of this reaction mixture was measured as 9.4 which was primarily due to the basic nature of the solvent. It may be concluded that by using sodium hydroxide solution as a solvent, the most favoured reaction pathway resulted in the metal source not being incorporated into the final structure in any way, resulting in the formation of a well-known material, $Na_3AsO_4{\cdot}H_2O$. The other arsenic source used within this work was arsenic (V) oxide and it was found to be generally far more unreactive as an arsenic source, with it almost always being present as unreacted starting material at the end of the reactions. In those reactions in Table 3.1 where As_2O_5 was used as a starting material, only simple structures were produced due to this unreactivity. It would appear that when used in a reaction, arsenic oxide required activation, such as by a strongly acidic source, in order to react with the metal source.

As detailed in Section 1.3 of Chapter 1, it has been reported that arsenate frameworks may often be synthesised under conditions which are less harsh than those required to form an analogous phosphate material. Having said this, the resulting frameworks are commonly very similar in structure, with the tetrahedral units detailed above, often with a hydroxyl group present as part of the tetrahedra. Although the Group IV and V metals are most often found with octahedral coordination geometry, it has shown that hafnium readily also forms decahedra within frameworks[12], allowing a potentially large series of materials to be recorded in the future.

The three novel hafnium arsenate structures, $HfF(H_2O)(AsO_4)$, $Hf_2F_9(AsO_4H){\cdot}(NH_4)_3(H_2O)$ and $HfF(AsO_4)_2(NH_4)_3$, were all synthesised under solvothermal conditions; the first in highly acidic conditions, the second in a slightly milder acidic reaction mixture and the third was produced in a strongly basic solution.

The tightly packed and three-dimensional framework of $HfF(H_2O)(AsO_4)$ was the first of these structures to be synthesised and is also the simplest. The HfF_2O_5

decahedra were found to be bonded to one another via Hf–F–Hf bonds along the *c*-axis. Four of the polyhedral oxygen atoms were refined to be bonded to fully coordinated arsenate tetrahedra and the remaining oxygen atom was determined to in fact be a weakly bonded water molecule, with the hydrogen atom positions calculated via neutron diffraction data. The hydrogen atoms were shown to be orientated towards a small cavity within this tightly packed, high-density framework, where they were held in place by hydrogen-bonding to nearby oxygen atoms.

Both the single crystal and EDS data suggested that the layered framework refined as $Hf_2F_9(AsO_4H)\cdot(NH_4)_3(H_2O)$ contained a much larger percentage of fluorine than oxygen, both by weight and atomically. In this case, the hafnium was octahedrally coordinated and present as both HfF_4O_2 and HfF_5O units, where the fluorine atoms are terminal. It appears that the presence of such groups within the octahedra cause the termination of polyhedral chains within the structure, thus resulting in a layered material rather than a three-dimensional framework. The acidic conditions of this reaction have resulted in the protonation of the arsenate group, giving AsO_4H, which also appears to bring about the termination of chains from this oxygen site, increasing the layering rather than three-dimensional structure of $Hf_2F_9(AsO_4H)\cdot(NH_4)_3(H_2O)$. The fluoride anions and the oxygen anions, both in the HfF_5O and AsO_4H polyhedra, form hydrogen bonding interactions to the interlayer ammonium cations and water molecules. There are potential ion exchange properties for this material which could be investigated due to the three positively charged ammonium cations and also the water molecule in this framework, some or all of which could be exchanged for an ion or neutrally-charged group.

The third hafnium arsenate framework, $HfF(AsO_4)_2(NH_4)_3$, was once again a layered framework, again with fluorine incorporated on terminal sites. It appears that these fluoride anions once again result in the termination of the structure, resulting in a layered material rather than a three-dimensional one. Several different ammonium cation environments exist in $HfF(AsO_4)_2(NH_4)_3$, both present as interlayer species and found within the ten-membered polyhedral rings. The rings are made up of corner-sharing $HfFO_5$ octahedra and AsO_4 tetrahedra, with bridging oxygen atoms. Once again, ion exchange would be a possibility by exchanging the ammonium cations for another small cationic species, such as Li^+. TGA data indicated that the ammonium cations were lost from the framework at two different temperatures, presumably due to a greater level of hydrogen-bonding for the cations within the cavities created by the ten-membered rings.

The final arsenate material to have been characterised during this work was a niobium framework, $NbF_2(AsO_4)(NH_4)_3$. This is another example of a layered framework where there are terminal fluoride groups and there are once again ammonium cations present between the layers. Complex single crystal refinements showed that within this highly disordered structure, it was established that the main framework consisted of corner-sharing NbF_2O_4 octahedra and AsO_4 tetrahedra, linked together to form small, four-membered rings, which were found to be empty. It may be possible to fill these holes with a very small, neutrally-charged molecule but the feasibility of this would have to be investigated further. Furthermore, ion exchange of the ammonium cations may once again be worth studying but the strong hydrogen bonding interactions observed will need to be taken into account. However these interactions have resulted in a thermally stable structure in which two out of the three ammonium cations may be removed without any further decomposition of the material until the third is removed and followed by the commencement of the framework itself decomposing at approximately 500 °C.

There is great deal of further work that could be carried out in this currently narrow field, particularly using a fluoride source to promote such reactions and in the synthesis of layered materials. Having shown that three hafnium arsenate materials may be synthesised under similar conditions, it stands that there is potential for extension of this work to other metals within Groups IV and V, with synthesis taking place under conditions such as those used in the above reactions. As these results stand, their potential ion exchange properties may be investigated further and possibly improved with more research into arsenate frameworks of Groups IV and V so that exchange may be successfully carried out without any detrimental effect to the remainder of the framework. This has been hinted at the work above but requires further investigation. It may also be possible to attempt syntheses with more extreme conditions in comparison with those discussed here. This may lead to frameworks which are more densely packed and completely dehydrated, offering further applications.

3.6-References

---

[1] C. Masquelier, A. K. Padhi, K. S. Nanjundaswamy, J. B. Goodenough, *J. Solid State Chem.*, 1998, **135**, 228-234.

[2] J. Rojo, A. Laarañaga, J. Mesa, M. Urtiaga, J. Pizarro, M. Arriortua, T. Rojo, *J. Solid State Chem.*, 2002, **165**, 171-177.

[3] G. Yang, L. Li, J. Chen, R. Xu, *J. Chem. Soc. Chem. Commun.*, 1989, 810-811.

[4] L. Li, L. Wu, J. Chen, R. Xu, *Acta. Cryst. C*, 1991, **47**, 246-249.

[5] H. Kessler, *Stud. Surf. Sci. Catal.*, 1989, **52**, 17.

[6] H. Kessler, *Mater. Res. Soc. Symp. Ser.*, 1991, **233**, 47.

[7] N. E. Brese, M O'Keefe, *Acta. Cryst. B*, 1991, B**47**, 192-197.

[8] M. T. Weller, P. F. Henry, M. E. Light, *Acta. Cryst. B*, 2007, **63**, 426-432.

[9] G. Socrates, *Infrared and Raman Characteristic Group Frequencies: Tables and Charts*, Third Edition, Wiley, 2006.

[10] G. Wallez, J.-P. Souron, M. Quarton, *Solid State Sci.*, 2006, **8**, 1061-1066.

[11] X. Wang, L. Liu, A. J. Jacobson, *J. Mater. Chem.*, 2002, **12**, 1824-1827.

[12] M. K Minacheva, É. M. Brainina, *Russ. Chem. Bull.*, 1973, **22**,672-674.

Chapter 4

Group IV and V Phosphate Frameworks

A significant number of Group IV and V phosphate frameworks have been reported, especially in comparison with the number of analogous arsenate materials, as discussed in Chapter 3. Some of these phosphates are structurally and compositionally very simple, such as τ-$Zr(HPO_4)_2$[1], and others are more complex and contain extra-framework charge-balancing cations, such as $[Ti_3(PO_4)_4(H_2O)_2]\cdot NH_4$[2]. These two compounds have two key features in common; they were both synthesised under pressure and they both adopt structures which are formed from MO_n and PO_4 polyhedra.

Many of the materials synthesised and characterised in the following work have layered structures, as in the known hafnium phosphate α-$Hf_2O(PO_4)_2$[3]. Although this is a very simple example, many of the known Group IV and V phosphates contain charge-balancing cations such as ammonium, as in $(NH_4)_2[(Ti_3O_2)(HPO_4)_2(PO_4)_2]$[2]. This is also commonly seen in the structures reported in this chapter.

As described in the previous chapter, solvothermal techniques have found to yield successful results for the type of frameworks discussed in these chapters, meaning that they were the primary reaction technique employed in these phosphate reactions. A fluoride source was also commonly used as a mineralising agent, in order to try and promote the reactions, especially as phosphates can often require harsher reaction conditions than the corresponding arsenate[4]. Fluorides have been used as mineralising agents in the synthesis of phosphate frameworks to promote a reaction since the end of the 1980s[5,6].

The novel phosphate frameworks characterised in the following sections were produced after much altering and fine-tuning of the reaction conditions. The single crystals that were synthesised were primarily characterised by X-ray single crystal diffraction. Other techniques were employed to support these refinements; such as EDS, IR and TGA. The bulk powders were analysed *via* powder X-ray diffraction and were a mixture of product and starting materials. These techniques are discussed briefly in the arsenate framework introduction at the start of Chapter 3 and in greater detail in Chapter 2.

Although the production of single crystals was not achieved in many of the reactions attempted, the reaction conditions for the successfully synthesised and characterised arsenate frameworks are shown below in Table 4.1. In a typical reaction, the starting materials were mixed and stirred briefly, then transferred to a 23 mL Parr hydrothermal bomb. The bomb was heated in an oven at the temperature and duration detailed in Table 4.1. The product in each case was retrieved by filtration under vacuum, washed with hot distilled water and dried in air. The following reactions in this chapter are a description and discussion of the new materials synthesised. Around 100 other reactions in addition to those shown here were attempted by varying the reaction conditions, for example by varying the reaction duration, temperature, but mostly resulted in the production of powders, which were determined to be either only starting materials or known materials, such as $(NH_4)(TiOPO_4)$[7]. There were also a number of reactions which resulted in the formation of glasses or single crystals that were too small to be analysed.

Table 4.1: Reaction conditions for successful Group IV and V phosphate syntheses.

Starting materials	Temp. / °C	Reaction period / h	Type of single crystals produced	Product	Section in thesis
Titanium (III) fluoride (0.954 mmol, 0.100 g) and ammonium dihydrogen phosphate (2.861 mmol, 0.329 g) were dissolved in ethanol (10 cm^3). Starting pH = 3.8; final pH = 3.1.	175	168	Colourless needle	$TiF_2(PO_4)(HPO_4)(NH_4)_3$	4.1
Zirconium (IV) fluoride (0.598 mmol, 0.100 g), ammonium dihydrogen phosphate (1.794 mmol, 0.206 g) and 1,4-diazabicyclo[2.2.2]octane (DABCO) (0.598 mmol, 0.0671g) were dissolved in distilled water (10 cm^3). Starting pH altered to 8.8 using concentrated ammonia solution.	140	336	Colourless needle	$ZrF_2(PO_4)(HPO_4)(NH_4)_3$	4.2
Hafnium (IV) fluoride (0.393 mmol, 0.100 g) and ammonium dihydrogen phosphate (1.179 mmol, 0.136 g) were dissolved in concentrated ammonia solution (10 cm^3).	175	144	Colourless block	$Hf_2F_2(H(PO_4)_2)(NH_4)_2$	4.3
Hafnium (IV) fluoride (0.393 mmol, 0.100 g) and ammonium dihydrogen phosphate (1.179 mmol, 0.136 g) were dissolved in distilled water (10 cm^3). Starting pH = 2.8;	200	144	Colourless block	$Hf_2(PO_4)_3(NH_4)$	4.4

final pH = 1.7.					
Niobium (V) fluoride (0.532 mmol, 0.100 g) and ammonium dihydrogen phosphate (1.597 mmol, 0.184 g) were dissolved in ethanol (10 cm^3). Starting pH = 2.6; final pH = 2.7.	175	168	Colourless needle	$NbO_2(HPO_4)_2(NH_4)_3$	4.5
Titanium (III) fluoride (0.954 mmol, 0.100 g), ammonium dihydrogen phosphate (2.861 mmol, 0.329 g) and 1,4-diazabicyclo[2.2.2]octane (DABCO) (0.954 mmol, 0.107 g) were dissolved in distilled water (10 cm^3).	140	504	Colourless octahedral blocks within major phase of beige powder	$(NH_4)(TiPO_4)_2$	[7]
Tantalum (V) fluoride (0.362 mmol, 0.100 g) and ammonium dihydrogen phosphate (1.087 mmol, 0.125 g) were dissolved in distilled water (10 cm^3). Starting pH altered to 8.5 with concentrated ammonia solution.	200	144	Colourless needles present as minor phase within cream powder	Starting material: $(NH_4)H_2PO_4$	
Zirconium (IV) fluoride (0.598 mmol, 0.100 g), ammonium dihydrogen phosphate (1.794 mmol, 0.206 g) and 1,4-diazabicyclo[2.2.2]octane (DABCO) (0.598 mmol, 0.0671g) were dissolved in distilled water (10 cm^3). Starting pH = 4.5.	140	336	Mixture of colourless octahedral blocks and colourless needle within bulk phase of white powder	Both types of single crystal: $(NH_4)(TiPO_4)_2$	[7]

4.1 -$TiF_2(PO_4)(HPO_4)(NH_4)_3$

A colourless needle-like crystal was selected for single crystal X-ray diffraction and a summary of the crystallographic data collected is shown in Table 4.2 and the material was found to be analogous to the zirconium structure discussed in Section 4.2. The framework is made up a triclinic unit cell, with alternating TiF_2O_4 octahedra and PO_4 tetrahedra, which are connected in a corner-sharing manner *via* bridging oxygen atoms, as seen in Figure 4.1 and the bond lengths are given in Table 4.3. As shown diagrammatically below, these linkages occur in such a way that an infinite chain of four-membered rings exists along the *a*-axis. These discrete chains form along just one axis so do not form a two-dimensional layer but rather chains which are held together by hydrogen bonds to ammonium cations which are present between the layers, as discussed later on.

Table 4.2: Crystal data for $TiF_2(PO_4)(HPO_4)(NH_4)_3$.

Chemical Formula	$TiF_2(PO_4)(HPO_4)(NH_4)_3$		
Crystal Appearance	Colourless needle	T/ K	120
Crystal Size/ mm	0.2 x 0.02 x 0.02	λ/Å	0.71073
M	330.92997	Reflections collected	9234
Crystal System	Triclinic	Unique reflections	2283
Space Group	*P*-1	R_{int}	0.0464
a, b, c/ Å	5.0667(2), 8.0420(3), 12.4821(5)	$R_1[I > 2\sigma(I)]^a$	0.0786
α, β, γ / °	75.579(2), 88.645(2), 88.415(1)	*R*1(all data)	0.0831
V/ Å^3	492.31(3)	wR_2(all data)	0.2474
Z	3		

Within the TiF_2O_4 octahedra, all four of the oxygen atoms were found to bridge to neighbouring phosphorus atoms, forming part of the phosphate tetrahedra and thus building up the chains within this structure. The two terminal atoms within each polyhedron were determined to be fluorine atoms rather than two more oxygen atoms. The thermal parameters during the single crystal refinement were more satisfactory when the structure was solved with fluorine on these sites and EDS also confirmed semi-quantitatively that a relatively small percentage of fluorine, in comparison with the percentage of oxygen, was definitely present within this material. Bond valence calculations[8] were also used to support the presence of these fluorine atoms, as summarised in Table 4.4. This table shows that these sites would have been underbonded if refined as oxygen atoms. The sites are also too close to the ammonium cations to be hydroxyl groups, where the closest F - - H distance is only 2.52 Å, as detailed in Table 4.5 The fluorine atoms are directed into the gaps present between the layers of polyhedra, as may be seen in Figure 4.1. They then form hydrogen bonds to the ammonium cations which lie in the layers, as discussed later.

There are two different phosphate groups within the above structure: one being simple PO_4 tetrahedra and the other being a hydrogen phosphate group, with one of the terminal oxygen atoms actually existing as a hydroxyl group. It was possible for the hydrogen atom position to be identified during the single crystal refinement and it is therefore shown in Figures 4.1 and 4.2. The existence of a hydroxyl group on this site was also supported by bond valence calculations[8], where the oxygen atom in question was calculated to be slightly underbonded, which was rectified when the hydrogen atom was taken into account. Refinement of the hydrogen atom position also determined that the resulting O–H bond was directed towards the ammonium cations at an acceptable angle to be involved in hydrogen bonding with the ammonium cations, with O5 and H13 making up the hydroxyl group.

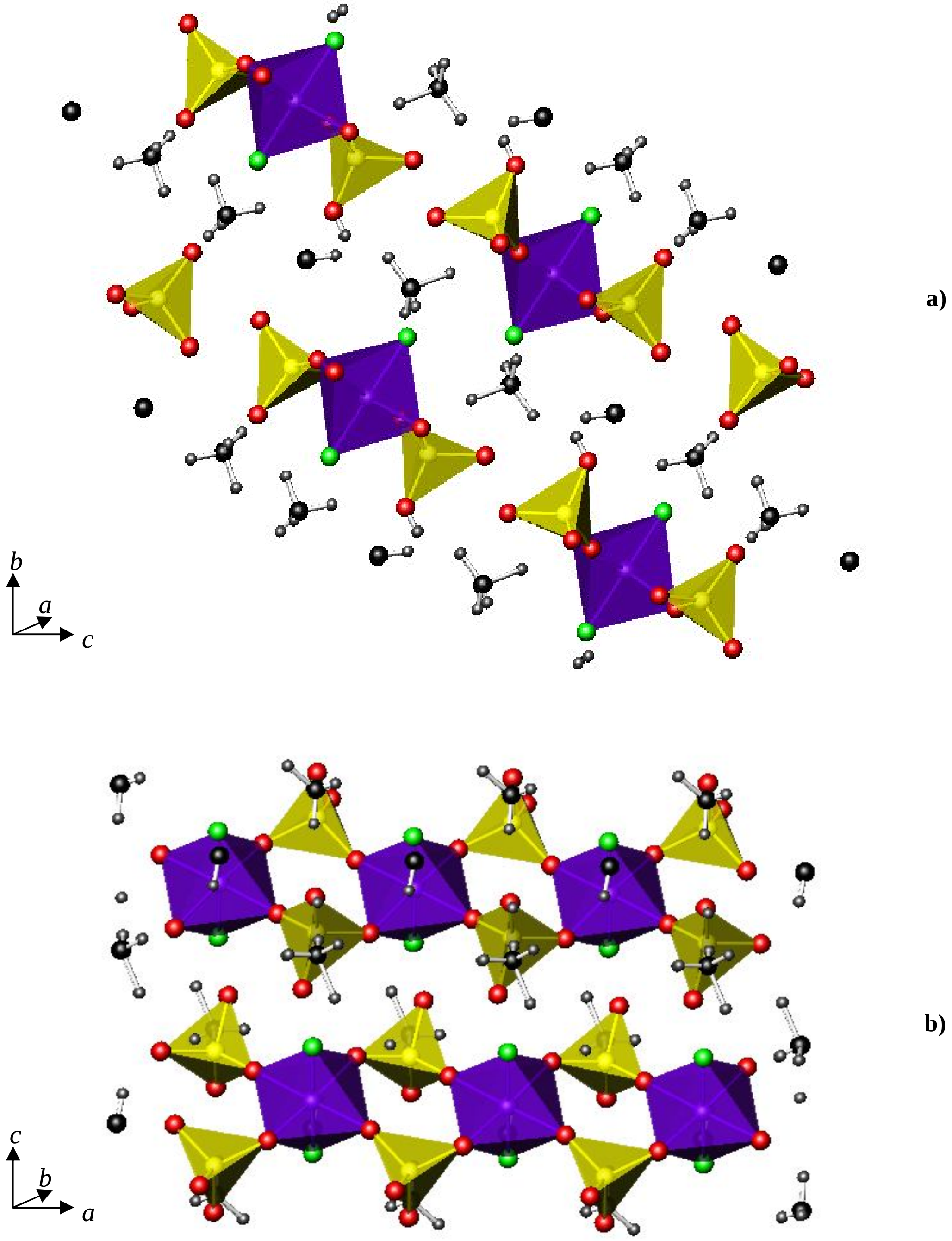

Figure 4.1: Structure of $TiF_2(PO_4)(HPO_4)(NH_4)_3$ viewed down the a) *a*- and b) *b*-axes, where the titanium octahedra are shown in purple, the phosphate tetrahedra in yellow, the oxygen atoms in red, the fluorine atoms in green and the ammonium cations are shown as black spheres to represent the nitrogen atoms with the hydrogen atoms which could be located in grey.

Table 4.3: Bond lengths in $TiF_2(PO_4)(HPO_4)(NH_4)_3$.

Bond	Bond length/ Å	Bond	Bond length/ Å
Ti1–O3	1.963(5)	P2–O4	1.544(5)
Ti1–O4	1.978(5)	P2–O8	1.531(6)
Ti1–O6	1.880(5)	P2–O9	1.536(5)
Ti1–O10	1.907(5)	P2–O10	1.548(5)
Ti1–F1	1.837(5)	P3–O3	1.549(5)
Ti1–F2	1.906(5)	P3–O5	1.522(6)
		P3–O6	1.556(5)
		P3–O7	1.536(5)

Table 4.4: Bond lengths and bond valence calculations for TiF_2O_4 octahedra.

Atom	Ti–O/F bond length/ Å	P–O/F bond length/ Å	Bond valence
O3	1.963(5)	1.549(5)	1.87
O4	1.978(5)	1.544(5)	1.86
O6	1.880(5)	1.556(5)	2.01
O10	1.907(5)	1.548(5)	1.98
F1	1.837(5)	N/A	0.81
F2	1.906(5)	N/A	0.68

As was previously mentioned, there are ammonium cations between the chains of TiF_2O_4 and phosphate polyhedra. The single crystal refinement suggested that three different nitrogen environments exist and for two of these it was possible to locate all four of the hydrogen atoms. However, only one hydrogen atom could be identified for the third ammonium cation. The hydrogen atoms which could be definitely identified are all shown in the above diagrams. The ammonium cations are held in place by hydrogen bonds which form between the cations and the polyhedra, existing as N–H - - O/F. Not only do these hydrogen bonds hold the ammonium cations within the framework but they also hold the discrete polyhedral chains in place, causing them to form a layer-like arrangement. The expected direction of these hydrogen bonds may be seen more clearly in Figure 4.2, which also shows that there is quite a high level of hydrogen bonding, to both the fluorine and oxygen atoms. However, there is a range of hydrogen-bonding distances seen within this structure, suggesting that some of the interactions are stronger than others. Other than the long interaction for N1–H16 - - O5, the remaining long distances are those that involve the more electronegative fluorine, thus still resulting in reasonably strong hydrogen bonds. Table 4.5 gives a summary of the hydrogen bonds that hold the structure of $TiF_2(PO_4)(HPO_4)(NH_4)_3$ together.

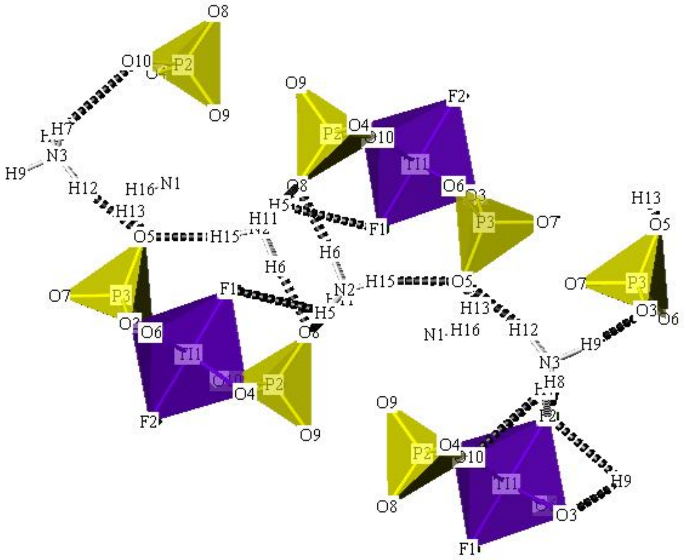

Figure 4.2: Hydrogen bonding between the fluorine atoms and the ammonium cations in $TiF_2(PO_4)(HPO_4)(NH_4)_3$.

Table 4.5: Hydrogen bonding of $TiF_2(PO_4)(HPO_4)(NH_4)_3$, (where *d* = distance between stated atoms and *A* = acceptor).

N–H - - A	d(N–H)/ Å	d(H - - A)/ Å	d(N - - A)/ Å	Angle NHA/ °
N1–H16 - - O5	0.78	2.71	2.96	100.99
N2–H5 - - F1	1.02	2.52	2.82	96.27
N2–H6 - - O8	0.99	1.78	2.77	175.30
N2–H11 - - O8	0.57	2.30	2.86	171.25
N2–H15 - - O5	0.88	1.97	2.84	165.13
N3–H7 - - F2	0.86	2.12	2.87	146.87
N3–H8 - - F2	0.87	1.97	2.82	163.89
N3–H9 - - O3	1.21	1.66	2.86	171.56
N3–H12 - - O5	1.01	1.90	2.89	165.66

The effect of this hydrogen bonding may also be seen by looking at a graphical representation of the TGA, as shown in Figure 4.3. This graph displays the appropriate mass losses for the three ammonium cations and shows that they were lost in two stages. Firstly, a mass loss of 10.90 %, which corresponds to two ammonium cations, occurred approximately 240 °C and the third was removed from the structure at the higher temperature of 280 °C, suggesting that it was held in place by stronger hydrogen bonds to the oxygen and fluorine atoms in the structure. Here, a mass loss of 5.45 % was observed. It is not possible to say with certainty which of the ammonium groups was lost at which temperature. However, based on the interactions and distances given in Table 4.3, it may be deduced that the ammonium cation with N3 at its centre would have stronger hydrogen bonding interactions that N2. It must be remembered that only one of the hydrogen atoms which bonds to N1 was located during single crystal analysis, thus meaning that this cation may not be compared accurately. The thermal removal of all three cations is shown in Figure 4.3.

The TGA indicated that the ammonium cations within $TiF_2(PO_4)(HPO_4)(NH_4)_3$ were lost higher temperatures than in the analogous zirconium material. This is presumably due to the shorter and stronger hydrogen bonds present holding the ammonium cations in place, in comparison with the length and strength of those in $ZrF_2(PO_4)(HPO_4)(NH_4)_3$, which may be seen for comparison in Tables 4.5 and 4.9. The average length for a hydrogen bonding interaction within this titanium phosphate is 2.10 Å in comparison with 2.39 Å in the zirconium material. This considerable difference has resulted in $TiF_2(PO_4)(HPO_4)(NH_4)_3$ being thermally more stable than its zirconium analogue, as supported by the TGA data.

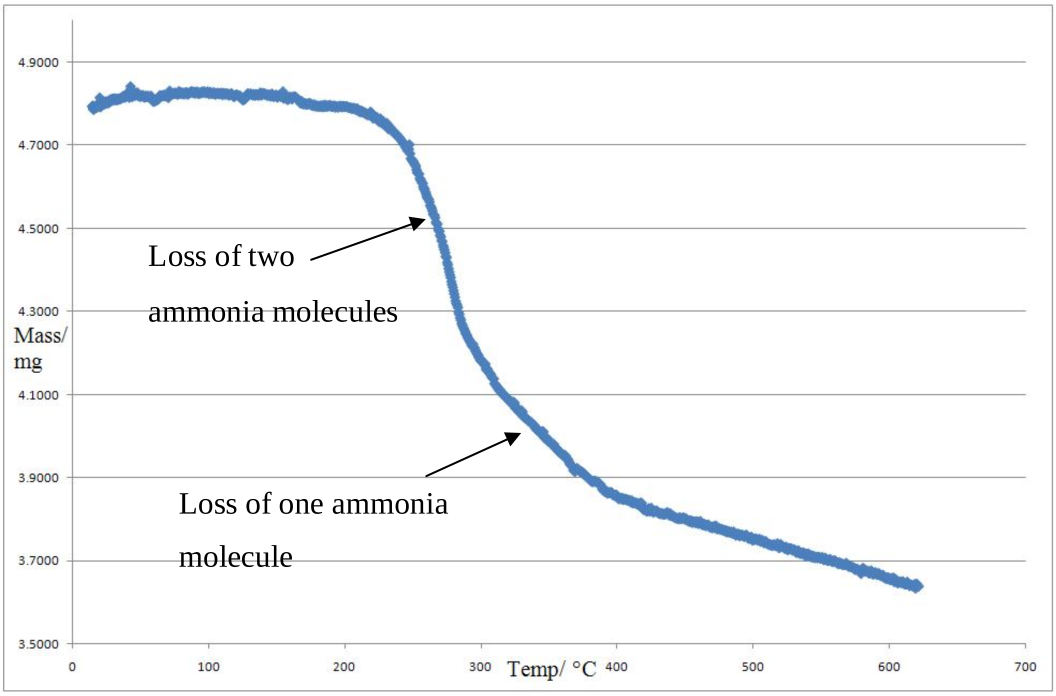

Figure 4.3: TGA for $TiF_2(PO_4)(HPO_4)(NH_4)_3$, showing the loss of all three ammonium cations.

When collecting the EDS data, an SEM image of $TiF_2(PO_4)(HPO_4)(NH_4)_3$ was taken and is shown in Figure 4.4. Finally, an IR spectrum was also recorded of this material and showed a broad absorption at 3402-3144 cm^{-1}, which is due to the N–H bonds in the hydrogen-bonded ammonium cations. This band is a considerably lower than usually expected due to the high level of hydrogen bonding in the structure. There is also an N–H bend for the ammonium cations, with a peak being seen at 1432 cm^{-1}. The O–H in the phosphate tetrahedra shows an absorption peak at 3683-3465 cm^{-1}, with a further band seen at 1150-1090 cm^{-1} which is due to the P–O stretches[9].

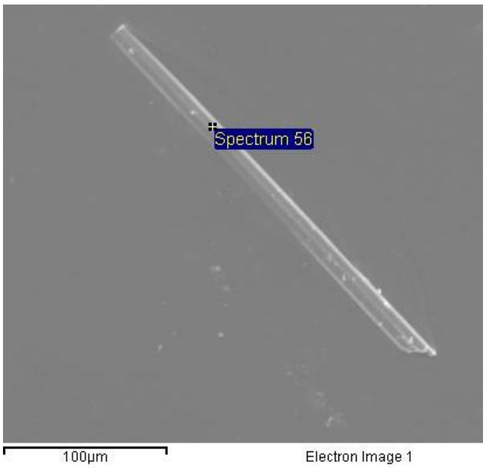

Figure 4.4: SEM image of a single crystal of $TiF_2(PO_4)(HPO_4)(NH_4)_3$.

4.2-$ZrF_2(PO_4)(HPO_4)(NH_4)_3$

A colourless needle-like single crystal was selected for single crystal X-ray diffraction and the crystal data that was collected are shown in Table 4.6. The framework is made up of ZrF_2O_4 octahedra and PO_4 tetrahedra, arranged within a triclinic unit cell and the bond lengths are shown in Table 4.7. Bridging oxygen atoms link the octahedra and tetrahedra, where the polyhedra are corner-sharing, as seen in Figure 4.5. These polyhedra form four-membered rings, which make up a chain formation along the *a*-axis, in the same way as seen in the analogous titanium structure discussed in Section 4.1. These rings consist of two ZrF_2O_4 octahedra, one PO_4 tetrahedron and also one hydrogen phosphate tetrahedron, where the hydroxyl group is always orientated in the same direction and on the same side of the four-membered ring. The two types of phosphate group are discussed in more detail later.

Table 4.6: Crystal data for $ZrF_2(PO_4)(HPO_4)(NH_4)_3$.

Chemical Formula	$ZrF_2(PO_4)(HPO_4)(NH_4)_3$		
Crystal Appearance	Colourless needle	T/ K	120
Crystal Size/ mm	0.2 x 0.02 x 0.02	λ/Å	0.71073
M	374.28697	Reflections collected	9101
Crystal System	Triclinic	Unique reflections	2370
Space Group	*P*-1	R_{int}	0.1202
a, *b*, *c*/ Å	5.2420(3), 8.1316(5), 12.6158(8)	$R_1[I > 2\sigma(I)]^a$	0.0697
α, β, γ / °	74.065(4), 88.386(4), 87.923(4)	*R*1(all data)	0.1218
V/ Å^3	516.66(6)	wR_2	0.1216
Z	3		

Table 4.7: Bond lengths in $ZrF_2(PO_4)(HPO_4)(NH_4)_3$.

Bond	Bond length/ Å	Bond	Bond length/ Å
Zr1–O2	2.102(5)	P2–O2	1.550(5)
Zr1–O3	2.086(5)	P2–O4	1.548(5)
Zr1–O4	2.053(5)	P2–O7	1.541(5)
Zr1–O6	2.026(5)	P2–O11	1.517(5)
Zr1–F1	1.982(5)	P3–O3	1.543(5)
Zr1–F8	2.009(4)	P3–O5	1.531(6)
		P3–O6	1.542(6)
		P3–O10	1.524(6)

Within each of the ZrF_2O_4 octahedra, all four of the oxygen atoms are equatorial and bridge to the neighbouring phosphate groups, forming four-membered rings and the subsequent chains. An EDS data collection verified that there was fluorine present within this structure, with a smaller percentage being present than oxygen but a very similar level when compared with $TiF_2(PO_4)(HPO_4)(NH_4)_3$, as discussed in Section 4.1, and the bond valences were also calculated[8], which are summarised in Table 4.8, which show that the axial sites refined as terminal fluorine atoms would be underbonded if refined as oxygen atoms. The closest ammonium cation to a fluorine site is 2.03 Å, thus being two close for the polyhedral site to be refined as a hydroxyl group. By being directed into the cavities between the layers of polyhedra, these fluorine atoms are able to form hydrogen bonds with the ammonium cations within the gaps, as detailed later on in this section.

As briefly mentioned, there are two different types of phosphate groups within this structure; PO_4 tetrahedra and hydrogen phosphate tetrahedra. In the PO_4 units, two of the oxygen atoms bridge to neighbouring ZrF_2O_4 polyhedra and the other two are terminal, which were calculated to be acceptable distances away from the ammonium cations to form hydrogen bonding interactions. The remaining phosphate groups are very similar, in that they have two bridging and two terminal oxygen atoms. However, one of these terminal oxygen atoms was in fact found to be a hydroxyl group. This was concluded *via* single crystal analysis, where the likely site for the hydrogen atom was able to be determined and is shown in Figure 4.5. Bond valence calculations[8] also supported that O10 was underbonded and required an additional proton. It was also seen that the P–O bond for this hydroxyl group was slightly longer than the others in both phosphate environments in this framework, with a bond length of 1.52 Å. The hydroxyl group so ensured that the final formula of this structure was correctly charge-balanced.

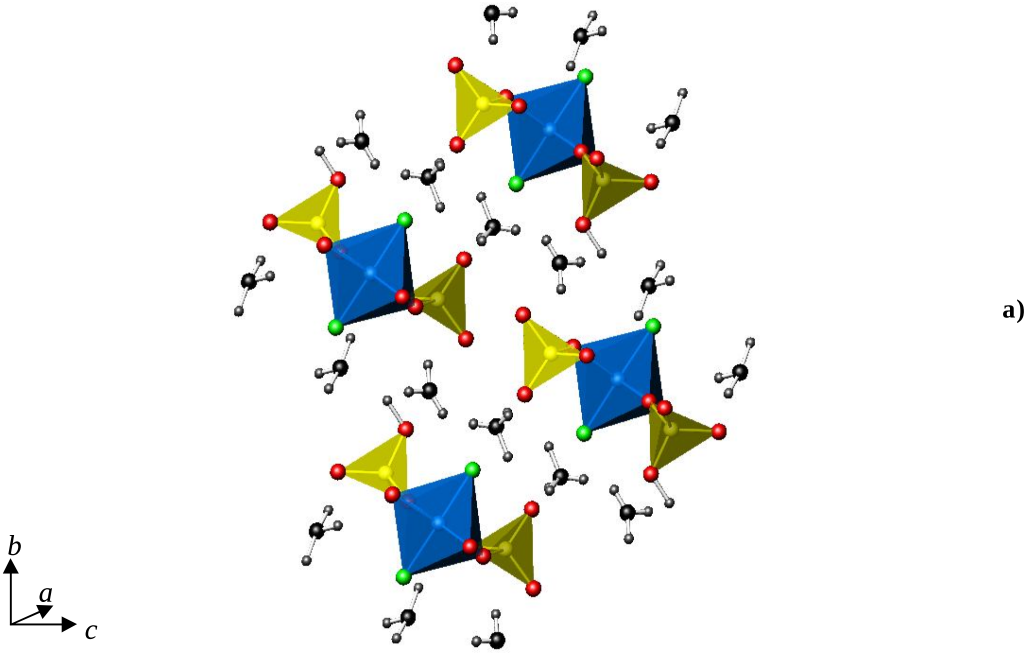

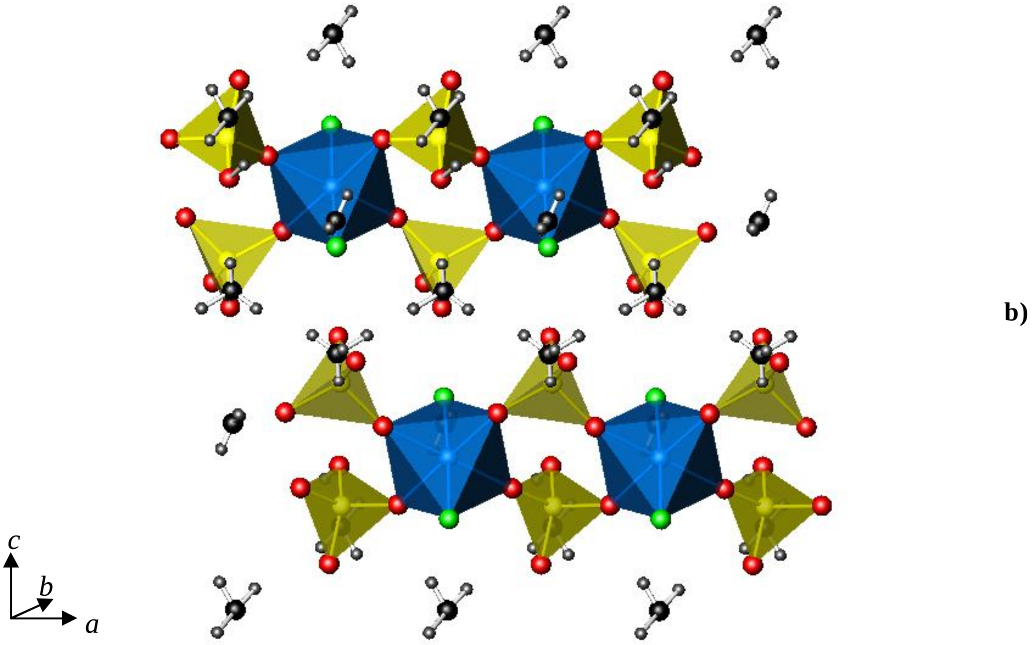

Figure 4.5: Structure of $ZrF_2(PO_4)(HPO_4)(NH_4)_3$ viewed down the a) *a*- and b) *b*-axes, where the zirconium octahedra are shown in blue, the phosphate tetrahedra in yellow, the oxygen atoms in red, the fluorine atoms in green, the hydrogen atoms, including the hydroxyl group, in grey and the ammonium groups as black and grey, where the hydrogen atoms could be located.

Table 4.8: Bond lengths and bond valence calculations for ZrF_2O_4 octahedra.

Atom	Zr–O/F bond length/ Å	P–O/F bond length/ Å	Bond valence
O2	2.102(5)	1.550(5)	1.82
O3	2.086(5)	1.543(5)	1.87
O4	2.053(5)	1.548(5)	1.93
O6	2.026(5)	1.542(6)	1.98
F1	1.982(5)	N/A	0.69
F8	2.009(4)	N/A	0.64

There are ammonium cations present between in the gaps between the chains of polyhedra. The nitrogen atoms were located via single crystal analysis and also some of the hydrogen atoms but not all could be seen in the refinement. The hydrogen atoms positions which could be refined are shown in Figure 4.5. These ammonium cations are held in place within the structure by hydrogen bonds which form between the oxygen and fluorine atoms in the polyhedra and the ammonium cations. Figure 4.6 shows the probable direction along which these bonds would lie, from the hydrogen atoms which were able to be refined and the polyhedral atoms. These hydrogen bonds will be relatively strong due to the number of bonds which may form in the cavities of this structure. Table 4.9 summarises the main hydrogen bonding interactions although, as may be seen in Figure 4.6, there are others in existence but these are weaker and longer.

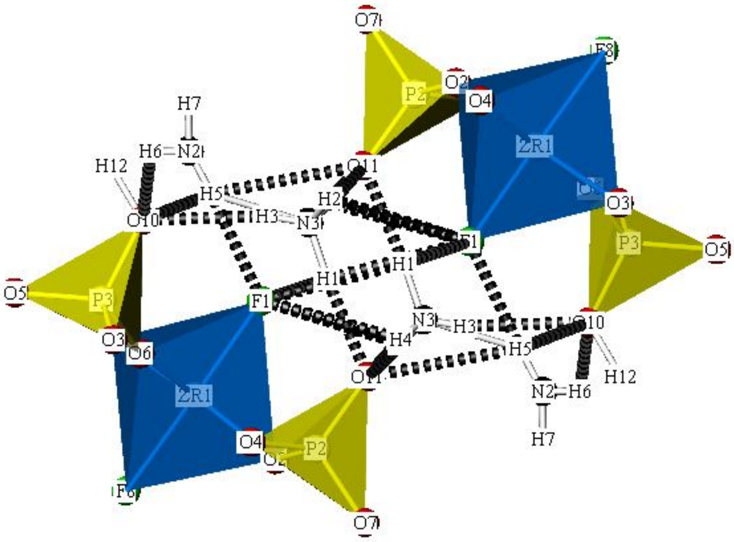

Figure 4.6: Hydrogen bonding between the oxygen and fluorine atoms and the ammonium cations in $ZrF_2(PO_4)(HPO_4)(NH_4)_3$.

Table 4.9: Hydrogen bonding of $ZrF_2(PO_4)(HPO_4)(NH_4)_3$, (where *d* = distance between stated atoms and *A* = acceptor).

N–H - - A	d(N–H)/ Å	d(H - - A)/ Å	d(N - - A)/ Å	Angle NHA/ °
N1–H9 - - O6	0.90	2.75	3.41	131.17
N1–H10 - - O3	0.78	2.14	2.90	164.65
N2–H5 - - F1	0.83	2.03	2.85	165.53
N2–H6 - - O10	0.71	2.64	3.00	113.88
N2–H7 - - O7	0.84	2.77	2.94	93.46
N3–H1 - - F1	1.02	2.78	3.04	94.67
N3–H2 - - O11	0.94	2.03	2.95	166.77
N3–H3 - - O10	0.73	2.14	2.85	168.32
N3–H4 - - O11	0.79	2.20	2.96	162.08

TGA data showed that there was an appropriate mass loss for the three ammonium cations, starting at around 175 °C, where there was a mass loss of 12.4 %. All three ammonium cations were lost in the same step, suggesting that they were all held in place by hydrogen bonds of very similar strength. Due to the fact that these cations started to be lost from the structure at a fairly low temperature, this suggests that only relatively weak hydrogen bonds were present to hold them in place, when compared with those in the titanium analogue, discussed in Section 4.1. Table 4.9 shows the lengths of the hydrogen bonding interactions between the ammonium cations and the polyhedral atoms in $ZrF_2(PO_4)(HPO_4)(NH_4)_3$ and they are, on average, 0.29 Å longer than those in $TiF_2(PO_4)(HPO_4)(NH_4)_3$. These longer bonds are therefore weaker and result in the ammonium cations being lost at a lower temperature in the zirconium structure, decreasing the thermal stability. The overall loss of all three cations is shown in Figure 4.7.

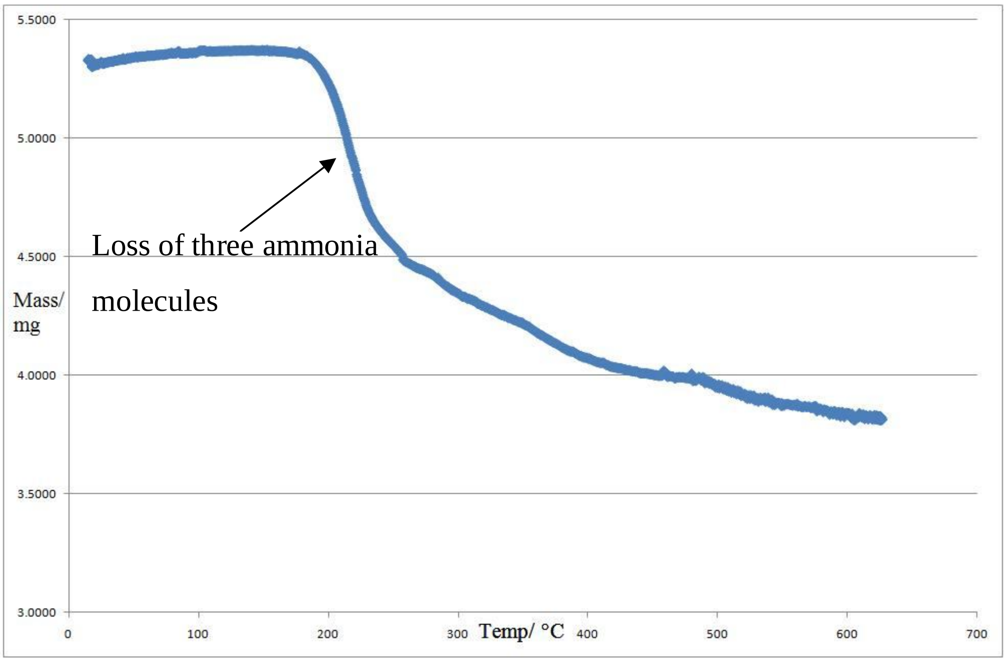

Figure 4.7: TGA for $ZrF_2(PO_4)(HPO_4)(NH_4)_3$, showing the loss of all three ammonium cations.

An SEM image of $ZrF_2(PO_4)(HPO_4)(NH_4)_3$ was collected at the same time as the EDS data and is shown in Figure 4.8. A broad absorption was seen at 3433-3170 cm^{-1} in the IR spectrum of this sample, which is due to the N–H stretch of the ammonium cations. This band is a lower than usually expected due to the hydrogen bonding in the structure. There is also a peak seen at 1444 cm^{-1} due to the N–H bend in the ammonium cations. There is a stretch seen at 1119-981 cm^{-1} which is due to the P–O stretches[9]. There is also a broad band at around 3500 cm^{-1}, which is partially obscured by the N–H stretch but this is likely to be due to the O–H bond in the hydrogen phosphate group.

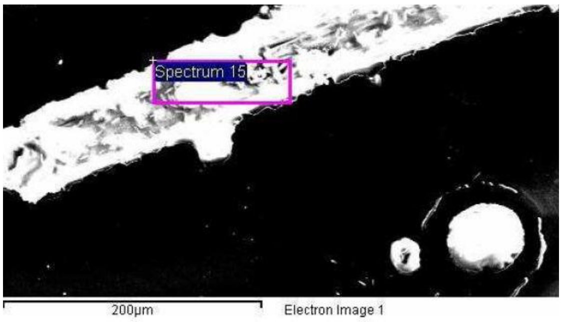

Figure 4.8: SEM image of a single crystal of $ZrF_2(PO_4)(HPO_4)(NH_4)_3$.

4.3-$Hf_2F_2(H(PO_4)_3)(NH_4)_2$

A colourless cube-like single crystal was selected for single crystal X-ray diffraction and the collected crystallographic data are shown in Table 4.10. The monoclinic unit cell makes up a framework which consists of alternating $HfFO_5$ octahedra and PO_4 tetrahedra, which are corner-sharing and are connected to one another *via* bridging oxygen atoms, as seen in Figures 4.9. The alternating polyhedra build up to form four-membered rings, forming a two-dimensional network along the *b*- and *c*-axes, with the bond lengths as shown in Table 4.11.

For each of the $HfFO_5$ octahedra, all five of the oxygen atoms bridge to form part of the neighbouring phosphate groups. The single fluorine atom was found to be terminal, thus in a different environment to the oxygen atoms. The presence of this fluorine atom was confirmed both by thermal parameters within the single crystal refinement and by EDS analysis, with the EDS data semi-quantitatively showing that only a very small percentage of fluorine was present within the structure. Bond valence values were calculated[8] and are shown in Table 4.12, which also supported the theory that there was a fluorine atoms present, as opposed to a hydroxyl group. These fluorine atoms are directed into the interlayer spaces and are thus involved in hydrogen bonding interactions with the ammonium cations in these spaces, which is discussed further on.

Table 4.10: Crystal data for $Hf_2F_2(H(PO_4)_3)(NH_4)_2$.

Chemical Formula	$Hf_2F_2(H(PO_4)_3)(NH_4)_2$
Crystal Appearance	Colourless block
Crystal Size/ mm	0.2 x 0.2 x 0.2
M	719.82618
Crystal System	Monoclinic
Space Group	$C2/c$
a, b, c/ Å	17.0481(8), 8.7424(3), 9.1722(3)
α, β, γ / °	90.000(0), 103.790(3), 90.000(0)
V/ $Å^3$	1327.63(1)
Z	8
T/ K	120
λ/Å	0.71073
Reflections collected	7594
Unique reflections	1372
R_{int}	0.0537
$R_1[I > 2\sigma(I)]^a$	0.0295
$R1$(all data)	0.0337
wR_2(all data)	0.0715

Table 4.11: Bond lengths in $Hf_2F_2(H(PO_4)_3)(NH_4)_2$.

Bond	Bond length/ Å	Bond	Bond length/ Å
Hf1–O1	2.045(4)	P1–O2	1.520(5)
Hf1–O2	2.043(4)	P1–O2	1.520(5)
Hf1–O4	2.071(4)	P1–O6	1.523(5)
Hf1–O5	2.036(5)	P1–O6	1.523(5)
Hf1–O6	2.072(4)	P2–O1	1.533(5)
Hf1–F1	2.009(4)	P2–O4	1.520(5)
		P2–O5	1.520(5)
		P2–O7	1.534(5)

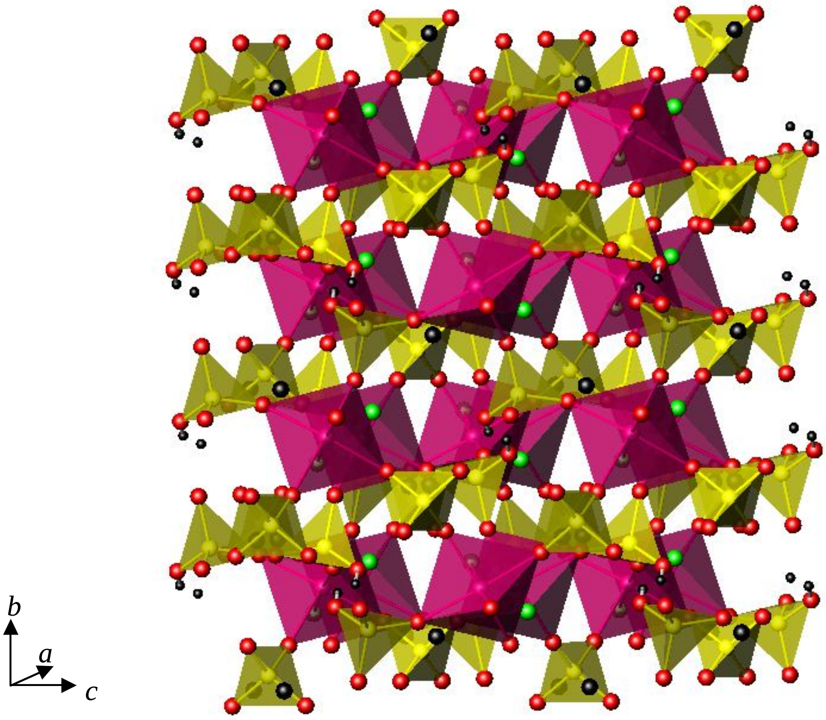

a)

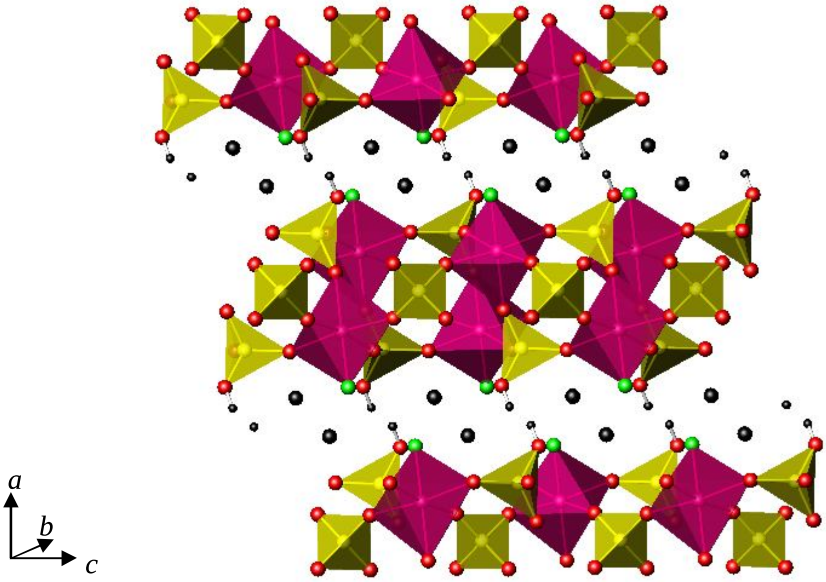

b)

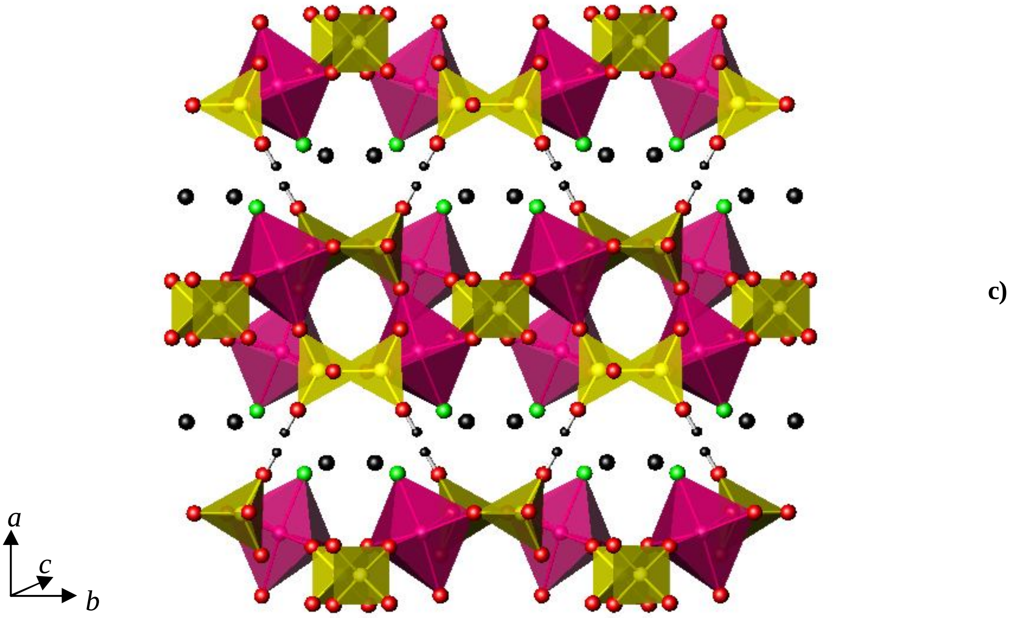

Figure 4.9: Structure of $Hf_2F_2(H(PO_4)_3)(NH_4)_2$ viewed down the a) *a*-, b) *b*, and c) *c*-axes, where the hafnium octahedra are shown in magenta, the phosphate tetrahedra in yellow, the oxygen atoms in red, the fluorine atoms in green and the ammonium cations are shown as black spheres to represent the nitrogen atoms.

Table 4.12: Bond lengths and bond valence calculations for $HfFO_5$ octahedra and AsO_4 tetrahedra.

Atom	Hf–O/F bond length/ Å	P–O/F bond length/ Å	Bond valence	O–H bond length/ Å	Bond valence
O1	2.045(4)	1.533(5)	1.97		
O2	2.043(4)	1.520(5)	2.02		
O4	2.071(4)	1.520(5)	1.98		
O5	2.036(5)	1.523(5)	2.03		
O6	2.072(4)	1.523(5)	1.96		
F1	2.009(4)	N/A	0.64		
O7	N/A	1.534(5)	1.25	0.85	1.99

It can be seen in the figures above that there are hydroxyl groups present as part of the phosphate groups. The hydrogen atoms were located during the single crystal refinement and the bond valence values[8] shown in Table 4.12 also support their presence. The hydrogen atoms are in fact partially occupied and are shared by the opposite phosphate group, resulting in the unit formula ($H(PO4)_2$). However, all of the sites are shown in the diagrams for clarity. Figure 4.10 shows the hydrogen atoms more clearly and it can be seen that the partially occupied hydrogen atom always lies along a plane between the two oxygen atoms with which it is associated, as would be expected due to the existence of hydrogen bonding between these groups.

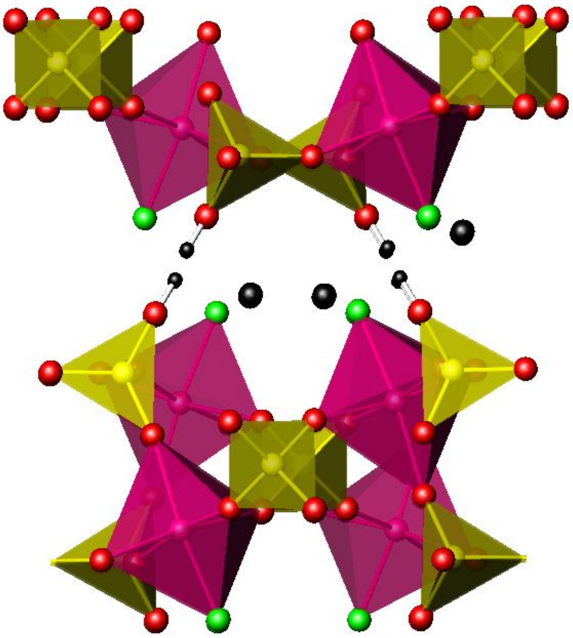

Figure 4.10: Partially occupied hydrogen atoms in $Hf_2F_2(H(PO_4)_3)(NH_4)_2$.

Between the layers of octahedra and tetrahedra, there are ammonium cation environments and these cations are held in place by hydrogen bonds from the oxygen and fluorine atoms. However, it was not possible to locate the hydrogen atoms, (other than the partially occupied one on the hydroxyl group of the phosphate tetrahedra), *via* single crystal analysis. All of the possible hydrogen bonding is shown in Figure 4.11, where the dotted lines are between the nitrogen atoms and the polyhedral fluorine and oxygen atoms, in the absence of located protons. These dotted lines show the expected directions along which the hydrogen atoms should be positioned and thus the predicted hydrogen bonding interactions. There will be a high level of hydrogen bonding present to hold the ammonium cations within this framework but it is not possible to say with certainty where the hydrogen atoms would actually lie.

This high level of hydrogen bonding is supported by considering the data collected by TGA, which is represented graphically Figure 4.12. It may be seen that there were the appropriate mass losses of approximately 2.52 % for each of the two ammonium cations but they were lost sequentially, with the first mass loss at around 250 °C. At the higher temperature of 370 °C, the second ammonium cation was removed from the structure, meaning that it was held in place by stronger hydrogen bonds to the oxygen and fluorine atoms in the structure. The O–H of the partially occupied hydroxyl group in the phosphate units was then removed from the structure at approximately 400 °C, where a mass loss of 2.37 % was observed. This loss was the start of the main framework decomposing and this loss may also be seen in Figure 4.12.

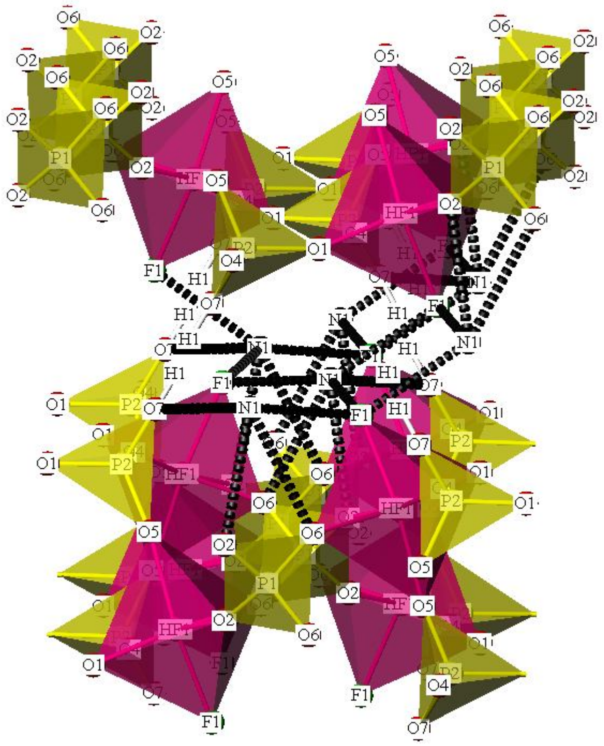

Figure 4.11: Hydrogen bonding in $Hf_2F_2(H(PO_4)_3)(NH_4)_2$.

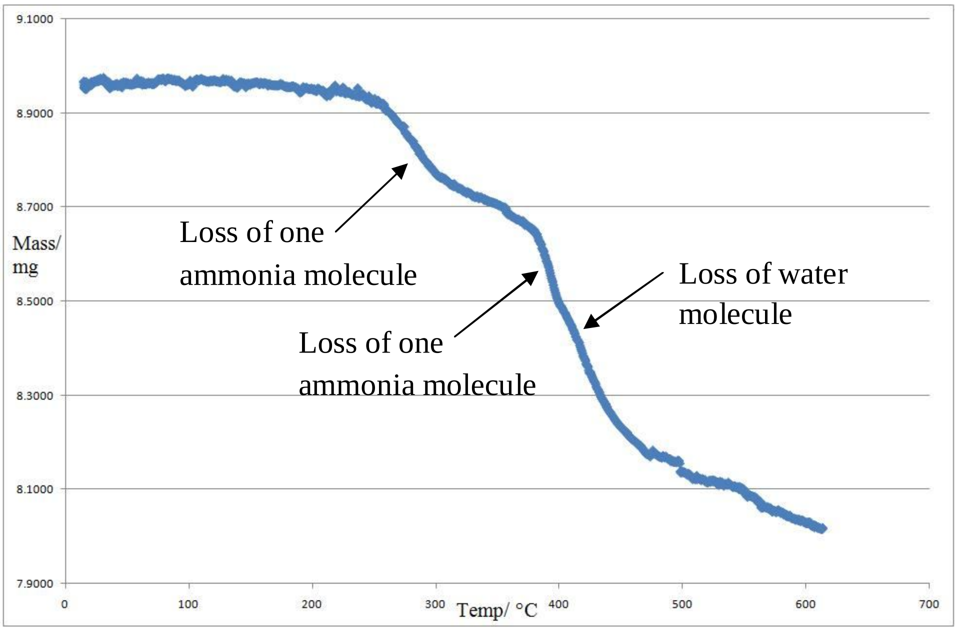

Figure 4.12: TGA for $Hf_2F_2(H(PO_4)_3)(NH_4)_2$, with the mass losses for both ammonium environments and hydroxyl group shown.

An SEM image of $Hf_2F_2(H(PO_4)_2)(NH_4)_2$ was taken during the EDS data collection and is shown in Figure 4.13. A broad absorption was seen at 3434-3150 cm^{-1} due to the N–H bonds in the ammonium cations, also causing this peak to be lower than expected as a result of the hydrogen bonding within this structure. A further peak was observed at 1431 cm^{-1} due to the N–H bend within the ammonium cations. The O–H in the phosphate tetrahedra shows a stretch at 3570-3456 cm^{-1} and there is also a stretch seen at 1201-1014 cm^{-1} which is due to the P–O stretches[9].

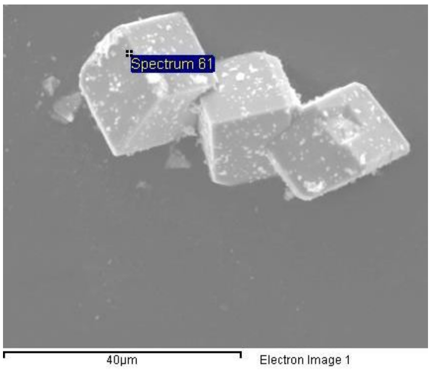

Figure 4.13: SEM image of a single crystal of $Hf_2F_2(H(PO_4)_3)(NH_4)_2$.

4.4-$Hf_2(PO_4)_3(NH_4)$

A colourless cube-like single crystal was selected for single crystal X-ray diffraction and the crystallographic information from the data collection is shown in Table 4.13. The framework consists of HfO_6 octahedra and PO_4 tetrahedra, which display hexagonal symmetry and are connected in a corner-sharing manner *via* bridging oxygen atoms, as seen in Figure 4.14, with the bond lengths given in Table 4.14. Both the HfO_6 octahedra and PO_4 tetrahedra are fully coordinated, to six and four neighbouring oxygen atoms respectively, resulting in a three-dimensional network along all three axes. Within the tightly packed framework, there are small cavities visible down the *a*- and *b*-axes, with a maximum diameter of 5.78 Å between O4 and O4. This size of cavity was determined to be large enough to contain ammonium cations, (as shown in Figure 4.14), where the nitrogen atom position was located *via* the single crystal refinement. The ammonium cations are discussed in more detail later on in this section.

Table 4.13: Crystal data for $Hf_2(PO_4)_3(NH_4)$.

Chemical Formula	$Hf_2(PO_4)_3(NH_4)$		
Crystal Appearance	Colourless block	T/ K	120
Crystal Size/ mm	0.1 x 0.1 x 0.1	λ/Å	0.71073
M	659.93258	Reflections collected	3584
Crystal System	Hexagonal	Unique reflections	409
Space Group	*R*-3*c*	R_{int}	0.0390
a, b, c/ Å	8.6617(2), 8.6617(2), 24.1618(1)	$R_1[I > 2\sigma(I)]^a$	0.0178
α, β, γ / °	90.000(0), 90.000(0), 120.000(0)	*R*1(all data)	0.0210
V/ Å^3	1569.88(1)	wR_2(all data)	0.0440
Z	9		

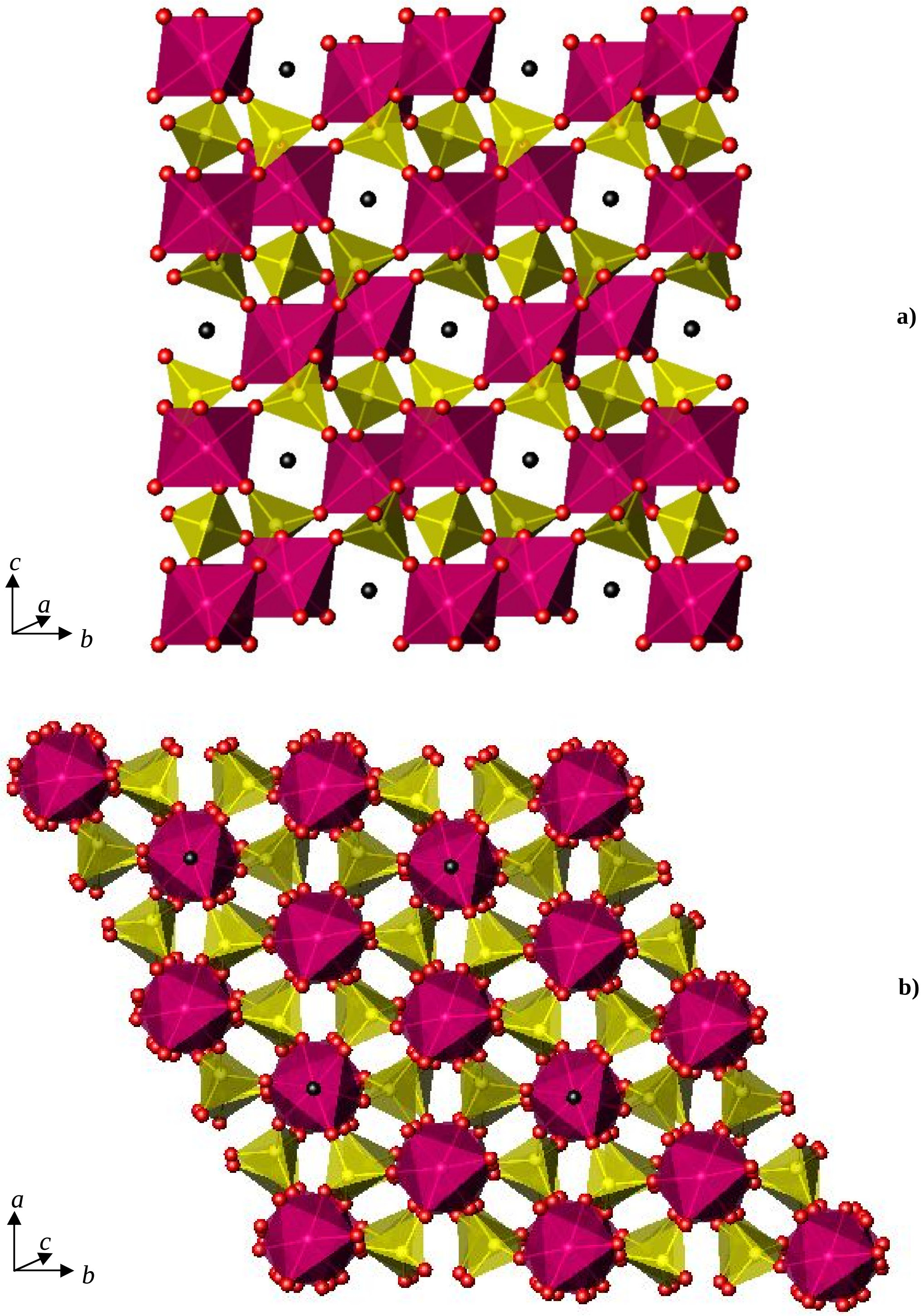

Figure 4.14: Structure of $Hf_2(PO_4)_3(NH_4)$ viewed down the a) *a*- and b) *c*-axes, where the hafnium octahedra are shown in magenta, the phosphate tetrahedra in yellow, the oxygen atoms in red and the ammonium cations are shown as black spheres to represent the nitrogen atoms.

Table 4.14: Bond lengths in $Hf_2(PO_4)_3(NH_4)$.

Bond	Bond length/ Å	Bond	Bond length/ Å
Hf1–O1	2.053(5)	P1–O1	1.525(3)
Hf1–O4	2.061(3)	P1-O4	1.528(3)

As mentioned above, there are ammonium cations present within the cavities of this structure. The hydrogen atoms were not located during the single crystal refinement but their possible locations may be calculated by looking at the directions along which there are likely to be hydrogen bonds, as depicted by dotted lines in Figure 4.15. Although all of the oxygen atoms within this framework are fully coordinated, they are still able to form hydrogen bonding interactions to the ammonium cations. The distances between the central nitrogen atom for each ammonium cation and these polyhedral oxygen atoms are all in the region of 2.9 Å, a reasonable length for a hydrogen bond.

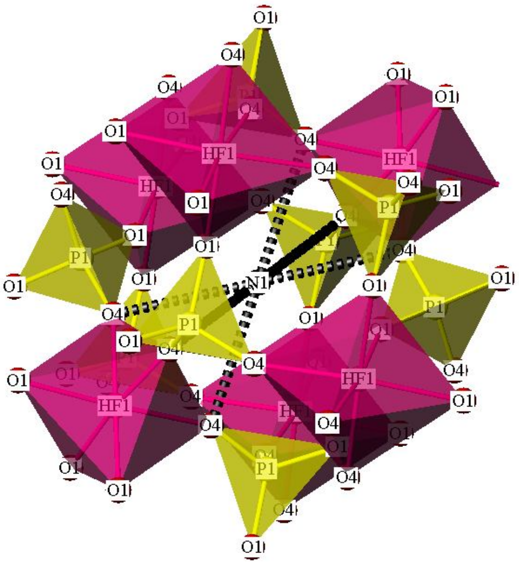

Figure 4.15: Hydrogen bonding between the oxygen atoms and the ammonium cations in $Hf_2(PO_4)_3(NH_4)$.

An appropriate mass loss of 2.73 % for this single ammonium cation environment was observed at approximately 270 °C *via* TGA. The strong hydrogen bonds within this tightly packed framework are the reason that this relatively high temperature is required in order for the ammonium cation to be removed from the cavities in this framework. There was no further mass loss seen in the TGA run, where the sample was heated to 650 °C, as would be expected in this structure, due to the compact and strongly bound framework not starting to decompose by this point.

EDS confirmed the presence of oxygen but the absence of fluorine in this structure and an SEM image of a $Hf_2(PO_4)_3(NH_4)$ single crystal was recorded at the same time as this data collection and is shown in Figure 4.16. A broad but very low value absorption was seen at 3372-3125 cm^{-1} in the IR spectroscopy analysis of this material, which is due to the N–H bonds in the ammonium cations. This peak is at such a low value due to the strong hydrogen bonding that exists between the ammonium cations and the tightly-packed polyhedral network. A further peak at 1434 cm^{-1} exists due to the N–H bend for the ammonium cations. An absorption due to the P–O bond stretch is observed at 1207-967 cm^{-1}[19].

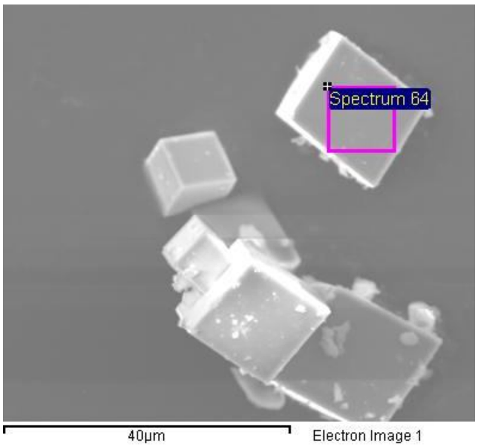

Figure 4.16: SEM image of a single crystal of $Hf_2(PO_4)_3(NH_4)$.

4.5-$NbO_2(HPO_4)_2(NH_4)_3$

A colourless needle-like single crystal was selected for single crystal X-ray diffraction and a summary of the crystallographic data that was collected is shown in Table 4.15. The structure exists with triclinic symmetry and consists of NbO_6 octahedra and distorted PO_4 tetrahedra, where all of the oxygen atoms are disordered over two sites due to alternating PO_4 tetrahedra throughout the structure, which may be seen in Figure 4.17. This diagram also shows that the polyhedra are corner-sharing and alternate to from four-membered rings. These four-membered rings are made up of two NbO_6 octahedra and two PO_4 tetrahedra, which then extend to form a chain along the *a*-axis and the bond lengths are given in Table 4.16. These discrete chains are very similar to those found in $TiF_2(PO_4)(HPO_4)(NH_4)_3$ and $ZrF_2(PO_4)(HPO_4)(NH_4)_3$, (in Sections 4.1 and 4.2), where the chains form along just one axis rather than building up into a two-dimensional layer. As is also seen in these two materials, the whole structure of $NbO_2(HPO_4)_2(NH_4)_3$ is held together by hydrogen bonding interactions between the oxygen atoms of the polyhedra and the ammonium cations present between the chains, as discussed in more detail later.

Within each NbO_6 octahedron, the four equatorial oxygen atoms bridge to the neighbouring phosphate groups, and the remaining two, (O4), are at the terminal positions and are directed into the spaces between the chains. Data collected during EDS confirmed semi-quantitatively that there was no fluorine present in this structure, supporting that theory that this atom was an oxygen atom and bond valence calculations[8] indicated that no protonation was necessary. These terminal oxygen atoms are directed into the regions between the chains of polyhedra, increasing the strength of the hydrogen bonding interactions.

In each of the PO_4 units, two of the oxygen atoms form bridges to the neighbouring niobium atoms, also forming part of the NbO_6 octahedra. The other two oxygen atoms within each tetrahedron are terminal; one of which was in fact refined as a hydroxyl group. This hydroxyl group means that a chain is not able to form along this direction, meaning that a layered framework in not able to form. It was not possible to locate the hydrogen atoms during the single crystal refinement and both terminal oxygen atoms exhibit Nb–O bond lengths which are longer than the bridging ones, suggesting that both may in fact be partially occupied hydroxyl groups. Due to the level of disorder amongst the oxygen atoms in this structure, it was not possible to predict accurately which of these atoms would be protonated.

Table 4.15: Crystal data for $NbO_2(HPO_4)_2(NH_4)_3$.

Chemical Formula	$NbO_2(HPO_4)_2(NH_4)_3$
Crystal Appearance	Colourless needle
Crystal Size/ mm	0.05 x 0.05 x 0.05
M	370.97928
Crystal System	Triclinic
Space Group	$P1$
a, b, c/ Å	5.1537(4), 7.1625(6), 8.0301(6)
α, β, γ / °	110.694(4), 91.577(5), 110.858(4)
V/ $Å^3$	255.10(8)
Z	2
T/ K	120
λ/Å	0.71073
Reflections collected	4511
Unique reflections	901
R_{int}	0.0549
$R_1[I > 2\sigma(I)]^a$	0.0919
$R1$(all data)	0.1009
wR_2(all data)	0.2518

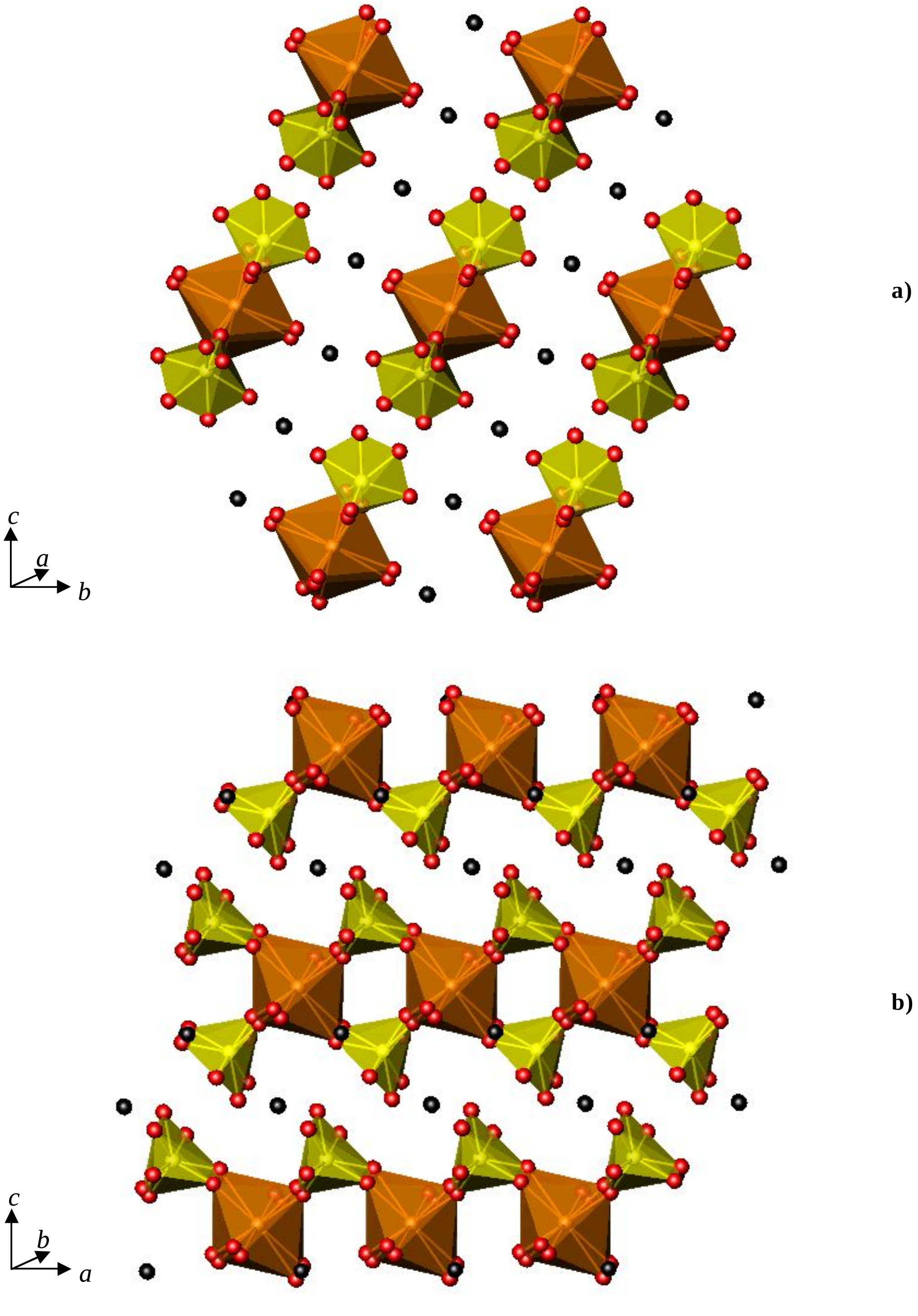
a)
c
a
b
b)
c
b
a

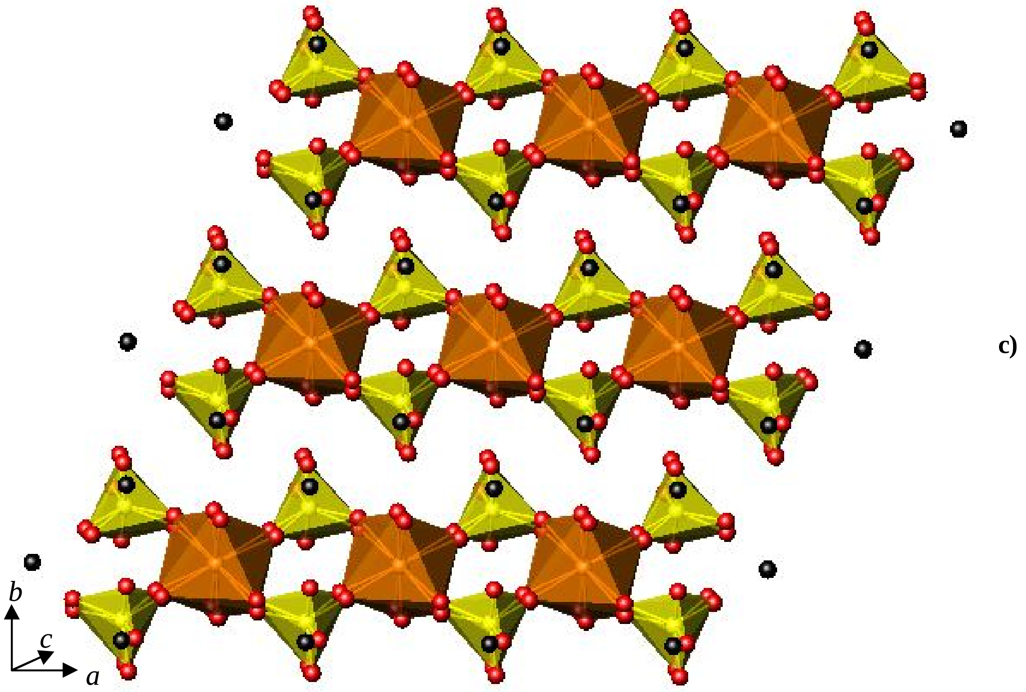

Figure 4.17: Structure of $NbO_2(HPO_4)_2(NH_4)_3$ viewed down the a) *a*-, b) *b*- and c) *c*-axes, where the niobium octahedra are shown in orange, the phosphate octahedra in yellow, the oxygen atoms in red and the ammonium cations are shown as black spheres to represent the nitrogen atoms.

Table 4.16: Bond lengths in $NbO_2(HPO_4)_2(NH_4)_3$.

Bond	Bond length/ Å	Bond	Bond length/ Å
Nb1A–O3A	1.944(6)	P1A–O1A	1.559(7)
Nb1A–O4A	1.981(8)	P1A–O2A	1.505(6)
Nb1A–O5A	1.979(8)	P1A–O3A	1.545(7)
Nb1A–O3A	1.944(6)	P1A–O5A	1.455(8)
Nb1A–O4A	1.981(8)		
Nb1A–O5A	1.979(8)		

As discussed above, both the terminal oxygen atoms of the NbO_6 octahedra and the hydroxyl groups of the phosphate tetrahedra are able to form hydrogen bonding interactions with the ammonium cations. Although it was not possible to locate any of the hydrogen atoms, either as part of the hydrogen phosphate groups or the ammonium cations, their likely positions may be estimated by looking at the direction of the various hydrogen bonds, which may be seen in Figure 4.18, where all of the possible directions for the N–H bonds are shown. As may be seen in Figure 4.18, the predicted directions of these N–H bonds are as would be expected for an ammonium group. The disordered oxygen atoms within this diagram are labelled as A and B, such as O4A and O4B at the terminal octahedral sites. These ammonium cations all exist in very similar environments, with them present between the "layers" of chains as seen when the structure is viewed down the *a*-axis, rather than all around the chains as seen for $TiF_2(PO_4)(HPO_4)(NH_4)_3$ and $ZrF_2(PO_4)(HPO_4)(NH_4)_3$, (in Sections 4.1 and 4.2).

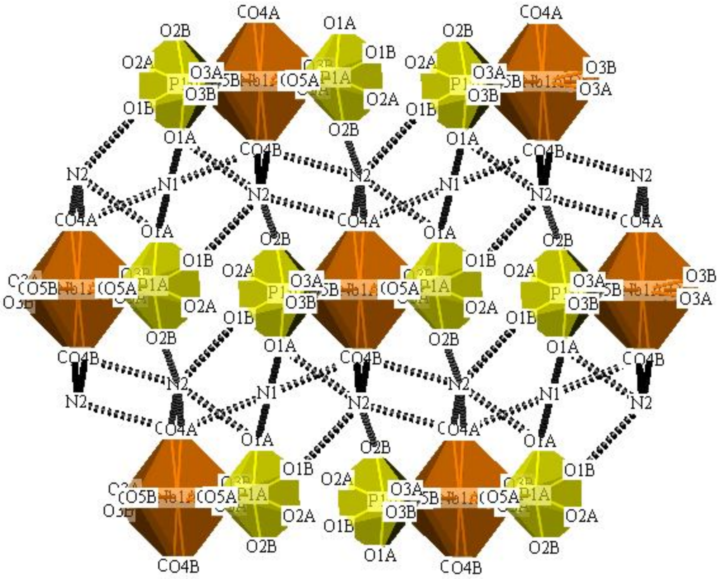

Figure 4.18: Hydrogen bonding between the oxygen atoms and the ammonium cations in $NbO_2(HPO_4)_2(NH_4)_3$.

These similar ammonium environments were also observed *via* TGA, where there was an appropriate mass loss of 9.99 % for the loss of all three ammonium cations at around 230 °C. This one large mass loss suggests that the ammonium cations were all held in place by hydrogen bonds of very similar strength, due to them all existing in very similar environments. This overall loss of cations is shown in Figure 4.19.

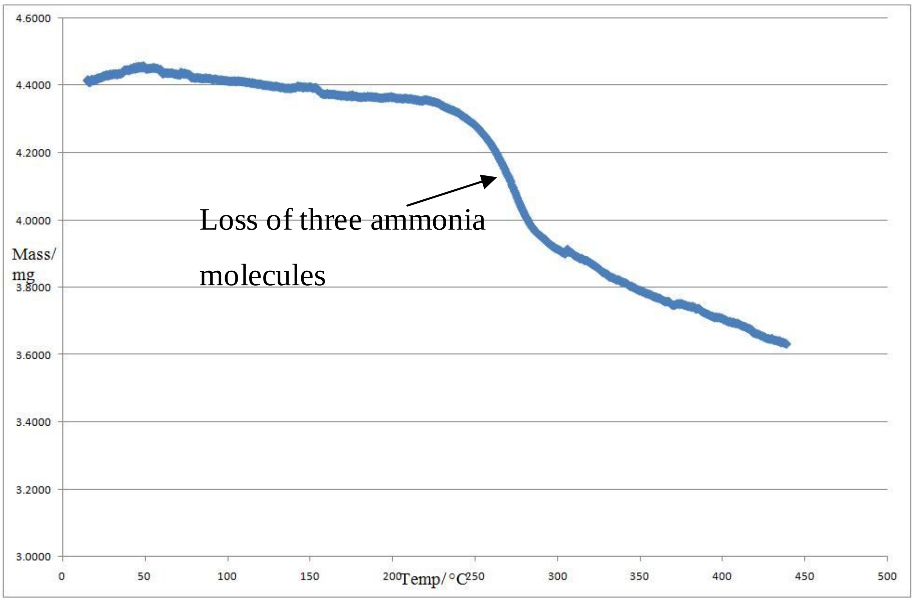

Figure 4.19: TGA for $NbO_2(HPO_4)_2(NH_4)_3$, showing the loss of all three ammonium cations.

During the EDS data collection an SEM image of a single crystal of $NbO_2(HPO_4)_2(NH_4)_3$ was recorded and is shown in Figure 4.20. A broad IR absorption was seen at the low value of 3395-3165 cm^{-1} was seen as a result of the N–H bonds in the hydrogen-bonded ammonium cations in this structure. There is also a peak due to the ammonium cations in the IR spectrum, which exists at 1445 cm^{-1} and is a result if the N–H bend. There is a stretch seen at 1107-988 cm^{-1} which is due to the P–O stretches[9], with another broad band seen at 3675-3386 cm $^{-1}$ due to the O–H stretch of the hydroxyl group in the hydrogen phosphate unit.

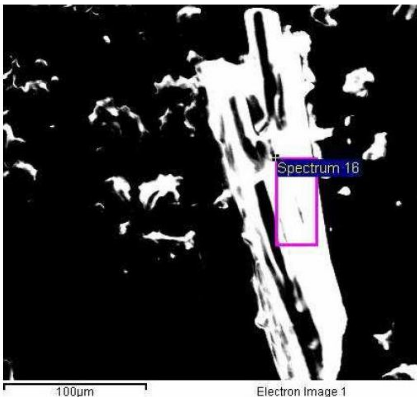

Figure 4.20: SEM image of a single crystal of $NbO_2(HPO_4)_2(NH_4)_3$.

4.6-Conclusions for Group IV and V Phosphate Frameworks

Five novel phosphate frameworks have been solvothermally synthesised and fully characterised, primarily by single crystal X-ray diffraction. Although there have been considerably more Group IV and V phosphate materials reported than the analogous arsenate frameworks, there are still very few fluorinated examples. This lack of fluorinated materials was unexpected, especially when considering the previous reported successes of using a fluoride source as a mineraliser, as discussed in Chapter 1, where M–F–M linkages may be present, as was shown in the structures discussed above. When a fluoride anion exists in this manner, it greatly alters the environment in which the metal centre is found. The result is often an increase in its coordination, such as from five- to six-coordination in the case of CJ2[10,11], $(NH_4)_{0.93}(H_3O)_{0.07}GaPO_4(OH)_{0.5}F_{0.5}$. The fluoride anions in this material may either fully occupy their sites or partially share them with hydroxyl groups. The synthesis of the templated structure $[(CH_3)_2NH(CH_2)_2NH(CH_3)_2]_{0.5}[Zr_2F_2(PO_4)(HPO_4)_2]\cdot 0.5H_2O$ was achieved under hydrothermal conditions[12], where the material exists as a layered structure but with the template also incorporated. The fluoride anions within zirconium-centred octahedra result in the termination of chains along this direction, causing a layered structure to be reported.

As Table 4.1 shows, single crystals were produced in a small number of reactions other than those discussed in the bulk of this chapter, such as $(NH_4)_2(TiOPO_4)$[7]. This material was synthesised *via* a lower temperature route than the novel frameworks presented in Table 4.1. Two different reactions resulted in the formation of single crystals of $(NH_4)_2(TiOPO_4)$, one of which had a reaction temperature of 140 °C and a duration of 504 h, suggesting that a higher temperature was required to produce a fluorinated version of this material, such as $TiF_2(PO_4)(HPO_4)(NH_4)_3$. A large number of Group IV and V phosphates that are not fluorinated have been reported so it is not unexpected that some of the single crystals that were produced and did not incorporate a fluoride group had previously been well documented, such as was seen in the case of $(NH_4)_2(TiOPO_4)$. However, the concept of using a fluoride anion as a mineraliser has not previously been studied in detail.

As may be seen in Table 4.1, the type of phosphate framework investigated here requires a wide range of both reaction durations and temperatures. As would be expected, it would appear that those reactions that were carried out at a lower temperature were only successful when heated for a prolonged period of time, *i.e.* several days, allowing the activation energy for the formation of the stated material to be reached in each case. This may particularly be seen when comparing $TiF_2(PO_4)(HPO_4)(NH_4)_3$ and $ZrF_2(PO_4)(HPO_4)(NH_4)_3$, where the analogous zirconium reaction had to be synthesised at a lower temperature to prevent decomposition of the DABCO in the reaction mixture. This suggests that either the ZrF_4 must be considerably more reactive than TiF_3 in this type of reaction environment or the DABCO promoted the reaction and reduced the activation energy of the reaction. As discussed in the previous paragraph, $(NH_4)_2(TiOPO_4)$ was synthesised in the titanium reaction with DABCO.

Four new phosphate frameworks containing Group IV metals were recorded in this work: $TiF_2(PO_4)(HPO_4)(NH_4)_3$, $ZrF_2(PO_4)(HPO_4)(NH_4)_3$, $Hf_2F_2(H(PO_4)_3)(NH_4)_2$ and $Hf_2(PO_4)_3(NH_4)$. There was also one novel Group V phosphate material characterised: $NbO_2(HPO_4)_2(NH_4)_3$. The syntheses of these structures were all carried out solvothermally but in solutions at a range of pH values. As was the case with the arsenate frameworks discussed in Chapter 3, the ammonium cation in ammonium dihydrogen phosphate appears to have acted as a structure-directing agent in many of the novel phosphate materials discussed in this chapter. By acting as a *pseudo*-template, the ammonium cations have been incorporated into each of the structures, regardless of the pH at which the reaction was carried out.

The reaction conditions under which $TiF_2(PO_4)(HPO_4)(NH_4)_3$ was synthesised were mildly acidic, with ethanol being used as the solvent and a fluoride source as a mineraliser. The framework was found to consist of corner-sharing TiF_2O_4 octahedra and alternating phosphate and hydrogen-phosphate tetrahedra, which were linked together to form four-membered rings. These rings then link to one another to form layers of chains along the *a*-axis, with the two fluoride anions per TiF_2O_4 octahedron being terminal and thus preventing bridging in this direction to build up a three-dimensional network. Although the cavities in the four-membered rings were discovered to be empty, there were found to be ammonium cations present between the layers, which are able to hydrogen-bond to the polyhedral fluorine and oxygen atoms which are directed into the interlayer spaces. The outcome of these hydrogen bonds is a rigid and strongly-bound framework, supported by the TGA data which suggested that the ammonium cations were only removed from the structure at the relatively high temperature of 240 °C and upwards. It may be possible to carry out ion exchange with this structure but this would require heating to a temperature in excess of 240 °C which may not be economically viable and may also lead to the structure to start decomposing as the stabilising cations were removed and an attempt was made to replace them.

Analogous to the titanium framework, $ZrF_2(PO_4)(HPO_4)(NH_4)_3$ was also synthesised and fully characterised. However, this structure required a weakly basic reaction mixture in order for single crystals of this material to be successfully synthesised. The only difference between these two structures was the temperature at which the ammonium cations were lost from the interlayer spaces of the framework. This is presumably due to the noticeable longer and weaker hydrogen bonds present holding the ammonium cations in place, in comparison with the length and strength of those in $TiF_2(PO_4)(HPO_4)(NH_4)_3$. The same issues with ion exchange will exist for both of these phosphate frameworks.

The first of the two hafnium phosphate structures to be produced was $Hf_2F_2(H(PO_4)_3)(NH_4)_2$, which was subjected to relatively strongly basic reaction conditions, by the starting materials being dissolved in concentrated ammonium solution. The main framework of this material is constructed from alternating $HfFO_5$ octahedra and PO_4 tetrahedra which are corner-sharing *via* bridging oxygen atoms. A two-dimensional network occurs along the *b*- and *c*-axes, which is again as a result of the fluoride anions in this structure, causing the termination of chains along this direction. Between these chains, there are ammonium cations which are held in place by hydrogen bonds from the polyhedral oxygen and fluorine atoms. In this structure, the PO_4 were concluded to in fact contain a partially occupied hydroxyl group, where the hydrogen atom is in fact shared by the phosphate group on the other side of the interlayer space. The partially occupied hydroxyl site is unusual and also appears to increase the level of hydrogen bonding in the framework, causing the ammonium cations not to be removed from the structure until the high temperatures of 250 °C and 370 °C. The result of all of the hydrogen bonding is a very strongly bound and stable framework.

The second hafnium phosphate to be characterised here, $Hf_2(PO_4)_3(NH_4)$, was found to exist as a much simpler framework and not to contain any fluorine atoms, as supported by both the single crystal analysis and the EDS data. The mildly acidic conditions used in this synthesis also appear to have been the reason for a reduced percentage of ammonium cations. The HfO_6 octahedra and PO_4 tetrahedra are fully coordinated and are once again corner-sharing, by being connected *via* bridging oxygen atoms. The lack of terminal fluoride groups within $Hf_2(PO_4)_3(NH_4)$ allows the formation of a tightly packed, three-dimensional network in which there are small cavities down both the *a*- and the *b*-axes. By being fully coordinated, the phosphate groups in this structure do not require hydrogenation, preventing the termination of the three-dimensional network at this point. These cavities were determined to be just large enough to contain the ammonium cations present in this structure. The TGA data suggested that the ammonium cations were removed from the structure at around 270 °C. The TGA run did not show any further loss of mass on heating the sample to 650 °C, as would be expected due to this compact and strongly bound framework not starting to decompose by this point. If the ammonium cations could be ion exchanged, this material may have interesting storage properties due to the cavities that are present and the hydrogen bonding.

The final phosphate to be synthesised here was in fact a niobium phosphate, solved to have the structural formula $NbO_2(HPO_4)_2(NH_4)_3$. The conditions used were acidic, using ethanol as the solvent and once again there was no fluorine present in the final structure, as shown semi-qualitatively in the EDS data. This simple, layered framework was made up of disordered NbO_6 octahedra and hydrogen phosphate tetrahedra where the hydroxyl group prevents the building up of a three-dimensional structure. These polyhedra link to form four-membered rings, in which there were no ammonium cations. These cations were all found to be present between the layers and are able to hydrogen-bond to the polyhedral oxygen atoms. The loss of the interlayer species took place at the moderately high temperature of 230 °C, again suggesting that the hydrogen bonds were holding the cations firmly in place, which may hinder ion exchange potential.

Although there are already a large number of known phosphate frameworks, this work has detailed a relatively unexplored avenue of research, where a fluoride source has been used as a mineraliser. In three of the novel materials, M–F bonds were shown to exist within the frameworks, without the inclusion of a bulky organic template, as was the case in the synthesis of $[(CH_3)_2NH(CH_2)_2NH(CH_3)_2]_{0.5}[Zr_2F_2(PO_4)(HPO_4)_2]\cdot 0.5H_2O$[11]. The examples within this work have made use of a fluoride mineraliser to promote the reaction and have also incorporated groups with ion exchange potential. In the other two structures, the fluoride source appeared purely to act as an agent to promote the reaction. Nevertheless, all five of these materials open up a potential new field of research, where future work may result in the synthesis of further, similar structures of other transition metals. Currently, there are possible applications in the ion exchange field, as long as this can be achieved without decomposition of the main framework. These properties will need to be tested and their properties improved upon if further work is carried out.

4.7-References

---

[1] A. M. K. Andersen, P. Norby, J. Hanson, *Inorg. Chem.*, 1998, **37**, 876-881.

[2] D. M. Poojary, A. I. Bortun, L. N. Bortun, A. Clearfield, *J. Solid State Chem.*, 1997, **132**, 213-223.

[3] G. Wallez, J.-P. Souron, M. Quarton, *Solid State Sci.*, 2006, **8**, 1061-1066.

[4] C. Masquelier, A. K. Padhi, K. S. Nanjundaswamy, J. B. Goodenough, *J. Solid State Chem.*, 1998, **135**, 228-234.

[5] H. Kessler, *Stud. Surf. Sci. Catal.*, 1989, **52**, 17.

[6] H. Kessler, *Mater. Res. Soc. Symp. Ser.*, 1991, **233**, 47.

[7] M. M. Eddy, T. E. Gier, N. L. Keder, G. D. Stucky, D. E. Cox, J. D. Bierlein, G. Jones, *Inorg. Chem.*, 1988, **27**, 1856-1858.

[8] N E Brese, M O'Keefe, *Acta. Cryst. B*, 1991, B**47**, 192-197.

[9] G. Socrates, *Infrared and Raman Characteristic Group Frequencies: Tables and Charts*, Third Edition, Wiley, 2006.

[10] L. Yu, W. Pang, L. Li, *J. Solid State Chem.*, 1990, **87**, 241-244.

[11] G. Férey, T. Loiseau, P. Lacorre, F. Taulelle, *J. Solid State Chem.*, 1993, **105**, 179-190.

[12] M. Wloka, S. I. Troyanov, E. Kemnitz1, *J. Solid State Chem.*, 1998, **135**, 293-301.

Chapter 5

Group IV and V Templated Frameworks

Nitrogen-containing templating cations have been used in the synthesis of framework materials since the 1960s. There are two important roles that these cations may perform; their size and shape can result in novel pore structures and also they only count for a relatively small proportion of the framework charge because they are usually far larger than a metal cation that would normally be present. As a result, the framework only has to have a low charge, thus meaning it will have a greater stability.

By using solvothermal synthesis techniques when producing hybrid open frameworks, where an inorganic framework contains an embedded organic unit, it meaning that a much larger range of structural types can be produced for each system[1]. When positively-charged organic starting materials are used, such as protonated amines or ammonium cations, the inorganic network condensates *via* weak electrostatic interactions between the inorganic and organic groups. This “templating effect” may give rise to the suggested larger variety of structures[2, 3].

The hydrothermal synthesis of $H_3NCH_2CH_2NH_3[In_2(HPO_4)_4]$ was achieved by using ethylenediamine (en) as template[4]. The en was in fact incorporated into the channels of the final, crystalline open-framework. The dicationic en ions were held in the centre of these channels by hydrogen-bonding to the phosphate oxygen atoms and they also charge-balance the overall structure. The final framework was rigid and stable in an ambient environment. Other templated structures have been reported, such as $AlPO_4$-20 where tetramethylammonium hydroxide (TMAOH) was used as a template, resulting in a sodalite framework topology with a template stoichiometry of around one unit per sodalite cage[5].

Due to an absence of templated arsenate and phosphates within the scope of this work, examples such as those above were used as guidance in the synthesis of novel frameworks. The new materials discussed in the following section which were characterised and were deduced to be layered structures with the template groups between the layers.

Solvothermal techniques have found to be the most successful routes to forming single crystals of new materials, and they are now the primary reaction technique employed in this chemistry. In order to try and promote the reactions, a fluoride source was used as a mineralising agent, by promoting crystallisation of the product. The primary analytical technique for these samples was X-ray single crystal diffraction, which was supplemented by other techniques, such as TGA, EDS and IR. These methods are discussed in the introduction into arsenate frameworks at the start of Chapter 3 and in greater detail in Chapter 2.

The reaction conditions for the successfully synthesised and characterised templated frameworks are shown below in Table 5.1. In a typical reaction, the starting materials were mixed and stirred briefly, then transferred to a 23 mL Parr hydrothermal bomb. The bomb was heated in an oven at the temperature and duration detailed in Table 5.1. The product in each case was retrieved by filtration under vacuum, washed with hot distilled water and dried in air. The following two reactions are a description and discussion of the new materials synthesised.

However, many of the reactions that were attempted in order to try and template materials did not result in the production of single crystals of novel materials. As may be seen in Table 4.1 in Chapter 4, there were a number of reactions that contained DABCO but where the template was not incorporated into the final structure. Table 5.1 below also shows one other reaction which produced single crystals but unfortunately these could not be analysed *via* single crystal diffraction. Other reaction conditions, such as different templates, including piperazine and tetramethylammonium chloride, generally resulted in either only starting materials being present as powders or glasses which could not be analysed.

Table 5.1: Reaction conditions for successful Group IV and V templated framework syntheses.

Starting materials	Temp. / °C	Reaction period / h	Type of single crystals produced	Product	Section in thesis
Titanium (III) fluoride (0.954 mmol, 0.100 g), ammonium dihydrogen phosphate (2.861 mmol, 0.329 g) and 1,4-diazabicyclo[2.2.2]octane (DABCO) (0.954 mmol, 0.107g) were dissolved in distilled water (10 cm^3). Starting pH = 6.3; final pH = 1.9.	140	240	Colourless sheet	$TiF_2(PO_4)$[DABCO-H]	5.1
Hafnium (IV) fluoride (0.393 mmol, 0.100 g), ammonium dihydrogen arsenate (0.73 mmol, 0.188 g) and 1,4-diazabicyclo[2.2.2]octane (DABCO) (0.393 mmol, 0.0441g) were dissolved in distilled water (10 cm^3). Starting pH = 5.2.	150	120	Colourless sheet	$[Hf_2F_8(AsO_4)]$[DABCO-H_2](NH_4)	5.2
Titanium (III) fluoride (0.954 mmol, 0.100 g), ammonium dihydrogen phosphate (2.861 mmol, 0.329 g) and 1,4-diazabicyclo[2.2.2]octane (DABCO) (0.954 mmol, 0.107 g) were dissolved in distilled water (10 cm^3). Starting pH = 9.0.	140	504	Minor phase of colourless needles within beige powder	Single crystals were twinned and could not be separated and by analysed *via* single crystal analysis.	

5.1-$TiF_2(PO_4)$[DABCO-H]

A colourless sheet-like crystal was selected for single crystal X-ray diffraction and the crystallographic information obtained is shown in Table 5.2. The framework has tetragonal symmetry and consists of TiF_2O_4 octahedra and PO_4 tetrahedra, which are connected *via* bridging oxygen atoms, where the polyhedra are corner-sharing, as seen in Figure 5.1. The bond lengths within these polyhedra are shown in Table 5.3, along with those in the $[DABCO\text{-}H]^+$ groups. These polyhedra form four-membered rings, made up of two TiF_2O_4 octahedra and two PO_4 tetrahedra. These rings then extend to form chains along both the *b*- and c-axes, resulting in a two-dimensional layer. Between these layers, $[DABCO\text{-}H]^+$ groups are located and these are discussed in more detail later on.

Table 5.2: Crystal data for $TiF_2(PO_4)$[DABCO-H].

Chemical Formula	$TiF_2(PO_4)$[DABCO-H]		
Crystal Appearance	Colourless sheet	T/ K	120
Crystal Size/ mm	0.2 x 0.2 x 0.01	λ/Å	0.71073
M	294.01607	Reflections collected	2026
Crystal System	Tetragonal	Unique reflections	273
Space Group	*I*4/*mmm*	R_{int}	0.0349
a, *b*, *c*/ Å	6.3059(3), 6.3059(3), 17.8492(2)	$R_1[I > 2\sigma(I)]^a$	0.0447
α, β, γ / °	90.000(0), 90.000(0), 90.000(0)	*R*1(all data)	0.0464
V/ Å^3	709.76(1)	wR_2(all data)	0.1304
Z	4		

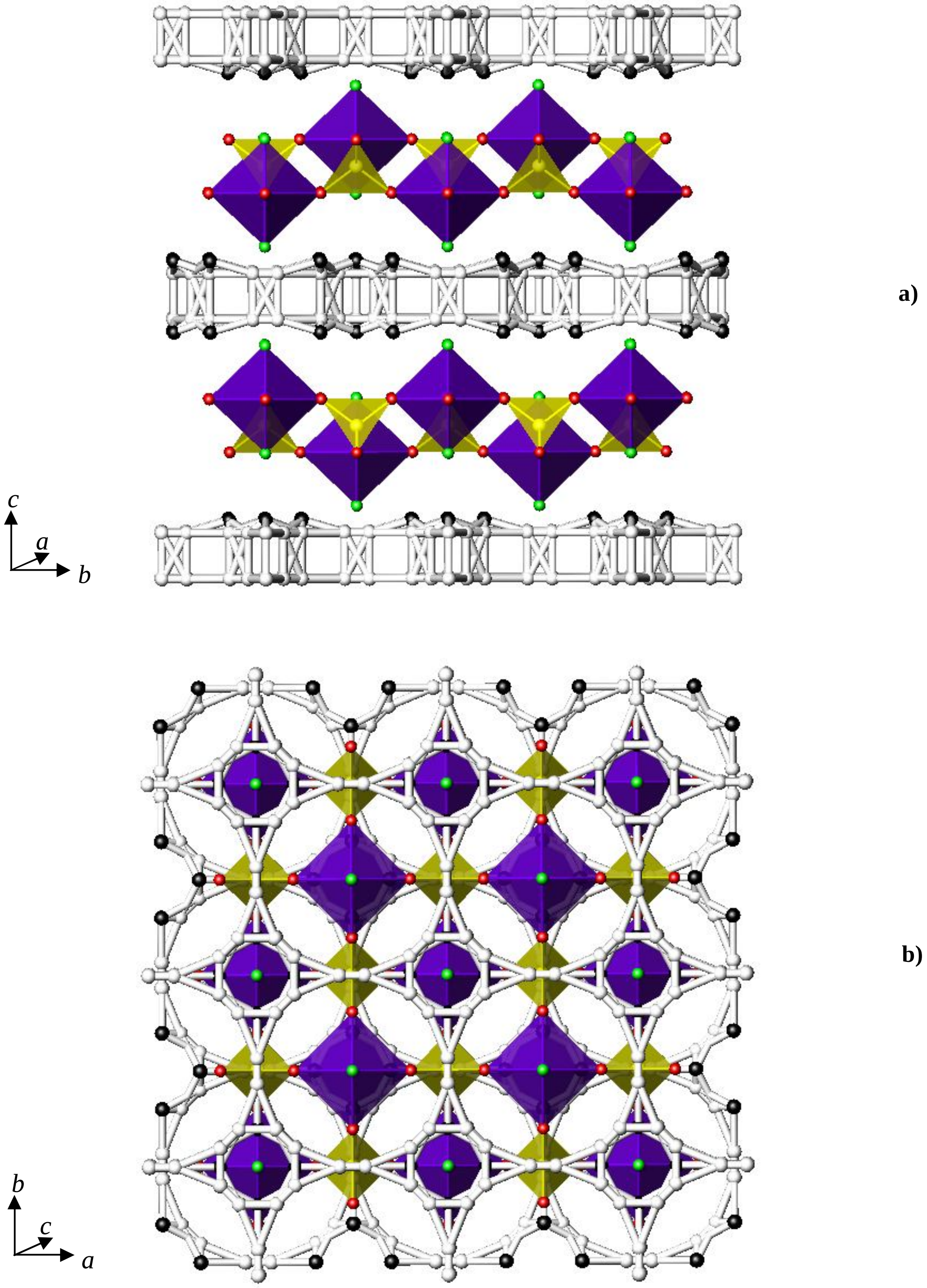

Figure 5.1: Structure of $TiF_2(PO_4)$[DABCO-H] viewed down the a) *a*- and c) *c*-axes, where the titanium octahedra are shown in purple, the phosphate tetrahedra in yellow, the oxygen atoms in red and the DABCO-H units as black and white.

Table 5.3: Bond lengths in $TiF_2(PO_4)$[DABCO-H].

Bond	Bond length/ Å	Bond	Bond length/ Å
Ti1–O1	1.934(3)	N1–C3	1.53(3)
Ti1–F1	1.840(6)	N1–C4	1.465(19)
Ti1–F2	1.865(6)	C3–C3	1.58(4)
P2–O1	1.526(3)	C3–C4	1.61(3)
		C4–C4	1.21(4)

Within each of the octahedra, all four of the oxygen atoms are bridging to the neighbouring phosphate groups, building up the layers as mentioned above. EDS confirmed semi-quantitatively that there was fluorine within this material but at a considerably lower percentage than the amount of oxygen. The thermal parameters in the single crystal refinement and bond valence calculations[6] were used to locate these fluorine atoms. The bond valence values are given in Table 5.4. The two fluorine atoms exist at the axial points of each octahedron and are terminal. As shown in Table 5.4, the two fluorine sites would be underbonded if refined as oxygen atoms. The presence of these fluorine atoms results in the termination of chains along this direction, resulting in a layered structure. These axial sites cause the fluorine atoms to be directed into the cavities between the layers of the polyhedra and thus are able to interact with the $[DABCO\text{-}H]^+$ units *via* hydrogen bonding. The hydrogen bonding seen here is discussed in more detail later on. These fluorine atoms are ≈ 2.6 Å from the nitrogen atoms of the $[DABCO\text{-}H]^+$ cations, thus being too close for a hydroxyl group to be present rather than the fluorine atom, again supporting the existence of fluorine atoms on these sites.

In the PO_4 units, all four of the oxygen atoms bridge to neighbouring titanium polyhedra, making each phosphate group fully coordinated. The result is the presence of two-dimensional layers of polyhedra in this structure, as previously mentioned. These layers are shown in Figure 5.1.

Table 5.4: Bond lengths and bond valence calculations for TiF_2O_4 octahedra.

Atom	Ti–O/F bond length/ Å	P–O/F bond length/ Å	Bond valence
O1	1.934(3)	1.526(3)	2.01
O1	1.934(3)	1.526(3)	2.01
O1	1.934(3)	1.526(3)	2.01
O1	1.934(3)	1.526(3)	2.01
F1	1.840(6)	N/A	0.81
F2	1.865(6)	N/A	0.75

As previously indicated, $[DABCO\text{-}H]^+$ units are present between the layers of polyhedra. The nitrogen atoms were fully refined, with the carbon atoms being disordered over several sites. After full refinement of the $[TiF_2(PO_4)]^-$ layers, the template unit must be described as having one hydrogen atoms per DABCO unit, in order for the overall formula to charge balance correctly, thus giving $[DABCO\text{-}H]^+$. However, it was not possible to locate the hydrogen atom during the single crystal refinement. These $[DABCO\text{-}H]^+$ structures are held in place within the structure by hydrogen bonds that form between the fluorine atoms of the layers and the hydrogen atom of the $[DABCO\text{-}H]^+$ cation, which is thought to be disordered between the two nitrogen atoms in each $[DABCO\text{-}H]^+$ unit. As may be seen in Figure 5.1, the polyhedral layer alternates in the direction in which it faces, meaning that a large enough “cavity” between the layers exists, so that the $[DABCO\text{-}H]^+$ cations may be positioned within this space. As depicted in Figure 5.2, alternate polyhedral fluorine atoms (F2) are close enough to the disordered hydrogen atoms in order that they may form hydrogen bonds. The remaining fluorine atoms (F1) are directed towards the C–C bridging sections of the interlayer species so they are therefore too far away (≈ 3.7 Å) from where the N–H bonds would be for any hydrogen bonding to occur. The likely direction for these hydrogen bonds is shown in Figure 5.2. These hydrogen bonds exist between F2 and the single disordered hydrogen atom on each $[DABCO\text{-}H]^+$ unit, as supported by the

TGA data that was collected for this material. This data suggested that the structure started to break down at around 570 °C, with a mass loss of 4.99 %, which corresponds to $[DABCO\text{-}H]^+$. This is not a very high temperature for the decomposition of such a material, which results from the weak hydrogen bonding causing a lower thermal stability of this material. Once the interlayer species has been lost from this structure, it appears that the framework is thermally unstable and does not require much more energy for its decomposition to start.

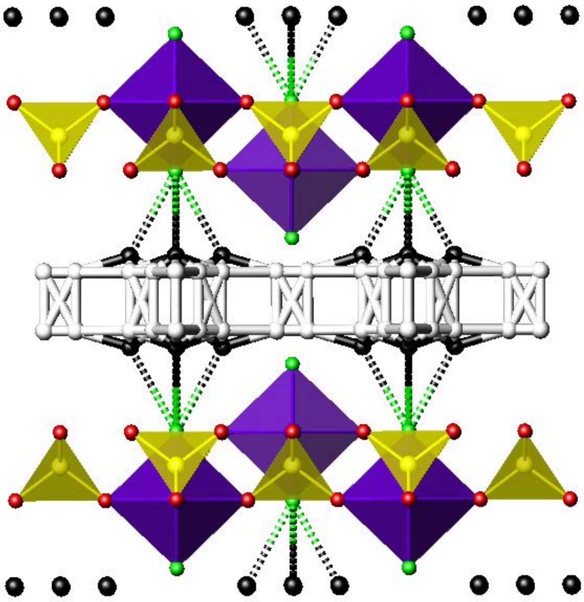

Figure 5.2: Hydrogen bonding between the fluorine atoms and the DABCO-H units in $TiF_2(PO_4)$[DABCO-H].

During the EDS data collection, an SEM image of $TiF_2(PO_4)$[DABCO-H] was recorded and is shown in Figure 5.3. Due to the N–H bonds in the disordered DABCO-H units, there is a broad IR absorption seen at 3529-3343 cm^{-1}. This band is only a little lower than usually expected due to the small amount of hydrogen bonding between the fluorine atoms and the DABCO-H. An N–H bend is represented by an absorption peak at 1411 cm^{-1}. At 2842 cm^{-1}, there is a peak present due to the C–H bonds in the DABCO-H groups and stretch may be observed at 1057-861 cm^{-1} which is due to the P–O stretches[7].

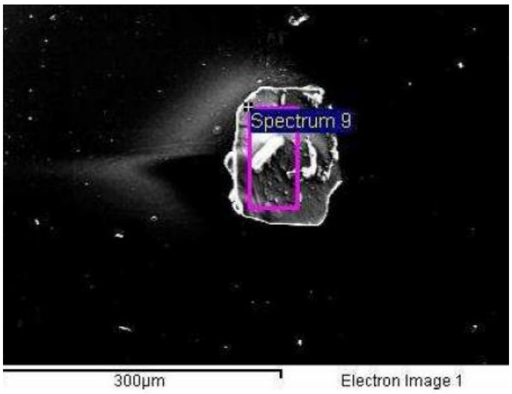

Figure 5.3: SEM image $TiF_2(PO_4)$[DABCO-H].

5.2-[$Hf_2F_8(AsO_4)$][DABCO-H_2](NH_4)

A colourless sheet-like single crystal was selected for single crystal X-ray diffraction and the crystallographic data collected are shown in Table 5.5. The framework exhibits orthorhombic symmetry and consists of alternating HfF_4O_2 octahedra, where the two oxygen atoms are equatorial, and AsO_4 tetrahedra, as seen in Figure 5.4. These alternating octahedra and tetrahedra exist as corner-sharing units in a “zig-zag” chain along the *a*-axis, as seen in Figure 5.4. Bridging oxygen atoms connect the polyhedra connect to one another and it can be seen that all of the oxygen atoms in this structure are in fact bridging. Their bond lengths, and all of the other within the structure are given in Table 5.6.

When viewed down the *b*-axis, it can be seen that the AsO_4 tetrahedra are fully coordinated to four different hafnium polyhedra, resulting in a rigid, layered structure. Of the two different hafnium environments within this framework, one exists as regular hafnium-centred HfF_4O_2 octahedra. However, the other octahedral environment exhibits partial occupancy of one of the fluorine atoms. Of the four terminal fluorine atoms, one (F9), is partially occupied over two sites, with approximately equal occupancy over each. These fluorine sites are all terminal, resulting in the termination of a three-dimensional structure but causing the formation of chains. However, both of these sites are shown in the diagrams for clarity, causing the hafnium polyhedra to appear as seven-coordinate, rather than the true six-coordinate. The two oxygen atoms within each hafnium-centred octahedron are both on equatorial sites and are adjacent to one another. They form bridges to the neighbouring arsenate groups, forming four-membered rings and thus the previously mentioned chain down the *a*-axis.

Table 5.5: Crystal data for $[Hf_2F_8(AsO_4)][DABCO\text{-}H_2](NH_4)$.

Chemical Formula	$[Hf_2F_8(AsO_4)][DABCO\text{-}H_2](NH_4)$
Crystal Appearance	Colourless sheet
Crystal Size/ mm	0.2 x 0.2 x 0.02
M	780.11377
Crystal System	Orthorhombic
Space Group	*Ama*2
a, b, c/ Å	9.4029(5), 17.2052(9), 9.9334(4)
α, β, γ / º	90.000(0), 90.000(0), 90.000(0)
V/ Å^3	1607.01(1)
Z	8
T/ K	120
λ/Å	0.71073
Reflections collected	6450
Unique reflections	1826
R_{int}	0.0277
$R_1[I > 2\sigma(I)]^a$	0.0752
$R1$(all data)	0.0763
wR_2(all data)	0.2067

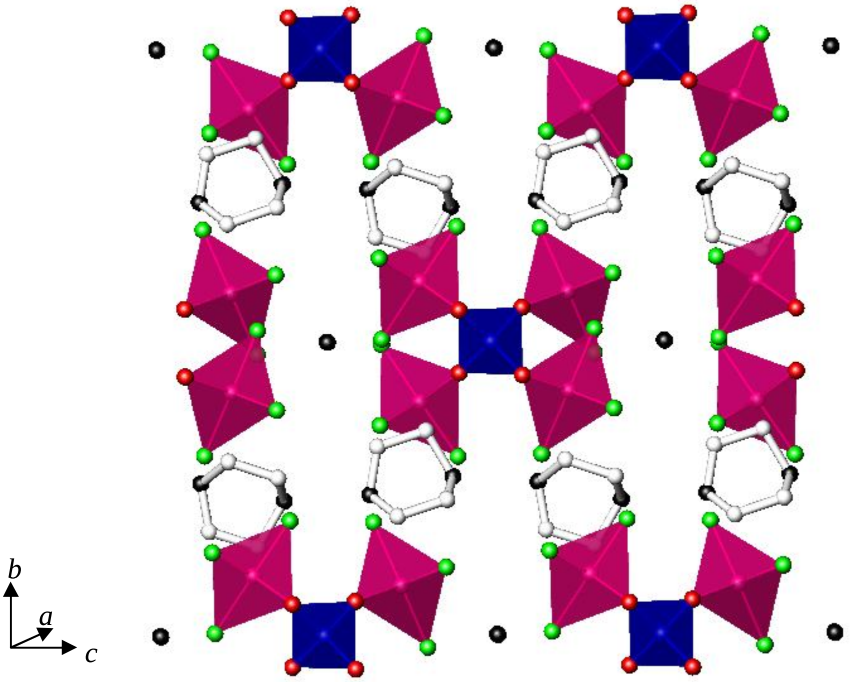

a)

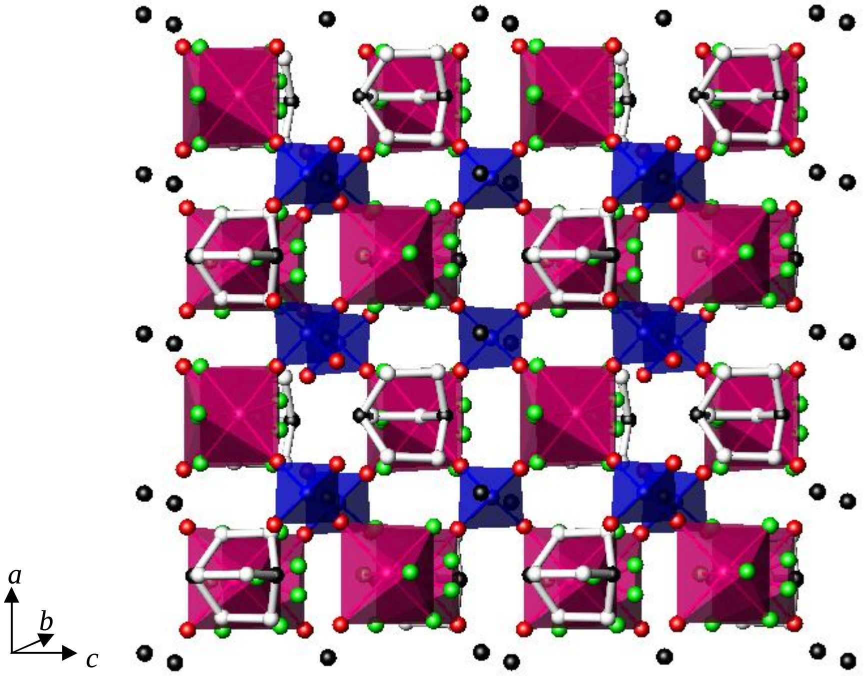

b)

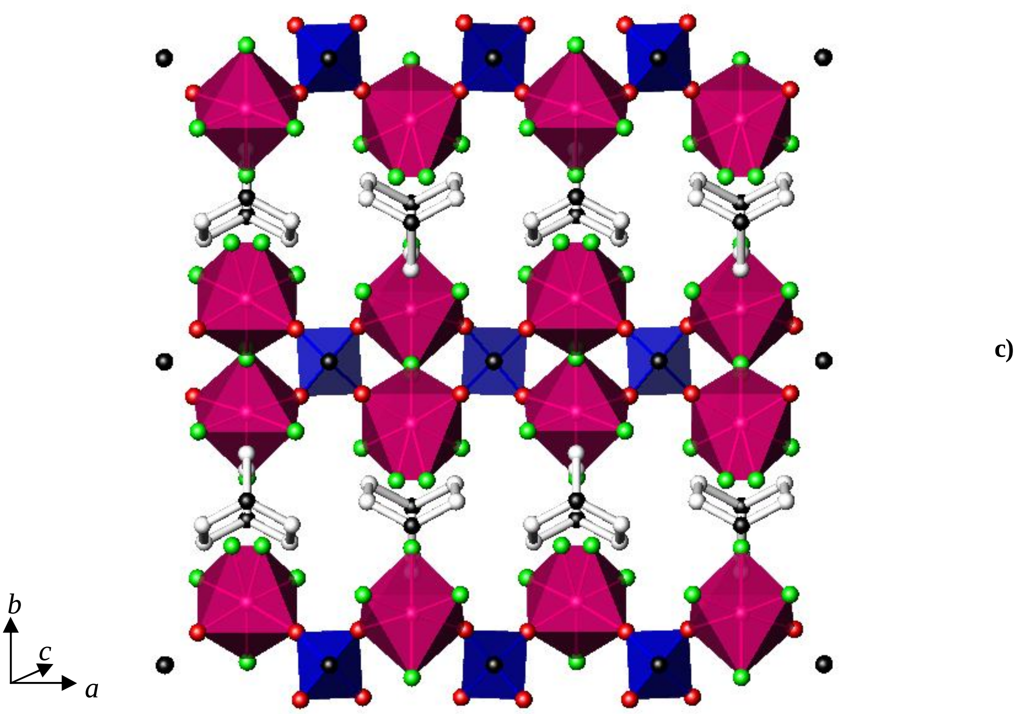

Figure 5.4: Structure of $[Hf_2F_8(AsO_4)][DABCO\text{-}H_2](NH_4)$ viewed down the a) *a*-, b) *b*- and c) *c*-axes, where the hafnium octahedra are shown in magenta, the arsenate tetrahedra in blue, the oxygen atoms in red, the fluorine atoms in green, the ammonium cations as black spheres to represent the nitrogen and the DABCO-H_2 units in black and white.

Table 5.6: Bond lengths in $[Hf_2F_8(AsO_4)][DABCO\text{-}H_2](NH_4)$.

Bond	Bond length/ Å	Bond	Bond length/ Å	Bond	Bond length/ Å
Hf1–O7	2.09(3)	Hf2–O8	2.01(5)	As3–O7	1.58(3)
Hf1–O7	2.09(3)	Hf2–O8	2.01(5)	As3–O7	1.58(3)
Hf1–F1	1.96(3)	Hf2–F3	2.03(3)	As3–O8	1.62(4)
Hf1–F2	1.99(2)	Hf2–F4	1.97(2)	As3–O8	1.62(4)
Hf1–F2	1.99(2)	Hf2–F4	1.97(2)	N1–C3	1.45(4)
Hf1–F5	2.03(3)	Hf2–F9	1.99(3)	N1–C4	1.55(7)
				N2–C1	1.60(6)
				N2–C2	1.43(9)
				C1–C3	1.53(4)
				C2–C4	1.51(8)

After full refinement of the $[Hf_2F_8(AsO_4)]^{3+}$ layers, single crystal analysis also indicated that there were species present between these layers. These small units were determined to be ammonium and $[DABCO\text{-}H_2]^{2+}$ cations, which were also required in order for the overall structure to be fully charge-balanced. However, the assumption must be made that the fluorine atoms have been correctly assigned within the $[Hf_2F_8(AsO_4)]^{3+}$ layers. EDS analysis showed semi-quantitatively that there were both oxygen and fluorine present in this structure but with a greater percentage of fluorine than oxygen. The octahedra is this structure were found to only bridge *via* two points (oxygen atoms) per octahedron and the other octahedral, terminal atoms were found to all be fluorine atoms, which are all in a similar environment, giving a greater percentage of fluorine atoms than oxygen. An SEM image of a single crystal of $[Hf_2F_8(AsO_4)][DABCO\text{-}H_2](NH_4)$ was recorded during the EDS analysis and is shown in Figure 5.5. Bond valence calculations[6] were also carried out and supported the presence of these fluorine atoms, as opposed to the presence of, for example, a water molecule. The calculated values are given in Table 5.7 but in calculating the bond valence sums, it was necessary to take the partially occupied fluorine atoms into account and when this was done, the two hafnium environments were calculated to be fully bonded. The values given in this table show that those sites which were refined as fluorine atoms would be underbonded if refined as oxygen atoms instead. As Table 5.7 indicates, these sites are an average of 2.70 Å from the nearest nitrogen atom within the $[DABCO\text{-}H_2]^{2+}$ units, which is too close for these sites to be hydroxyl groups. Therefore these sites were confirmed to be fluoride atoms. IR spectroscopy also supported the presence of the NH_4^+ and $[DABCO\text{-}H_2]^{2+}$ cations. A broad IR absorption was seen at 3414-3181 cm^{-1}, which may be assigned to the N–H bonds in the hydrogen-bonded ammonium cations. A further absorption due to the N–H bend in the ammonium cations is present at 1648 cm^{-1}.

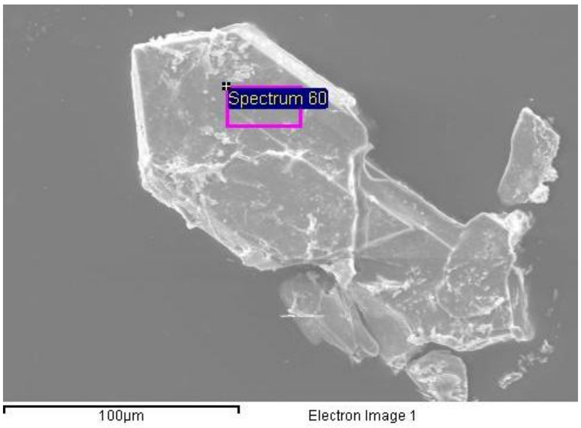

Figure 5.5: SEM image $[Hf_2F_8(AsO_4)][DABCO\text{-}H_2](NH_4)$.

Table 5.7: Bond lengths and bond valence calculations for HfF_4O_2 octahedra.

Atom	Hf–O/F bond length/ Å	As–O/F bond length/ Å	Bond valence
F1	1.96(3)	N/A	0.74
F2	1.99(2)	N/A	0.69
F3	2.03(3)	N/A	0.62
F4	1.97(2)	N/A	0.71
F5	2.03(3)	N/A	0.61
F9	1.99(3)	N/A	0.68
O7	2.09(3)	1.58(3)	1.72
O8	2.01(5)	1.62(4)	1.78

The ammonium cations are present in the gaps between the layers of chains of four-membered rings, running along the *a*-axis. It was apparent that the $[DABCO\text{-}H_2]^{2+}$ units also exist in interlayer spaces but in the direction of the *c*-axis. Neither the ammonium or DABCO-H_2 cations directly bond to the framework but are held in place by intramolecular, hydrogen bonding. Although it was not possible to locate the hydrogen atoms, Figure 5.6 shows the probable direction of the hydrogen bonding between the nitrogen atoms in the ammonium and DABCO-H_2 groups and the polyhedral fluorine atoms, thus suggesting the likely direction along which the hydrogen atom positions would be present. As depicted in the diagram, the two hydrogen atoms in each $[DABCO\text{-}H_2]^{2+}$ unit are most likely to be present in an expected orientation, with regards to the main DABCO structure, thus being directed towards to hydrogen-bonded fluorine atoms. It may also be seen that the four hydrogen atoms of each ammonium cation are tetrahedrally arranged, as would be expected if the hydrogen atoms had been allocated. Table 5.8 summarises the likely hydrogen bonding within this material.

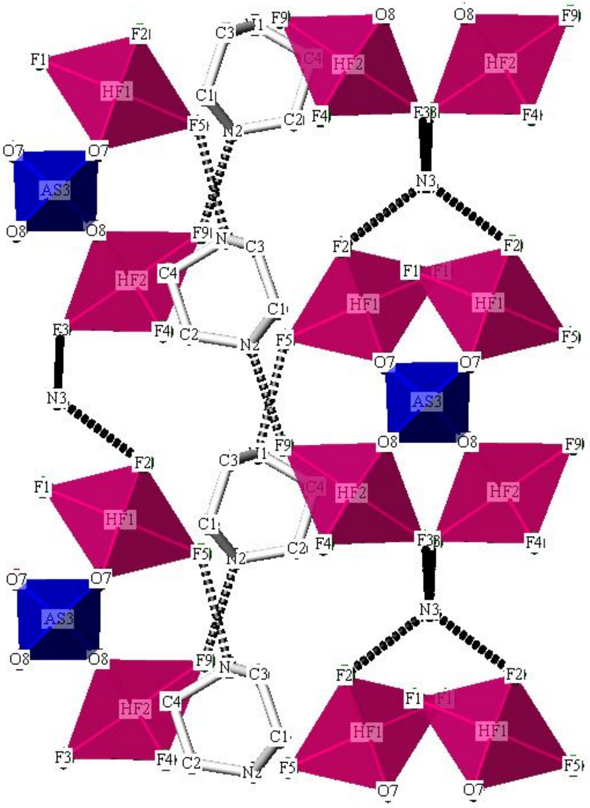

Figure 5.6: Hydrogen bonding between the ammonium and DABCO groups and the polyhedral fluorine atoms in $[Hf_2F_8(AsO_4)][DABCO\text{-}H_2](NH_4)$ with the hydrogen bonding shown as black dotted lines.

Table 5.8: Hydrogen bonding of $[Hf_2F_8(AsO_4)][DABCO\text{-}H_2](NH_4)$, (where *d* = distance between stated atoms and *A* = acceptor).

N - - A	d(N - - A)/ Å
N1 - - F5	2.70
N2 - - F9	2.51
N3 - - F2	2.67
N3 - - F2	2.67
N3 - - F3	2.85
N3 - - F3	2.85

Data from TGA is shown in Figure 5.7 and suggests that there were the appropriate mass losses for both the ammonium and $[DABCO\text{-}H_2]^{2+}$ cations to be present in this structure. These two interlayer species required different amounts of thermal energy to be removed from the framework, with the ammonium cation being lost first, at around 255 °C, when a mass loss of 2.31 % was observed, showing a relatively low thermal stability for this type of templated material. The DABCO-H_2 unit was then lost as one entity but required the higher temperature of approximately 380 °C in order for this to occur, with an appropriate mass loss of 14.64 %. This need for a higher temperature indicates that there is stronger hydrogen bonding between the $[DABCO\text{-}H_2]^{2+}$cations and the fluorine atoms than is present between the fluorine atoms and the ammonium cations. Figure 5.7 shows that a further large mass was lost at approximately 425 °C, which is due to the layered structure beginning to break down, with the loss of a mass of 17.81 %, which is equivalent to AsO_4^{3-}.

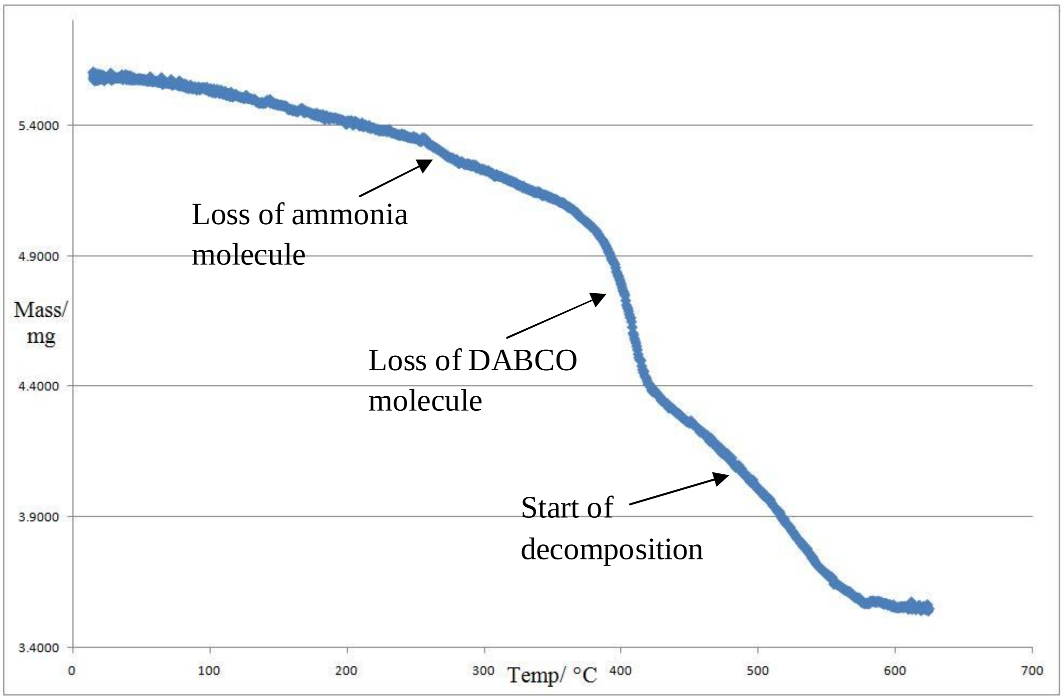

Figure 5.7: TGA for $[Hf_2F_8(AsO_4)][DABCO\text{-}H_2](NH_4)$, with the mass losses for both NH_4^+ and $DABCO\text{-}H_2$ shown.

5.3-Conclusions for Group IV and V Templated Frameworks

Organic amines have been used in the synthesis of framework materials since the 1960s, where their primary purpose was to make the reaction mixture more basic. However, it was commonly found that these nitrogen-containing compounds were present in the final framework structure, as was the case in the two novel frameworks presented here: $TiF_2(PO_4)$[DABCO-H] and $[Hf_2F_8(AsO_4)]$[DABCO-H_2](NH_4). This was also the case in the synthesis of $AlPO_4$-20, where tetramethylammonium hydroxide (TMAOH) was used as a template[5]. This aluminum phosphate has a neutrally-charged zeolite topology, meaning that the templating agent was not required to charge-balance the material but stabilised the large void within the structure. Until now, there has been a noticeable lack of templated frameworks for Groups IV and V, so therefore the discussion of these two materials opens up an interesting area with regards to stable, templated framework structures.

The nature of the templating agents used within the experiments discussed in this chapter meant that only low temperature reaction conditions could be used. In the case of DABCO, as used in the above successful syntheses, the structure starts to decompose at 156 °C, meaning that temperatures below this value must be used in order to potentially incorporate DABCO into a framework. As a result, it appeared that many of the attempted reactions did not progress as would have been expected, due to the required activation energy not being achieved, and only the starting materials were present after the powder samples had been filtered and dried. This was even found to be the case when the reaction mixtures were heated for a prolonged length as time, such as 336 h in one of the DABCO reactions, but TiF_3 and HfF_4 appear to be more reactive, allowing the above reactions to have progressed, as was also the case when comparing the phosphate frameworks discussed in Sections 4.1 and 4.2. All of the different templating agents that were investigated were also found to be susceptible to strongly acidic or basic conditions, causing these series of reactions, for each of the Group IV and V metals, to be unsuccessful in the production of single crystals.

Both of the frameworks that were synthesised and characterised in this chapter were produced under hydrothermal conditions, with the DABCO causing the final reaction mixture to be only very slightly acidic, almost neutral in comparison with the other, non-templated reactions in this work. A mineralising fluoride source was once again used in order to promote the reaction and resulted in fluorine being present in both of the final frameworks.

The layered structure of $TiF_2(PO_4)$[DABCO-H] was made up of TiF_2O_4 octahedra and PO_4 tetrahedra in a four-membered ring formation. These rings extend along the *b*-axis to form a chain, with the terminal fluorine atoms being directed into the interlayer spaces. The fluoride groups also ensure that the structure of $TiF_2(PO_4)$[DABCO-H] is two-dimensional rather than three-dimensional, where their positions cause the termination of a chain along this axis, preventing a three-dimensional framework to build up. The disordered $[\mathrm{DACBO\text{-}H}]^+$ cations were determined to be located within the spaces between the layers of this material, with the carbon and hydrogen atoms being disordered, where the hydrogen atom is thought to be disordered between the two nitrogen atoms in each DABCO-H unit. There is hydrogen bonding present between this disordered N–H bond and the polyhedral fluorine atoms but it will be weak due to the presence of only one disordered hydrogen atom on each DABCO-H unit. The relatively weak hydrogen bonding seen here will result in a lower thermal stability of this material than expected but it is still stable up to 570 °C, as suggested by the TGA data.

The main framework of the layered structure $[Hf_2F_8(AsO_4)][\mathrm{DABCO\text{-}H_2}](NH_4)$ consists of HfF_4O_2 octahedra and AsO_4 tetrahedra, which form a “zig-zag” chain along the *a*-axis. Viewed down the *b*-axis, it is apparent that the AsO_4 groups are fully bonded to four different hafnium polyhedra, resulting in a rigid, layered structure. However, the hafnium-centred octahedra are not fully coordinated due to the terminal fluorine atoms, preventing the building up of a three-dimensional network. Within this material, ammonium cations were found to be present in addition to $[\mathrm{DABCO\text{-}H_2}]^{2+}$ cations. Both of these units exist in the interlayer spaces and form hydrogen bonds to the polyhedral fluorine atoms. TGA pointed to the two different interlayer species being removed from the structure at different temperatures, with the ammonium cations being lost first at 255 °C. The DABCO-H_2 unit required the higher temperature of approximately 380 °C in order to be removed from the structure. The good thermal stability of this material due to its templated nature means that ion exchange with the ammonium atoms may be possible without the framework collapsing on their removal, where the main structure only starts to decompose at 425 °C. Due to the existence of only one ammonium cation per formula unit, this exchange would be small but also more likely to be possible without structural collapse.

These materials have shown potential for possible ion exchange properties. There is potential for larger cations to be exchanged into the cavities of the structures, due to the dimensions of the DABCO units currently present, as well as the ammonium cation in $[Hf_2F_8(AsO_4)][DABCO\text{-}H_2](NH_4)$. This material appears to offer particularly interesting potential in this area as a consequence of its thermal stability once the interlayer cations have been removed from the structure but this would need to be investigated further.

5.4-References

---

[1] M. J. Rosseinsky, *Micro. And Meso. Mater.*, 2004, **73**, 15-30.

[2] G. Férey, *C. R. Acad. Sci. Paris*, 1998, **1**, 1-13.

[3] P. J. Hagrman, D. Hagrman, J. Zubieta, *Angew. Chem. Int. Ed.*, 1999, **38**, 2638-2684.

[4] S. S. Dhingra, R. C. Haushalter, *J. Chem. Soc. Chem. Commun.* 1993, 1665-1667.

[5] A. K. Cheetham, G. Férey, T. Loiseau, *Angew. Chem. Int. Ed.*, 1999, **38**, 3269-3292.

[6] N. E. Brese, M O'Keefe, *Acta. Cryst. B*, 1991, B**47**, 192-197.

[7] G. Socrates, *Infrared and Raman Characteristic Group Frequencies: Tables and Charts*, Third Edition, Wiley, 2006.

Chapter 6

Iron Phosphate Materials

There are already many known iron phosphate frameworks, both natural and synthetic. Over recent years, this family of oxoframework materials has been of considerable interest due to their small channels with potential ion exchange and magnetic properties, such as $NaFe_2(PO_4)(HPO_4)$[1]. This synthetic, complex iron phosphate hydrogen-phosphate was prepared under hydrothermal conditions and has been shown to possess antiferromagnetic interactions.

A great deal of the early work on synthetic iron phosphates focused on mineral-like compounds that were templated by alkali metals. Two such materials were the caesium-templated framework $CsFe_3(PO_4)_3(H_2O)_2$[2] and the sodium-templated $Na_7Fe_4(PO_4)_6$[3]. More recent work has been primarily aimed at hybrid organic-inorganic frameworks. There are literature examples of iron phosphate structures which incorporate organic sub-units such as oxalate[4] and bipyridyl[5] ions.

One of the most recent uses of these materials to be investigated is within the area of rechargeable lithium batteries[6, 7, 8], where they may potentially be used as either the anode[9] or the cathode[10]. In order for a material to be viable as a potential rechargeable battery, the starting materials in its synthesis must be inexpensive and have low toxicity, as is the case for $LiFePO_4$, where the starting materials are also naturally abundant. Several synthetic routes have been investigated with the aim to optimise the properties of this material; including direct solid state methods[11], hydrothermal syntheses[12] and sol-gel reactions[11].

Over one hundred natural iron phosphates have been structurally characterised and many of these have also acted as a basis for the synthesis of synthetic iron phosphates, where specific properties are desired; such as $LiFePO_4$, a member of the olivine-type family. The oxoframework has interesting properties as a rechargeable battery material, as briefly mentioned above, with a cell voltage of 3.5 V[13]. $LiFePO_4$ exists as a natural mineral but may be produced synthetically by reaction of $Li(OH)\cdot H_2O$ with H_3PO_4 at high temperature[14], followed by the addition of an alcoholic solution of iron (III) acetylacetonate. There are also several other iron phosphate minerals which have been well-documented[15], such as barbosalite, $Fe_3(PO_4)_2(OH)_2$[16, 17], to the more complex, lipscombite solid solution, which includes $Fe_{1.176}(PO_4)(OH)_{0.57}(H_2O)_{0.43}$[18]. It has been concluded that the structure of lipscombite can contain mixed valence iron structures, when analysed *via* by powder X-ray diffraction.

The original aim of the work presented here was to produce complex iron phosphate materials, containing hybrid organic-inorganic groups. It was hoped that iron phosphates could be synthesised that contained oxalate and methylboronic groups. As well as straightforward syntheses, this was also attempted using templating agents such as piperazine and DABCO. Although the synthesis of these complex iron phosphates was not achieved, simple but novel iron phosphates were produced and are discussed herein. The presence of cavities within this type of framework is currently of considerable interest due to their potential use as a precursor to battery materials or for lithium insertion reactions. During this study, a further material was produced and was found to be a synthetic lipscombite. Although the structure of this mineral has been characterised *via* both its natural and synthetic analogues, there has not previously been a single crystal structure of a synthetic lipscombite reported.

Many other reactions were carried out by varying the reaction conditions, such as reaction temperature, reaction duration and starting materials themselves. The reaction conditions for the successfully synthesised and characterised phosphate frameworks are shown below in Table 6.1, as are those reactions which produced single crystals but of materials that were not novel. Many other reactions, (in the region of 50), were attempted by varying the reaction conditions but resulted in the production of powders of either known iron phosphates, of which there are many both synthetic and natural known structures, or simply a mixture of the starting materials. In a typical reaction, the starting materials were mixed and stirred briefly, then transferred to a 23 mL Parr hydrothermal bomb. The bomb was heated in an oven at the temperature and duration detailed in Table 6.1. The product in each case was retrieved by filtration under vacuum, washed with hot distilled water and dried in air. The following reactions in this chapter are a description and discussion of the new materials synthesised.

Table 6.1: Reaction conditions for iron phosphate materials.

Starting materials	Temp. / °C	Reaction period / h	Type of single crystals produced	Product	Section in thesis
Iron (II) oxalate dihydrate (1.11 mmol, 0.200 g), orthophosphoric acid (2.50 mmol, 0.245 g) and piperazine (1.09 mmol, 0.0941 g) were dissolved in distilled water (4.006 g). Starting pH = 2.5.	200	48	Pale green sheet	$Fe_2O(HPO_4)$	6.1
Iron (III) chloride (1.23 mmol, 0.200 g), methylboronic acid (3.29 mmol, 0.197 g) and orthophosphoric acid (6.77 mmol, 0.663 g) were combined and dissolved in distilled water (10 cm^3). Starting pH altered to 1.5 with concentrated ammonia solution.	170	168	Pale green block	$(NH_4)_3Fe_3(HPO_4)_6$	6.2
Iron (III) nitrate nonahydrate (0.495 mmol, 0.200 g), methylboronic acid (2.31 mmol, 0.138 g), 1,4-diazabicyclo[2.2.2]octane (0.990 mmol, 0.111 g) and orthophosphoric acid (1.16 mmol, 0.114 g) were combined and the volume was made up to 10 cm^3 with distilled water. This solution was stirred for 2 h at 60 °C. Starting pH altered to 7.0 with concentrated ammonia solution.	170	72	Mixture of black octahedral star-shaped single crystals and pale green powder, (an unidentified minor second phase).	$Fe_{1.34}(PO_4)OH_{0.96}$	6.3
Iron (II) oxalate dihydrate (1.11 mmol, 0.200 g), orthophosphoric acid (2.50 mmol, 0.245	160	72	Orange needle	$Fe_3(HPO_4)(H_2O)_4$	[19]

g) and distilled water (1.95 mmol, 0.0350 g) were combined and stirred together.	200	48			
Iron (II) oxalate dihydrate (1.11 mmol, 0.200 g), orthophosphoric acid (2.50 mmol, 0.245 g) and piperazine (1.09 mmol, 0.0941 g) were dissolved in distilled water (4.006 g).	160	24	Minor phase of colourless sheets within a major phase of brown powder	Oxalic acid: $H_2C_2O_4\cdot 2H_2O$	
Iron (II) oxalate dihydrate (1.11 mmol, 0.200 g) and ammonium dihydrogen phosphate (3.34 mmol, 0.384 g) were dissolved in distilled water (10 cm^3). Starting pH = 4.3.	150	24	Minor phase of yellow blocks within majority phase of yellow powder	Starting material: $Fe(C_2O_4)\cdot H_2O$	
Iron (II) oxalate dihydrate (1.11 mmol, 0.200 g) and ammonium dihydrogen phosphate (1.11 mmol, 0.128 g) were dissolved in distilled water (10 cm^3). Concentrated ammonia solution added to adjust the pH to 7.4.	150	24	Dark yellow-green needles within a major brown powder phase	Humboldtine: $Fe(C_2O_4)\cdot H_2O$	[20, 21]
Iron (II) oxalate dihydrate (1.11 mmol, 0.200 g) and ammonium dihydrogen phosphate (1.11 mmol, 0.128 g) were dissolved in distilled water (10 cm^3). Concentrated ammonia solution added to adjust the pH to 9.0.	140	48	Minor phase of pale yellow sheets within green powder	$Fe_4(OH)_3(PO_4)_3$	[22]

Iron (II) oxalate dihydrate (1.11 mmol, 0.200 g) and ammonium dihydrogen phosphate (1.11 mmol, 0.128 g) were dissolved in distilled water (10 cm^3). Concentrated ammonia solution added to adjust the pH to 9.0.	150	72	Yellow sheets within majority phase of yellow-green powder	$Fe_4(PO_4)(C_2O_4)(H_2O)_2$	[23]
Iron (III) nitrate nonahydrate (1.23 mmol, 0.200 g), methylboronic acid (3.29 mmol, 0.197 g) and orthophosphoric acid (6.77 mmol, 0.663 g) were dissolved in distilled water (10 cm^3). Concentrated ammonia solution was added to adjust the pH to 1.7.	170	168	Green sheets within a major phase of beige powder	$Fe_2(NH_4)(OH)(PO_4)(H_2O)_2$	[24]

6.1-$Fe_2O(HPO_4)$

A pale green needle-like single crystal was selected for single crystal X-ray diffraction and a summary of the crystallographic information is shown in Table 6.2. The framework possesses monoclinic symmetry and contains four different iron environments, each of which is a strongly distorted $Fe(II)O_6$ octahedron, as shown in Figure 6.1, where Fe–O = 1.9–2.3 Å. These bond lengths are given in Table 6.3, along with all of the P–O bond lengths. These octahedra share non-adjacent edges forming an infinite, zig-zag chain parallel to the *c*-axis direction, as shown in Figure 6.1. Two of the oxygen atoms in each octahedron link to phosphorus atoms of the hydrogen phosphate, (HPO_4), tetrahedra and there are two unique phosphate groups, one of which, based on P6, bridges the chains of FeO_6 octahedra, as seen in Figure 6.2. Also shown in this diagram is a small cavity formed between these linked chains.

The closest cross-cavity O - - O distance is 3.42 Å, between O1 of an $HP(6)O_4$ tetrahedron and O16 of an FeO_6 octahedron. The hydrogen atoms of the two different HPO_4 units, which could not be located in the structure determination, are likely to be sited on the terminal oxygen atoms, O1 and O3, which are directed towards the centre of the cavities. This is supported by bond valence calculations[25]. Moderately strong hydrogen bonds, with O (donor) - - O (acceptor) distances of 3.02 and 2.83 Å, are present between these hydroxyl groups and the oxygen atoms located opposite, O16 and O8 respectively. The likely directions of these hydrogen bonds lie across the main cavities, as shown in Figures 6.3.

Table 6.2: Crystal data for $Fe_2O(HPO_4)$.

Chemical Formula	$Fe_2O(HPO_4)$
Crystal Appearance	Pale green needle
Crystal Size/ mm	0.04 x 0.04 x 0.01
M	223.67
Crystal System	Monoclinic
Space Group	*Cc*
a, b, c/ Å	12.9274(26), 6.5566(1), 9.6670(2)
α, β, γ / °	90.000(0), 116.482(3), 90.000(0)
V/ $Å^3$	733.4(8)
Z	4
T/ K	120
λ/Å	0.71073
Reflections collected	3363
Unique reflections	1451
R_{int}	0.0785
$R_1[I > 2\sigma(I)]^a$	0.0674
$R1$(all data)	0.1112
wR_2(all data)	0.1582

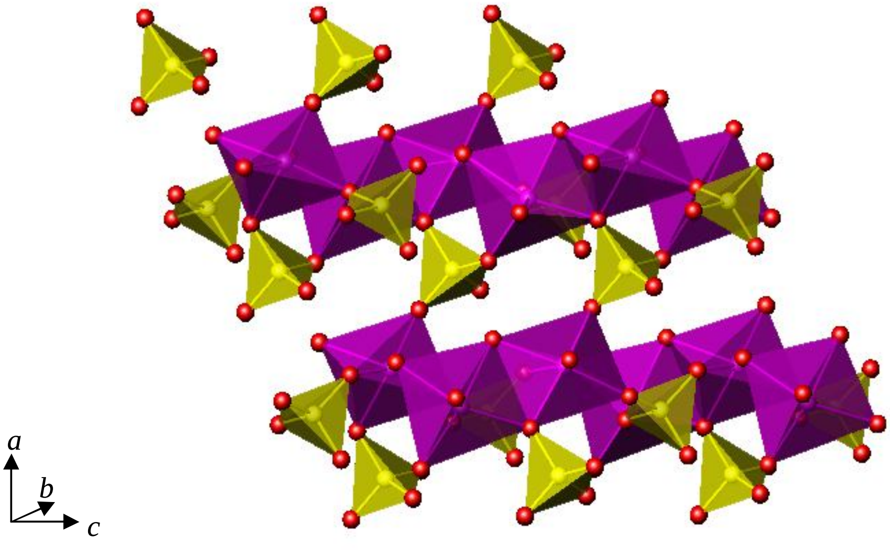

b)

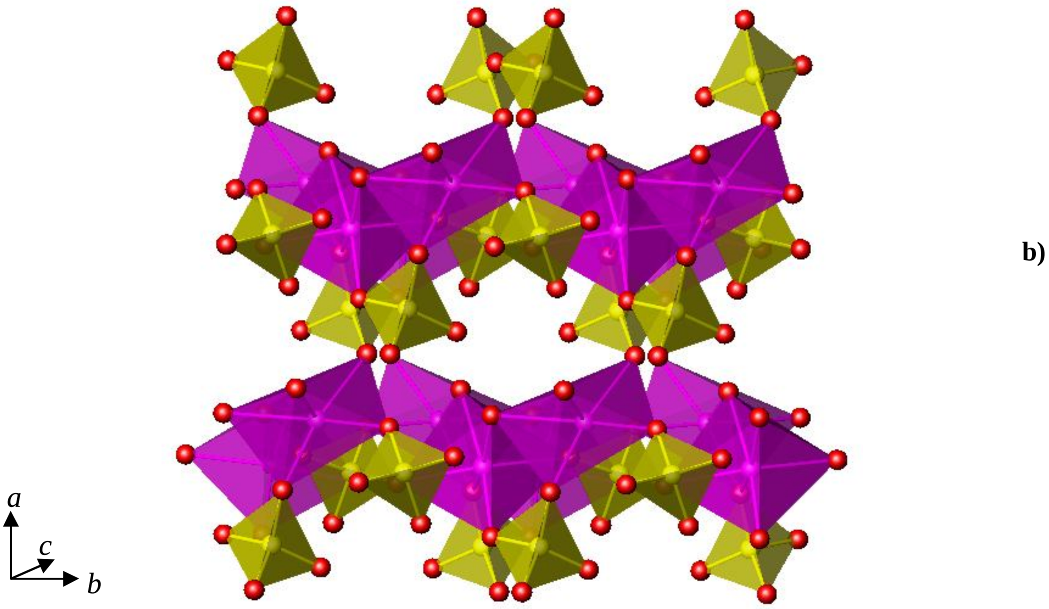

Figure 6.1: Structure of $Fe_2O(HPO_4)$ viewed down the a) *b*- and b) c-axes, where the iron octahedra are shown in pink, the phosphate tetrahedra in yellow and the oxygen atoms in red.

Table 6.3: Bond lengths in $Fe_2O(HPO_4)$.

Bond	Bond length/ Å	Bond	Bond length/ Å	Bond	Bond length/ Å
Fe1–O1	2.08(2)	Fe3–O1	2.04(2)	P1–O2	1.47(3)
Fe1–O3	2.04(2)	Fe3–O3	2.25(2)	P1–O3	1.52(2)
Fe1–O4	2.00(3)	Fe3–O6	2.14(3)	P1–O4	1.56(3)
Fe1–O8	2.19(3)	Fe3–O7	2.12(3)	P1–O6	1.54(4)
Fe1–O10	1.911(15)	Fe3–O9	1.900(17)	P6–O1	1.58(2)
Fe2–O2	2.14(3)	Fe4–O2	2.10(3)	P6–O5	1.49(3)
Fe2–O4	2.15(3)	Fe4–O6	2.12(4)	P6–O7	1.52(3)
Fe2–O5	2.13(3)	Fe4–O7	2.15(3)	P6–O8	1.53(3)
Fe2–O8	2.13(2)	Fe4–O5	2.15(3)		
Fe2–O9	2.209(18)	Fe4–O9	2.303(17)		
Fe2–O10	2.162(15)	Fe4–O10	2.198(15)		

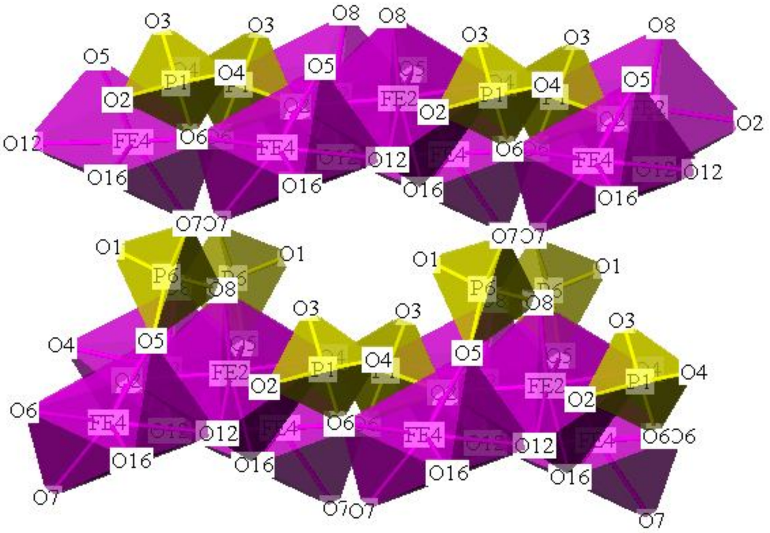

Figure 6.2: Cavity present within $Fe_2O(HPO_4)$, where FeO_6 are shown as pink octahedra and hydrogen phosphate groups as yellow tetrahedra.

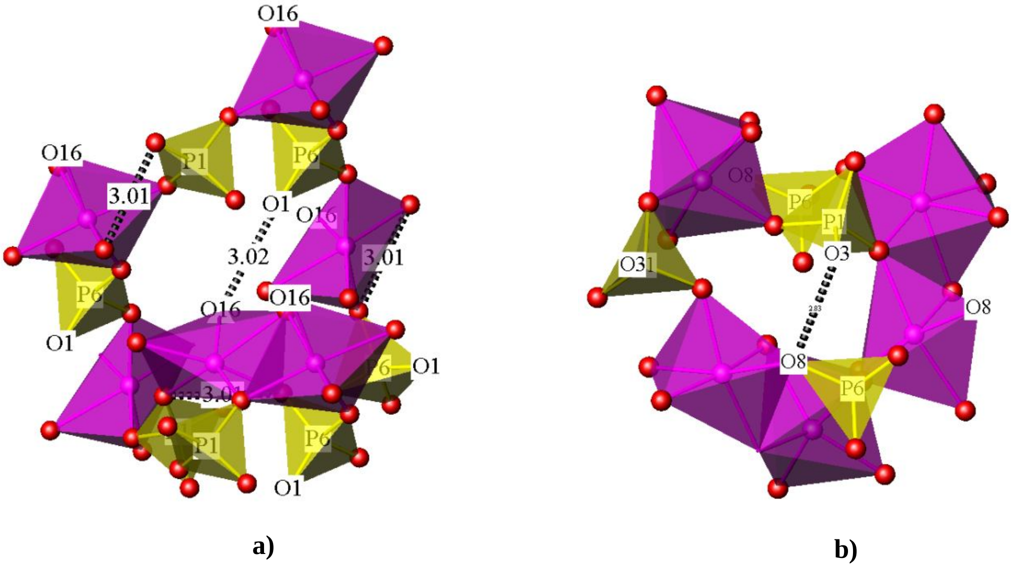

a)

b)

Figure 6.3: Probable hydrogen bonding for a) O1 and b) O3 within $Fe_2O(HPO_4)$ cavities, with possible hydrogen bonds shown as dashed lines.

The structure of $Fe_2O(HPO_4)$ can be compared with that of $Fe(PO_4)(H_2O)_2$[26], a simple iron phosphate framework which is based on Fe(III) rather than Fe(II). Both materials were synthesised hydrothermally and both frameworks are made up of a network of alternate corner-sharing iron and phosphorus oxopolyhedra, though in this literature case, cavities are formed that contain the water molecules. There is no other example in the literature of iron phosphate framework with a structure as simple as the one described here, where there is not a cation or molecule within the structural cavities.

EDS showed semi-quantitatively the presence of iron, phosphorus and oxygen in agreement with the stoichiometries calculated from the SXD structure determinations. During this analysis, an SEM image of $Fe_2O(HPO_4)$ was taken and shown in Figure 6.4.

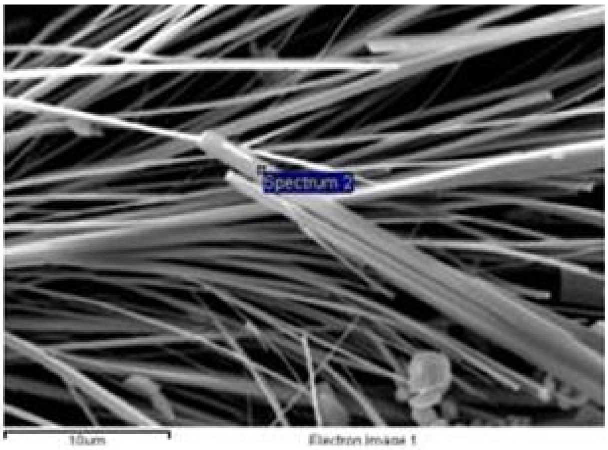

Figure 6.4: SEM image of a single crystal of $Fe_2O(HPO_4)$.

6.2-$(NH_4)_3Fe_3(HPO_4)_6$

A green block-like single crystal was selected for single crystal X-ray diffraction and a summary of the data collected is given in Table 6.4. Triclinic symmetry exists within the framework, which consists of $Fe(III)O_6$ octahedra and PO_4 tetrahedra which alternate to form edge-sharing chains parallel to the *b*- and *c*-axes, as shown in Figure 6.5. The bond lengths within the structure are shown in Table 6.5.

Bond valence calculations[25], combined with residual electron density seen in a single crystal refinement involving only the heavier atoms, was used to determine likely positions of the hydrogen atoms. These were subsequently located as hydrogen phosphate groups and the probable locations of the hydrogen atoms are shown in Figure 6.5. The hydroxyl groups are most likely located on the terminal oxygen atoms of the PO_4 group. The other three oxygen atoms in each phosphate group form P–O–Fe linkages, making up part of the neighbouring FeO_6 octahedra, thus not requiring any further contribution to bond valence sums from hydrogen atoms. The hydroxyl oxygen atoms were also found to have longer P–O bonds than the others in the phosphate groups, again indicating that hydrogen atoms were present.

Table 6.4: Crystal data for $(NH_4)_3Fe_3(HPO_4)_6$.

Chemical Formula	$(NH_4)_3Fe_3(HPO_4)_6$
Crystal Appearance	Green block
Crystal Size/ mm	0.2 x 0.2 x 0.05
M	317.63
Crystal System	Triclinic
Space Group	P-1
a, b, c/ Å	7.1290(3), 8.8372(3), 9.4621(3)
α, β, γ / °	64.649(2), 70.328(2), 69.541(2)
V/ $Å^3$	492.27(3)
Z	1
T/ K	120
λ/Å	0.71073
Reflections collected	5764
Unique reflections	2072
R_{int}	0.0234
$R_1[I > 2\sigma(I)]^a$	0.0280
$R1$(all data)	0.0318
wR_2(all data)	0.0669

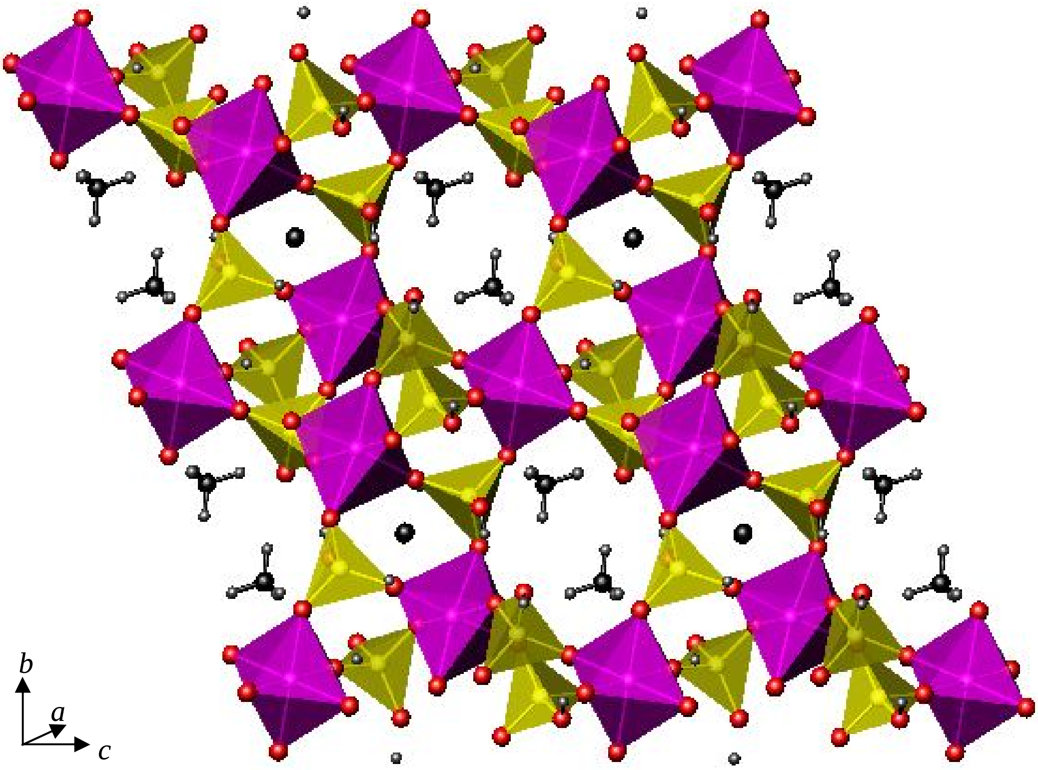

Figure 6.5: Structure of $(NH_4)_3Fe_3(HPO_4)_6$ viewed down the *a*-axis, where the iron octahedra are shown in pink, the phosphate tetrahedra in yellow, the oxygen atoms in red and the ammonium cations shown as black spheres to represent the nitrogen atoms and grey spheres to represent the hydrogen atoms.

Table 6.5: Bond lengths in $(NH_4)_3Fe_3(HPO_4)_6$.

Bond	Bond length/ Å	Bond	Bond length/ Å
Fe1–O1	2.021(2)	P3–O4	1.532(2)
Fe1–O2	1.958(2)	P3–O8	1.590(2)
Fe1–O4	2.042(2)	P3–O9	1.526(2)
Fe2–O6	1.943(2)	P3–O10	1.502(2)
Fe2–O7	2.051(2)	P4–O2	1.514(2)
Fe2–O9	2.029(2)	P4–O3	1.573(2)
Fe2–O10	1.951(2)	P4–O7	1.537(2)
Fe2–O11	1.959(2)	P4–O11	1.519(2)
Fe2–O12	2.051(2)	P5–O1	1.524(2)
		P5–O5	1.593(2)
		P5–O6	1.520(2)
		P5–O12	1.533(2)

The overall framework composition of this structure is $[Fe(III)_3(HPO_4)_6]^{3-}$. In order to charge-balance the overall structure, the extra-framework species can therefore be assigned as NH_4^+. An IR spectrum also supported the presence of N–H stretched within this material. The unit cell of this structure contains three ammonium cations that are distributed over two different cavities that exist within the framework, which can be seen in Figure 6.5. The two equivalent NH_4^+ groups are represented by tetrahedra and are found together within one large cavity, which has a cross-cavity dimension of 4.70 Å, as shown more clearly in Figure 6.6. The third ammonium cation, (with N2 as the central atom), lies on a centre of inversion and thus the hydrogen atoms were found to be disordered. Attempts to locate the protons of this ammonium cation failed and all of the hydrogen atoms which bond to N2 was omitted from the refinement but are included in the final formula. This second type of ammonium cation is located in a second, smaller cavity in the framework, which has a maximum cross-cavity distance of only 3.02 Å, as depicted in Figure 6.7. Table 6.6 shows the hydrogen bonding interactions between the two ammonium cations within the same cavity and the polyhedral oxygen atoms. It may be seen that all of the hydrogen bonding interactions for the two ammonium cations within the same cavity are as would be expected from a tetrahedral cation.

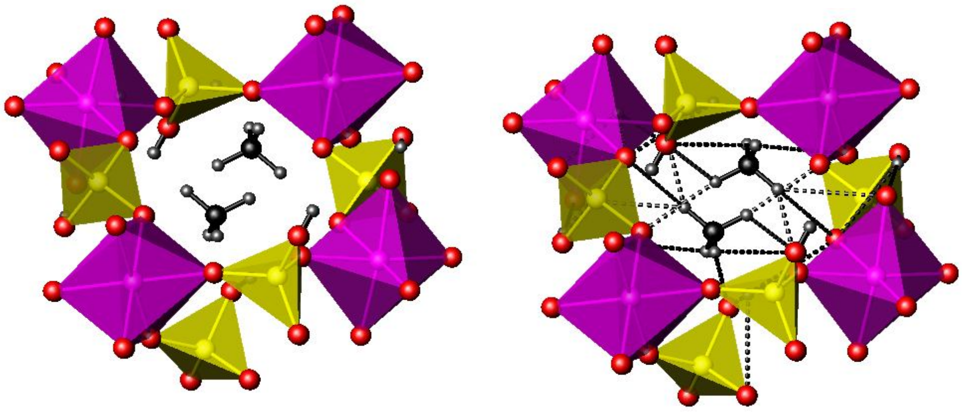

a) b)

Figure 6.6: Larger cavity present within $(NH_4)_3Fe_3(HPO_4)_6$: a) without hydrogen bonds shown, b) with hydrogen bonds shown. In both figures, FeO_6 are shown as pink octahedra, HPO_4 as yellow tetrahedra and the ammonium cations as black spheres to represent the nitrogen atoms and grey spheres to represent the hydrogen atoms.

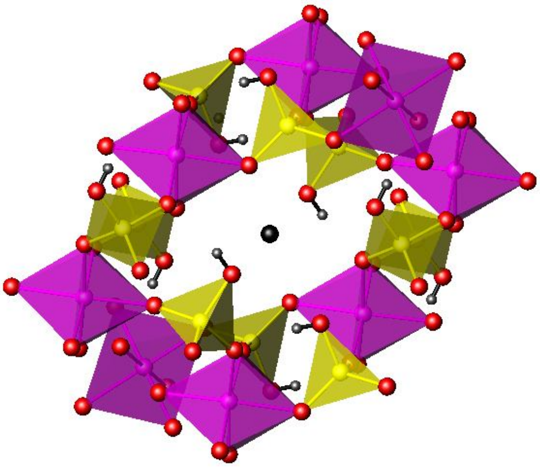

Figure 6.7: Smaller cavity present within $(NH_4)_3Fe_3(HPO_4)_6$, where FeO_6 are shown as pink octahedra, HPO_4 as yellow tetrahedra and the ammonium cations as black spheres to represent the nitrogen atoms and grey spheres to represent the hydrogen atoms.

Table 6.6: Hydrogen bonding distances and angles in $(NH_4)_3Fe_3(HPO_4)_6$, where *d* = distance between stated atoms.

N–H - - A	d(N–H)/ Å	d(H - - O)/ Å	d(N - - O)/ Å	Angle NHO/ °
N1–H2 - - O3	0.89	2.48	2.95	112.88
N1–H3 - - O12	0.90	2.75	3.41	131.78
N1–H6 - - O8	0.86	2.06	2.91	171.08
N1–H7 - - O4	0.78	2.76	3.28	126.38

There are only a few examples of iron phosphates that contain ammonium cations in their framework cavities, including $(NH_4)Fe_3(H_2PO_4)_6(HPO_4)_2{\cdot}(H_2O)_4$[27] which was also synthesised hydrothermally. In this structure there is only one ammonium environment and, although the two structures are comparable, the new structure discussed here contains a greater proportion of ammonium cations, which could be used for effective ion exchange. Another example of an ammonium iron phosphate is $(NH_4)Fe_2(PO_4)_2$[28], synthesised *via* a high-temperature, high-pressure hydrothermal route carried out in gold ampoules. Within this structure, there are two different ammonium environments, both of which are found within the same cavity. Each of the ammonium cations forms hydrogen bonds to the surrounding oxygen atoms of the iron- and phosphorus-centred polyhedra, in common with $(NH_4)_3Fe_3(HPO_4)_6$.

TGA supported the presence of the ammonium cations in this structure, as already suggested in the single crystal refinement. These data, shown in Figure 6.8, show that the ammonium cations are lost from the framework in two stages starting at approximately 200 °C with the loss of 2.26 % of the structural mass, where one ammonium cation is removed from the structure. A second larger weight-loss stage, of 5.52 %, probably corresponding to the decomposition of two ammonium cations, occurred at around 300 °C. Further decomposition of the residual iron hydrogen phosphate occurs with the loss of water, (from the P–OH groups), at around 450 °C. Powder X-ray diffraction data collected from the product showed it to be a simple iron phosphate structure, such as $FePO_4$, when the JCPDS powder diffraction file was viewed.

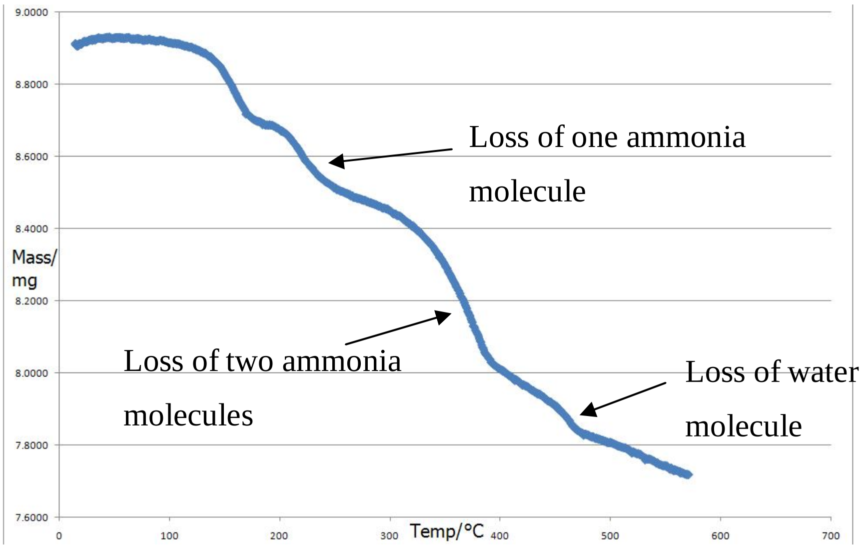

Figure 6.8: TGA plot for thermal decomposition of $(NH_4)_3Fe_3(HPO_4)_6$.

EDS analysis showed semi-quantitatively the presence of iron, phosphorus and oxygen in agreement with the stoichiometries calculated from the SXD structure determinations. The nitrogen atoms were not seen due to their small atomic number in comparison with iron. However, the EDS confirmed that there were no other cations such as K^+ or Rb^+ present within this structure. An SEM image of single crystals of $(NH_4)_3(Fe_3(HPO_4)$ is shown in Figure 6.9.

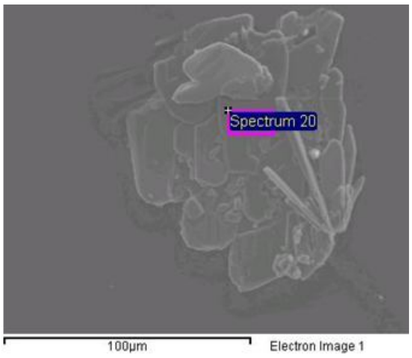

Figure 6.9: SEM image of a single crystal of $(NH_4)_3Fe_3(HPO_4)_6$.

6.3-$Fe_{1.34}(PO_4)OH_{0.96}$

A black jack-stone shaped single crystal was selected for single crystal X-ray diffraction and the data are summarised in Table 6.7. A compound with a composition close to the one discussed here has previously been reported[18] but its structure was only analysed from powder diffraction data rather than single crystal analysis. This structure is the synthetic analogue of lipscombite, a well-studied mineral[29].

The framework exists with tetragonal symmetry and is built up from chains of FeO_6 octahedra which run along both the *a*- and *b*-axes, as shown in Figure 6.10. With the face-sharing octahedra being unfavourably close together, Fe - - Fe contacts develop across the shared faces. To relieve this, the iron site is partially occupied, at about the ⅔ level, resulting in the non-stoichiometric formula for the iron phosphate backbone of $Fe_{1.34}(PO_4)O$. The iron cations are likely to adopt the +3 oxidation state based on previous studies of lipscombites by Mössbauer spectroscopy[30]. Furthermore, iron (III) nitrate nonahydrate was used in the synthesis of $Fe_{1.34}(PO_4)OH_{0.96}$, in the absence of any reductant. For simplicity, all of the atom sites are shown at full occupancy in Figure 6.10.

In order to change-balance the compound formula, protons must be introduced into the structure to produce the composition $Fe(III)_{1.34}(PO_4)OH_{0.96}$. Difference Fourier maps calculated from the SXD data showed likely positions for these protons on the oxygen atom forming the corner of the face-shared FeO_6 octahedra and in positions directed towards the centres of the FeO_6 octahedra. It is therefore likely that where iron vacancies occur in the FeO_6 octahedral chain the iron atoms are, in part, replaced by protons. Hydrogen atoms were included on these sites, and their coordinates refined, in the final stages of the structure refinement. It proved impossible to refine the hydrogen atom site occupancy, which was subsequently fixed to give an overall stoichiometry of $Fe(III)_{1.34}(PO_4)OH_{0.96}$. However, it is possible that partial reduction of the iron may occur with inclusion of additional charge balancing protons, as has been found in other phases from the lipscombite solid solution[31].

Table 6.7: Crystal data for $Fe_{1.34}(PO_4)OH_{0.96}$.

Chemical Formula	$Fe_{1.34}(PO_4)OH_{0.96}$
Crystal Appearance	Black block
Crystal Size/ mm	0.03 x 0.02 x 0.02
M	189.44
Crystal System	Tetragonal
Space Group	$I4_1/amd$
a, b, c/ Å	5.2061(3), 5.2061(3), 12.9609(1)
α, β, γ / °	90.000(0), 90.000(0), 90.000(0)
V/ $Å^3$	351.29(4)
Z	4
T/ K	120
λ/Å	0.71073
Reflections collected	1338
Unique reflections	128
R_{int}	0.0759
$R_1[I > 2\sigma(I)]^a$	0.0399
*R*1(all data)	0.0499
wR_2(all data)	0.0752

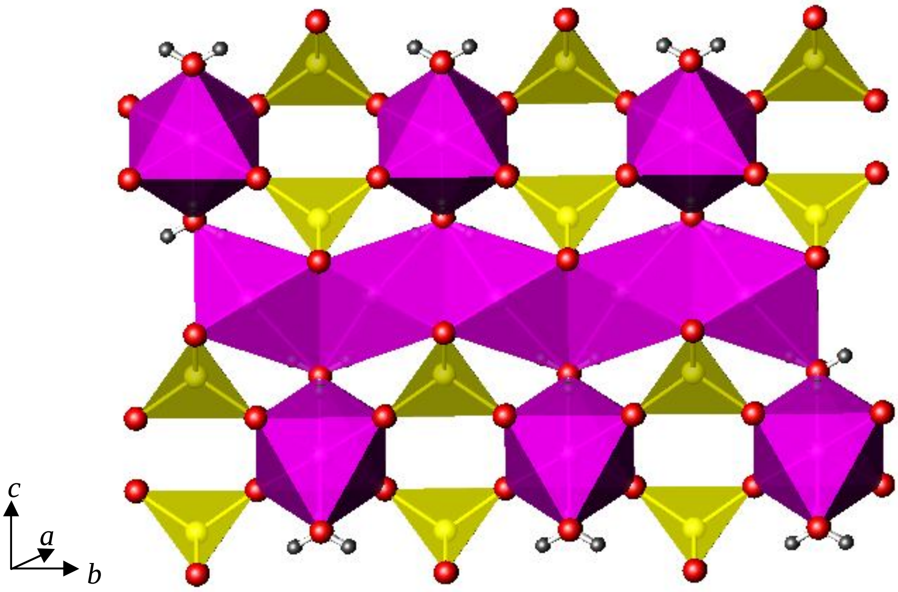

Figure 6.10: Structure of $Fe_{1.34}(PO_4)OH_{0.96}$ viewed down the *a*-axis, where the iron octahedra are shown in pink, the phosphate tetrahedra in yellow, the oxygen atoms in red and the hydrogen atoms in grey.

Within the chains, the occupied iron sites are displaced from the centres of the octahedra by approximately 0.18 Å, almost exactly along the direction of the chain. Using this information, a likely model for the cation and proton distribution along the chain can be constructed to minimise the Fe - - Fe repulsions across the octahedral faces. Every third iron atom is absent and replaced by one hydrogen atom. Where two adjacent iron sites are occupied, they are displaced in opposite directions along the chain and towards a neighbouring octahedral space, which is occupied only by protons. This structural model is summarised in Figure 6.11 and the bond lengths within this structure are given in Table 6.8, where the displacement of the iron sites results in two possible Fe–O bond lengths for both O1 and O3.

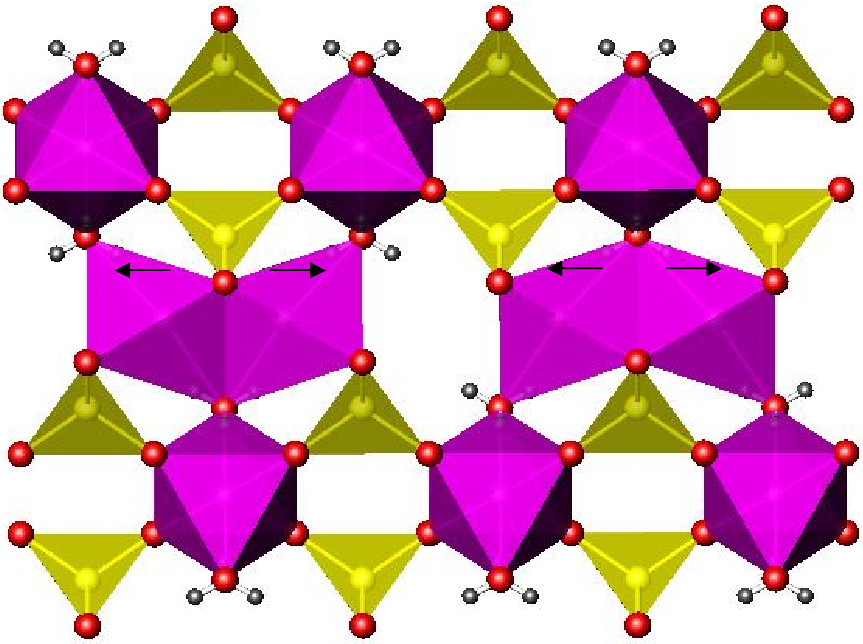

Figure 6.11: Structure of $Fe_{1.34}(PO_4)OH_{0.96}$, viewed down the *a*-axis. Two-thirds of the iron sites are occupied and local displacements are indicated by the black arrows. Iron octahedra are shown in pink, the phosphate tetrahedra in yellow, the oxygen atoms in red and the hydrogen atoms in grey.

Table 6.8: Bond lengths in $Fe_{1.34}(PO_4)OH_{0.96}$.

Bond	Bond length/ Å
Fe2–O1	1.903(8)
Fe2–O1	2.135(8)
Fe2–O3	1.978(15)
Fe2–O3	2.188(14)
P3–O1	1.532(4)

TGA data supported the single crystal refinement in suggesting the presence of the hydroxyl group in this material. Data collected on heating a sample from 25 °C to 650 °C showed a weight loss of 9.91 % between 300 °C and 450 °C consistent with decomposition of hydroxide, (at a level expected from the formula $Fe_{1.34}(PO_4)OH_{0.96}$), and loss of water. Powder X-ray diffraction data of the product showed that the thermal decomposition product was consistent with the literature patterns of $FePO_4$ or $Fe_4(P_4O_{12})_3$.

There are several reports of synthetic lipscombites with the same structure as seen here but with differing stoichiometries. For example, $Fe_{2.95}(PO_4)_2(OH)_2$ ($\equiv Fe_{1.48}(PO_4)OH$)[18], was also synthesised under hydrothermal conditions and has a structure based on ⅔Fe(III) and ⅓Fe(II) in FeO_6 octahedra. However, this structure displays a significantly higher level of site filling by iron, nearly 75%, when compared with $Fe_{1.34}(PO_4)OH_{0.96}$. A compound and structure with a lower ratio of iron to phosphate groups is $Fe_{1.176}(PO_4)(OH)_{0.57}(H_2O)_{0.43}$[18], corresponding to pure Fe(III). However, both this material and $Fe_{2.95}(PO_4)_2(OH)_2$ were only synthesised and studied as powders, which may account for differences in reported stoichiometry, especially if these were determined from refined site occupancies.

EDS analysis showed semi-quantitatively the presence of iron, phosphorus and oxygen in agreement with the stoichiometries calculated from the SXD structure determinations. An SEM image of a single crystal of this material is shown in Figure 6.12, showing the morphology and dimensions of the “jackstone-shaped” single crystals.

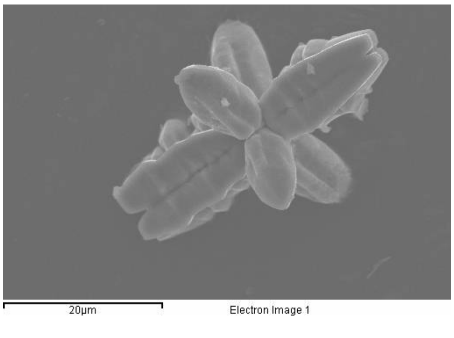

Figure 6.12: SEM image of a single crystal of $Fe_{1.34}(PO_4)OH_{0.96}$.

6.4-Conclusions for Iron Phosphate Materials

Two new iron phosphate are presented here, $Fe(II)_2O(HPO_4)$ and $(NH_4)_3Fe(III)_3(HPO_4)_6$[32]. A third iron phosphate structure, $Fe_{1.34}(PO_4)OH_{0.96}$, is also discussed, which offers an improved model for a known mineral structure. As Table 6.1 also shows, there were several reactions which resulted in the formation of single crystals but where the structures were already known. Given the number of previously reported iron phosphates, this is not surprising. Several of the single crystal structures that were solved *via* single crystal analysis were found to be starting materials but this was in those reactions with only a short reaction time, generally of 24 h. Those reaction mixtures which were heated for longer tended to result in the production of more complex structures, such as those discussed in this chapter. Table 6.1 also shows that, with the exception of $Fe_3(HPO_4)(H_2O)_4$[19], the reaction mixtures for the more complex of these known structures and also the novel frameworks contained either a template or ammonia solution. This indicates that the production of these iron phosphate single crystals is aided by the presence of a structure-directing agent. By using a range of starting materials within the attempted reactions, it was shown that iron (II) oxalate was readily reactive under these synthetic conditions and was used as a starting material in many of the reactions where single crystals were produced. This was also found to be the case for both orthophosphoric acid and ammonium dihydrogen phosphate.

$Fe(II)_2O(HPO_4)$ was synthesised under acidic, hydrothermal conditions and consists of edge-sharing FeO_6 octahedra which form infinite zig-zag chains that are linked by hydrogen phosphate groups. There are small cavities seen between these chains and these are cross-linked by hydrogen bonds that form between the iron octahedra and the hydrogen phosphate tetrahedra. Given the current interest in iron phosphate phases as battery materials, the framework discussed here is of considerable interest. It is worth noting that there is no other example in the literature of an iron phosphate framework with a structure as simple as that of the one described here, where there is not a cation or molecule within the structural cavities. This phase may be used as a precursor to a simple iron phosphate material for use in high capacity battery materials.

The second novel iron phosphate discussed in this chapter, $(NH_4)_3Fe(III)_3(HPO_4)_6$, is made up of alternating FeO_6 and HPO_4 which form an edge-sharing chain and was synthesised hydrothermally, under acidic conditions. These chains are cross-linked by further hydrogen phosphate groups, resulting in two types of cavity, both of which are occupied by ammonium cations. Due to the current, intense interest in iron phosphate phases as battery materials, this framework is of great interest. This phase may act as a precursor to a simple iron phosphate material for use in battery applications as it readily decomposes on heating to produce a fine powder of a phase such as $FePO_4$ or $Fe_4(P_4O_{12})_3$, which may lead to high capacity battery materials.

Alternatively, it may be possible that the cavities within the $(NH_4)_3Fe_3(HPO_4)_6$ framework, which currently contain ammonium cations, could be used for direct ion exchange. If the NH_4^+ cations could be exchanged for lithium cations, it would be possible to produce highly-mobile lithium ions. Lithium insertion reactions have previously been reported for materials with the lipscombite structure, producing $Li_xFe_{1.19}PO_4F_{0.11}(OH)_{0.46}(H_2O)_{0.43}$[33]. With the structure presented in this work, there is relatively large proportion of ammonium cations and these may be ion exchanged with lithium cations. This would result in the Fe(III) complex phosphate becoming $Li_3Fe_3(HPO_4)_6$. Further ion exchange of the protons present in the channels could produce $Li_9Fe_3(PO_4)_6$, with high capacity battery potential, and this will be investigated further in the near future by other members of the research group.

The third structure presented in this chapter has the formula $Fe_{1.34}(PO_4)OH_{0.96}$ and may be used to produce an improved model for a synthetic lipscombite, where previous models had only been analysed *via* powder X-ray diffraction. The structure contains a chain of face-sharing Fe(III) octahedra with partial Fe-site occupancy. Under the hydrothermal conditions used, this phase grows as “jackstone-shaped” single crystals. As mentioned, lithium insertion reactions have previously been successfully carried out with the lipscombite structure[29], suggesting that this may be achieved here, especially now a more accurate model of the structure has been presented.

6.5-References

---

[1] C. N. R. Rao, *Proc. Indian Acad. Sci.* (*Chem. Sci.*), 2001, **113**, 363–374.

[2] K.-H. Lii, C.-H. Huang, *J. Chem. Soc., Dalton Trans*, 1995, **1995**, 571-574.

[3] K.-H. Lii, *J. Chem. Soc., Dalton Trans*, 1996, **1996**, 819-822.

[4] Y.-C. Jiang, S.-L. Wang, K.-H. Lii, N. Nguyen, A. Ducouret, *Chem. Mater.*, 2003, **15**, 1633-1638.

[5] W.-J. Chang, P.-C. Chang, K.-H. Lii, *J. Solid State Chem.*, 2003, **172**, 6-11.

[6] Y. Song, P. Y Zavalij, M. Suzuki, M. S. Whittingham, *Inorg. Chem.*, 2002, **41**, 5778-5786.

[7] P. P. Prosini, M. Lisi, S. Scaccia, M Carewska, F Cardelline, M. Pasquali, *J. Electrochem. Soc.*, 2002, **149**, A297-A301.

[8] Y. Song, S. Sang, P. Y. Zavalij, M. S. Whittingham, *Mater. Res. Bull.*, 2002, **37**, 1249-1257.

[9] J.-M. Chen, Y. j Li, W.-M. Hurng, M. S. Whittingham, U.S. Patent 5,514,490, 1996.

[10] A. K. Padhi, K. S. Nanjundaswamy, J. B. Goodenough, *J. Electrochem. Soc.*, 1997, **144**, 1188-1194.

[11] A. S. Andersson, B Kalska, L Häggström, J O Thomas, *Solid State Ionics*, 2000, **130**, 41-52.

[12] S. Yang, P. Y. Zavalij, M. S. Whittingham, *Electrochem. Comm.*, 2001, **3**, 505-508.

[13] S. Shi, C. Ouyang, Z. Xiong, L. Liu, Z. Wang, H. Li, D.-S. Wang, L. X. Huang, *Phys. Rev.* B, 2005, 71, 144404.1-144404.6.

[14] M. A. E. Sanchez, G. E. S. Brito, M. C. A. Fantini, G. F. Goya, J. R. Matos, *Solid State Ionics*, 2006, **177**, 497–500.

[15] Y. Song, P. Y. Zavalij, N. A. Chernova, M. S. Whittingham, *Chem. Mater.*, 2005, **17**, 1139-1147.

[16] M. L. Lindberg, C. L. Christ, *American Crystallographic Association: Program and Abstracts*, 1959, 20-21.

---

[17] G. J. Redhammer, G. Tippelt, G. Roth, W. Lottermoser, G. Amthauer, *Phys. Chem. Miner.*, 2000, **27**, 419-429.

[18] R. Cini, L. G. Marzilli, *Inorg. Chem.*, 1988, **27**, 1856-1858.

[19] I. Vencato, Y. P. Mascarenhas, E. Mattievich, *Am. Miner.*, 1986, **71**, 222-226.

[20] F. Mazzi, C. Garavelli, *Periodico, di Mineralogia*, 1957, **26**, 269-303.

[21] S. Caric, *Bulletin de la Societé Française de Mineralogie et de Cristallographie,* 1959, **82**, 50-56.

[22] C. C. Torardi, W. M. Reiff, L. Takacs, *J. Solid State Chem.*, 1989, **82**, 203-215.

[23] Z. A. D. Lethbridge, P. Lightfoot, *J. Solid State Chem.*, 1999, **143**, 58-61.

[24] A. Choudhury, S. Natarajan, *Proc. Ind. Acad. Sci., Serie: Chem. Sci.*, 1999, **111**, 627-637.

[25] N. E. Brese, M. O'Keefe, *Acta. Cryst. B*, 1991, B**47**, 192-197.

[26] Y. Song, P. Y. Zavalij, M. Suzuki, M. S. Whittingham, *Inorg. Chem.*, 2002, **41**, 5778-5786.

[27] A. Mgaidi, H. Boughzala, A. Driss, R. Clerac, C. Coulon, *J. Solid State Chem.*, 1999, **144**, 163-168.

[28] S. Boudin, K.-H. Lii, *Inorg. Chem.*, 1998, **37**, 799-803.

[29] Y. Song, P. Y. Zavalij, N. A. Chernova, M. S. Whittingham, *Chem. Mater.*, 2005, **17**, 1139-1147.

[30] T Loiseau, P Lacorre, Y Calage, J M Grenèche, G Férey, *J. Solid State Chem.*, 1993, **105**, 417-427.

[31] M. Dollé, S. Patoux, T. Richardson, *J. Power Sources*, 2005, **144**, 208-213.

[32] K. V. Redrup, M. T. Weller, *Dalton Trans.*, 2009, D.O.I.: 10.1039/b902519g.

[33] M. Dollé, S. Patoux, T. Richardson, *J. Power Sources*, 2005, **144**, 208-213.

Chapter 7

Sodium Tungstate Materials

It is well-documented that the Group V and VI metals, including tungsten, are able to form isopoly acids and their salts in aqueous solutions at intermediate and low pHs. Simple sodium tungstate structures, such as Na_2WO_4[1], may be synthesised in this way, by dissolving tungsten oxide in a strongly alkaline solution, resulting in the formation of tetrahedral MO_4^{2-} ions. It is from these anions that the simple sodium tungstates can be crystallised.

Although there are already many known sodium tungstate structures, most of these, such as $Na_{10}(H_2W_{12}O_{42})\cdot20H_2O$[2], are heavily hydrated, due to the solution methods commonly used in their synthesis, resulting in large open-frameworks. As well as containing many waters of hydration, the majority of the previously-reported sodium tungstate structures have been found to have a low H : Na ratio, due to neutral reaction conditions, leading to only a low degree of structure-strengthening hydrogen bonding, also seen in the above example of a known sodium tungstate framework, $Na_{10}(H_2W_{12}O_{42})\cdot20H_2O$.

Previous investigations have shown that the polytungstate unit within these materials is almost always made up of WO_6 octahedra but the number of terminal oxygen atoms within each octahedron has been shown to vary, resulting in altered properties. Until recently it was thought that MO_6 octahedra with more than two neighbouring terminal oxygen atoms were unstable[3, 4], such as $Na_{10}(H_2W_{12}O_{42})\cdot27H_2O$[5] and $Na_{10}(H_2W_{12}O_{42})\cdot20H_2O$[6], where each polytungstate unit has only two protonated terminal oxygen atoms. However, $Na_5(H_3W_6O_{22})\cdot18H_2O$[7] contains two types of WO_6 octahedra, each of which has three terminal oxygen atoms in a *fac* configuration and the remaining three oxygen atoms bridge to other WO_6 octahedra. It was shown that the terminal oxygen atoms in $Na_5(H_3W_6O_{22})\cdot18H_2O$ are partially protonated as OH groups and thus stabilised and causing increased ionic-type interactions with the sodium cations than is usually seen in sodium tungstate frameworks.

The original aim of these syntheses was to investigate the complexation of tungstate ions with carboxylic acids; namely malic and tartaric acid. Although there was no carboxylate group incorporated into either of the final structures, these acids appeared to play an important role in controlling the pH of the reaction mixtures. By using acidic conditions, it was hoped that it would be possible to increase the incorporation of hydrogen cations as hydroxyl groups into the framework, resulting in stronger hydrogen bonding to hold the framework together and thus a more tightly packed structure. If this is the case, the resulting materials may possess potential interesting properties in the field of high density liquids. During studies into hydrothermal reaction conditions, it had previously been noted that the pH of a solution will affect the outcome of a hydrothermal reaction[8].

Although the production of single crystals was not achieved in many of the attempted reactions, the reaction conditions for the successfully synthesised and characterised tungstate frameworks are shown below in Table 7.1. This table also shows the only other reaction within this section of work in which single crystals were produced. During approximately 40 other reactions in this investigation, only powders were produced, which were analysed *via* powder X-ray diffraction. It was determined that the powders were either starting materials or known sodium tungstates, of which there are many. In a typical reaction, the starting materials were mixed and stirred briefly, then transferred to a 23 mL Parr hydrothermal bomb. The bomb was heated in an oven at the temperature and duration detailed in Table 7.1. The product in each case was retrieved by filtration under vacuum, washed with hot distilled water and dried in air. The following reactions in this chapter are a description and discussion of the new materials synthesised.

Table 7.1: Reaction conditions for sodium tungstate materials.

Starting materials	Temp. / °C	Reaction period / h	Type of single crystals produced	Product	Section in thesis
Sodium tungstate dihydrate (0.625 mmol, 0.200 g) and L-(-)-malic acid (1.875 mmol, 0.251 g) were each dissolved in distilled water (2.5 cm^3). The two solutions were combined and *N*, *N*-dimethylformamide (5 cm^3) was added drop-wise. Starting pH = 3.3.	220	168	White sheet	$Na_2[H_{10}W_{12}O_{42}]\cdot 20H_2O$	7.1
Sodium tungstate dihydrate (0.625 mmol, 0.206 g) and L-(+)-tartaric acid (0.625 mmol, 0.0938 g) were each dissolved in distilled water (2.5 cm^3). The two solutions were combined and *N*, *N*-dimethylformamide (5 cm^3) was added dropwise. Starting pH = 7.3.	220	168	White sheet	$Na_5[H_7W_{12}O_{42}]\cdot 20H_2O$	7.2
Sodium tungstate dihydrate (0.625 mmol, 0.206 g) and L-(-)-malic acid (0.313 mmol, 0.0419 g) were each dissolved in distilled water (2.5 cm^3). The two solutions were combined and *N*, *N*-dimethylformamide (5 cm^3) was added dropwise.	220	168	White sheet within major phase of brown solid	Stacked layers of crystals which could not be sufficiently separated to be solved *via* single crystal diffraction	

7.1-$Na_2[H_{10}W_{12}O_{42}]\cdot 20H_2O$

A white sheet-like single crystal was selected for single crystal X-ray diffraction and the crystallographic information is shown in Table 7.2. The monoclinic framework is made up of $W_{12}O_{42}$ clusters which are separated by sodium cations and water molecules and is shown in Figure 7.1. All of the bond lengths within the structure are given in Table 7.3. These clusters are made up of edge-sharing and corner-sharing WO_6 octahedra, which form a doughnut shape, shown in Figure 7.2. Each cluster is constructed from four groups of three-edge sharing octahedra which are then linked to one other by corner-sharing linkages.

Within this structure, there is one sodium cation environment, existing as an NaO_6 octahedron. Two of the equatorial oxygen atoms were seen to bond to neighbouring tungsten cations, (W3 and W4), also forming part of the WO_6 octahedra. Bond valence calculations[9] indicated that the four terminal oxygen atoms were all heavily underbonded, suggesting that there were in fact water molecules. The remaining water molecules within this structure were all found to be waters of crystallisation, depicted as red oxygen atoms in Figure 7.1. Although the hydrogen atoms were not identified by single crystal analysis, probable hydrogen bonding contact distances are present between the water molecule oxygen atoms and the WO_6 octahedra. This hydrogen bonding produces a rigid polyoxometallate (POM) structure.

Table 7.2: Crystal data for $Na_2[H_{10}W_{12}O_{42}]\cdot 20H_2O$.

Chemical Formula	$Na_2[H_{10}W_{12}O_{42}]\cdot 20H_2O$
Crystal Appearance	White sheet
Crystal Size/ mm	0.3 x 0.2 x 0.03
M	3294.42
Crystal System	Monoclinic
Space Group	$P2_1/c$
a, b, c/ Å	11.9865(4), 14.0300(5), 15.5104(4)
α, β, γ / °	90.000(0), 105.588(2), 90.000(0)
V/ $Å^3$	2512.45
Z	2
T/ K	120
λ/Å	0.71073
Reflections collected	31236
Unique reflections	5765
R_{int}	0.0994
$R_1[I > 2\sigma(I)]^a$	0.0453
$R1$(all data)	0.0780
wR_2(all data)	0.1100

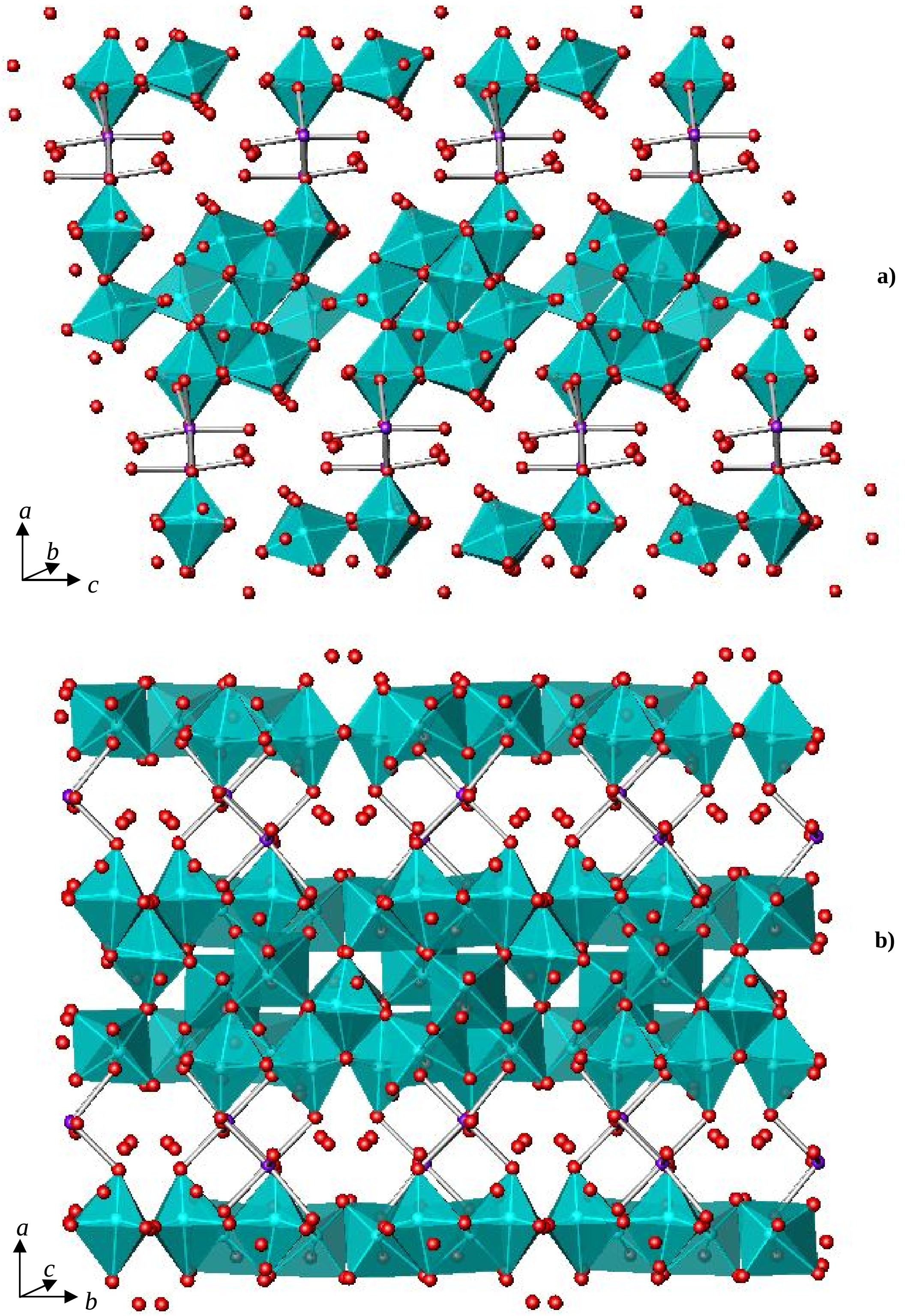

Figure 7.1: Structure of $Na_2[H_{10}W_{12}O_{42}]\cdot 20H_2O$ viewed down the a) *b*- and b) c-axes, where the tungsten octahedra are shown in turquoise, the sodium cations as purple spheres and the oxygen atoms in red.

Table 7.3: Bond lengths in $Na_2[H_{10}W_{12}O_{42}]\cdot 20H_2O$.

Bond	Bond length/ Å	Bond	Bond length/ Å	Bond	Bond length/ Å
W1–O1	1.972(8)	W4–O3	2.284(8)	Na1–O11	2.401(10)
W1–O2	1.726(9)	W4–O13	1.875(8)	Na1–O15	2.385(10)
W1–O3	1.900(8)	W4–O15	1.763(9)	Na1–OW1	2.328(12)
W1–O4	2.231(8)	W4–O16	1.723(9)	Na1–OW2	2.462(11)
W1–O5	2.065(8)	W4–O17	1.902(8)	Na1–OW6	2.361(12)
W1–O20	1.784(8)	W4–O18	2.236(9)	Na1–OW10	2.315(11)
W2–O4	2.236(8)	W5–O6	1.720(8)		
W2–O5	1.861(8)	W5–O9	1.909(9)		
W2–O7	1.844(9)	W5–O17	1.949(9)		
W2–O8	1.748(9)	W5–O18	2.199(8)		
W2–O9	1.894(9)	W5–O19	1.736(8)		
W2–O10	1.972(8)	W5–O20	2.176(8)		
W3–O3	2.196(8)	W6–O1	1.916(9)		
W3–O10	1.891(8)	W6–O4	2.258(8)		
W3–O11	1.772(9)	W6–O7	2.105(9)		
W3–O12	1.727(8)	W6–O14	1.784(9)		
W3–O13	1.936(8)	W6–O18	1.916(9)		
W3–O14	2.203(9)	W6–O21	1.730(8)		

The cavity in the centre of each cluster has a W–W distance of 5.6 Å and the closest O–O distance is 2.9 Å. This value may be compared with literature examples of polytungstates, such as $Na_{10}(H_2W_{12}O_{42})\cdot 20H_2O$[2] which is made up of very similar identical clusters. However, there is a high level of protonation within the clusters of the structure discussed here and the probable sites for hydroxyl groups within the $W_{12}O_{42}$ clusters were identified using bond valence calculations. Although it was again not possible to locate the hydrogen atoms during the single crystal refinement, as has been the case in other polytungstate studies, these calculations suggested that the protons were in fact disordered over eighteen sites, (namely O2, O3, O8, O11, O12, O15, O19 and O21 in Figure 7.2, of which there are two of each per cluster unit). Partial occupancy of these hydroxyl groups results in the final formula being charge-balanced. Each hydrogen atom of these hydroxyl groups is able to form hydrogen bonds to other, non-hydrated oxygen atoms, both within the centre of the cluster and on the outer side of the unit. These hydrogen bonds cause a slightly more tightly packed structure than expected, with the material having a density of 4.29 gcm^{-3}, which is compared with known examples in Table 7.3, meaning that this material may have potential uses within the field of high density liquids.

The high level of protonation within the clusters of $Na_2[H_{10}W_{12}O_{42}]\cdot20H_2O$ is as a result of the acidic reaction conditions used in the synthesis of this material and has resulted in a high H : Na ratio, as shown in Table 7.4. Although malic acid only has a pK_a of 3.4, it was used a ratio of 3 : 1 with sodium tungstate dihydrate, resulting in an acidic solution. The shortest distance between the centres of two neighbouring clusters is 9.34 Å, which can be compared with 10.55 Å for the less protonated $Na_{10}(H_2W_{12}O_{42})\cdot20H_2O$[2] and also with 10.87 Å for $Na_5[H_7W_{12}O_{42}]\cdot20H_2O$, the structure discussed in Section 7.2. This closer packing of the $W_{12}O_{42}$ clusters is a direct result of the greater level of hydrogen bonding between the disordered hydroxyl groups and the remaining oxygen atoms.

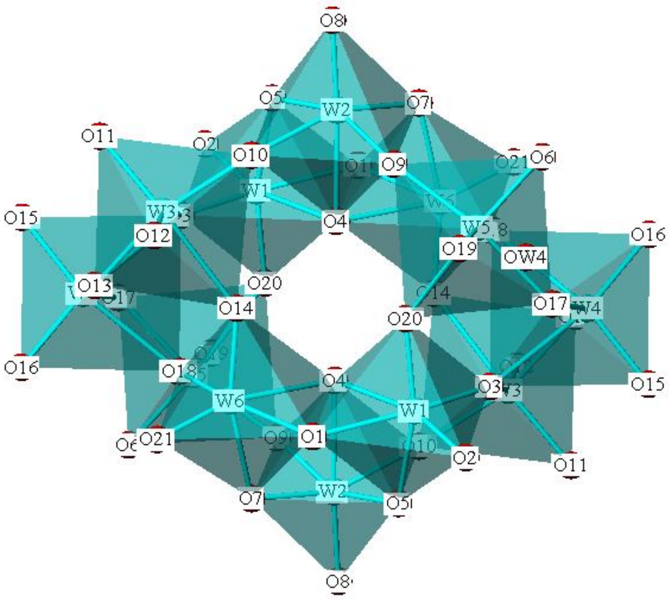

Figure 7.2: $W_{12}O_{42}$ cluster in $Na_2[H_{10}W_{12}O_{42}]\cdot20H_2O$, where WO_6 are shown as turquoise octahedra.

Table 7.4: A comparison between $Na_2[H_{10}W_{12}O_{42}]\cdot20H_2O$ and literature sodium tungstate structures.

POM	*Z*	Molar % water/%	Density of packing of POMs/gcm^{-3}	Units/Å^3 (* 10^{-4})	Ref
$Na_2[H_{10}W_{12}O_{42}]\cdot20H_2O$	4	10.9	4.29	3.99	5.1
$Na_5[H_7W_{12}O_{42}]\cdot20H_2O$	1	10.7	3.56	6.42	5.2
$Na_6W_7O_{24}\cdot14H_2O$	4	12.2	3.74	2.73	[10]
$Na_5(H_3W_6O_{22})\cdot18H_2O$	2	17.1	3.52	5.58	[7]
$Na_{10}(H_2W_{12}O_{42})\cdot20H_2O$	1	10.4	4.20	7.29	[2]
$Na_{10}(H_2W_{12}O_{42})\cdot27H_2O$	2	13.5	4.10	3.43	[11]

EDS analysis showed semi-quantitatively the presence of tungsten, sodium and oxygen. An SEM image is shown in Figure 7.3.

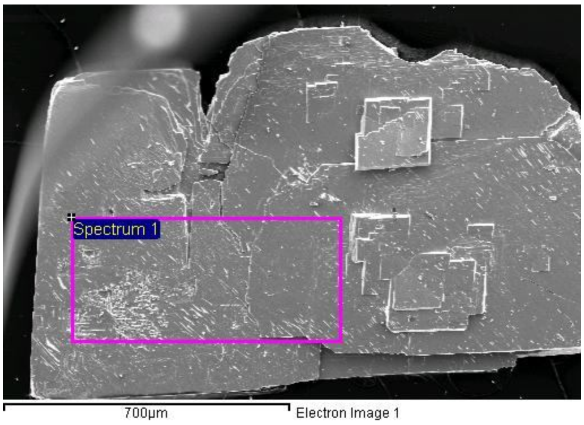

Figure 7.3: SEM image $Na_2[H_{10}W_{12}O_{42}]\cdot20H_2O$.

7.2-$Na_5[H_7W_{12}O_{42}]\cdot 20H_2O$

A white sheet-like single crystal was selected for single crystal X-ray diffraction and the data are shown in Table 7.5. The triclinic framework is made up of $W_{12}O_{42}$ clusters which are separated by sodium cations and water molecules and is shown in Figure 7.4. The tungstate clusters are comprised of both edge-sharing and corner-sharing WO_6 octahedra, as shown in Figure 7.5. Four groups constructed from three edge-sharing octahedra are linked to each other *via* corner-sharing linkages, in order to make up the $W_{12}O_{42}$ units. These clusters were found to form a doughnut shape, with a hole in its centre, as seen in Figure 7.5. The shortest W–W distance across the ring is 5.7 Å and the closest cross-cluster O–O distance is 2.9 Å, which may be compared with literature examples of polytungstates, such as $Na_{10}(H_2W_{12}O_{42})\cdot 20H_2O$[2] which is made up of almost identical clusters, both in structure and size. The shortest distance between the centres of two neighbouring clusters in the structure presented here was found to be 10.87 Å. Once again, this value is comparable to the distance of 10.55 Å seen in $Na_{10}(H_2W_{12}O_{42})\cdot 20H_2O$. The similarity in these values presumably represents the similar levels of hydration in the two structures. With these two structures, the only difference is the number of hydroxyl groups on the $W_{12}O_{42}$ cluster.

Within this framework, there are three different sodium environments. The first of these, Na1, is an almost perfect octahedron, where the NaO_6 unit is formed from three oxygen atoms of the polytungstate cluster and the other three from water molecules. The second sodium ion environment, Na2, exhibits decahedral geometry with NaO_7 units, which are formed by coordination from two polytungstate oxygen atoms and five water molecules. The third type of sodium ion, Na3, exists between two Na2 cations, with which bridging water molecules are shared. This sodium ion is essentially octahedrally coordinated by six water molecules with two much longer interactions with the two water molecules that bridge to two Na2 cations. The bond lengths for these Na–O bonds are shown in Table 7.6, along with the remainder of the bonds in this structure.

Within the layered arrangement of $W_{12}O_{42}$ clusters, there is a large void between the layers along the *b*-axis. A final electron density difference map[12] showed only a very small amount of scattered electron density within these voids, which was evenly distributed throughout this inter-layer region. This indicates that there may be a small level of disordered molecules, probably further water molecules but also possibly tartaric acid, in this region of the crystal structure. The potential exists for such species to hydrogen bond to O8 of the $W_{12}O_{42}$ unit, (as labelled in Figure 7.5), which was found to be under-bonded in the bond valence calculations[9].

Table 7.5: Crystal data for $Na_5[H_7W_{12}O_{42}]\cdot 20H_2O$.

Chemical Formula	$Na_5[H_7W_{12}O_{42}]\cdot 20H_2O$
Crystal Appearance	White sheet
Crystal Size/ mm	0.1 x 0.05 x 0.03
M	3360.36
Crystal System	Triclinic
Space Group	*P*-1
a, b, c/ Å	10.8677(4), 12.4370(4), 12.5313(4)
α, β, γ / °	72.260(2), 76.107(2), 87.059(2)
V/ $Å^3$	1558.52(1)
Z	1
T/ K	120
λ/Å	0.71073
Reflections collected	28074
Unique reflections	5498
R_{int}	0.0999
$R_1[I > 2\sigma(I)]^a$	0.0474
*R*1(all data)	0.0624
wR_2(all data)	0.1278

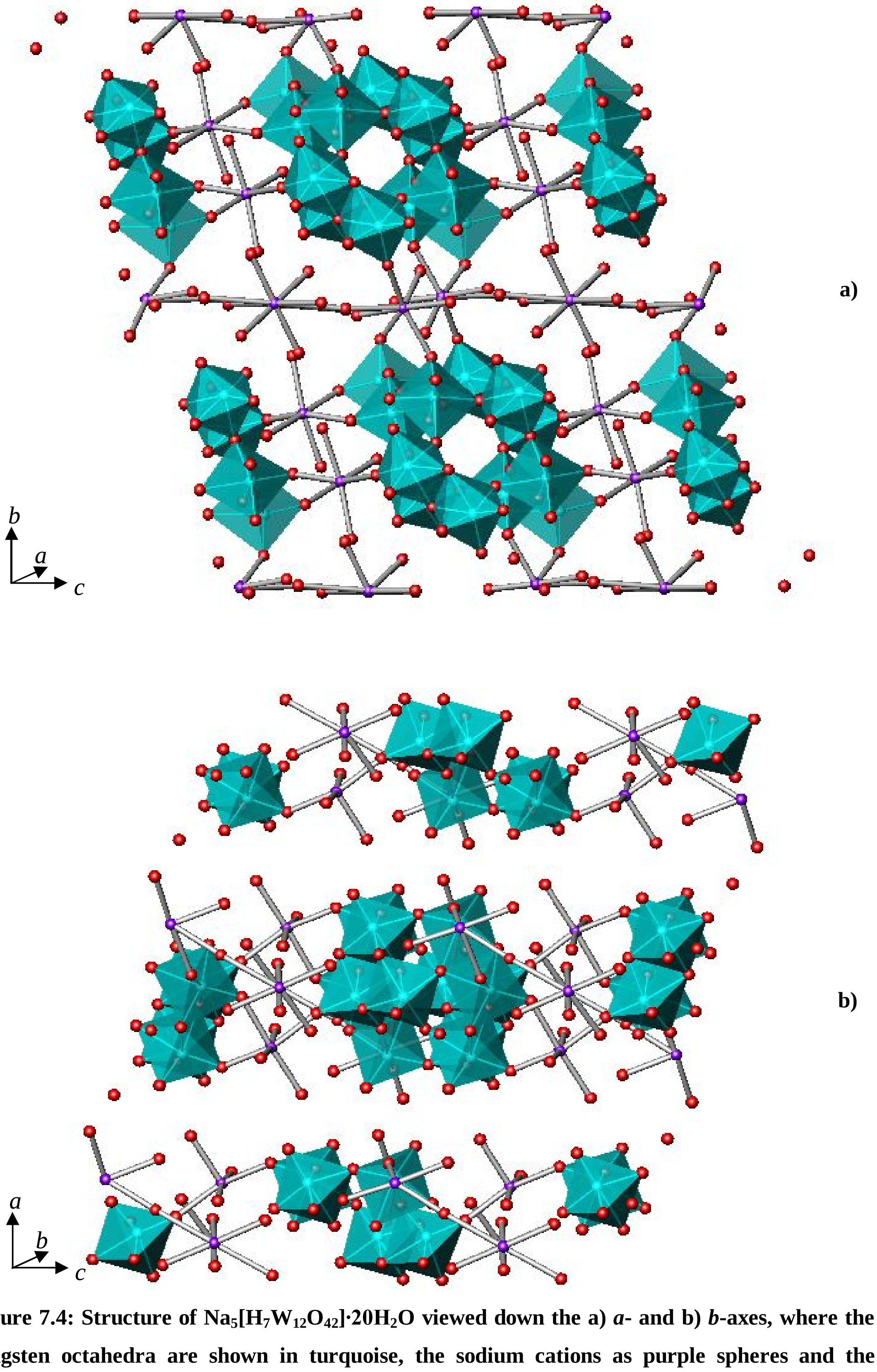

Figure 7.4: Structure of $Na_5[H_7W_{12}O_{42}]\cdot 20H_2O$ viewed down the a) *a*- and b) *b*-axes, where the tungsten octahedra are shown in turquoise, the sodium cations as purple spheres and the oxygen atoms in red.

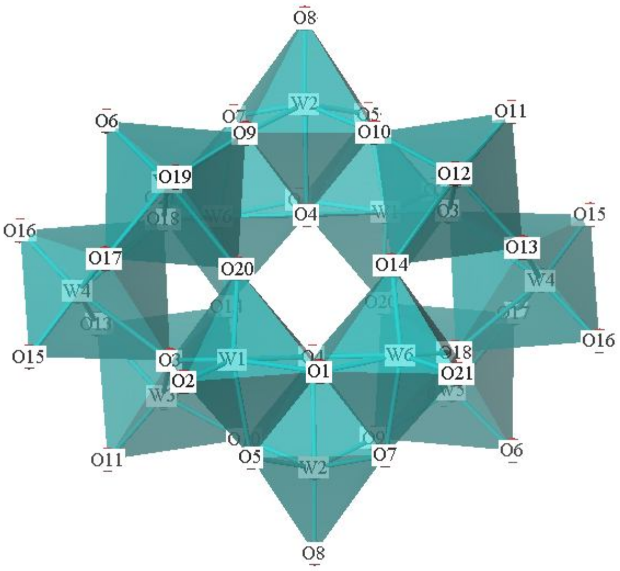

Figure 7.5: $W_{12}O_{42}$ cluster in $Na_5[H_7W_{12}O_{42}]\cdot20H_2O$, where WO_6 are shown as turquoise octahedra.

Table 7.6: Bond lengths in $Na_5[H_7W_{12}O_{42}]\cdot20H_2O$.

Bond	Bond length/ Å	Bond	Bond length/ Å	Bond	Bond length/ Å
W1–O1	1.95(10)	W4–O3	2.309(10)	Na1–O6	2.414(12)
W1–O2	1.747(10)	W4–O13	1.900(10)	Na1–O16	2.441(12)
W1–O3	1.897(10)	W4–O15	1.745(10)	Na1–O21	2.349(11)
W1–O4	2.268(9)	W4–O16	1.744(11)	Na1–OW1	2.392(13)
W1–O5	2.077(9)	W4–O17	1.892(10)	Na1–OW2	2.353(13)
W1–O20	1.814(10)	W4–O18	2.268(10)	Na1–OW3	2.44(2)
W2–O4	2.242(10)	W5–O6	1.738(11)	Na2–O2	2.377(15)
W2–O5	1.880(10)	W5–O9	1.901(10)	Na2–O11	2.410(15)
W2–O7	1.865(10)	W5–O17	1.971(10)	Na2–O15	2.463(15)
W2–O8	1.731(11)	W5–O18	2.215(10)	Na2–OW4	2.45(2)
W2–O9	1.942(10)	W5–O19	1.736(10)	Na2–OW5	2.46(2)
W2–O10	1.980(10)	W5–O20	2.30(11)	Na2–OW6	2.36(2)
W3–O3	2.203(10)	W6–O1	1.964(10)	Na2–OW7	2.30(2)
W3–O10	1.866(10)	W6–O4	2.261(9)	Na3–OW5	3.000(18)
W3–O11	1.748(11)	W6–O7	2.103(10)	Na3–OW8	2.401(11)
W3–O12	1.774(10)	W6–O14	1.801(10)	Na3–OW9	2.390(12)
W3–O13	1.955(10)	W6–O18	1.917(10)	Na3–OW10	2.396(13)
W3–O14	2.206(10)	W6–O21	1.740(10)		

It was not possible to locate hydrogen atom positions from the SXD data. This has been found to be the case in other polytungstate studies, where bond valence calculations have been used to locate some, if not all, of the hydrogen atoms[13]. Bond valence calculations[9] on the $W_{12}O_{42}$ cluster indicated that O2, O6 and 12 were heavily underbonded and thus form part of three hydroxyl groups. However, there are two of each of O2, O6 and O12 within each $W_{12}O_{42}$ cluster, giving six hydroxyl groups but disorder and partial occupancy are likely to occur for these six possible hydrogen atoms, resulting in a final cluster with the formula $[W_{12}O_{35}(OH)_7]$. An alternative possibility would be that the additional protons are bonded directly to water molecules producing H_3O^+, which may hydrogen bond to the terminal oxygen atoms. However, the observed low bond valences of O2, O6 and O12 make the protonated cluster more likely.

Having calculated which oxygen atoms are likely to be hydroxyl groups, it is also possible to see that these W–O bond lengths are significantly shorter when compared with the other W–O bonds within each octahedron. This can be illustrated by comparing the terminal O2 which is thought to be partially hydrated with the other oxygen atoms bonded to W2. W1–O2 has a bond length of 1.75 Å in comparison to the other bonds in this octahedron having a minimum bond length of 1.96 Å. This short bond, when coupled with the bond valence calculations[9], strongly suggests that there is at least partial hydrogenation of these oxygen atoms.

As well as hydrogen bonding on O2, O6 and O12, further hydrogen bonding is likely to be present involving the water molecules within the framework and other oxygen atoms in the $H_7W_{12}O_{42}$ unit. This hydrogen bonding produces a rigid arrangement of structure and the unique three dimensional distribution of POMs seen in Figure 7.4. The hydrogen bonds themselves are not shown due to the high level that exists, which would complicate the diagram. The density of $Na_5[H_7W_{12}O_{42}]\cdot 20H_2O$ is rather low in comparison with other polyoxotungstates at 3.56 gcm^{-3}, such as in the case of $Na_{10}(H_2W_{12}O_{42})\cdot 27H_2O$[7], with its higher water content, is 4.10 gcm^{-3}. This low density is due to its medium-high water content and its high H : Na ratio (1.4). This ratio seems to be influenced by the use of tartaric acid in the reaction mixture which has a fairly low pK_a of 2.98; used in a 1 : 1 ratio with sodium tungstate dihydrate. Within the structure discussed in this section, there is a moderately high H : Na ratio, which also results in a high level of hydrogen bonding within the clusters, augmenting the strength of the framework as a whole and the ability for the cluster to hold a small, neutrally-charged molecule. Table 7.7 shows a comparison of the H : Na ratios for literature examples.

Table 7.7: A comparison between $Na_5[H_7W_{12}O_{42}]\cdot20H_2O$ and literature sodium tungstate structures.

POM	*Z*	Molar % water/%	Density of packing of POMs/gcm^{-3}	Units/Å^3 (* 10^{-4})	Ratio of H : Na	Ref
$Na_5[H_7W_{12}O_{42}]\cdot20H_2O$	1	10.7	3.56	6.42	1.4	5.2
$Na_2[H_{10}W_{12}O_{42}]\cdot20H_2O$	2	10.9	4.29	3.99	5	5.1
$Na_5(H_3W_6O_{22})\cdot18H_2O$	2	17.1	3.52	5.58	0.6	[7]
$Na_{10}(H_2W_{12}O_{42})\cdot20H_2O$	1	10.4	4.20	7.29	0.2	[2]
$Na_{10}(H_2W_{12}O_{42})\cdot27H_2O$	2	13.5	4.10	3.43	0.2	[5]

EDS analysis showed semi-quantitatively the presence of tungsten, sodium and oxygen. An SEM image is shown in Figure 7.6.

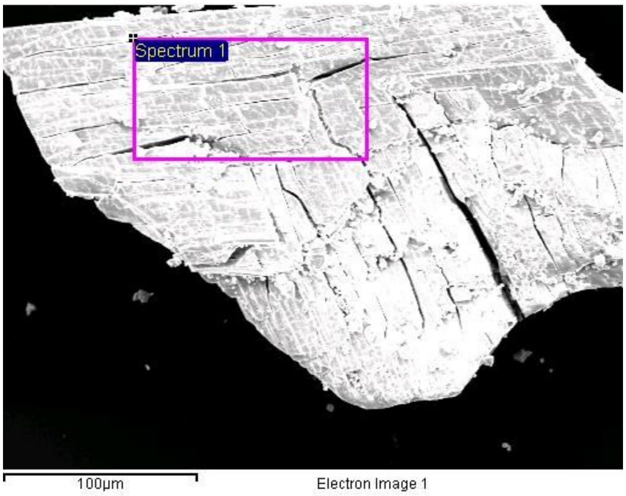

Figure 7.6: SEM image $Na_5[H_7W_{12}O_{42}]\cdot20H_2O$.

7.3-Conclusions for Sodium Tungstate Materials

The two sodium tungstate frameworks presented here[14], $Na_2[H_{10}W_{12}O_{42}]\cdot 20H_2O$ and $Na_5[H_7W_{12}O_{42}]\cdot 20H_2O$, are both made up of WO_6 octahedra, which form $W_{12}O_{42}$ clusters with a central cavity but result in slightly different framework structures. The only other reaction to result in the formation of single crystals could not be analysed *via* single crystal diffraction due to stacked layers which could not be separated. By comparing these three sets of reaction conditions, as well as those where single crystals were not produced, it may be seen that very specific conditions were required for the synthesis of those frameworks detailed in Sections 5.1 and 5.3. It may be seen that the ratio of the sodium tungstate dihydrate and carboxylic acid influences the outcome, presumably by due to the effect of pH on the reaction solution. Known sodium tungstate materials were found to be synthesised when a cooler temperature or shorter reaction duration was used, supporting the requirement that these novel materials require hotter and longer reaction conditions in order to contain less water and a level of protonation.

In $Na_2[H_{10}W_{12}O_{42}]\cdot 20H_2O$, there is just one NaO_6 environment, through which the $W_{12}O_{42}$ clusters are bonded to one another. Due to the acidic conditions used in this reaction, this structure contains a high level of protonation within the $W_{12}O_{42}$ clusters and thus a high H : Na ratio. As an outcome of this, strong hydrogen bonds are present between the resulting disordered hydroxyl groups and the remaining oxygen atoms, causing tight packing within the framework. As a result of this tight packing, $Na_2[H_{10}W_{12}O_{42}]\cdot 20H_2O$ has been found to have a high density of 4.29 gcm^{-3}, which could be of use within the field of high density liquids.

The second sodium tungstate discussed here is moderately highly protonated, giving the formula $Na_5[H_7W_{12}O_{42}]\cdot 20H_2O$. The $W_{12}O_{42}$ cluster is formed from both corner-sharing and edge-sharing WO_6 polyhedra. Sodium ions exist in both NaO_6 octahedral and NaO_7 decahedral coordination geometries between the layered POM units, resulting in a rigid framework. Bond valence calculations[9] showed that the hydroxyl groups within this framework are directed towards the exterior of the clusters. The cavities have the potential to be filled by a small, neutrally-charged molecule which may form hydrogen bonds with the oxygen atoms at the centre of the cavities.

7.4-References

---

[1] N. N. Greenwood, A. Earnshaw, *Chemistry of the Elements: Second Edition,* Elsevier Butterworth Heinemann 2003, 1009-1016.

[2] H. T. Evans, O. W. Rollins, *Acta. Cryst. B*, 1976, **B32**, 1565-1567.

[3] W. N. Lipscomb, *Inorg. Chem.*, 1965, **4**, 132-134.

[4] M. T. Pope, *Heteropoly And Isopoly Oxometalates*, Springer, Berlin, 1983, 19.

[5] A. Chrissafidou, J. Fuchs, H. Hartl, R. Palm, *Zeits. Natur., Teil B. Anorg. Chem., Org. Chem.*, 1995, **50**, 217-222.

[6] H. T. Evans, O. W. Rollins, *Acta. Cryst. B*, 1976, **B32**, 1565-1567.

[7] H. Hartl, R. Palm, J. Fuchs, *Angew. Chem.*, 1993, **105**, 1545-1547.

[8] Z. Matamoros-Veloza, K. Yanagisawa, J. C. Rendón-Angeles, S. Oishi, *J. Phys.: Condens. Matter.*, 2004, **16**, S1361–S1372.

[9] N. E. Brese, M. O'Keefe, *Acta. Cryst. B*, 1991, B**47**, 192-197.

[10] K. G. Burtseva, T. S. Cehrnaya, M. I. Sirota, *Doklady Akademii Nauk SSSR*, 1978, **243**, 104-107.

[11] A. Chrissafidou, J. Fuchs, H. Hartl, R. Palm, *Zeitschrift Fuer Naturforschung, Teil B. Anorganische Chemie, Organische Chemie*, 1995, **50**, 217-222.

[12] O. V. Dolomanov, H. Puschmann, *Olex 2*, University of Durham, 2004-2008.

[13] A. L. Nolan, C. C. Allen, R. C. Burns, G. A. Lawrance, E. N. Wilkes, T. W. Hambley, *Aust. J. Chem.*, 1999, **52**, 955-963.

[14] K. V. Redrup, M. T. Weller, *Dalton Trans.*, 2009, D.O.I.: 10.1039/b818103a.

Chapter 8

Conclusions

8.1-Overall Conclusions

The general aim of this project was to synthesise and characterise new framework materials with the intention of extending the range of known structures by using a variety of polyhedral, primarily octahedral and tetrahedral, building units. By using such a range of building units, it has been possible to produce new framework species which either have new or improved properties for a range of potential applications, such as ion exchange and energy storage.

The octahedral units within the novel frameworks were produced using transition metals, such as tungsten and iron. However, several transition metals were also investigated of which there were very few known framework structures before the characterisation of those studied here. For example, there were only a minimal number of reported hafnium arsenate and phosphate frameworks, thus presenting an ideal starting point to open up this area of framework chemistry.

The tetrahedral groups incorporated into in the novel materials in this work were arsenate and phosphate units. Although there are many known phosphate frameworks, there is a great deficit of the analogous arsenate materials, even considering that the arsenate framework often forms under less harsh conditions. Having said this, there is only a small number of both arsenate and phosphate frameworks for the larger Group IV and V metals.

Solvothermal syntheses were used for the synthesis of all the materials reported here. There was a wide range of solvents used within these reactions; from concentrated hydrochloric acid to water to concentrated ammonia solution. Other reaction conditions were changed for each of the solvents used, such as the duration of the experiment, the temperature at which the reaction was carried out and the concentration of the reagents.

By altering the reaction conditions, many novel frameworks were synthesised, as detailed in Chapters 3-7. These materials were then all fully characterised, with the primary method being Single Crystal X-ray Diffraction. Other analytical techniques were also employed in order to support the single crystal refinement; including powder and neutron diffraction, Thermogravimetric Analysis, Electron Dispersive Spectroscopy and Infrared Spectroscopy.

As discussed in Chapters 3-7, there was a considerable number of Group IV and V frameworks synthesised during the course of this work[1]. The majority of these were hafnium materials but the success in the synthesis of these led to similar reaction conditions being tried for the other metals within these two groups. The first of the hafnium frameworks to be produced was $HfF(H_2O)(AsO_4)$ and was also one of the most simple. This three-dimensional framework exists as a tightly packed, high density structure.

Most of the subsequent structures that were characterised were found to contain two-dimensional layers rather than this three-dimensional network, such as $HfF(AsO_4)_2(NH_4)_3$. In this structure, alternating $HfFO_5$ and AsO_4 polyhedra form four-membered rings, which then build up into two-dimensional layers. It appears that the presence of terminal fluorine atoms within the transition metal-centred polyhedra results in the formation of a two-dimensional material rather than a three-dimensional framework. These layers are separated from one another by ammonium cations and the framework is held together by hydrogen bonding interactions between the ammonium cations and the electronegative polyhedral atoms, namely fluorine and oxygen. In addition to the terminating affect of the fluorine atoms within many of the structures in this work, a similar influence on the dimensionality of some of the structures was seen due to the hydrogenation of arsenate and phosphate groups. This may be seen in the case of $Hf_2F_9(AsO_4H)\cdot(NH_4)_3(H_2O)$, where the acidic reaction conditions have resulted in a hydrogen-arsenate group within the framework, causing the termination of the structure along this axis. This hydrogenation may be partially explained due to the acidic reactions conditions used in many of the reaction mixtures where the effect is seen, as predicted due to a literature study[2], where the influence of pH due to the addition of an amine within metal phosphate reactions was investigated.

Several of the arsenate and phosphate materials are built up from four-membered rings from which discrete chains were found to form, such as in $TiF_2(PO_4)(HPO_4)(NH_4)_3$, where alternating titanium-centred octahedra and phosphate tetrahedra are linked *via* bridging oxygen atoms. Within this structure, it appears that the hydrogenation of the phosphate group acts in a similar manner to the polyhedral fluorine atoms, causing the termination of chains along this direction, thus resulting in the formation of a two-dimensional chain structure. The single crystal refinement for this structure and others which were found to exist in a similar manner showed that there were ammonium cations present between the chains. The resulting hydrogen bonding interactions led to rigid frameworks, with $TiF_2(PO_4)(HPO_4)(NH_4)_3$ found to be thermally stable up to 240 °C, at which point the ammonium cations start to be removed from the structure.

For all of these layered and chain structures, it was found that they are stable up to at least 175 °C when the ammonium cations started to be removed from the structure, with $ZrF_2(PO_4)(HPO_4)(NH_4)_3$ found to be the least thermally stable, presumably due to weaker hydrogen bonding than in the other, similar structures. After the removal of these interspatial ammonium cations, there was no evidence of any further structural decomposition until at least 460 °C in the $Hf_2F_9(AsO_4H)\cdot(NH_4)_3(H_2O)$ structure. This mass loss was calculated to represent the hydroxyl group of the hydrogen arsenate unit and therefore the start of the main framework decomposing. None of the other arsenate and phosphate frameworks in this study were found to decompose until greater temperatures, resulting in potential ion exchange applications due to the ammonium cations, provided that they could be removed from the framework without the use of too much energy but this would need to be investigated further.

There may also be potential, interesting applications within the field of hydrogen storage due to the presence of the ammonium cations. Although the hydrogen storage abilities of ammonia have been studied[3], a great deal of further investigative work would be required into the possibility of this potentially very interesting application. Further work would need to investigate, for example, whether structural collapse would occur during any changes to the material and also into the economic viability of the conditions required to allow such an application to work successfully.

Ion exchange may also be possible with the two templated structures discussed in Chapter 5 but the feasibility would need to be investigated. However, this may result in larger cations being incorporated into the structure due to the greater interspatial regions created by the presence of the DABCO units.

Of the iron phosphate frameworks that were characterised and detailed in Chapter 6[4], two were found to be novel and again possess potentially interesting properties. The existence of the ammonium cations within $(NH_4)_3Fe_3(HPO_4)_6$ once again offers potential ion exchange applications. However, lithium cation exchange reactions may eventually lead to $Li_9Fe_3(PO_4)_6$ forming, which may then have high capacity battery applications. Lithium insertion reactions have previously been successfully carried out, indicating that this route may be achievable[5]. Some work into this ion exchange has been attempted during this end of this work but has not yet reached a satisfactory result.

The final new structures reported within the work were two sodium tungstate materials[6]. Although these two frameworks are built up of the same $W_{12}O_{42}$ cluster, their final structures are slightly different to one another, resulting in a small variation in their properties. The first of these structures, $Na_2[H_{10}W_{12}O_{42}]\cdot 20H_2O$, contains a high level of protonation and thus a high H : Na ratio, as a result of the acidic reactions conditions. The resultant high level of hydrogen bonding causes the formation of a tightly packed framework with a density of 4.29 gcm^{-3}, allowing possible applications within the area of high density liquids. The second sodium tungstate material was found to be less protonated, resulting in a lower H : Na ratio, giving the formula $Na_5[H_7W_{12}O_{42}]\cdot 20H_2O$. The cavities in this structure have the potential to be filled by a small, neutrally-charged molecule, which would be able to form hydrogen bonds to those oxygen atoms of the $W_{12}O_{42}$ clusters that are directed towards the centre of the cavities.

As has been shown in the pages above, a number of novel structures has been synthesised and fully characterised, extending the range of known framework species, especially the Group IV and V arsenate and phosphate materials. By broadening the range of known frameworks of this type, a greater understanding of this area of chemistry may be achieved, particularly of the affect that the use of a fluoride source may have in the dimensionality of these materials. Also within this work, there have been several materials produced which possess potentially interesting applications which ought to be investigated further. It is hoped that the materials produced within this work and the methods explored to synthesise them may act as the starting point for the continuing progression of this area of inorganic framework materials.

8.2-References

---

[1] K. V. Redrup, M. T. Weller, being written.

[2] C. N. R. Rao, *Proc. Indian Acad. Sci.* (*Chem. Sci.*), 2001, **113**, 363–374.

[3] A. Klerke, C. H. Christensen, J. K. Nørskov, T. Vegge, *J. Mater. Chem.*, 2008, **18**, 2304-2310.

[4] K. V. Redrup, M. T. Weller, *Dalton Trans.*, 2009, D.O.I.: 10.1039/b902519g.

[5] M. Dollé, S. Patoux, T. Richardson, *J. Power Sources*, 2005, **144**, 208-213.

[6] K. V. Redrup, M. T. Weller, *Dalton Trans.*, 2009, D.O.I.: 10.1039/b818103a.

9-Appendix

The enclosed CD contains CIF data for the structures reported in this thesis.